NASA TECHNICAL NOTE

NASA TN D-8198 c.1

NASA TN D-8198

AERODYNAMIC CHARACTERISTICS OF A 1/6-SCALE MODEL OF THE ROTOR SYSTEMS RESEARCH AIRCRAFT WITH THE ROTORS REMOVED

Raymond E. Mineck, Carl E. Freeman, and James L. Hassell, Jr.

Langley Research Center
Hampton, Va. 23665

NATIONAL AERONAUTICS AND SPACE ADMINISTRATION • WASHINGTON, D. C. • JULY 1976

1. Report No.	2. Government Accession No.	3. Recipient's Catalog No.
NASA TN D-8198		

4. Title and Subtitle	5. Report Date
AERODYNAMIC CHARACTERISTICS OF A 1/6-SCALE MODEL OF THE ROTOR SYSTEMS RESEARCH AIRCRAFT WITH THE ROTORS REMOVED	July 1976
	6. Performing Organization Code

7. Author(s)	8. Performing Organization Report No.
Raymond E. Mineck, Carl E. Freeman, and James L. Hassell, Jr.	L-10435
	10. Work Unit No. 745-01-01-01

9. Performing Organization Name and Address	11. Contract or Grant No.
NASA Langley Research Center Hampton, Va. 23665	
	13. Type of Report and Period Covered
12. Sponsoring Agency Name and Address	Technical Note
National Aeronautics and Space Administration Washington, D.C. 20546	14. Sponsoring Agency Code

15. Supplementary Notes

Raymond E. Mineck and Carl E. Freeman: Langley Directorate, U.S. Army Air Mobility R&D Laboratory.

James L. Hassell, Jr.: Langley Research Center.

16. Abstract

A wind-tunnel investigation was conducted to refine the aerodynamic characteristics of the rotor systems research aircraft (RSRA). For the investigation, a 1/6-scale model without a main rotor or a tail rotor was used. The model provided the capability for testing different engine nacelle sizes, engine pylon fairings, and tail configurations. The engine thrust effects were modeled by small engine simulators (fans). Data were obtained primarily over an angle-of-attack range from -13° to 13° at several values of sideslip. Stability characteristics and control effectiveness were investigated.

The model with the scaled engine nacelles and the combination T-tail and lower horizontal tail displayed longitudinal and lateral-directional stability. Reducing the horizontal- or vertical-tail span reduced the longitudinal stability. Reducing the engine nacelle size increased the static stability of the model. Effective dihedral was essentially zero at 0° angle of attack and 0° wing incidence.

17. Key Words (Suggested by Author(s))	18. Distribution Statement
Compound helicopters Helicopters RSRA (rotor systems research aircraft)	Unclassified – Unlimited Subject Category 02

19. Security Classif. (of this report)	20. Security Classif. (of this page)	21. No. of Pages	22. Price*
Unclassified	Unclassified	189	$7.00

*For sale by the National Technical Information Service, Springfield, Virginia 22161

AERODYNAMIC CHARACTERISTICS OF A 1/6-SCALE MODEL OF THE ROTOR SYSTEMS RESEARCH AIRCRAFT WITH THE ROTORS REMOVED

Raymond E. Mineck,* Carl E. Freeman,*
and James L. Hassell, Jr.
Langley Research Center

SUMMARY

A wind-tunnel investigation was conducted to refine the aerodynamic characteristics of the rotor systems research aircraft (RSRA). For the investigation, a 1/6-scale model without a main rotor or a tail rotor was used. The model provided the capability for testing different engine nacelle sizes, engine pylon fairings, and tail configurations. The engine thrust effects were modeled by small engine simulators (fans). Data were obtained primarily over an angle-of-attack range from -13° to 13° at several values of sideslip. Stability characteristics and control effectiveness were investigated.

The model with the scaled engine nacelles and the combination T-tail and lower horizontal tail displayed longitudinal and lateral-directional stability. Reducing the horizontal- or vertical-tail span reduced the longitudinal stability. Reducing the engine nacelle size increased the static stability of the model. Effective dihedral was essentially zero at 0° angle of attack and 0° wing incidence.

INTRODUCTION

The role of helicopters is rapidly expanding in the world today, ranging from executive transports to air ambulances and rescue vehicles. Recognizing this fact, NASA and the U.S. Army have developed a unique rotorcraft to investigate advanced rotor concepts. This rotorcraft is designated the rotor systems research aircraft (RSRA). The RSRA was designed to be a flying test platform for evaluating various rotor concepts and control systems. To evaluate rotor performance and advanced control systems, the RSRA is equipped with a variable-incidence wing, auxiliary thrust engines, drag brakes, and fly-by-wire controls. The RSRA can be flown as a single-rotor helicopter, a compound helicopter, or a fixed-wing aircraft. The variable-incidence wing can provide upward or downward lift so that advanced rotor systems can be tested on the RSRA over

*Langley Directorate, U.S. Army Air Mobility R&D Laboratory.

a large range of rotor lift. Also, the auxiliary thrust engines and the drag brakes can be used to change the drag of the RSRA so that rotorcraft with a larger or smaller flat-plate drag can be simulated. Further details of the RSRA and its capabilities may be found in reference 1.

A wind-tunnel model of the RSRA without a main rotor or tail rotor has been tested in three phases to determine the aerodynamic characteristics of the RSRA with the rotors removed.

Phase I wind-tunnel test results indicated potential lateral- and longitudinal-stability problems. (See ref. 2.) Part of the problem was caused by an increased rate of downwash from the auxiliary thrust engines.

The Phase II results showed a significant improvement in the stability levels with a refined tail configuration. (See ref. 2.) The thrust effects still were not correctly simulated, so smaller scaled simulators of the auxiliary thrust engines were adapted to the model for Phase III testing.

Phase III wind-tunnel tests were conducted to refine further the tail configuration and the fairings which supported the auxiliary thrust engines. This report presents the results obtained in the Phase III tests of the model of the RSRA in the Langley V/STOL tunnel. The compound configuration with the rotors removed was the primary configuration tested and the subject of this report, although the pure helicopter and winged helicopter were also tested. Force and moment data were obtained at several thrust coefficients over ranges of angle of attack at several positive angles of sideslip.

SYMBOLS

The units used for the physical quantities defined in this paper are given in the International System of Units (SI) and parenthetically in the U.S. Customary Units. Measurements and calculations were made in U.S. Customary Units. Conversion factors relating the two systems are presented in reference 3.

The longitudinal data are resolved in the stability-axis system and the lateral data in the body-axis system. (See fig. 1.) The moment reference center was located 3.81 cm (1.5 in.) behind the center of the rotor hub. (See fig. 2.) All dimensions are given in the model scale.

b wing span, 229 cm (90.0 in.)

$\bar{c}$ mean aerodynamic chord

C_D	drag coefficient, D/qS
C_L	lift coefficient, L/qS
$C_{L_{i_w}}$	change in lift coefficient with wing incidence, dC_L/di_w
C_{L_α}	lift-curve slope, $dC_L/d\alpha$
C_l	rolling-moment coefficient, M_X/qSb
C_{l_β}	effective dihedral parameter, $dC_l/d\beta$
$C_{l_{\delta_a}}$	aileron effectiveness, $dC_l/d\delta_a$
C_m	pitching-moment coefficient, $M_Y/qS\bar{c}$
$C_{m_{i_t}}$	horizontal-tail effectiveness, dC_m/di_t
C_{m_α}	static longitudinal-stability derivative, $dC_m/d\alpha$
$C_{m_{\delta_e}}$	elevator effectiveness, $dC_m/d\delta_e$
C_n	yawing-moment coefficient, M_Z/qSb
C_{n_β}	static directional-stability parameter, $dC_n/d\beta$
$C_{n_{\beta,dyn}}$	dynamic directional-stability parameter, $C_{n_\beta} \cos \alpha - C_{l_\beta} \sin \alpha \frac{I_Z}{I_X}$
$C_{n_{\delta_a}}$	yaw due to aileron deflection, $dC_n/d\delta_a$
$C_{n_{\delta_r}}$	rudder effectiveness, $dC_n/d\delta_r$
C_T	thrust coefficient, T/qS
C_Y	side-force coefficient, F_Y/qS
C_{Y_β}	side-force derivative, $dC_Y/d\beta$

D	total aerodynamic force on airframe in drag direction, N (lbf)
F_Y	side force, N (lbf)
$\frac{I_Z}{I_X}$	ratio of moment of inertia about Z-axis to moment of inertia about X-axis, 4.542
i_t	lower horizontal-tail incidence, deg (see fig. 1(b))
i_w	wing incidence, deg (see fig. 1(b))
L	lift, N (lbf)
l_t	distance from moment reference center to center of pressure on horizontal tail, positive forward, m (in.)
M_X	rolling moment, N-cm (lbf-in.)
M_Y	pitching moment, N-cm (lbf-in.)
M_Z	yawing moment, N-cm (lbf-in.)
q	free-stream dynamic pressure, Pa (lbf/ft^2)
q_t	dynamic pressure at tail, Pa (lbf/ft^2)
S	wing area, 0.955 m^2 (10.28 ft^2)
S_t	lower horizontal-tail area, m^2 (ft^2) (see fig. 2(e))
T	thrust, N (lbf)
V_∞	free-stream velocity, m/sec (ft/sec)
α	angle of attack, deg (see fig. 1(a))
β	angle of sideslip, deg (see fig. 1(a))
Γ	geometric dihedral angle, deg

δ_a aileron deflection, deg

$\delta_{a,L}$ left aileron deflection, deg (see fig. 1(b))

δ_e elevator deflection, deg (see fig. 1(b))

δ_f flap deflection, deg (see fig. 1(b))

δ_r rudder deflection, deg (see fig. 1(b))

Subscripts:

max maximum

min minimum

MODEL AND APPARATUS

The model used in the wind-tunnel investigation was the 1/6-scale model of the RSRA shown in figure 2(a). (Also see table I.) This model did not have a main rotor or tail rotor. It was equipped with a removable, variable-incidence wing. The wing, which pivoted about the 3/4-chord location, could be set at incidence angles of -9°, -4.5°, 0°, 7.5°, and 15°. It had partial-span, single-slotted flaps inboard and plain ailerons outboard. Two sizes of auxiliary thrust engine simulators could be mounted on the model: the 20.32-cm (8.0-in.) diameter fans used in all three phases of the tunnel tests, and the smaller 13.97-cm (5.5-in.) diameter fans used only in the Phase III tests. (See fig. 2(b).) The fan-nacelle combination will be referred to as the large-diameter fans or the small-diameter fans.

Both sets of fans had a rotor and a stator. A ring with turbine blades was attached to the rotor. Dry, high-pressure air directed onto the turbine blades drove the fans to produce thrust. The small fans had one static-pressure orifice and three total-pressure probes mounted in the fan exit of each engine. The three total-pressure probes were connected to a manifold. A pressure transducer was used to measure the difference between the total pressure and the static pressure to obtain an average reference dynamic pressure at the exit. This exit reference dynamic pressure was used to calibrate the engine thrust.

The nacelles used with the small-diameter fans were 1/6-scale models of the TF34 engine nacelles to be used on the RSRA. The nacelles used with the large-diameter fans were larger in diameter and shorter in length than those used with the small-diameter

fans. Three criteria were used in positioning the large-diameter fans to simulate the jet exhaust and its effects. The edge of the fan exit was positioned at the proper longitudinal station, the proper distance from the fuselage, and the proper distance from the wing.

Several engine pylon fairings and engine positions were tested. The three types of pylon fairings were called the minimum fairing, the full fairing, and the gull fairing. (See fig. 2(c).) The minimum fairing was the box beam from the fuselage to the engine mounts with a rounded leading edge and a boattail trailing edge. This represented the minimum structure with minimal streamlining for mounting the engines. The full fairing had the leading edge faired into the fan cowl and the trailing edge extended farther aft than the minimum fairing. It was more streamlined than the minimum fairing although it had a greater wetted area. The gull fairing represented a modified box beam to reduce the interference between the engine and its support.

The full fairing was modified by cutting back the trailing edge of the fairing leaving 90 percent or 80 percent of the original fairing length. This reduced the wetted area of the full fairing. The modified full fairings were called the 90-percent full fairing and the 80-percent full fairing.

The minimum fairing was modified by filling in the area between the nacelle and support fairing and by building up the lower surface to provide a better flow field at the fan exits. (See fig. 2(d).) These were called the modified minimum fairings.

The entire engine-nacelle and pylon-fairing combination was moved forward 2.54 cm (1.00 in.) to change from the aft position to the forward position. The large-diameter fans were tested only with the full fairing at the aft fuselage station. The small-diameter fans were tested with three types of engine support fairings at both the forward and aft stations.

The horizontal and vertical tails were removable to permit testing the different tails shown in figures 2(e) and 2(f). Three different lower horizontal tails were tested: Tails A, B, and C. Tail A was used as the lower tail at the beginning of the Phase II wind-tunnel tests, and tail B was the lower tail developed during the Phase II tests. Tail B was formed from a smaller tail by placing sheet metal fairings bent into an airfoil shape over the outboard region of the tail. Tail C had the same area and span as tail B but had an NACA 0015 airfoil section and a constant chord. Tail C was modified by removing two 4.24-cm (1.67-in.) segments from the span; the resulting tails had a span of 118 cm (46.67 in.) or 110 cm (43.33 in.).

Tail C was equipped with a 30-percent-chord elevator. Each lower horizontal tail could be set at any incidence between -8° and 8°. The vertical tail also had provisions for mounting two different T-tails: a 43.6-cm (17.2-in.) span tail for compound

operations (tail E) and a 67.3-cm (26.5-in.) span tail for helicopter operations (tail D). Tail E was formed from a piece of aluminum plate with the leading edge rounded and the trailing edge blunted. The T-tails were restricted to 0° incidence.

The lower horizontal tails were designed with a small clearance between the root and the fuselage. This tail gap, which varied slightly along the root, was about 0.31 cm (0.12 in.) wide. Several combinations of the different components were tested. The designations used for the more extensively tested combinations are listed in table II.

A photograph of the model in the Langley V/STOL tunnel is shown in figure 3. The model was mounted on a strain-gage balance with a strut support in the forward part of the test section. The model could be set at various pitch angles relative to the strut to obtain different angle-of-attack ranges. The strut, which could be pitched and yawed, had an airfoil fairing which yawed with the strut and model.

High-pressure air was supplied to a plenum on top of the strut. Two S-shaped pipes carried the air across the balance to a plenum chamber within the model. The plenum chamber fed air through separate lines to each engine simulator. Each line had a valve to shut off one engine for engine-out testing or to balance the thrust between the two engines.

In the Phase I and Phase II wind-tunnel tests, strips of transition grit were not used. Therefore, to obtain the best comparison of results, no transition strips were used on the model with the large-diameter fans. For all other tests, transition strips were used on the wing, vertical tail, and horizontal tail.

TESTS AND CORRECTIONS

The tests were conducted in the Langley V/STOL tunnel, which has a test section measuring 4.42 m (14.50 ft) by 6.63 m (21.75 ft). All testing was done out of ground effect with the model close to the center line of the test section. At the highest velocity used in the tests, the free-stream dynamic pressure was 2633 Pa (55 lbf/ft^2); the Mach number was 0.195; and the Reynolds number, based on the mean aerodynamic chord, was 1.85×10^6.

Each engine-nacelle and pylon-fairing combination was calibrated when it was installed on the model. For the large-diameter fans, the thrust was calibrated against the fan speed. For the small-diameter fans, the resultant force from the thrust of each fan was calibrated against the difference between the dynamic pressure measured in the fan exit and the free-stream dynamic pressure. After calibration, the engine thrusts were balanced for zero yawing moment at static conditions.

The model was tested with windmill thrust, zero thrust, trim thrust, and sometimes at thrusts above or below trim thrust. At windmill thrust, the fans were turned by the free stream, so that they produced drag instead of thrust. At zero thrust $\left(C_T = 0\right)$, the dynamic pressure at the fan exit was set equal to the free-stream dynamic pressure for all angles of attack. At trim thrust, the thrust level was set for zero model drag $\left(C_D = 0\right)$ at 0^o model angle of attack. This trim thrust varied with configuration changes. The fan speed for this thrust level was maintained throughout the angle-of-attack range. At thrust levels above or below trim thrust, the thrust level was set for negative or positive drag at 0^o angle of attack, and the fan speed for this thrust level was maintained throughout the angle-of-attack range. Although the fan speed remained relatively constant, the thrust coefficient varied slightly throughout the angle-of-attack range.

Whenever possible, tests were conducted at a dynamic pressure of 2633 Pa (55 lbf/ft^2). The engine thrust was varied to achieve the desired thrust coefficient. When the maximum engine thrust was insufficient to achieve the desired thrust coefficients, the engines were operated at their maximum thrust level and the free-stream dynamic pressure was reduced.

Both engine positions and all pylon-fairing configurations were tested with various wing and flap combinations over angle-of-attack ranges at 0^o sideslip. Once the final engine position and pylon fairing had been determined, elevator deflection and horizontal-tail incidence were varied. To obtain directional data, the model was pitched through an angle-of-attack range at different angles of sideslip with the strut alined with the free stream. This procedure was followed to determine the effects of sideslip, rudder deflection, and aileron deflection.

The six-component strain-gage balance was calibrated with the two S-shaped air lines. These air lines supported part of the load, so that the balance output for a given load was smaller when the air line was attached. The largest decrease in balance sensitivity was about 4.3 percent in rolling moment. The air line also caused an interaction between the different balance components. The largest interaction correction was $\frac{0.512 \text{ N of axial force}}{1.000 \text{ N-m of rolling moment}} \left(\frac{0.013 \text{ lbf of axial force}}{1.000 \text{ lbf-in. of rolling moment}}\right)$. The sensitivity decrease and the interaction correction have been applied to the data obtained from the balance with the air line.

The model support system used for the tests was limited to an angle-of-attack range from -13^o to 13^o. To extend this range, the model was pitched on top of the strut. The three new angle-of-attack ranges used for some configurations were from -20^o to 6^o, -10^o to 16^o, and 0^o to 26^o. The data obtained in the overlapping part of the ranges are not in exact agreement. The lack of agreement may be caused by the changing strut tare, by problems associated with the air line, or by small changes in the thrust settings.

All data have been corrected for jet-boundary effects by the methods in reference 4 and for blockage effects by the method in reference 5.

PRESENTATION OF RESULTS

The results of the wind-tunnel investigation have been presented in coefficient form with the moments referenced to the station 3.81 cm (1.5 in.) behind the center of the rotor hub. This station represented the proposed aftermost center-of-gravity position of the aircraft. The longitudinal data are presented in the stability-axis system and the lateral data in the body-axis system. The results are presented as follows:

DISCUSSION OF RESULTS

Background

The Phase III wind-tunnel tests of the RSRA model were conducted to investigate configuration refinements to improve the level of stability and control as determined from the Phase II tests reported in reference 2. The Phase I tests were conducted with the large-diameter fans and full fairings. These tests revealed stability and control problems arising from a complex flow field in the region of the empennage. Analysis of the Phase I test results, however, led to several configuration changes and empennage options which were evaluated in the subsequent Phase II tests.

For the Phase II tests, the wing was shifted aft 3.81 cm (1.5 in.) and downward 3.81 cm (1.5 in.) to reduce the destabilizing trend caused by the wing aerodynamic center being too far forward relative to the assumed center-of-gravity location. The chord of the nacelle fairing was shortened to decrease the destabilizing increments caused by the fairing acting as a lifting surface forward of the assumed center of gravity and to decrease the rate of downwash in the region of the horizontal tail. Wing fences were installed on the upper surface beneath the engine fan cowl exit to delay flow separation with flaps deflected. The span of the vertical tail and rudder was increased 16.94 cm

(6.67 in.) to overcome static directional instability. This is referred to as the full-span (58.6 cm (23.1 in.)) vertical tail. Provisions were also made for installation of modified lower horizontal tails either alone or in combination with a T-tail.

Substantiation of Phase II Longitudinal Aerodynamics

Original Phase II configuration.- The original configuration for the Phase II tests incorporated (1) large-diameter fans mounted with the full pylon fairings in the rear position, (2) aft and downward shift of wing, (3) wing fences, (4) extended vertical-stabilizer and rudder span, and (5) lower tail A alone. This configuration was retested in the present investigation to establish baseline longitudinal aerodynamic data, and the results are presented for trim thrust in figure 4 for several values of wing incidence and for 15° wing incidence with flaps deflected. These data are substantially in agreement with Phase II test results (ref. 2, fig. 12) and confirm the static longitudinal instability over most of the middle angle-of-attack range. This instability is attributed to the combined effects of a strong downwash from the nacelle fairings acting on the inboard area of the horizontal tail and the destabilizing effect of the large-diameter fan nacelles. Flow surveys in the region of the horizontal tail were conducted during the Phase II tests and confirmed the existence of the strong downwash at the tail caused by vortex shedding from the nacelle fairing (ref. 2, pp. 30-33).

Final Phase II configuration.- Although testing during Phase II showed that the size of the nacelle-pylon fairing had significant effects on longitudinal stability, no practical modification was possible because of constraints imposed by the engine support struts on the model. Consequently, the selected final Phase II configuration had the same large-diameter fans with the full fairings as the original Phase II configuration. The only differences between the original and final Phase II configurations were the vertical- and horizontal-tail arrangements. The final configuration used an arrangement that was a combination of lower tail B and T-tail E.

This same configuration was retested in the present investigation to establish baseline longitudinal data for the final Phase II configuration. Results are presented in figure 5 for several values of wing incidence and for 15° wing incidence with flaps deflected for the trim-thrust condition. The tail modifications incorporated in the final Phase II configuration provided the required improvement in static longitudinal stability in the middle angle-of-attack range.

The longitudinal aerodynamics of this final Phase II configuration obtained in the Langley V/STOL tunnel and in the United Aircraft Research Laboratories (UARL) large subsonic wind tunnel during Phase II (ref. 2) are compared in figure 6. In general, the V/STOL tunnel data indicate 2 to 10 percent higher lift-curve slopes and values of maximum lift coefficient. Also, discrepancies are noted in the overall level of pitching-

moment coefficient which may be attributable to different model support interference effects in the two wind tunnels for the tail-on data. These discrepancies are opposite in trend at the extreme values of negative (-9°) and positive (15°) wing incidence. For the tail-on data, the pitching-moment slopes determined in the V/STOL tunnel are consistently more unstable than those determined in the UARL tunnel throughout the range of wing incidence. (Values of C_{m_α} are 2 to 10 percent higher.)

Refinement of Final Phase II Configuration

New baseline empennage.- For the new baseline empennage, lower tail B was replaced with Tail C, an untapered tail with the same area (0.253 m^2 (2.72 ft^2)) and the same span (127 cm (50.0 in.)) as tail B. (See fig. 2(e).) The vertical stabilizer and T-tail were not changed. (This empennage is also the Phase III baseline empennage.) The results of tests with this empennage refinement and with otherwise identical components of the final Phase II configuration are presented in figure 7. In general, the static longitudinal-stability characteristics were similar to those of the final Phase II configuration (compare figs. 5 and 7) except that the onset of tail stall was delayed to slightly higher angles of attack with the new baseline lower tail. The combination lower tail C and T-tail E provided the required level of stability.

Fan-size effects.- After the empennage for the final Phase II configuration was refined, the small-diameter fans were tested to determine the effects of the fan size. The model was configured with the full pylon fairings, the engine nacelles in the aft position, lower tail C, and T-tail E. The results are presented in figure 8 for trim thrust and several values of wing incidence. Very little difference is discernible in lift-curve slopes for the two fan sizes throughout the wing incidence range, but the angle of zero lift shifts about -1° for the smaller fan size. These results also show pronounced improvement in static longitudinal stability with the smaller fans. Static margin increases ranged from 13 to 17 percent chord.

Effects of Configuration Variables

The model was tested with different combinations of the model components such as the wing, tails, engines, and pylon fairings to determine the aerodynamic contribution of each component.

Fuselage, vertical tail, and horizontal tail C.- The fuselage (without the main rotor pylon) was tested with the 118-cm (46.67-in.) span lower tail C and the reduced-span vertical tail to obtain the basic aerodynamics of the tail with a minimum of interference. The results for several values of tail incidence are presented in figure 9. The tail lift-curve slope, based on the tail area, was 0.076/deg. The static longitudinal stability C_{m_α} with the tail on was -0.042/deg.

Fuselage, vertical tail, and T-tail D.- The fuselage (with the main rotor pylon) was tested with horizontal T-tail D mounted on the reduced-span vertical tail. The results with T-tail D are compared in figure 10 with results for the tails off and for tail C alone. The static longitudinal stability with T-tail was -0.019/deg.

Fuselage, wing, and vertical tail.- The configuration with the fuselage (including the main rotor pylon), wing, and vertical tail was tested with the wing set at incidence angles of -9°, 0°, 7.5°, and 15° and the flaps retracted. No horizontal tails were installed. The results are presented in figure 11 for the angle-of-attack range. Changing the wing incidence did not change the lift-curve slope $\left(C_{L_\alpha} = 0.073/\text{deg}\right)$ in the linear region. The change in lift coefficient with wing incidence $C_{L_{i_w}}$ was 0.0661/deg. As expected, the least drag was experienced when i_w was zero.

Fuselage, wing, vertical tail, and horizontal tails C and E.- The 127-cm (50.0-in.) span lower tail C and T-tail E were added to the wing-fuselage configuration just discussed. Both horizontal tails were set at 0° incidence. The results are presented in figure 12 for wing incidence angles of -9°, 0°, 7.5°, and 15° with the flaps retracted, and 15° wing incidence with the flaps deflected 30°. The most striking effect is the lack of static stability with the flaps deflected at negative angles of attack. The turbulent flow from the flaps was probably blanketing the tail. The tail was in an upwash field for -9° wing incidence for most of the angle-of-attack range. This configuration showed the most static longitudinal stability C_{m_α} of the five wing-flap combinations.

Fuselage, wing, vertical tail, and fans.- The model was tested at trim thrust with the small-diameter fans and minimum fairings in the forward position. The full-span vertical tail was installed and the horizontal tails were removed. These horizontal-tail-off data are presented in figure 13.

Fuselage, wing, vertical tail, Phase III baseline empennage, and different pylon fairings.- The model with the fuselage, wing, vertical tail, and horizontal tails C and E was tested with six different engine pylon fairings and the small-diameter fans with no air lines crossing the balance. (See fig. 2(c).) The fairings were (1) full fairing, (2) 90-percent-chord full fairing, (3) 80-percent-chord full fairing, (4) minimum fairing, (5) modified minimum fairing, and (6) gull fairing. The results are given in figure 14 for wing incidence angles of -4.5°, 0°, and 7.5°; the engines were at windmill thrust and mounted in the forward position. For -4.5° wing incidence, the configuration with the gull fairing displayed the highest minimum drag coefficient $\left(C_{D,\text{min}} = 0.102\right)$. Incorporation of the other five fairings resulted in minimum drag coefficients of about 0.096. Differences in pitching-moment slopes were not discernible. For 7.5° wing incidence, the full fairing had the lowest minimum drag $\left(C_{D,\text{min}} = 0.10\right)$ and the minimum fairing had the highest minimum drag $\left(C_{D,\text{min}} = 0.110\right)$.

Effect of position of engine-nacelle and pylon-fairing combination.- The effect of forward and aft position of the engine-nacelle and pylon-fairing combination on the aerodynamics of the model is presented in figure 15 for the minimum fairing and in figure 16 for the full fairing. The forward position is 2.54 cm (1.00 in.) ahead of the original aft position. The model was configured with the Phase III baseline empennage. Figure parts (a) to (c) present data for wing incidence angles of -4.5°, 0°, and 7.5° with the small-diameter fans windmilling. Figure parts (d) to (k) present data for wing incidence angles of -9°, -4.5°, 0°, 7.5°, and 15° (flaps retracted), and 0°, 7.5°, and 15° (flaps deflected 30°) at trim thrust. For the minimum fairing, drag (at windmill thrust) was slightly higher for the forward position than for the aft position at negative angles of attack but was lower for positive angles of attack. The lift-curve slope was slightly higher for the forward position than for the aft position. For the full fairing, drag was higher for the forward position than for the aft position at -4.5° wing incidence but lower at 0° and 7.5° wing incidence. A difference in lift-curve slope for the full fairing was not discernible. Generally, for both fairing types, the configuration was slightly more stable longitudinally with the aft position than with the forward position for the wing-flap configurations tested.

Effect of C_T variations.- Effects of thrust-coefficient C_T variations on the longitudinal characteristics of the complete configuration with the small-diameter fans in the aft position and the Phase III baseline empennage are shown in figure 17. Results are given for the range of wing incidence with the flaps deflected and retracted. For negative or zero wing incidence, thrust effects tended to reduce longitudinal stability. However, an increase in thrust increased static longitudinal stability for the positive wing incidence angles of the test. Without thrust the 7.5° and 15° wings with flaps deflected 30° were statically unstable or marginally stable for negative angles of attack. The addition of thrust stabilized these cases. The effect of thrust coefficient on the model with the wing removed is presented in figure 18. Two tail configurations were tested: the combination 110-cm (43.33-in.) cutback span lower tail C with T-tail E (fig. 18(a)), and T-tail D alone (fig. 18(b)). For the combination tail (fig. 18(a)), increasing the thrust coefficient decreased the static longitudinal stability. For T-tail D, increasing the thrust coefficient decreased the static stability at negative angles of attack. At positive angles of attack, the effect was small.

Definition of Phase III Baseline Configuration

The Phase III baseline configuration used for subsequent longitudinal and lateral-directional tests is shown in figure 2(a). This configuration consists of the fuselage, the rotor pylon, rotor hubs, small-diameter fans in the forward position, modified minimum pylon fairings, a variable-incidence wing, horizontal tails C and E, and the full-span vertical tail.

This configuration was chosen for further analysis because of several considerations: The engines were constrained to the forward position by center-of-gravity restrictions. The modified minimum pylon fairings were chosen because they created less interference on the empennage and they satisfied the engine manufacturer's requirements.

Longitudinal Aerodynamic Characteristics of Phase III Baseline Configuration

Effect of wing incidence and flap deflection.- The effect of wing incidence and flap deflection on the longitudinal aerodynamic characteristics of the Phase III baseline configuration is shown in figure 19. These data were obtained with the tail incidence set at zero and with all controls at the neutral position. Results for the model with the flaps retracted (i_w = -9°, -4.5°, 0°, 7.5°, and 15°) are presented in figure 19(a) for trim thrust and in figure 19(b) for zero thrust. Results for the flaps deflected 30° are presented in figure 19(c) for trim thrust and in figure 19(d) for zero thrust. In general, the model was stable throughout the angle-of-attack range investigated from negative to positive stall for all values of wing incidence, both with and without flaps deflected. The levels of static stability tended to be lowest in the middle angle-of-attack range between -7.5° and 7.5° except for $i_w = 15°$, which was more stable than the lower wing incidence angles. Within this angle-of-attack range, the lowest level of static stability was for $i_w = 0°$.

At a constant angle of attack with the horizontal tail on, positive wing-incidence and flap-deflection changes caused positive pitching-moment changes. (See fig. 19.) Without the horizontal tails, positive wing-incidence changes caused a negative pitching-moment change. (See figs. 11 and 13.) The horizontal tail apparently caused a positive increment in pitching moment because of the download on the tail from the wing and flap downwash. For example, at 0° angle of attack, the incremental pitching moment of the tail due to wing incidence $\Delta C_{m,tail}/\Delta i_w$ was found to be 0.017/deg, and the incremental pitching moment of the tail due to flap deflection $\Delta C_{m,tail}/\Delta \delta_f$ was found to be 0.012/deg. These trends suggest the feasibility of gearing the horizontal-tail incidence to both wing incidence and flap deflection to eliminate trim changes associated with these variables.

In the linear lift range, varying wing incidence did not change the lift-curve slope; however, the change in lift coefficient due to wing incidence $C_{L_{i_w}}$ was only about 60 percent of the change in lift coefficient due to angle of attack C_{L_α}. The reason for this difference between $C_{L_{i_w}}$ and C_{L_α} is associated with the absence of body lift and the loss of fuselage carryover lift when only wing incidence is varied (the fuselage remains fixed relative to the free stream).

Maximum lift coefficients achievable at both the positive and negative stalls are also related to wing incidence. In general, the highest values of $C_{L,max}$ were obtained

for zero wing incidence with the flaps deflected and retracted. (See fig. 15.) The loss in maximum lift capability was particularly severe for $i_w = 15^o$ and $\delta_f = 30^o$, as indicated in the following table:

i_w, deg	$C_{L,max}$ for –	
	$\delta_f = 0^o$	$\delta_f = 30^o$
0	1.55	2.11
7.5	1.32	1.92
15	1.14	1.56

Effect of horizontal-tail incidence.- The effect of horizontal-tail incidence on the longitudinal aerodynamic characteristics of the Phase III baseline configuration is presented in figure 20 and covers the entire range of wing incidence for both trim and zero thrust with flaps retracted and deflected. Only the lower horizontal-tail incidence was varied; T-tail E remained fixed at zero incidence. In general, variation of tail incidence between appropriate limits provided fairly uniform increments of pitching moments throughout the usable angle-of-attack range. The only indications of possible tail stall problems were for zero thrust with flaps deflected (figs. 20(m) and 20(n)). Even for these cases, the values of tail incidence were inappropriate for any practical trim condition.

Changes in thrust will affect downwash at the tail as well as dynamic pressure at the tail. The variation of downwash with angle of attack and the dynamic pressure at the tail affect the static longitudinal stability C_{m_α}. The dynamic pressure at the tail affects the horizontal-tail effectiveness $C_{m_{i_t}}$.

The horizontal-tail effectiveness, summarized in figure 21, is based on average values of $\Delta C_m/\Delta i_t$ for $\Delta i_t = \pm 4^o$ over the angle-of-attack range from -5^o to 5^o. The values of $C_{m_{i_t}}$ for zero thrust with flaps retracted are considerably less than would be expected from evaluation of the following expression:

$$C_{m_{i_t}} = \left(C_{L_\alpha}\right)_{tail} \frac{S_t}{S} \frac{l_t}{\bar{c}} \frac{q_t}{q} = -0.0665/\text{deg}$$

Losses in tail effectiveness are possibly associated with losses in dynamic pressure at the tail or with losses in tail lift-curve slope attributable to gaps between the sides of the fuselage and the root chord of the lower horizontal stabilizer. The combined losses are about 25 to 28 percent in $C_{m_{i_t}}$.

The effects of thrust on horizontal-tail effectiveness are small at negative values of wing incidence but become very appreciable with positive wing incidence and/or with flaps deflected. (See fig. 21.) This result is attributable to an increase in the ratio q_t/q due to the engine efflux being drawn down to the region of the horizontal tail by the combined effects of the wing and flaps.

As mentioned in the previous section, trim changes due to wing incidence and flap deflection can easily be compensated by properly gearing tail incidence to i_w and δ_f. If a $C_{m_{i_t}}$ value of approximately -0.05/deg is assumed to be reasonably appropriate for the entire range of i_w and C_T, the aforementioned trim changes due to i_w are essentially eliminated with a gearing ratio of 0.32° tail incidence per degree of i_w. Likewise, the trim changes due to flap deflection are essentially eliminated with a gearing ratio of 0.24° tail incidence per degree of δ_f.

Effect of sealing horizontal-tail—fuselage junction.- There was a slight gap between the root of the lower horizontal tail and the fuselage. This gap could lessen or eliminate the end-plate effect of the fuselage on the tail and thereby cause a reduction in tail lift-curve slope. To determine whether there were any significant effects, the tail-fuselage junction was sealed. A comparison of the sealed junction and the unsealed junction is shown in figure 22. Sealing the gap increased the longitudinal stability C_{m_α} and the horizontal-tail effectiveness $C_{m_{i_t}}$ by about 15 percent. At least half of the loss in horizontal-tail effectiveness cited in the previous section is therefore attributable to the gap between the fuselage and the horizontal tail.

Elevator effectiveness.- The effect of elevator deflection on the longitudinal aerodynamic characteristics of the Phase III baseline configuration was determined for $i_w = 7.5^\circ$ with flaps deflected and retracted at both zero and trim thrust. These results are presented in figure 23. For these tests, T-tail E was mounted on top of the full-span vertical tail at zero incidence and the lower tail C was set at zero incidence except where noted. In general, the variation of pitching moment with elevator deflection was linear at values of δ_e between -10° and 10°, where the elevator effectiveness was greatest.

In order to evaluate the effects of thrust and flap deflection on elevator effectiveness, the data of figure 23 have been cross-plotted in terms of $C_{m_{\delta_e}}$ as a function of α, and the results are presented in figure 24. Only the linear portions of the curves of C_m against α at values of δ_e between -10° and 10° were used to evaluate $C_{m_{\delta_e}}$. With the flaps retracted, thrust produces an increase in elevator effectiveness only in the negative angle-of-attack range; however, with the flaps deflected, thrust increases elevator effectiveness throughout the entire angle-of-attack range. This increase in elevator effectiveness $\left(C_{m_{\delta_e}}\right)$ due to thrust with flaps deflected averaged about 24 percent. These results are similar to the effects of thrust on horizontal-tail effectiveness $C_{m_{i_t}}$ discussed previously, and are caused by the same phenomenon. That is, dynamic

pressure in the region of the horizontal tail increased under conditions of high lift because the high dynamic pressure of the engine efflux was drawn downward by the wing- and flap-induced flow.

The elevator effectiveness with -4° horizontal-tail incidence, presented in figure 24(b), was obtained from cross plots of figures 23(e) and 23(f). In the positive angle-of-attack range, elevator effectiveness was not significantly affected by the change in horizontal-tail incidence; however, in the negative angle-of-attack range, elevator effectiveness suffered a severe loss for zero thrust. Under this condition the tail was probably stalled. Note, however, that with trim thrust there was no loss in elevator effectiveness in the negative angle-of-attack range (at least to $\alpha = -5^{\circ}$), indicating that thrust effects tended to delay tail stall.

Effect of reduced lower horizontal-tail span.- The tail of the aircraft should be as light as possible to avoid any center-of-gravity or weight problems. The tail weight can be lessened by reducing the span of the horizontal tail, provided that the loss in stability is small. A small loss in stability can be counteracted by sealing the gap between the root of the lower horizontal tail and the fuselage. The effect of reducing the span of lower tail C is presented in figure 25 for several values of wing incidence and flap deflection at trim thrust. Three tail spans were tested: the original 127-cm (50.0-in.) tail, a 118-cm (46.67-in.) tail, and a 110-cm (43.33-in.) tail. The static longitudinal stability C_{m_α} was computed at angles of attack between -5° and 5° for the various tails and the results are presented in figure 26. The minimum stability level occurs near 0° wing incidence for the flaps deflected and retracted. With the flaps retracted, the reduction of C_{m_α} at 0° wing incidence is about 19 percent for each 8.46-cm (3.33-in.) reduction in tail span. This percentage decreases as the wing incidence is changed from 0°. With the flaps deflected, the stability reduction increases as the wing incidence increases.

Effect of reduced vertical-tail span.- The weight of the tail can also be decreased by reducing the span of the vertical tail. This reduction affects the longitudinal stability because it reduces the horizontal distance between the assumed center of gravity and the center of pressure of the T-tail. (See fig. 2(f).) In addition, reducing the span brings the T-tail down closer to the region where the downwash is larger. The model was tested with the combination reduced-span lower tail C set at 0° incidence and T-tail E mounted on the full-span vertical tail and on the vertical tail which was reduced in span by 8.46 cm (3.33 in.). (See fig. 2(f).) The results are presented for several values of wing incidence and flap deflection for the 118-cm (46.67-in.) span lower tail C in figure 27 and for the 110-cm (43.33-in.) span lower tail C in figure 28. The static longitudinal stability was computed at angles of attack between -5° and 5° and the results are presented in figure 29.

Reducing the span of the vertical tail caused a small reduction in the static longitudinal stability. The reduction was larger for the 110-cm (43.33-in.) span lower tail C than for the 118-cm (46.67-in.) span lower tail C.

Horizontal-tail effectiveness with reduced-span lower tail.- The effect of lower horizontal-tail span on the longitudinal aerodynamic characteristics at several values of tail incidence with the wing incidence set at 0° and the flaps retracted is presented in figure 30. T-tail E was mounted on the reduced vertical tail. The results for the 118-cm (46.67-in.) span lower tail C are presented in figure 30(a), and the results for the 110-cm (43.33-in.) span lower tail C are presented in figure 30(b). Reducing the lower horizontal-tail span from 118 cm (46.67 in.) to 110 cm (43.33 in.) reduced the horizontal-tail effectiveness $C_{m_{i_t}}$ from -0.0475/deg to -0.0438/deg. The 127-cm (50.0-in.) span tail was not tested with the T-tail on the shortened vertical tail. However, the horizontal-tail effectiveness with the T-tail on top of the full-span vertical tail was computed from figure 20 to be -0.0498/deg. Each 6.6-percent reduction in tail span caused about a 6-percent reduction in horizontal-tail effectiveness.

Elevator effectiveness with reduced-span lower tail.- The effect of reduced lower tail span on the elevator effectiveness is presented in figure 31 with the wing incidence and lower horizontal tail incidence set at 0° and the flaps retracted. T-tail E was mounted on the reduced vertical tail. Reducing the lower tail C span from 118 cm (46.67 in.) to 110 cm (43.33 in.) reduced the elevator effectiveness from -0.0239/deg to -0.0218/deg. The elevator effectiveness for the 127-cm (50.0-in.) lower tail C with T-tail E on top of the full-span vertical tail was computed from figure 23 to be -0.0252/deg. This reduction is about the same as was obtained for the horizontal-tail effectiveness; that is, each 6.6-percent reduction in tail span produced a 6-percent reduction in horizontal-tail effectiveness.

Lateral-Directional Characteristics of Phase III Baseline Configuration

The lateral-directional stability characteristics of the Phase III baseline configuration were also evaluated. The effect of wing incidence and flap deflection on the lateral-directional coefficients was obtained at fixed positive values of sideslip angle over an angle-of-attack range from -13° to 13°. The results are presented in figure 32 for both trim thrust and zero thrust. These data were used to evaluate the static lateral-directional stability derivatives C_{l_β}, C_{n_β}, and C_{Y_β} as functions of angle of attack. These derivatives are based on coefficient increments between sideslip angles of 0° and 5°. The results, presented in figure 33, indicate that the model was directionally stable for all values of wing incidence and flap deflection throughout the angle-of-attack range appropriate for unstalled flight. The static directional-stability parameter C_{n_β} diminished in magnitude with increasing angle of attack and was in the marginal stability

range at the highest angles of attack for wing incidence angles of -9°, -4.5°, and 0°. Another point indicated by these data is that static directional stability is affected by thrust coefficient. In general, higher values of C_{n_β} were measured at $C_T = 0$ than at trim-thrust coefficients; thus, the effects of thrust are destabilizing. This destabilizing effect of thrust is probably the result of the partial shielding of the vertical tail from the free-stream flow by the higher velocity components of the engine efflux. In other words, thrust effects produced a sizable sidewash at the tail, which resulted in a reduced capability of the tail to provide restoring moments.

The onset of directional divergence under dynamic flight conditions is not solely dependent on the value of C_{n_β} becoming negative. An inertia coupling interacts with the effective dihedral derivative such that the condition for directional divergence is actually related to a negative (or unstable) value of $C_{n_{\beta,dyn}}$, where

$$C_{n_{\beta,dyn}} = C_{n_\beta} - \frac{I_Z}{I_X} C_{l_\beta} \sin \alpha$$

In order to test for possible directional divergence, C_{n_β} and C_{l_β} from figure 33 and the value of the inertia parameter $I_Z/I_X = 4.542$ for the RSRA fixed-wing configuration were used in the above expression for $C_{n_{\beta,dyn}}$ for the various wing incidence and flap deflection angles. These $C_{n_{\beta,dyn}}$ results are presented in figure 34, and indicate that no condition of directional divergence is expected throughout the investigated ranges of wing incidence, flap deflection, or angle of attack.

The lateral-stability characteristics of the model in terms of the effective dihedral parameter C_{l_β} are strongly dependent on wing incidence and flap deflection, in addition to the usual dependence on angle of attack. That is, C_{l_β} became more negative with increasing wing incidence, flap deflection, and angle of attack. (See fig. 33.) This is expected because C_{l_β} is normally a direct function of lift coefficient, which varies, of course, with i_w, δ_f, and α. An unexpected effective-dihedral characteristic is revealed by these data in that for $i_w = 0^{\circ}$ and $\delta_f = 0^{\circ}$, the value of C_{l_β} is essentially zero at $\alpha = 0^{\circ}$ and throughout much of the positive angle-of-attack range despite the rather large geometric dihedral of the wing ($\Gamma = 7^{\circ}$). This deficiency in positive effective dihedral (negative C_{l_β}) could cause poor lateral-directional flight behavior in the form of spiral instability. A possible explanation for the absence of effective dihedral for $i_w = 0^{\circ}$ is the unusually large and deep fuselage relative to the very low placement of the wing.

The fuselage interference on effective dihedral computed by the method described in reference 6 was 0.0017/deg; a geometric dihedral of 7° should produce a C_{l_β} value of about -0.0016/deg (-0.00023 per degree of Γ). Thus, the 7° geometric dihedral of

the wing was barely sufficient to overcome the unstable interference effects of the fuselage, and in order to provide positive effective dihedral, an increase in the value of geometric dihedral appears to be warranted.

The values of the side-force derivative C_{Y_β} were fairly large and stable throughout the angle-of-attack range and showed no appreciable dependence on wing incidence or flap deflection.

Directional control.- The effect of rudder deflection is presented in figure 35 for selected values of wing incidence and flap deflection at several values of sideslip angle. These data show the variation of the lateral coefficients with angle of attack for various fixed values of rudder deflection. The data have been cross-plotted in figure 36 to show the rudder control power. The results indicate that the rudder provides highly effective directional control $\left(C_{n_{\delta_r}}\right)$ throughout the range of angle of attack. Rudder effectiveness is not strongly dependent on the angle of sideslip, but it does increase with wing incidence and flap deflection at a constant angle of attack. The downwash from the wing probably draws the high-velocity free stream down over the rudder. The rudder effectiveness decreases with angle of attack. The induced downwash from the wing and flaps is dominated by the blockage of the fuselage so as to reduce the rudder effectiveness.

The model was tested with the left engine windmilling and the right engine operating to simulate an engine-out condition. Both trim thrust and excess thrust (high enough for a wave-off) were investigated. The results are presented in figure 37. Engine-out operation caused no significant rolling-moment problems. The data from figure 37 have been cross-plotted in figure 38 to determine the rudder deflection and sideslip angle required for engine-out operations. At trim thrust, about -13° of rudder deflection are needed to trim out the yawing moment at 0° sideslip for 0° wing incidence, and about -18° are needed for 7.5° wing incidence. With excess thrust, -21° of rudder deflection are needed. This leaves at least 9° of rudder deflection available for additional control. The engine-out case should not be a significant problem.

Roll control.- The effect of aileron deflection over the angle-of-attack range is presented in figure 39 for 0° wing incidence with 0° flap deflection and for 7.5° wing incidence with 30° flap deflection. Only the left aileron was deflected. An upward deflection of the left aileron produces a small but adverse yawing moment. The ailerons provide adequate control power for both combinations of wing incidence and flap deflection. Near stall, the aileron loses its control power. The aileron effectiveness was computed from the data in figure 39 at each angle of attack. These results are presented in figure 40. The effectiveness was nearly constant at 0.0017/deg for 0° wing incidence and about 0.0019/deg for 7.5° wing incidence. The aileron effectiveness decreases near stall, so that at about 12° angle of attack for 7.5° wing incidence with the flaps deflected, there is no roll control.

The problem of adverse yaw due to aileron deflection can be alleviated by adjusting the left and right aileron deflections. If the ailerons are deflected with one 2^{o} up and the other 1^{o} down, a favorable yaw due to aileron deflection results. These results are presented in figure 41.

SUMMARY OF RESULTS

The results from the Phase III wind-tunnel tests of a 1/6-scale model of the rotor systems research aircraft can be summarized as follows:

1. The combination lower tail and T-tail provided the required longitudinal stability for the compound configuration.

2. Reducing the size of the fans increased the static longitudinal stability. Reducing the lower horizontal- or vertical-tail span or moving the engine nacelles and pylon fairings forward decreased the longitudinal stability.

3. Sealing the gap between the horizontal-tail root and the fuselage increased both the static longitudinal stability and the horizontal-tail effectiveness.

4. Increasing the thrust tended to decrease the longitudinal stability at negative wing incidence angles and to increase the longitudinal stability at positive wing incidence angles.

5. The elevator, rudder, and aileron effectiveness were adequate. The adverse yaw due to aileron deflection could be alleviated with the proper differential aileron deflection.

6. Effective dihedral became more negative with increasing wing incidence, flap deflection, and angle of attack.

Langley Research Center
National Aeronautics and Space Administration
Hampton, Va 23665
April 27, 1976

REFERENCES

1. Linden, A. W.; and Hellyar, M. W.: The Rotor Systems Research Aircraft – A Flying Wind Tunnel. AIAA Paper No. 74-1277, Oct. 1974.

2. Flemming, R.; and Ruddell, A.: RSRA Sixth Scale Wind Tunnel Test – Final Report. Doc. No. SER-72011 (Contract NAS1-13000), Sikorsky Aircraft Div., United Aircraft Corp., Dec. 4, 1974. (Available as NASA CR-144964.)

3. Mechtly, E. A.: The International System of Units – Physical Constants and Conversion Factors (Second Revision). NASA SP-7012, 1973.

4. Gillis, Clarence L.; Polhamus, Edward C.; and Gray, Joseph L., Jr.: Charts for Determining Jet-Boundary Corrections for Complete Models in 7- by 10-Foot Closed Rectangular Wind Tunnels. NACA WR L-123, 1945. (Formerly NACA ARR L5G31.)

5. Herriot, John G.: Blockage Corrections for Three-Dimensional-Flow Closed-Throat Wind Tunnels, With Consideration of the Effect of Compressibility. NACA Rep. 995, 1950. (Supersedes NACA RM A7B28.)

6. Campbell, John P.; and McKinney, Marion O.: Summary of Methods for Calculating Dynamic Lateral Stability and Response and for Estimating Lateral Stability Derivatives. NACA Rep. 1098, 1952. (Supersedes NACA TN 2409.)

TABLE I.- MODEL DATA

Fuselage:	
Length, m (ft)	3.057 (10.03)
Frontal area, m^2 (ft^2)	0.172 (1.85)
Wing:	
Airfoil section	NACA 63_2415
Area, m^2 (ft^2)	0.954 (10.272)
Span, m (ft)	2.286 (7.500)
Mean aerodynamic chord, m (ft)	0.427 (1.40)
Aspect ratio	5.52
Taper ratio	0.66
Sweep of 25-percent chord line, deg	3.0
Dihedral, deg	7.0
Flaps (each):	
Area, m^2 (ft^2)	0.074 (0.80)
Span, percent of wing semispan	49.0
Chord, percent of local wing chord	33.0
Aileron:	
Area, m^2 (ft^2)	0.0465 (0.50)
Span, percent of wing semispan	34.0
Chord, percent of local wing chord	34.0
Vertical stabilizer:	
Airfoil section	NACA 0015
Area, m^2 (ft^2)	0.294 (3.164)
Span, m (ft)	0.813 (2.67)
Aspect ratio	2.25
Root chord, m (ft)	0.476 (1.56)
Rudder, percent of local chord	37.0

TABLE II.- MODEL CONFIGURATION NOMENCLATURE

Configuration designation	Fan size	Pylon fairing	Engine-nacelle position	Vertical tail	Horizontal tails		Data figure
					Lower	Upper (T-tail)	
Original Phase II	Large	Full	Aft	Full span	A	None	4
Final Phase II	Large	Full	Aft	Full span	B	E	5
Final Phase II with new baseline empennage	Large or small	Full	Aft	Full span	C	E	8
Phase III baseline	Small	Modified minimum	Forward	Full span	C	E	19
Wing removed (helicopter with auxiliary engines)	Small	Modified minimum	Forward	Cutback span	C None	E D	18(a) 18(b)

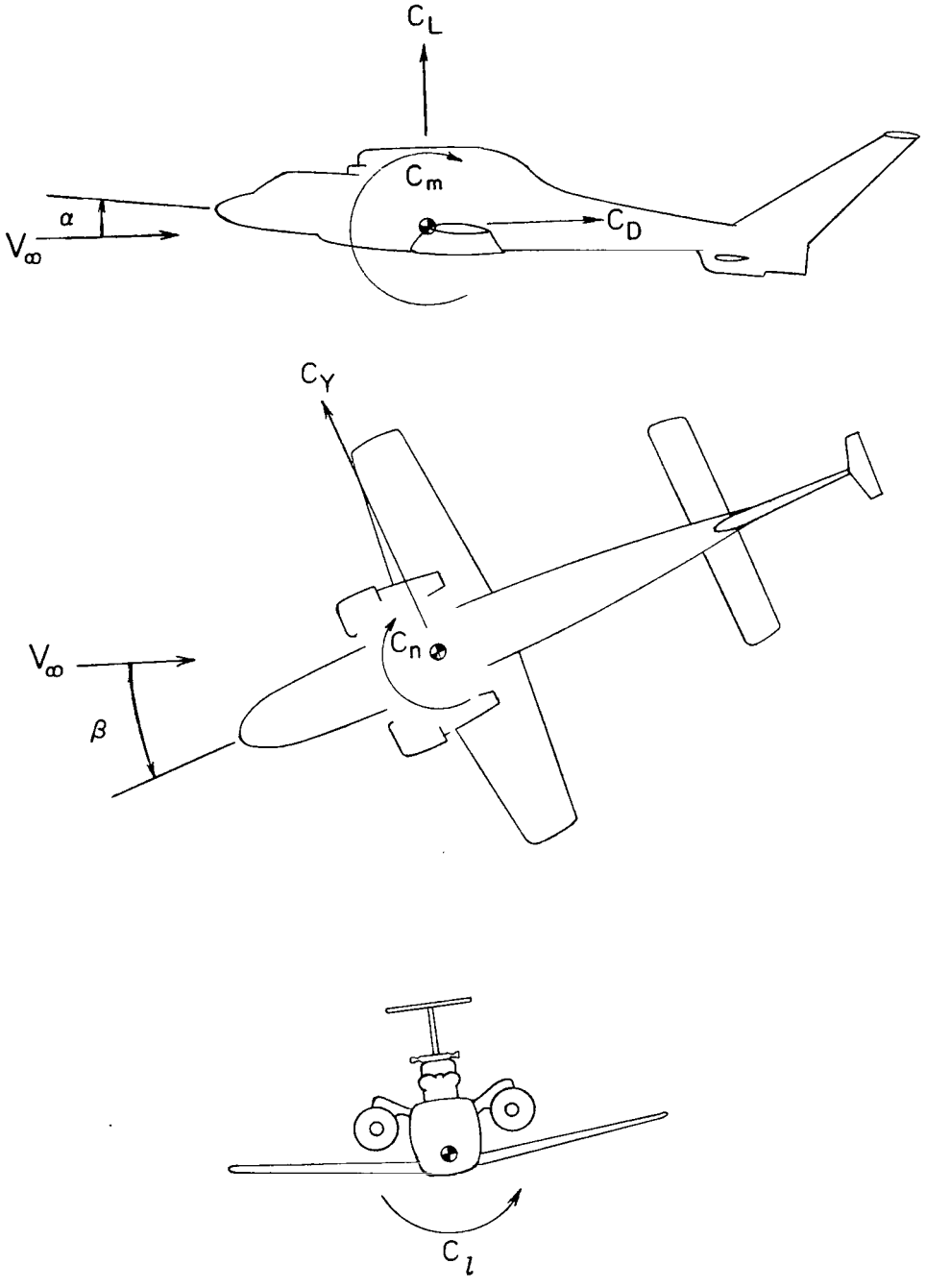

(a) System of axes.

Figure 1.- Axes and sign conventions. Positive directions are indicated by arrows.

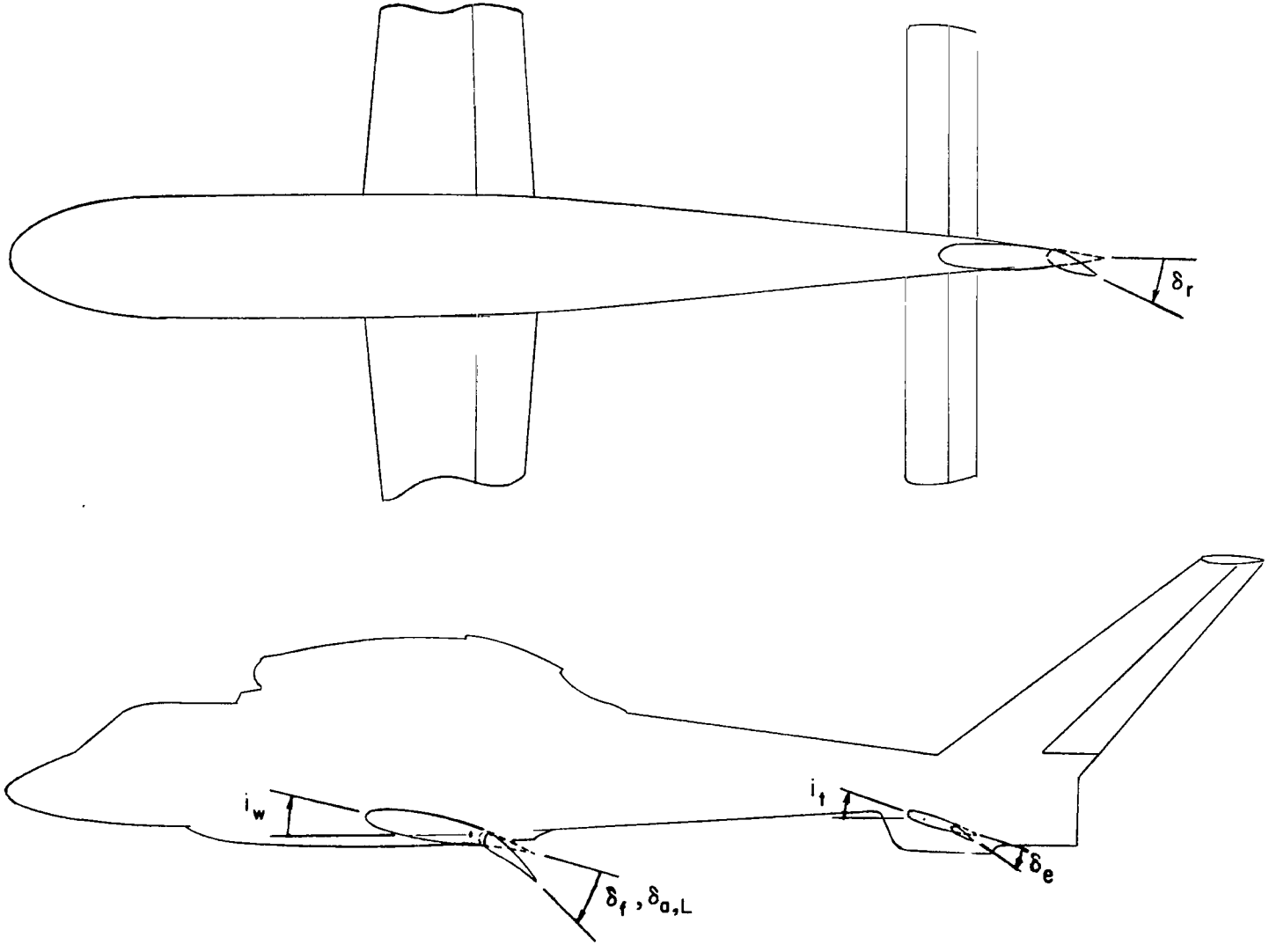

(b) Sign conventions.

Figure 1.- Concluded.

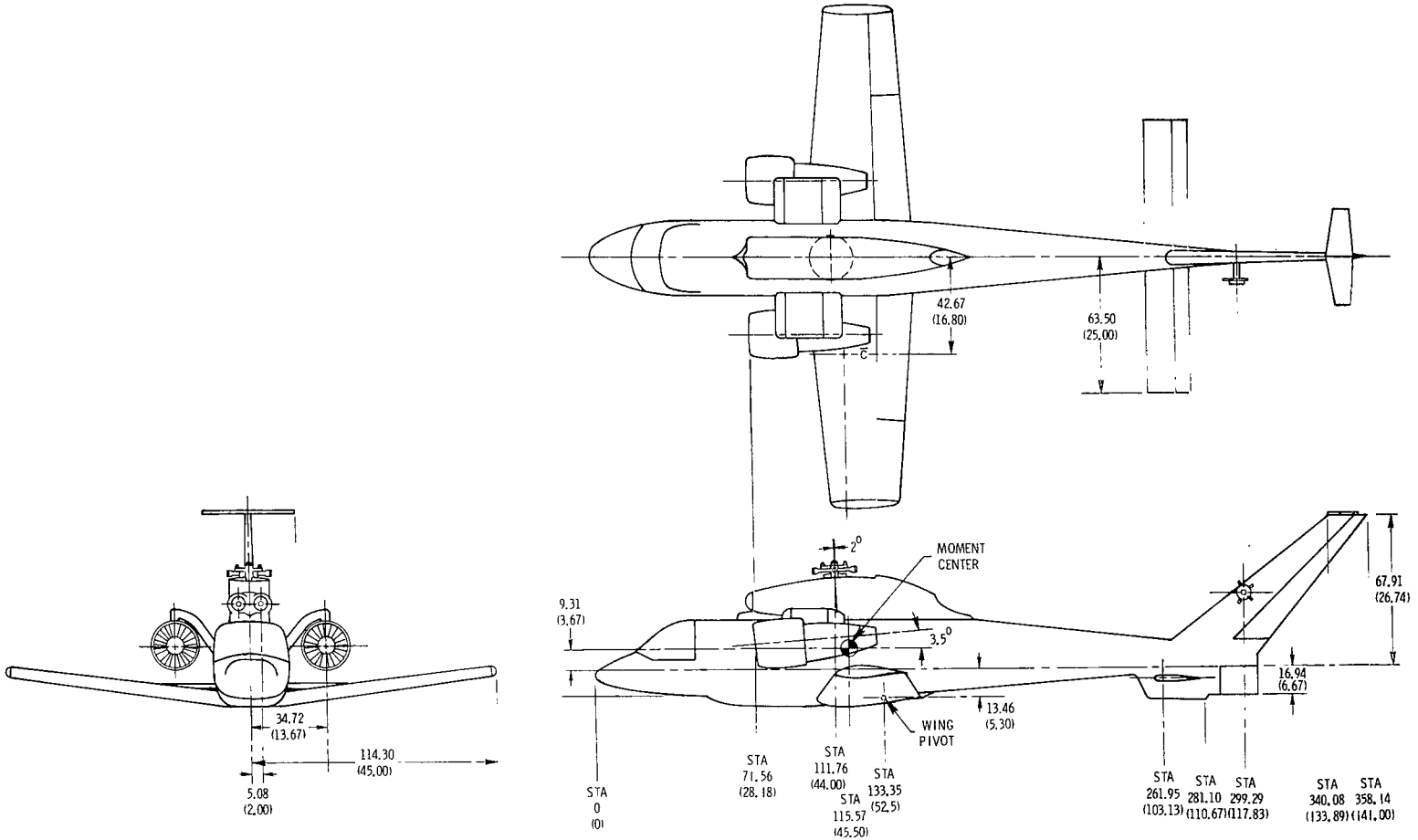

(a) Three-view sketch.

Figure 2.- Sketch of Phase III baseline configuration. All dimensions shown in cm (in.) unless otherwise specified.

SMALL DIAMETER

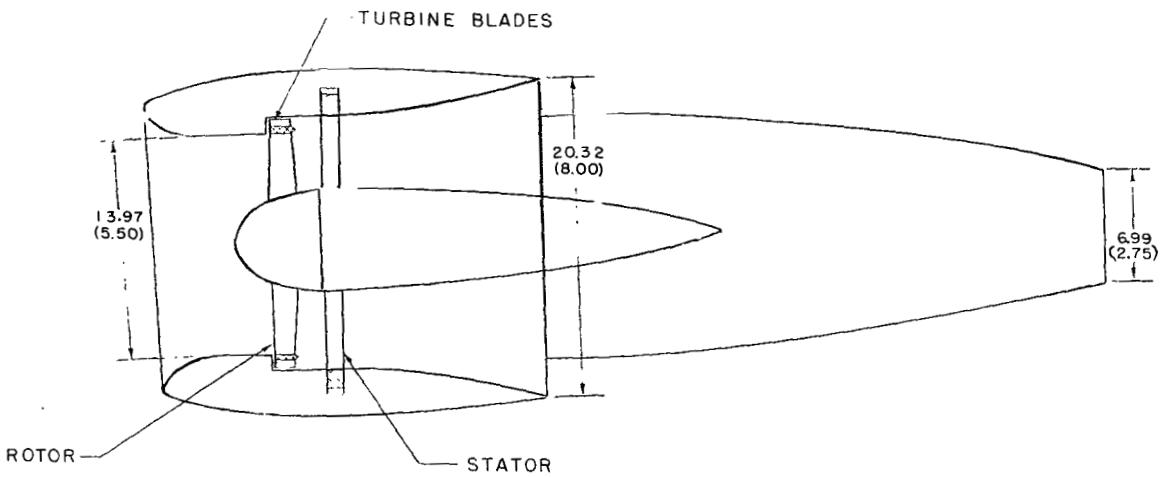

LARGE DIAMETER

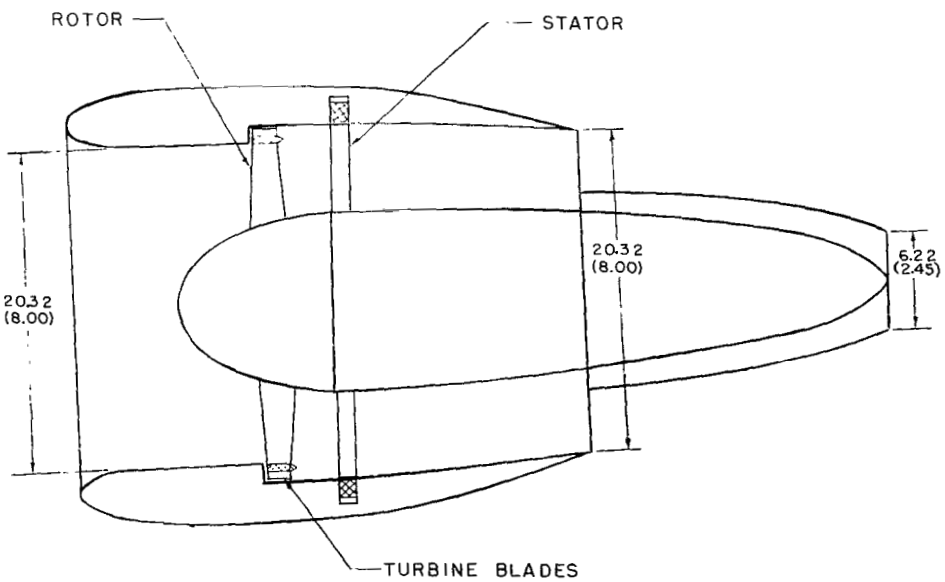

(b) Details of small- and large-diameter fans.

Figure 2.- Continued.

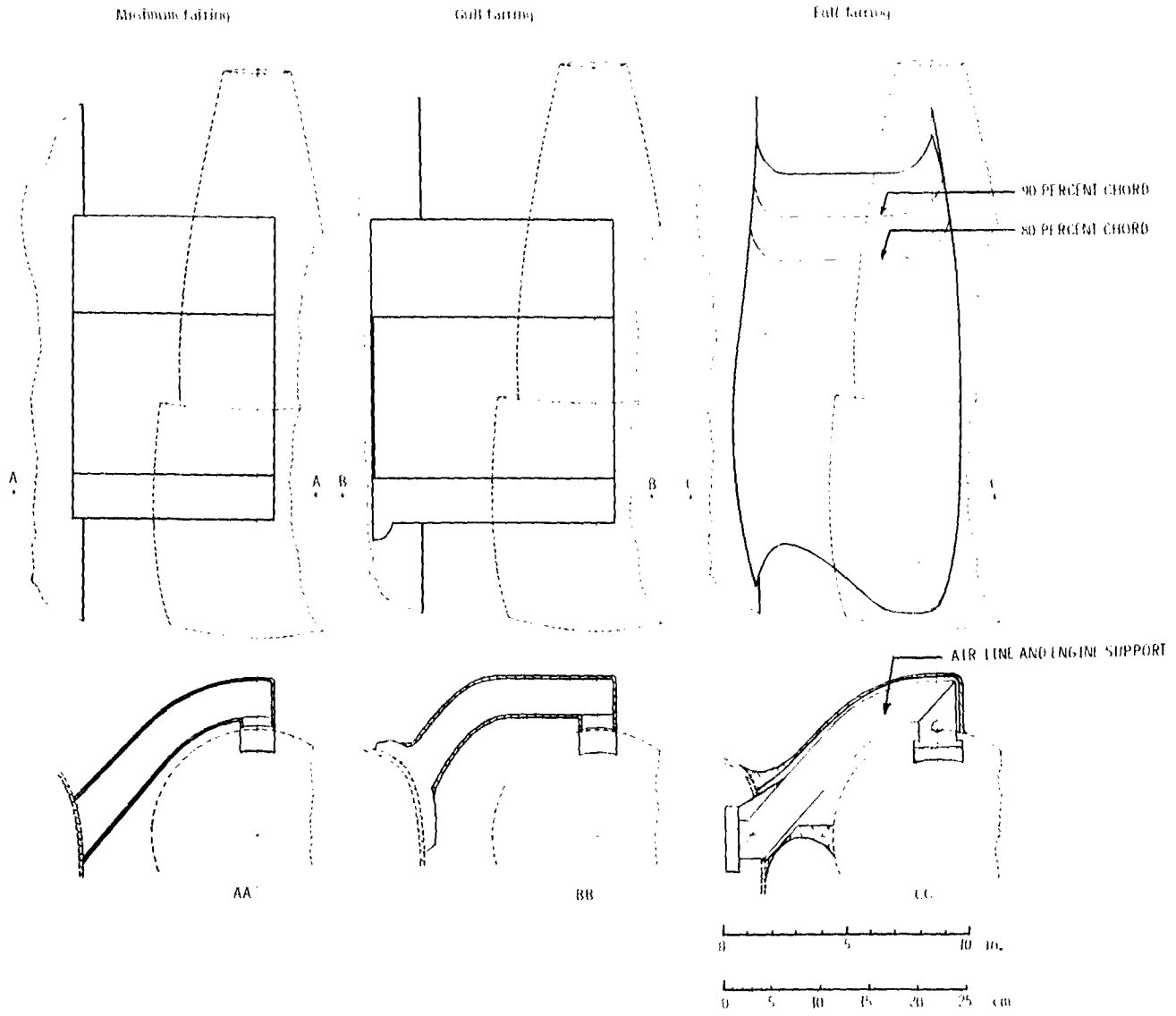

(c) Fairing details.

Figure 2.- Continued.

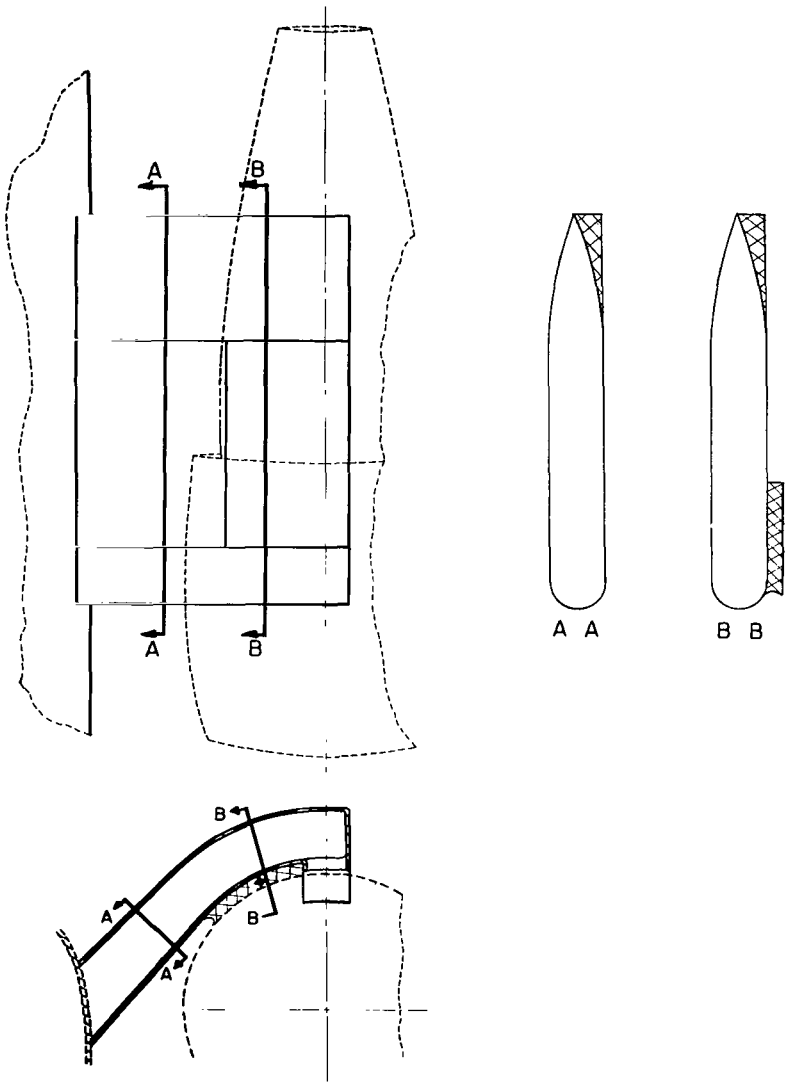

(d) Modification to minimum fairings. (Modifications denoted by crosshatched areas.)

Figure 2.- Continued.

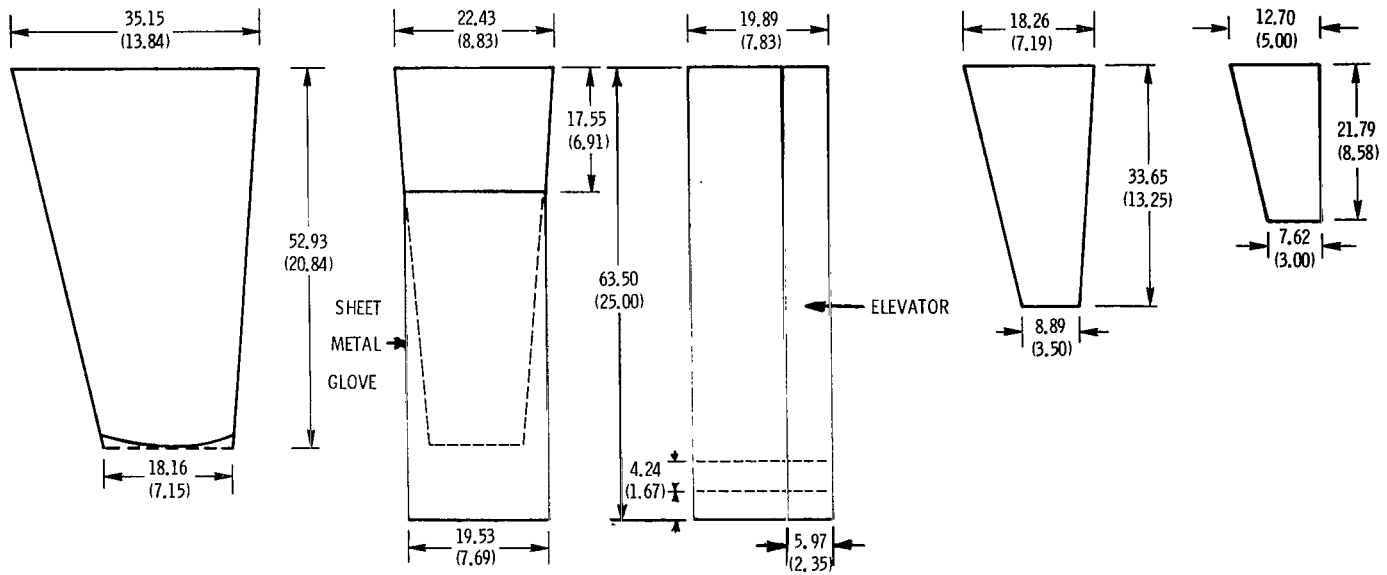

TAIL	A	B	C	D	E
AREA, $m^2(ft^2)$	0.282 (3.04)	0.253 (2.72)	0.253 (2.72)	0.091 (0.98)	0.046 (0.48)
TAPER RATIO	.518	.871	1.000	.487	.600
ASPECT RATIO	3.97	6.37	6.37	5.15	4.29

(e) Details of horizontal tails.

Figure 2.- Continued.

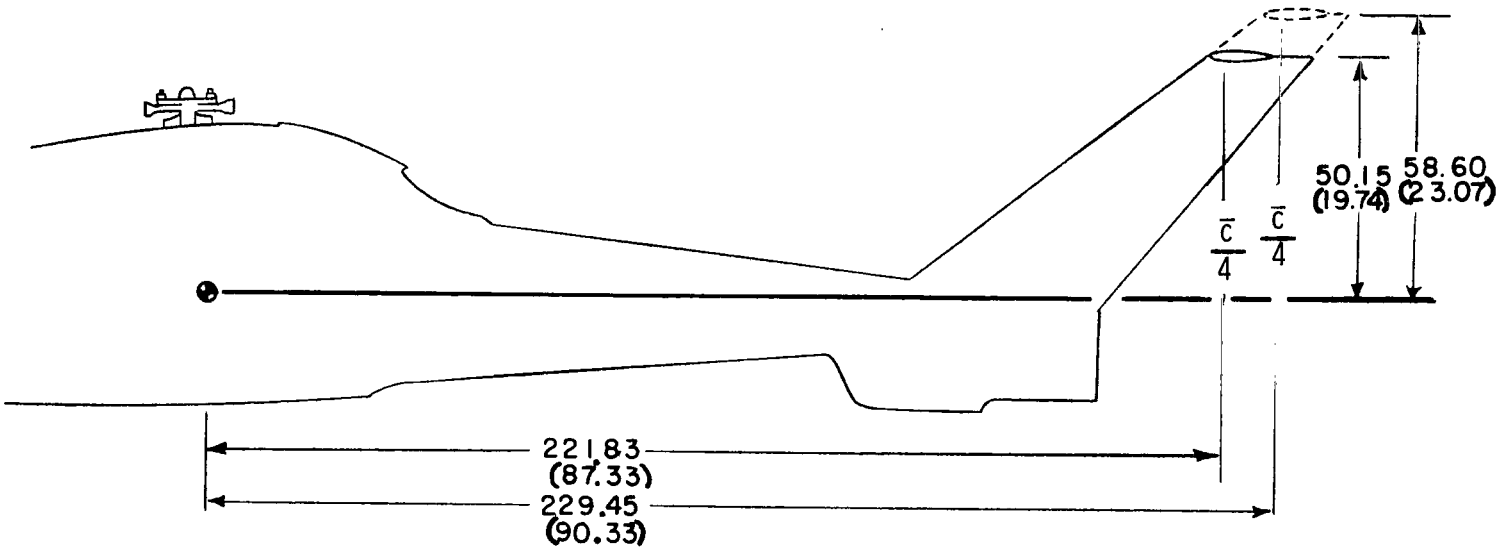

(f) Modifications to vertical tail and T-tail.

Figure 2.- Concluded.

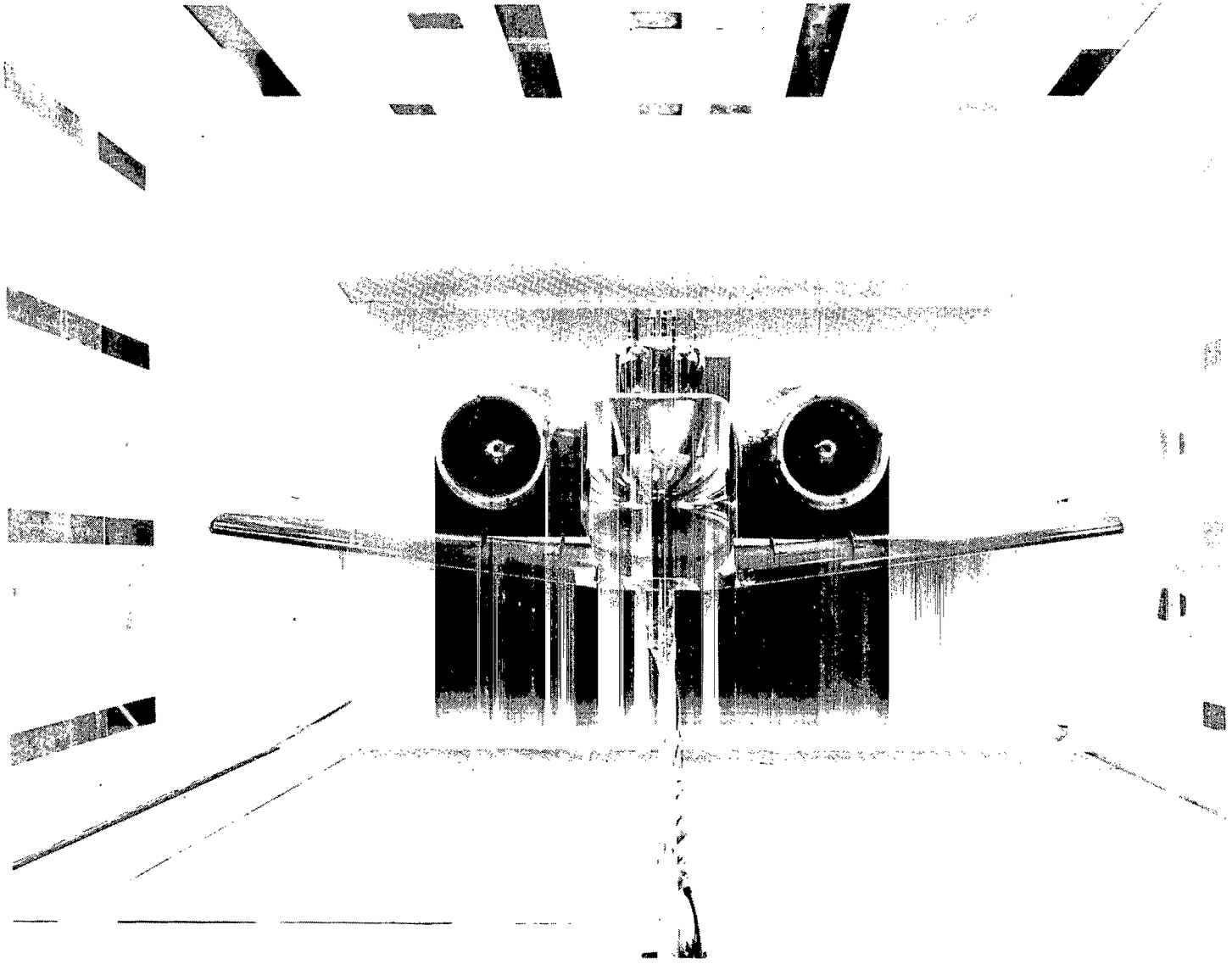

L-74-7109

(a) Model with large fans and full fairings.

Figure 3.- Model in Langley V/STOL tunnel.

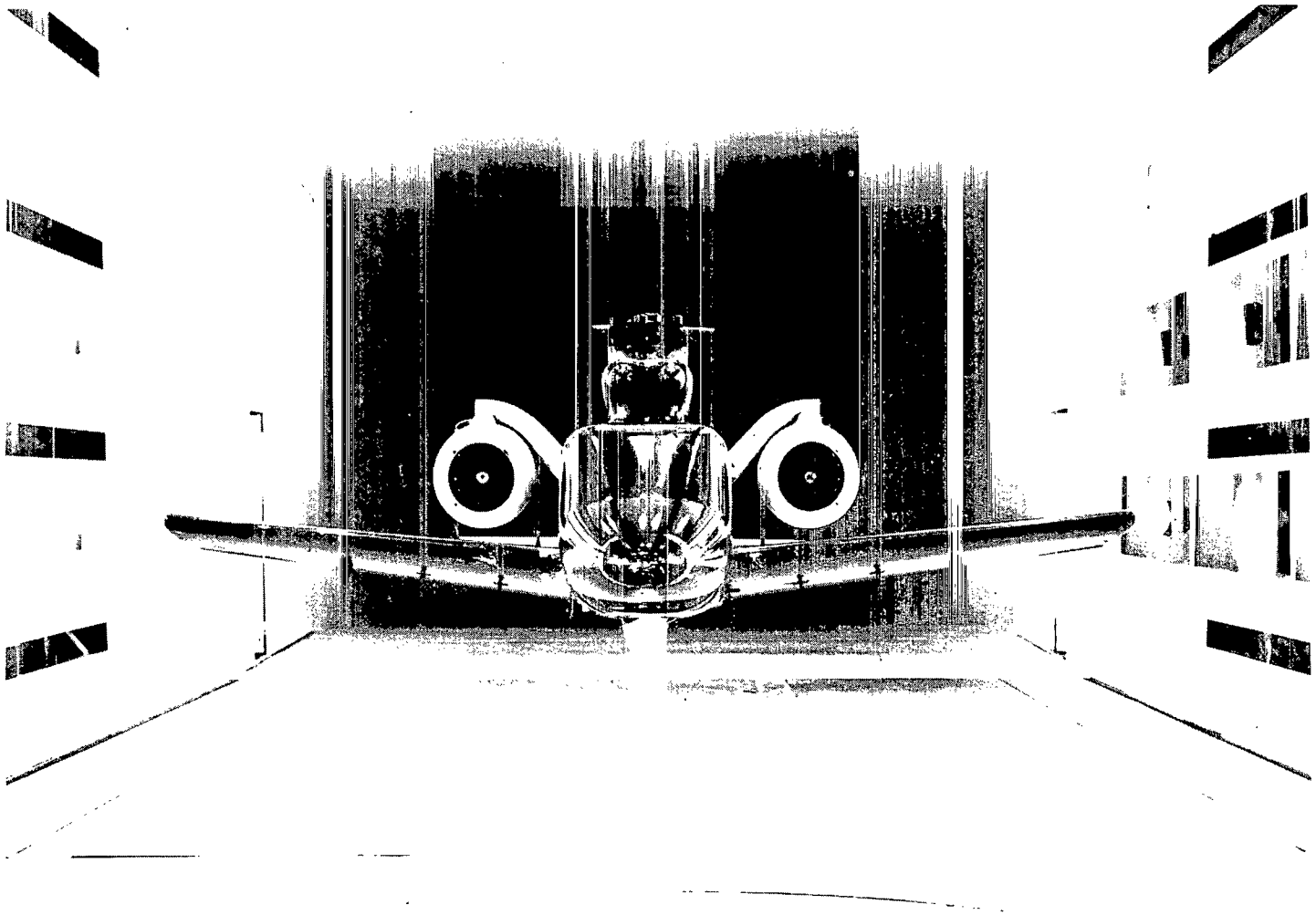

L-74-7304

(b) Model with small fans and minimum fairings.

Figure 3.- Continued.

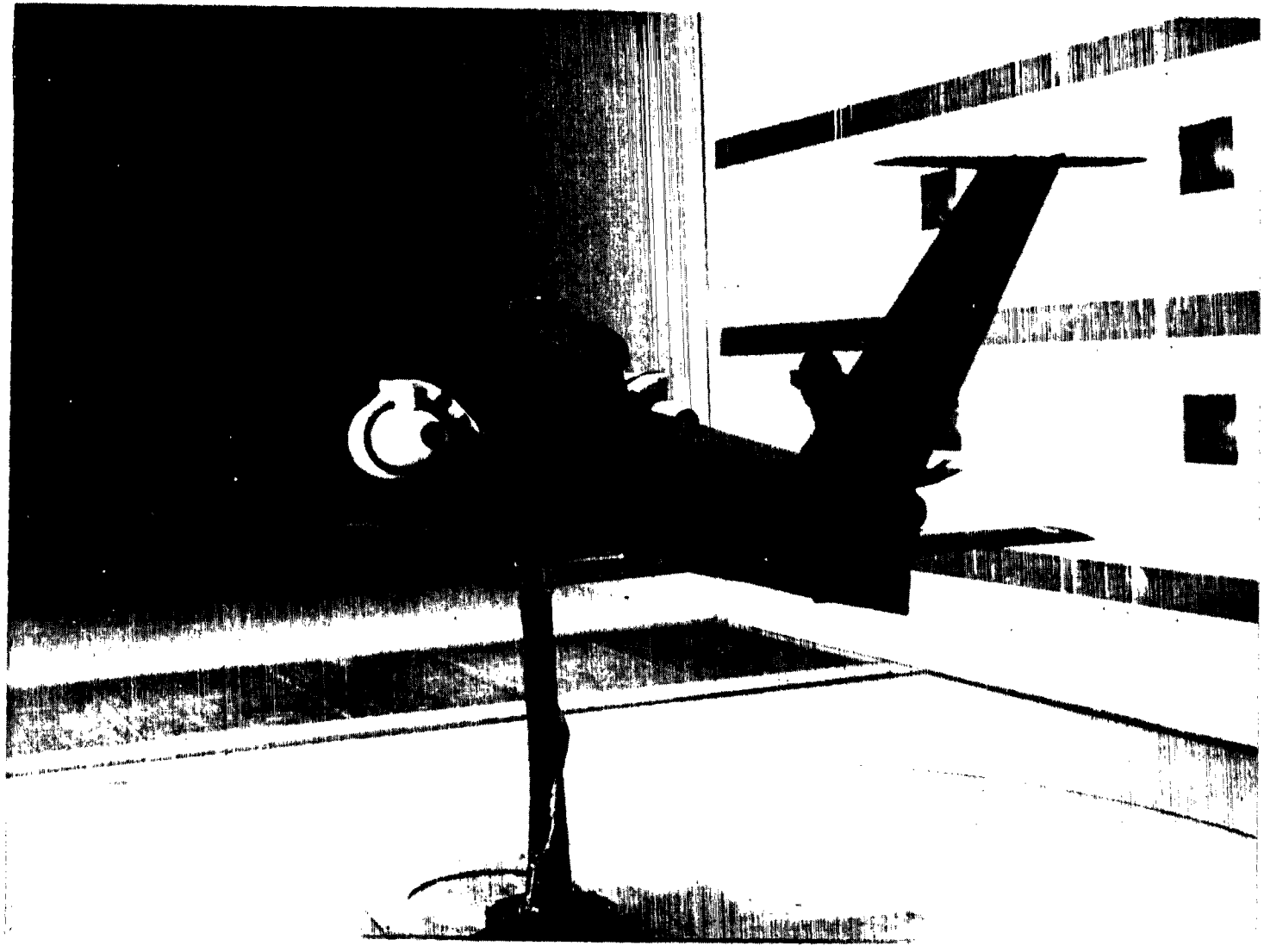

L-74-8450

(c) Model with small fans, modified minimum fairings, and with lower tail C and T-tail E.

Figure 3.- Continued.

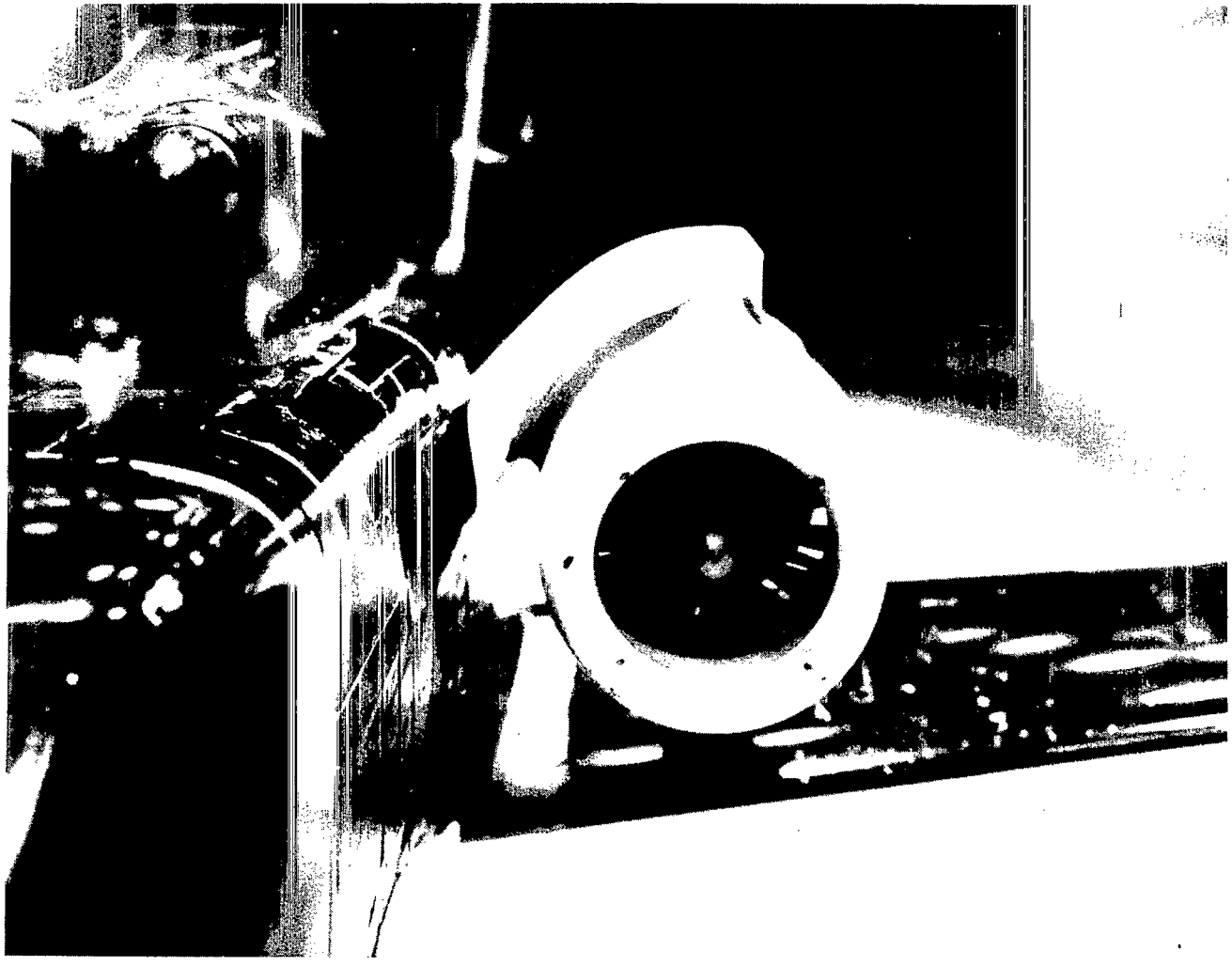

L-76-190

(d) Details of small fans with modified minimum fairings.

Figure 3.- Concluded.

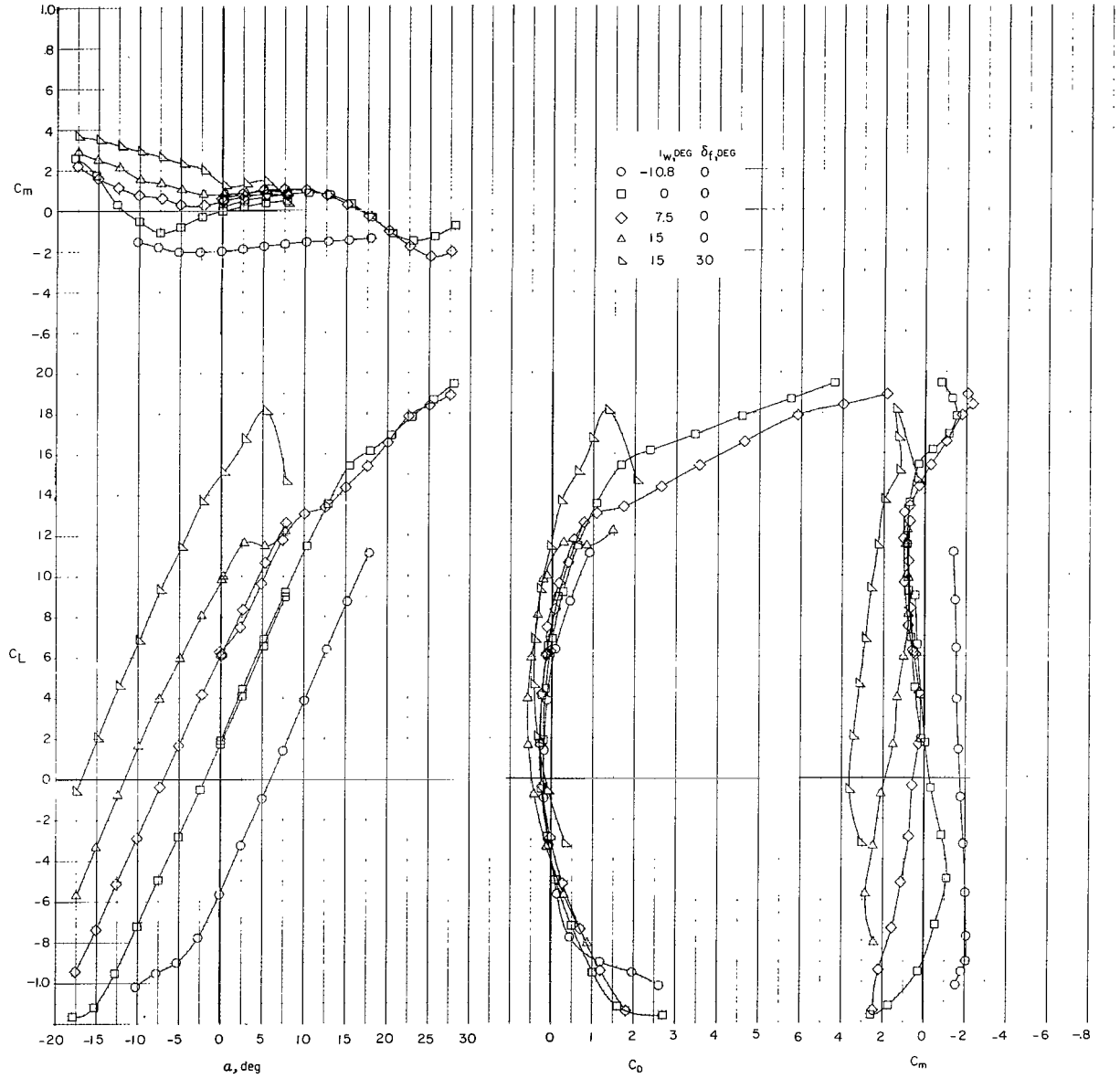

Figure 4.- Effect of i_w on longitudinal characteristics of original Phase II configuration, from Langley V/STOL tunnel. Trim thrust.

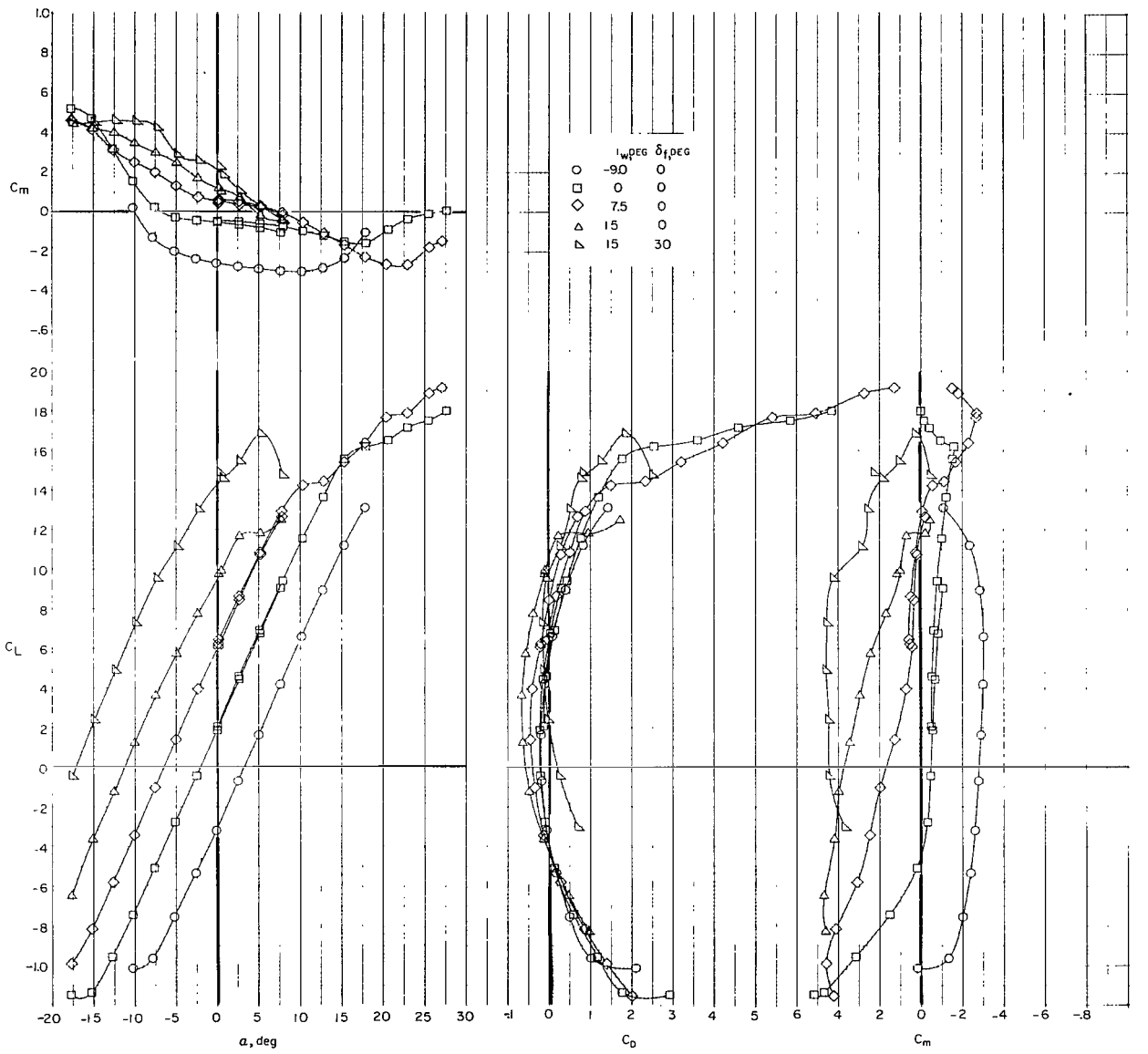

Figure 5.- Effect of i_w on longitudinal characteristics of final Phase II configuration, from Langley V/STOL tunnel. Trim thrust.

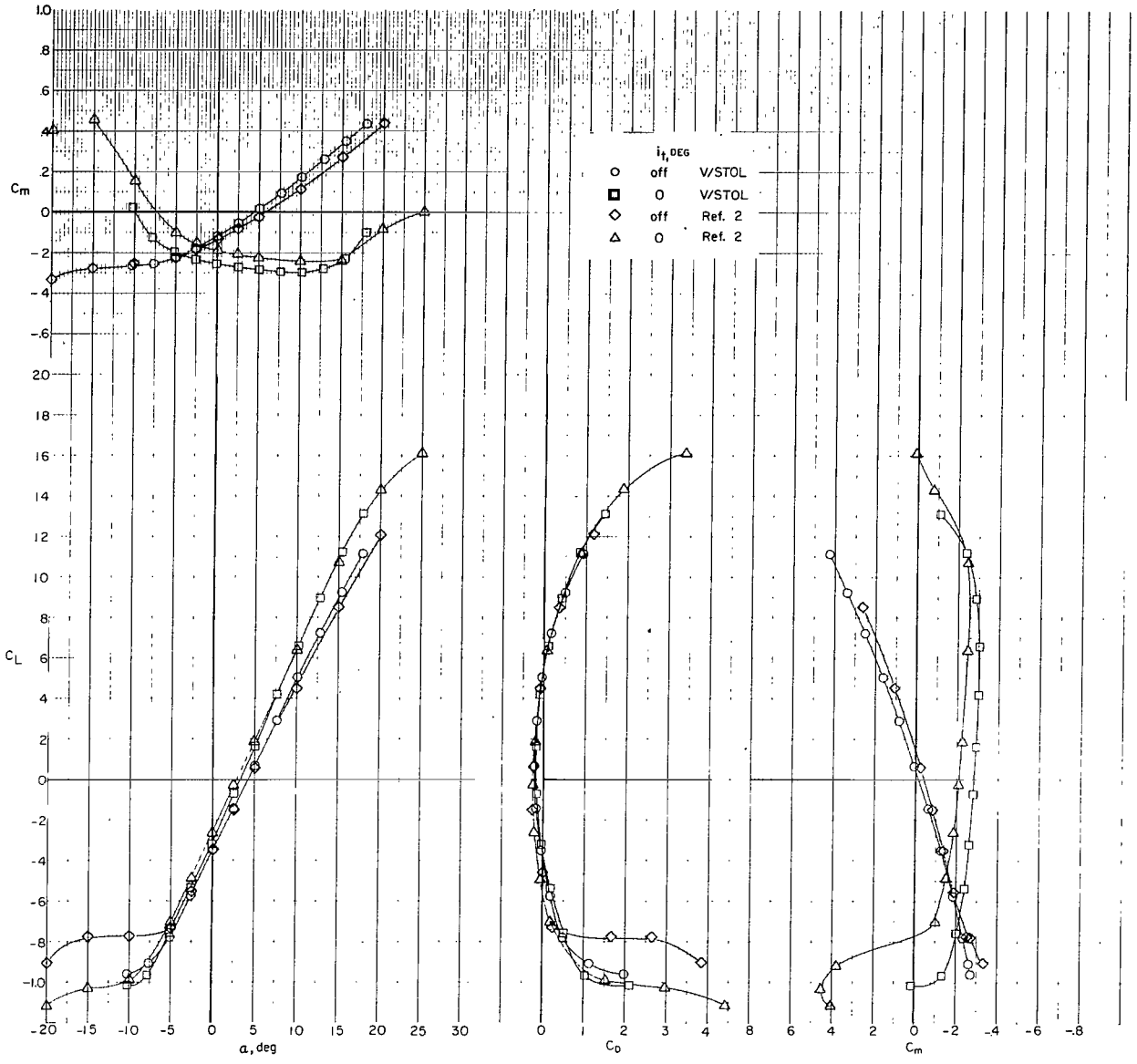

(a) $i_w = -9^o$; $\delta_f = 0^o$.

Figure 6.- Comparison of results from Langley V/STOL tunnel and from reference 2 for final Phase II configuration.

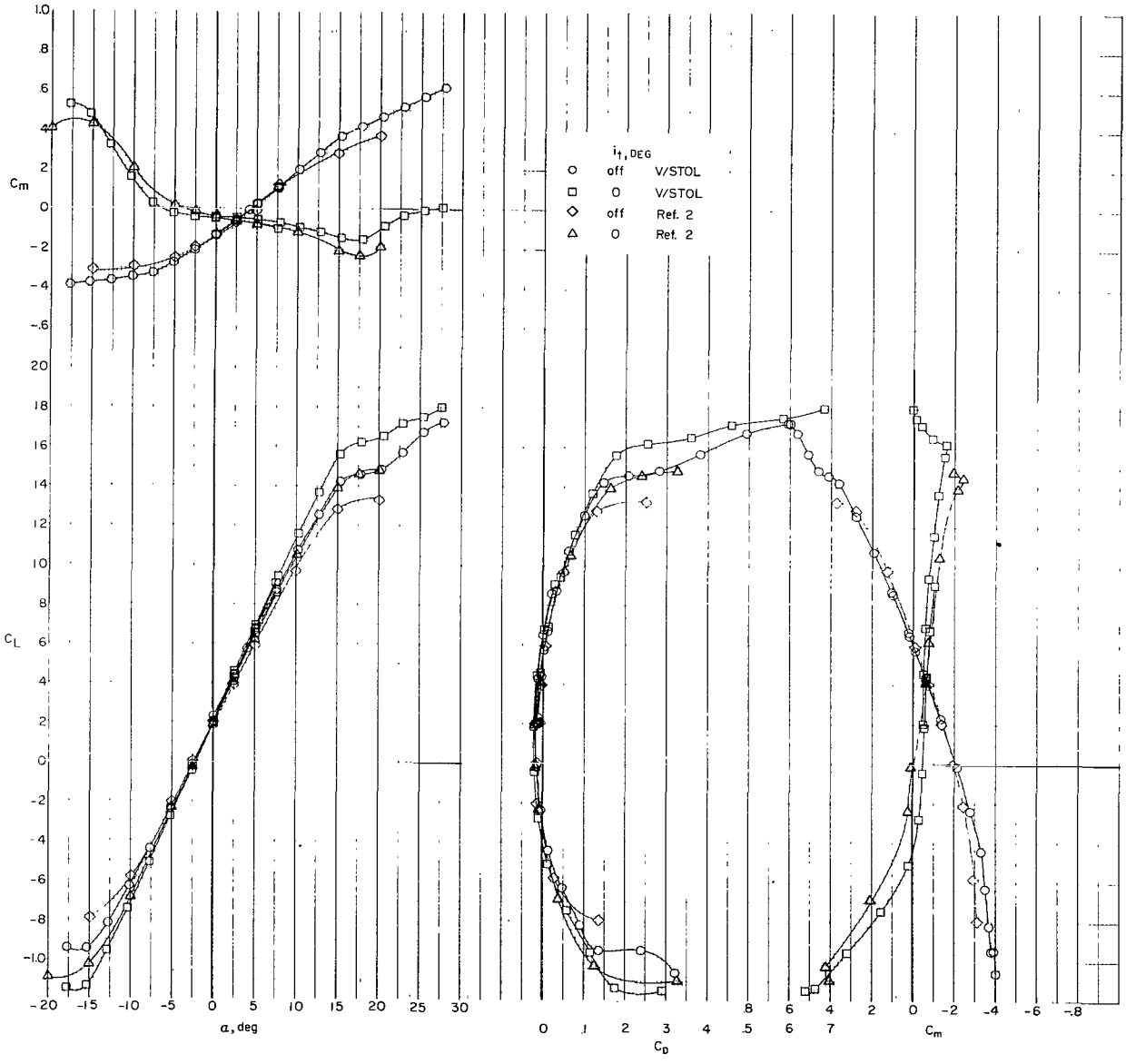

(b) $i_w = 0^o$; $\delta_f = 0^o$.

Figure 6.- Continued.

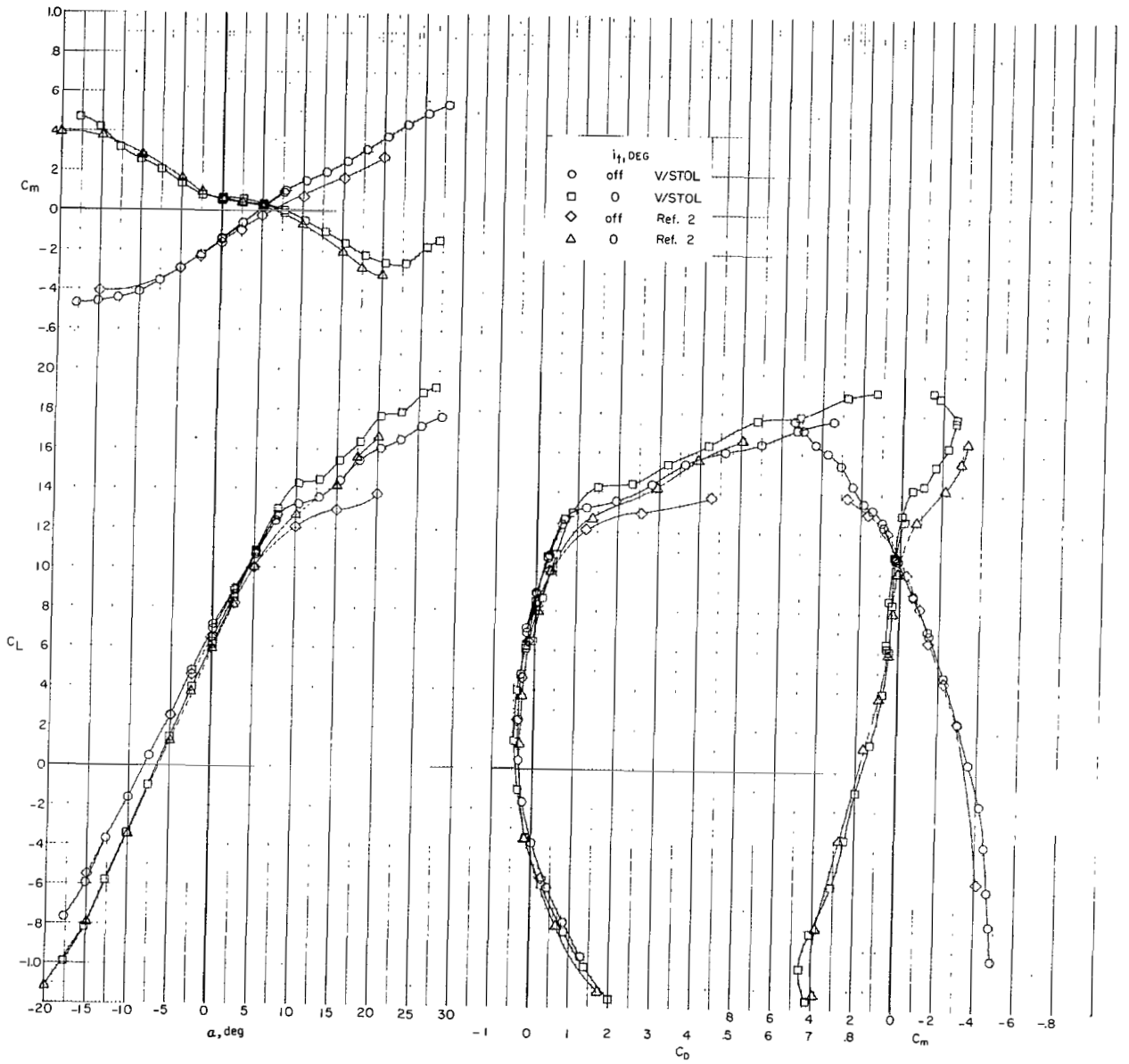

(c) $i_w = 7.5^o$; $\delta_f = 0^o$.

Figure 6.- Continued.

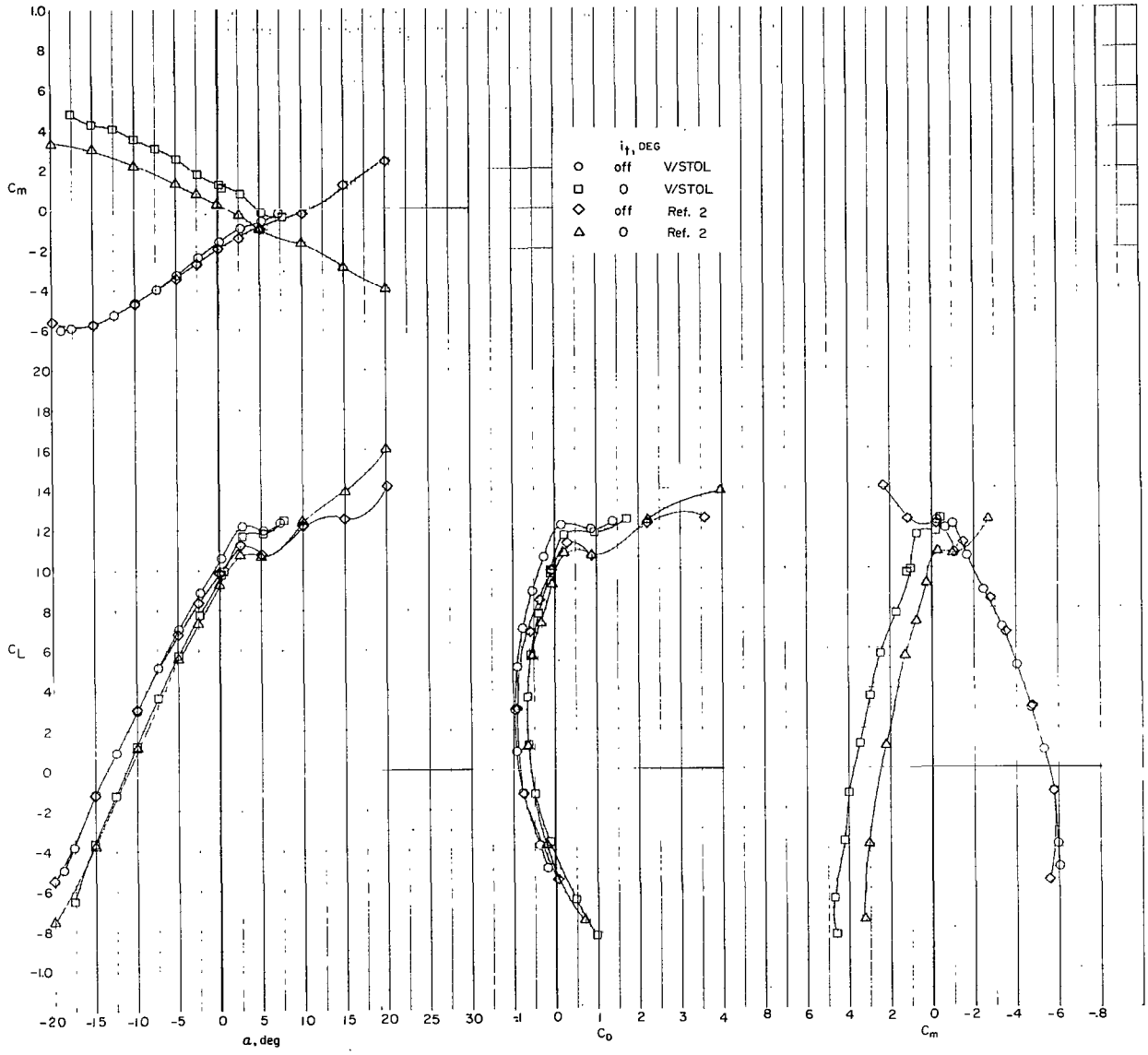

(d) $i_w = 15^o$; $\delta_f = 0^o$.

Figure 6.- Continued.

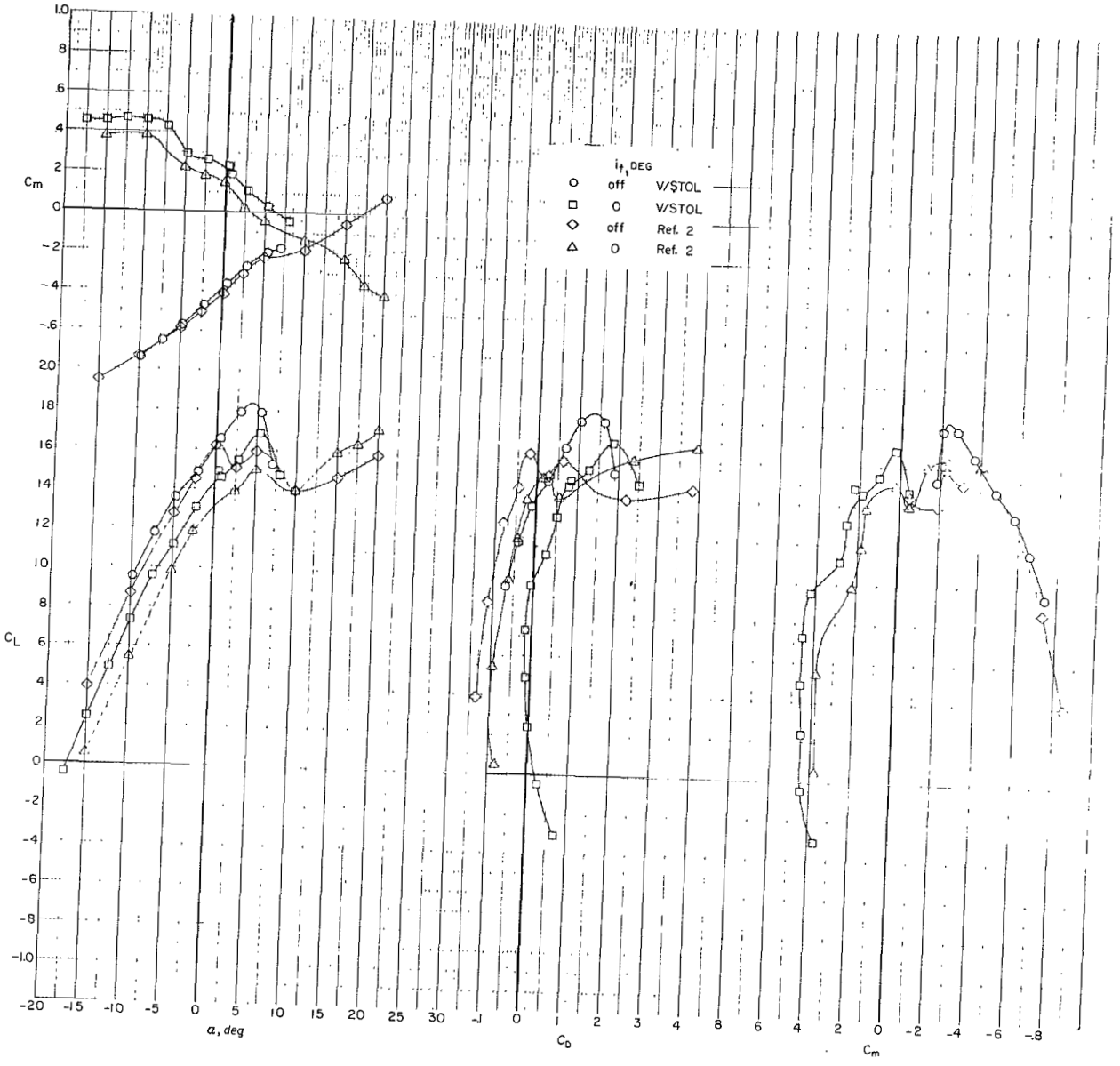

(e) $i_w = 15^o$; $\delta_f = 30^o$.

Figure 6.- Concluded.

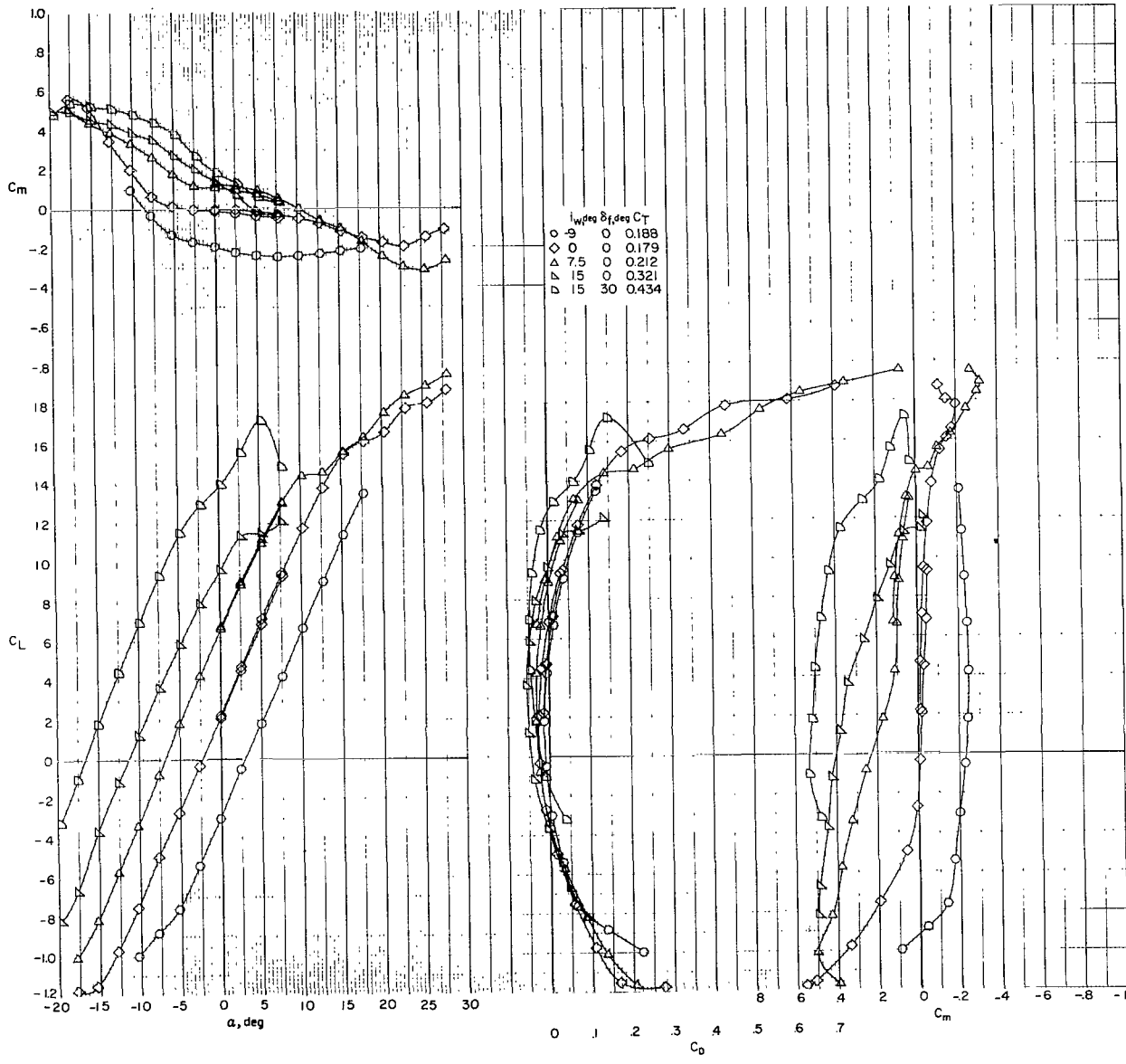

Figure 7.- Effect of i_w on longitudinal characteristics of final Phase II configuration with empennage refinement (lower tail C and T-tail E), from Langley V/STOL tunnel. Trim thrust.

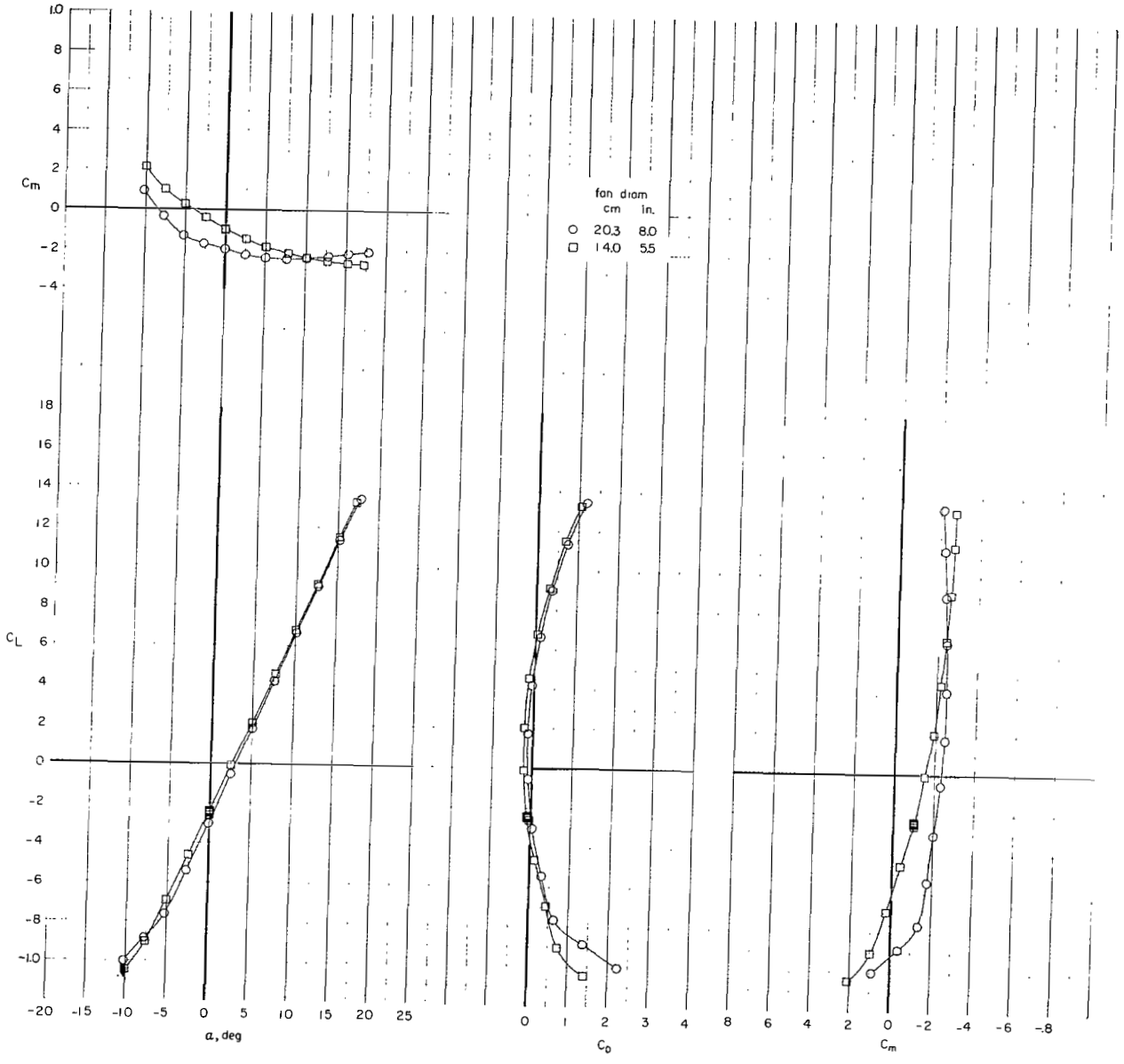

(a) $i_w = -9^o$; $\delta_f = 0^o$.

Figure 8.- Effect of fan size on longitudinal characteristics of final Phase II configuration with empennage refinement. Trim thrust.

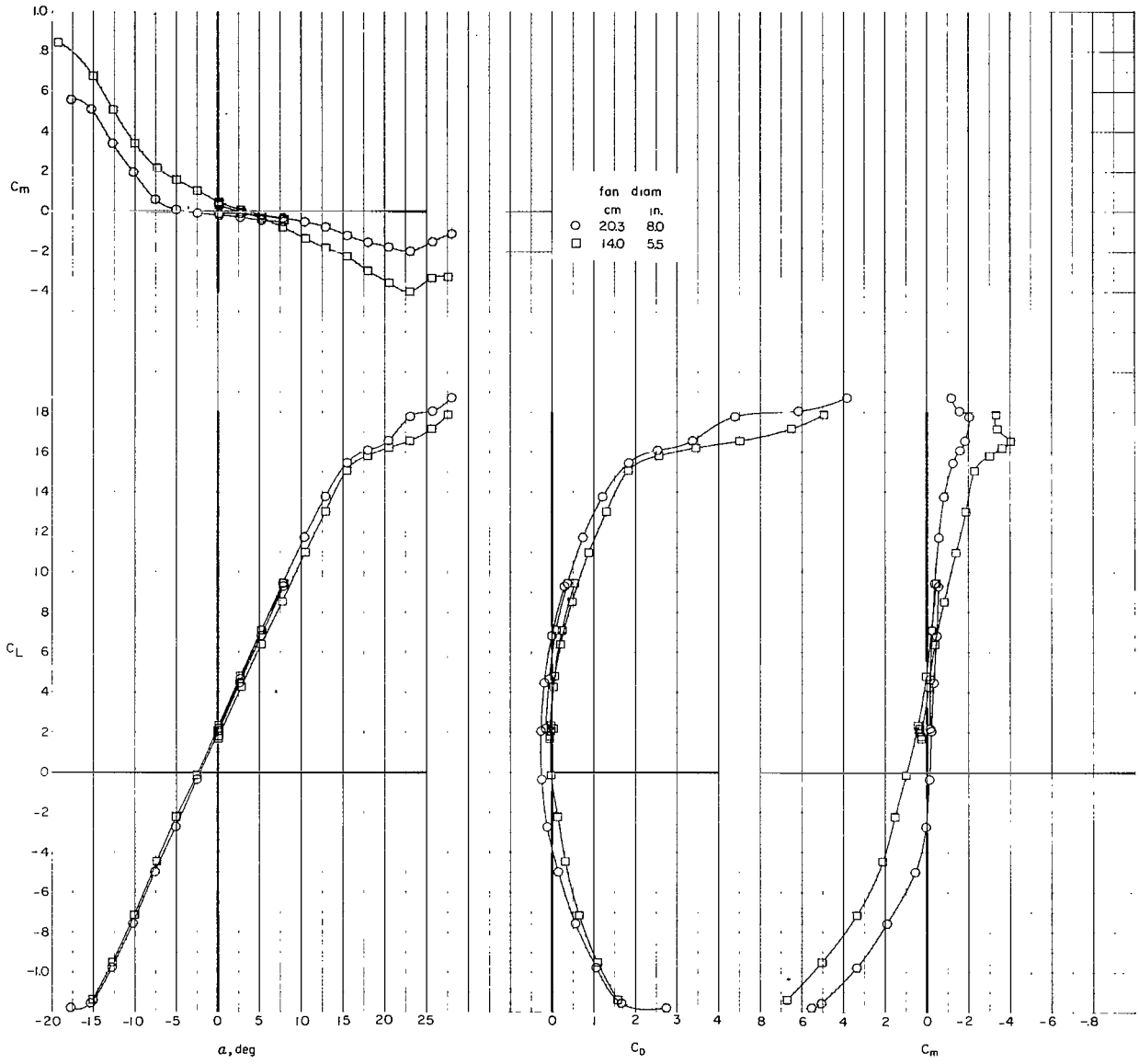

(b) $i_w = 0^o$; $\delta_f = 0^o$.

Figure 8.- Continued.

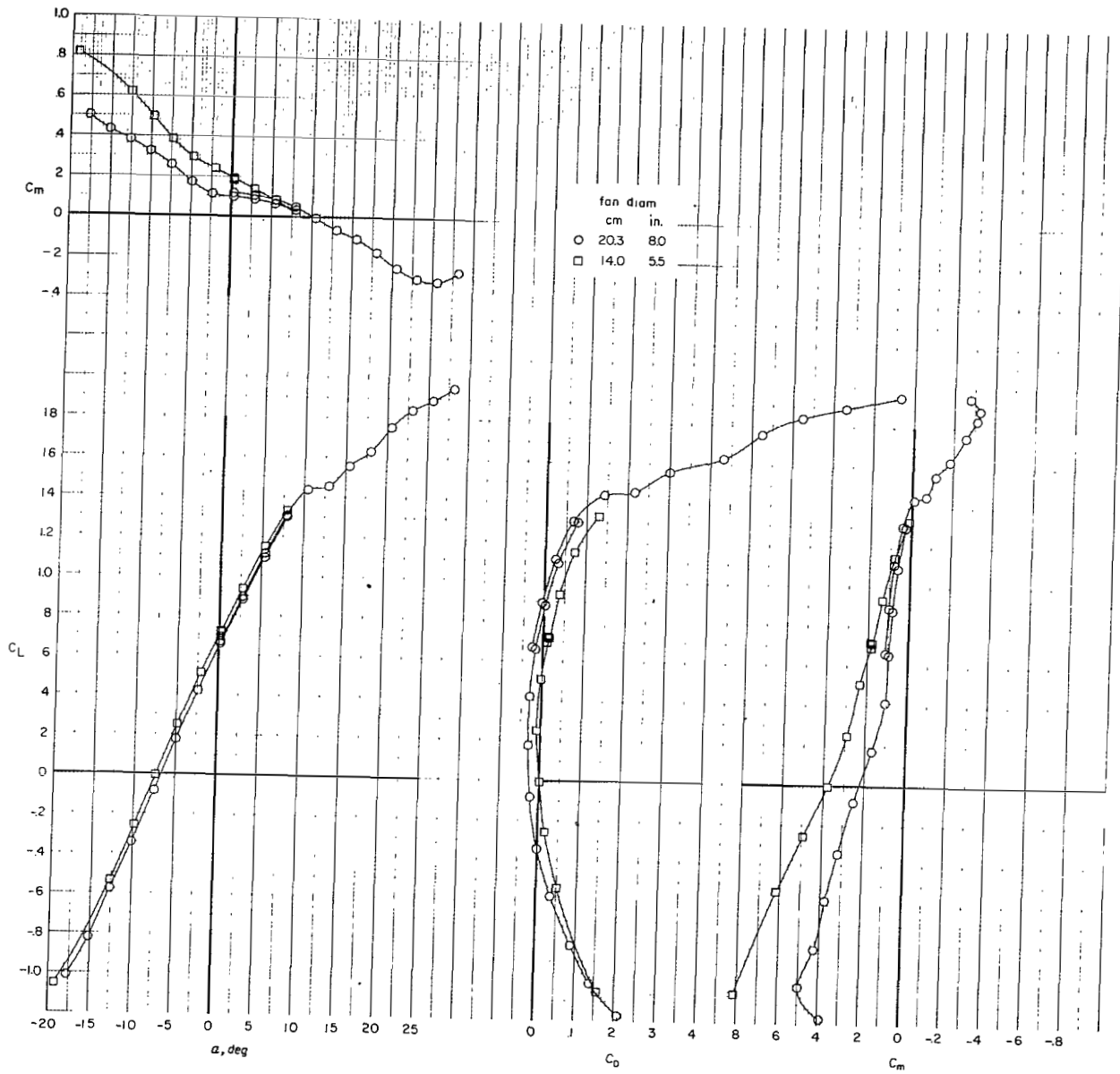

(c) $i_W = 7.5^o$; $\delta_f = 0^o$.

Figure 8.- Continued.

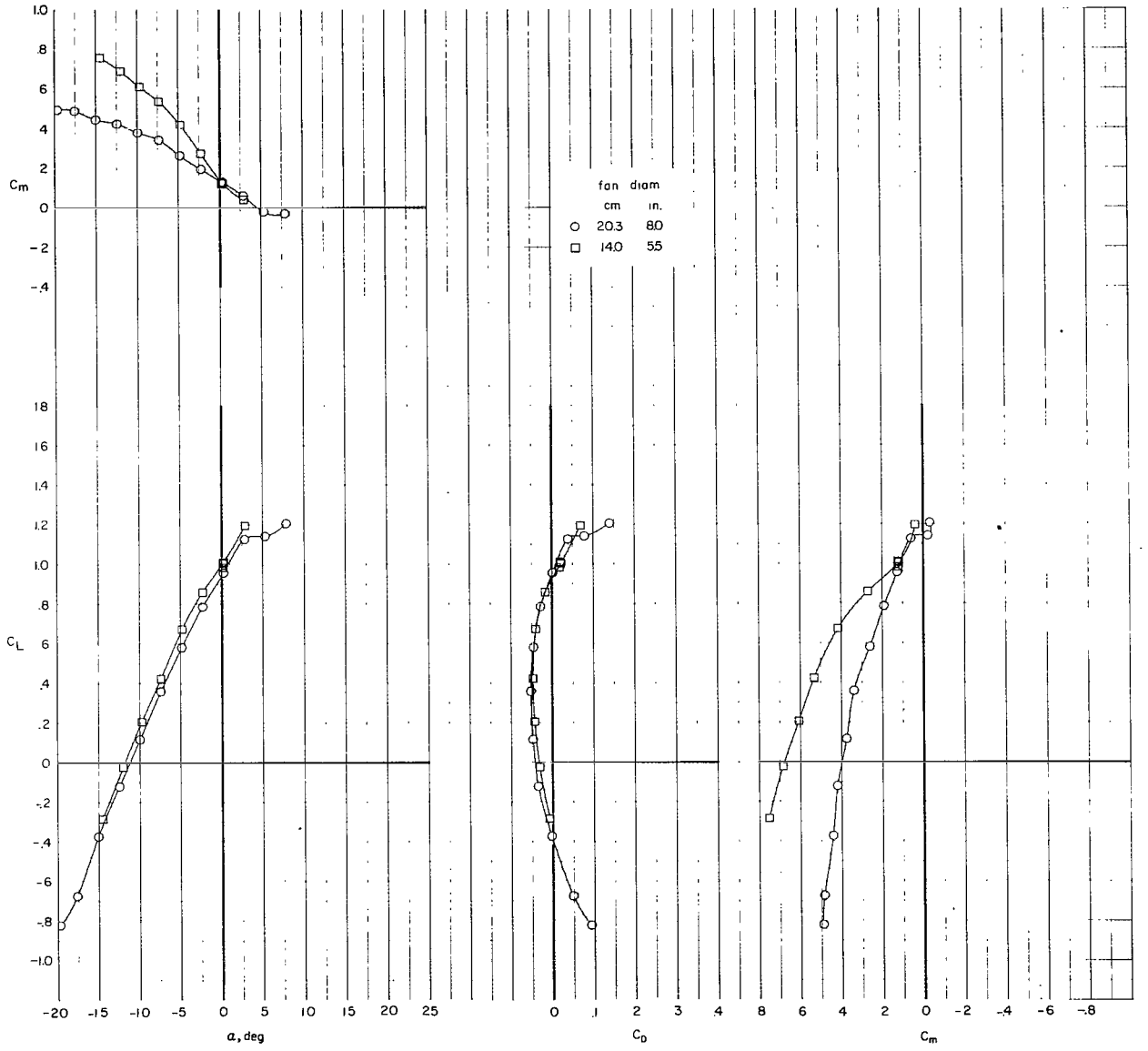

(d) $i_w = 15^o$; $\delta_f = 0^o$.

Figure 8.- Continued.

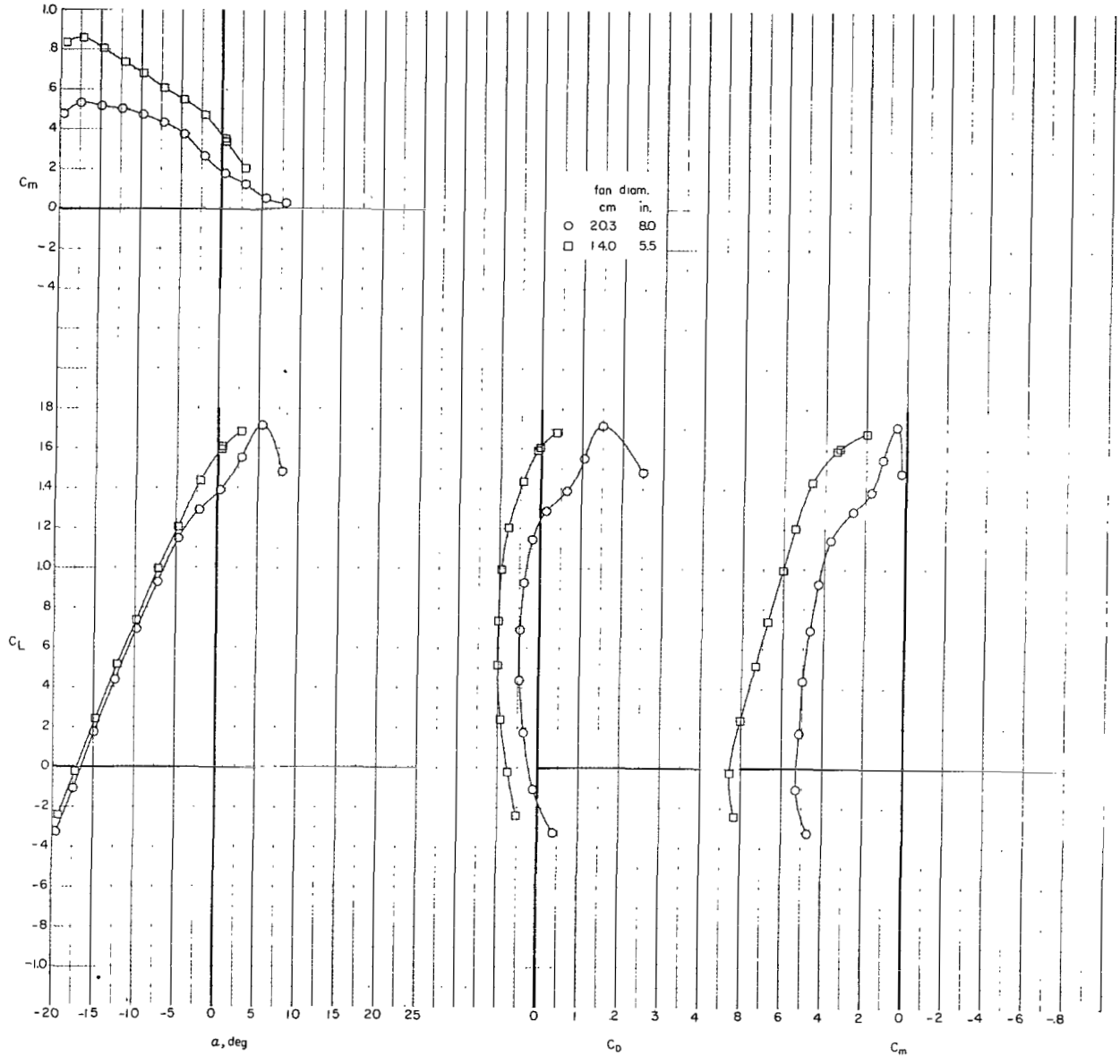

(e) $i_w = 15^o$; $\delta_f = 30^o$.

Figure 8.- Concluded.

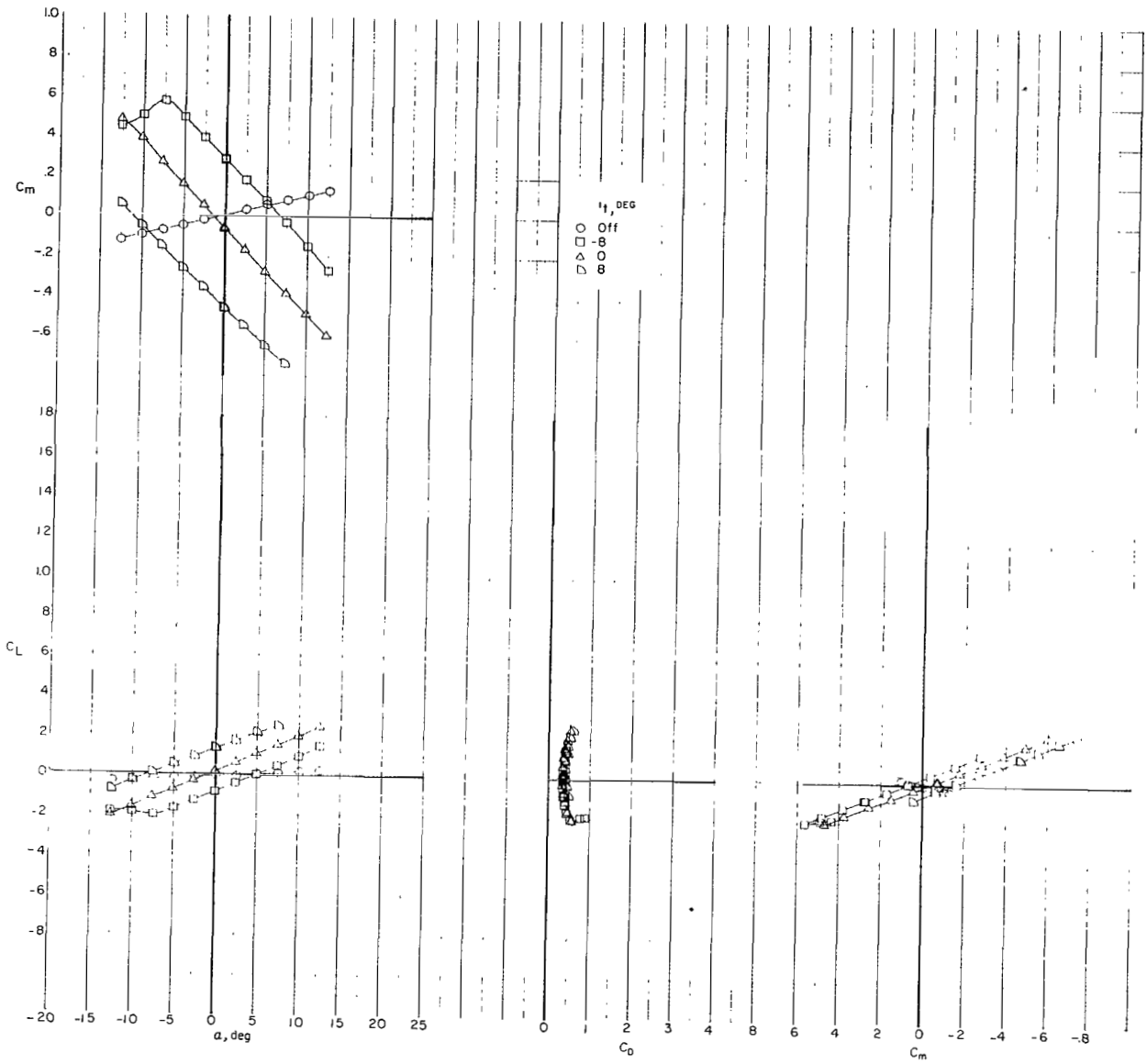

Figure 9.- Effect of lower horizontal-tail incidence i_t on longitudinal characteristics of model with fuselage, vertical tail, and 118-cm (46.67-in.) span tail C. Rotor pylon removed.

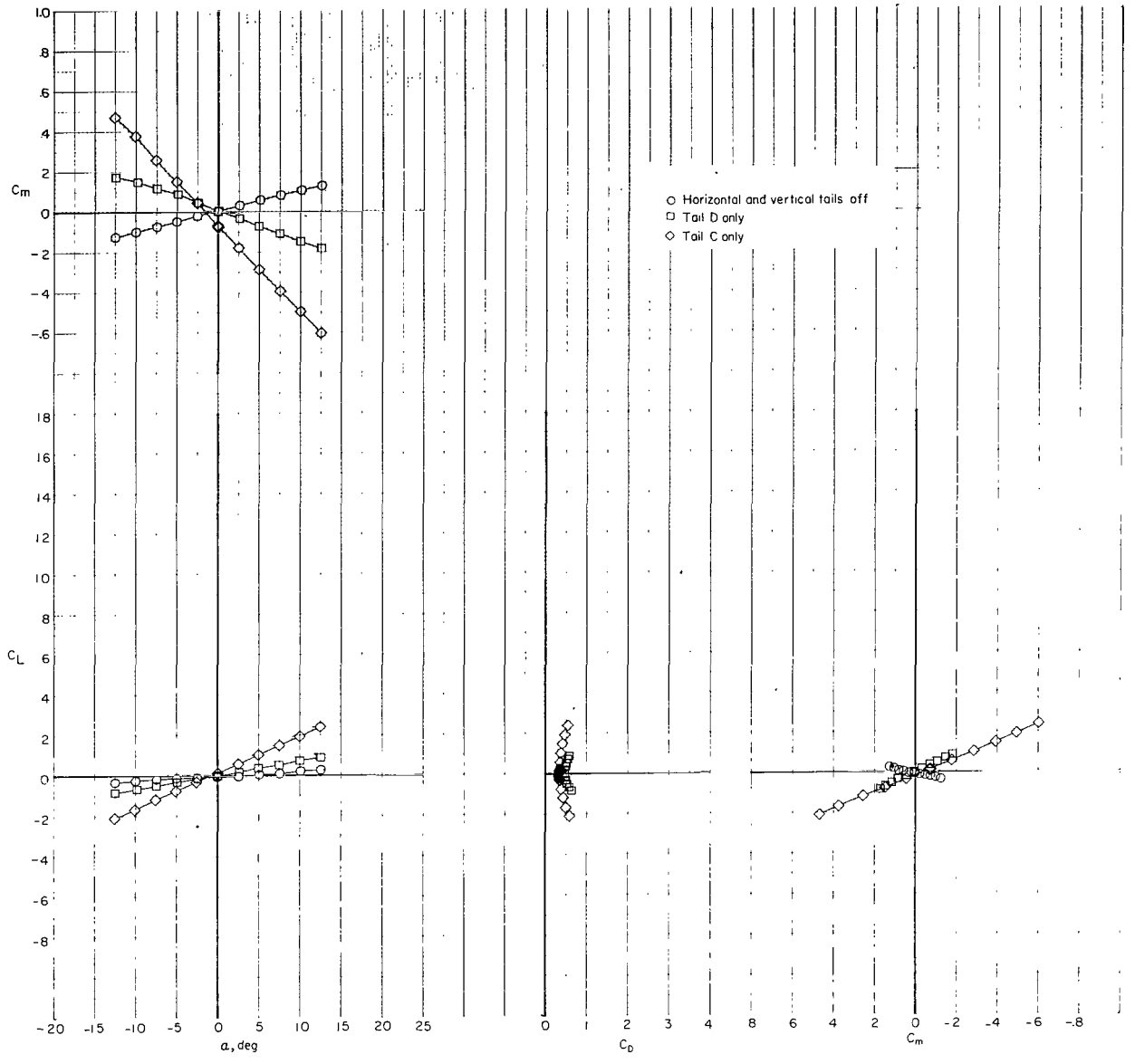

Figure 10.- Effect of T-tail D on longitudinal characteristics of configuration with fuselage, main rotor pylon, and reduced vertical tail.

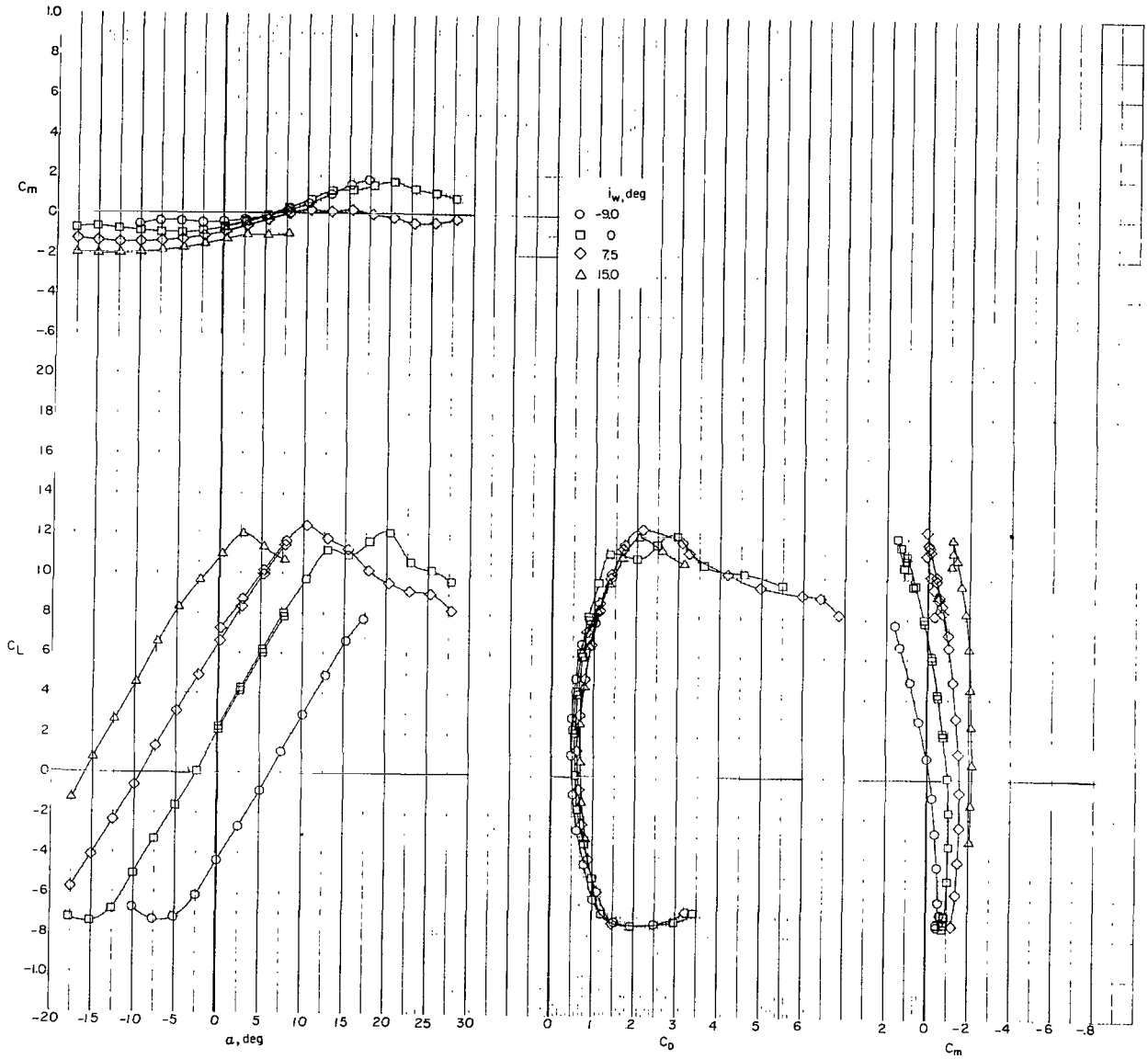

Figure 11.- Effect of wing incidence i_w on longitudinal characteristics of configuration with fuselage, wing, main rotor pylon, and vertical tail. $\delta_f = 0^o$.

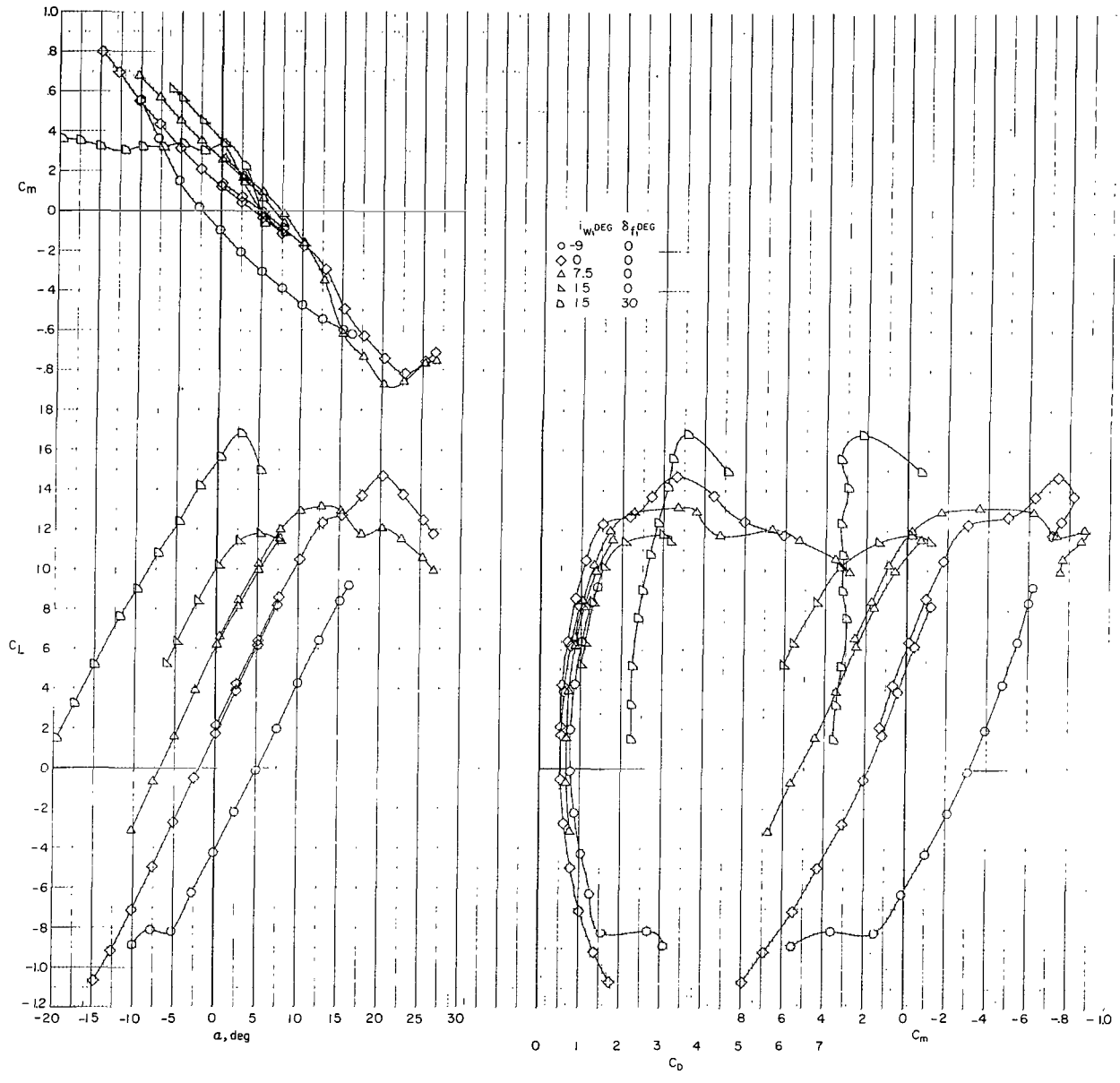

Figure 12.- Effect of wing incidence i_W on longitudinal characteristics of configuration with fuselage, wing, vertical tail, lower horizontal tail C, and T-tail E.

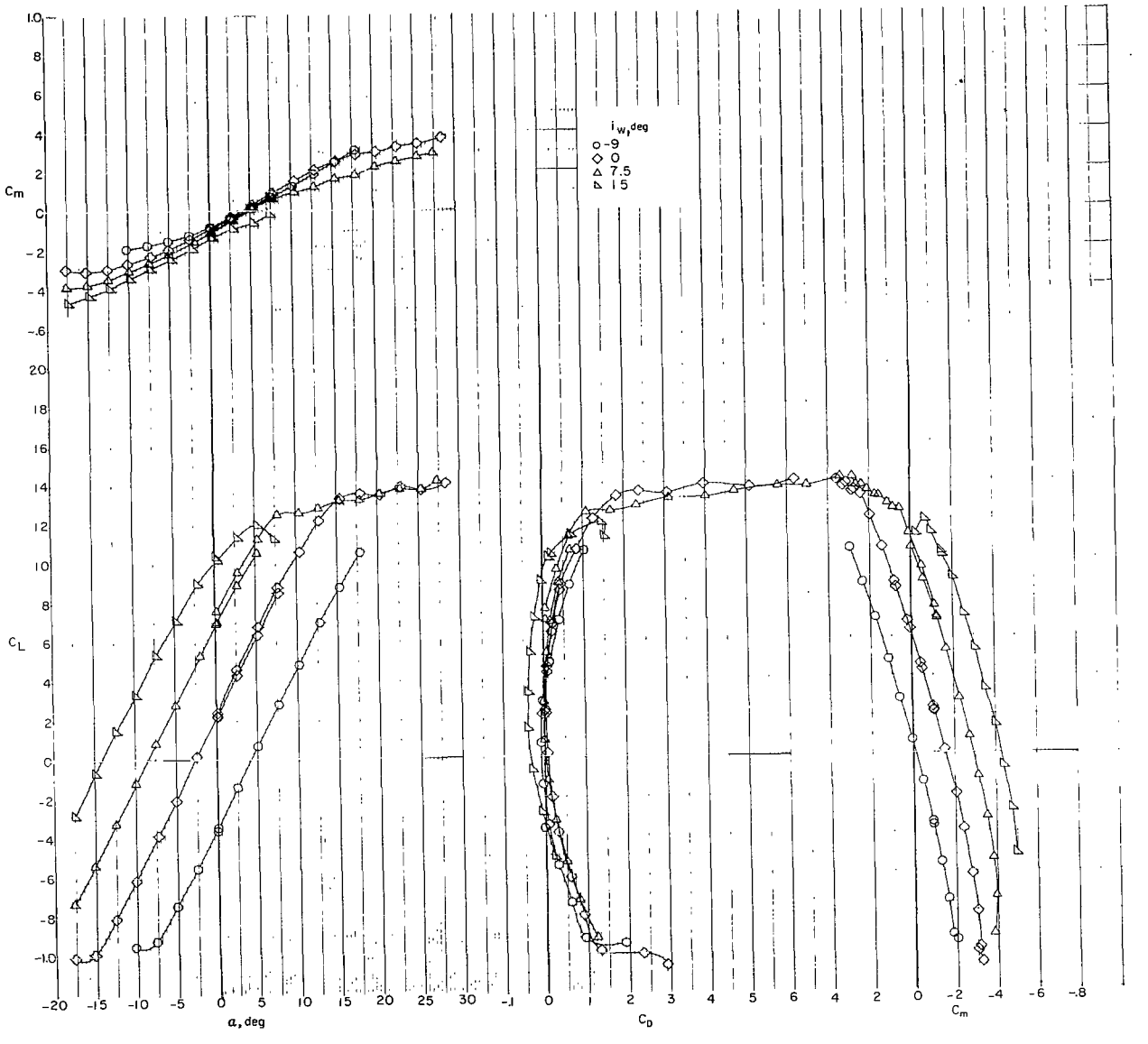

Figure 13.- Effect of i_w on longitudinal characteristics of configuration with fuselage, wing, vertical tail, and engines. Horizontail tails off; small-diameter fans and minimum fairings in forward position; trim thrust.

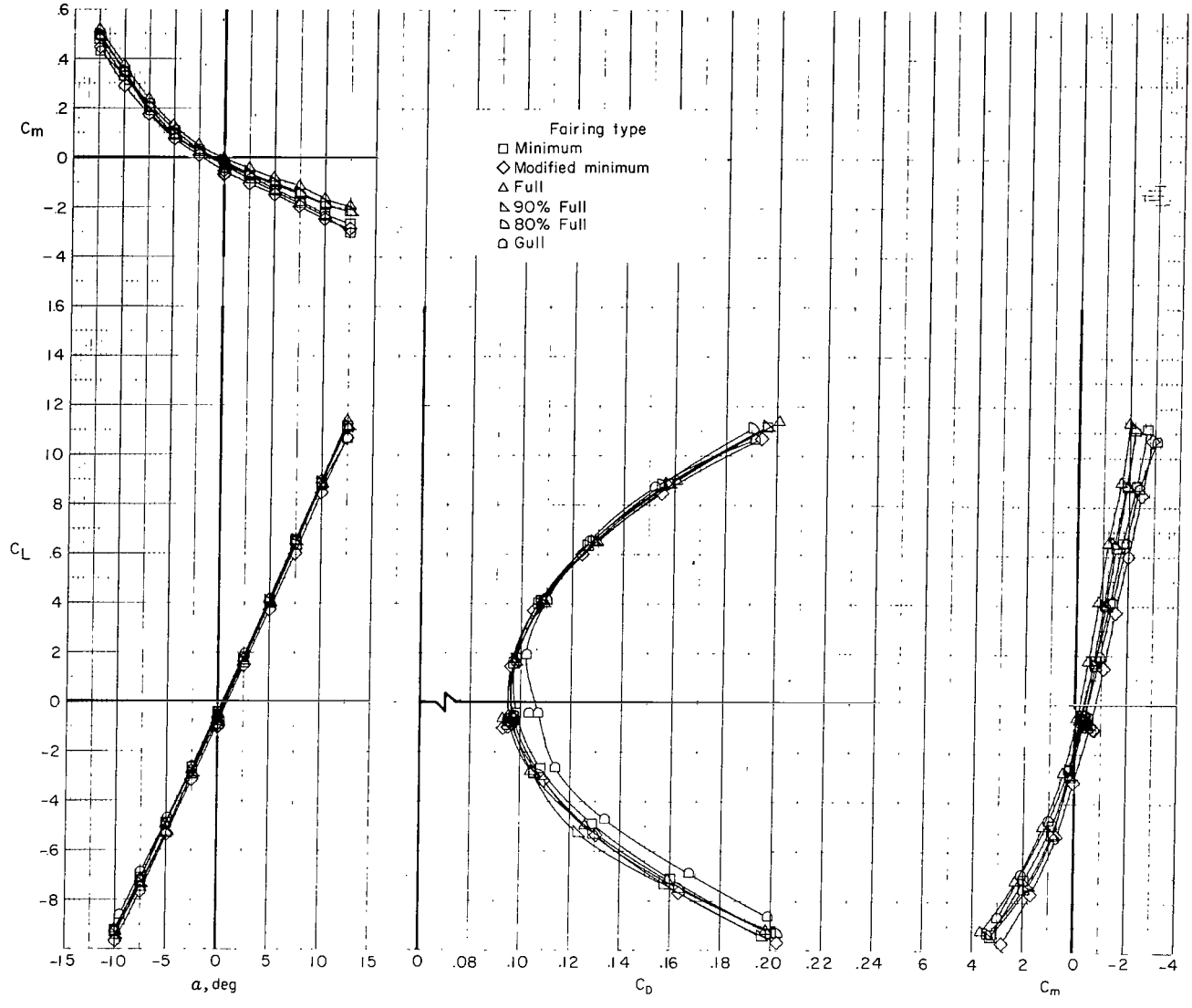

(a) $i_w = -4.5^o$.

Figure 14.- Effect of pylon fairing type on longitudinal characteristics of configuration with fuselage, wing, vertical tail, small-diameter fans, and horizontal tails C and E. Windmill thrust.

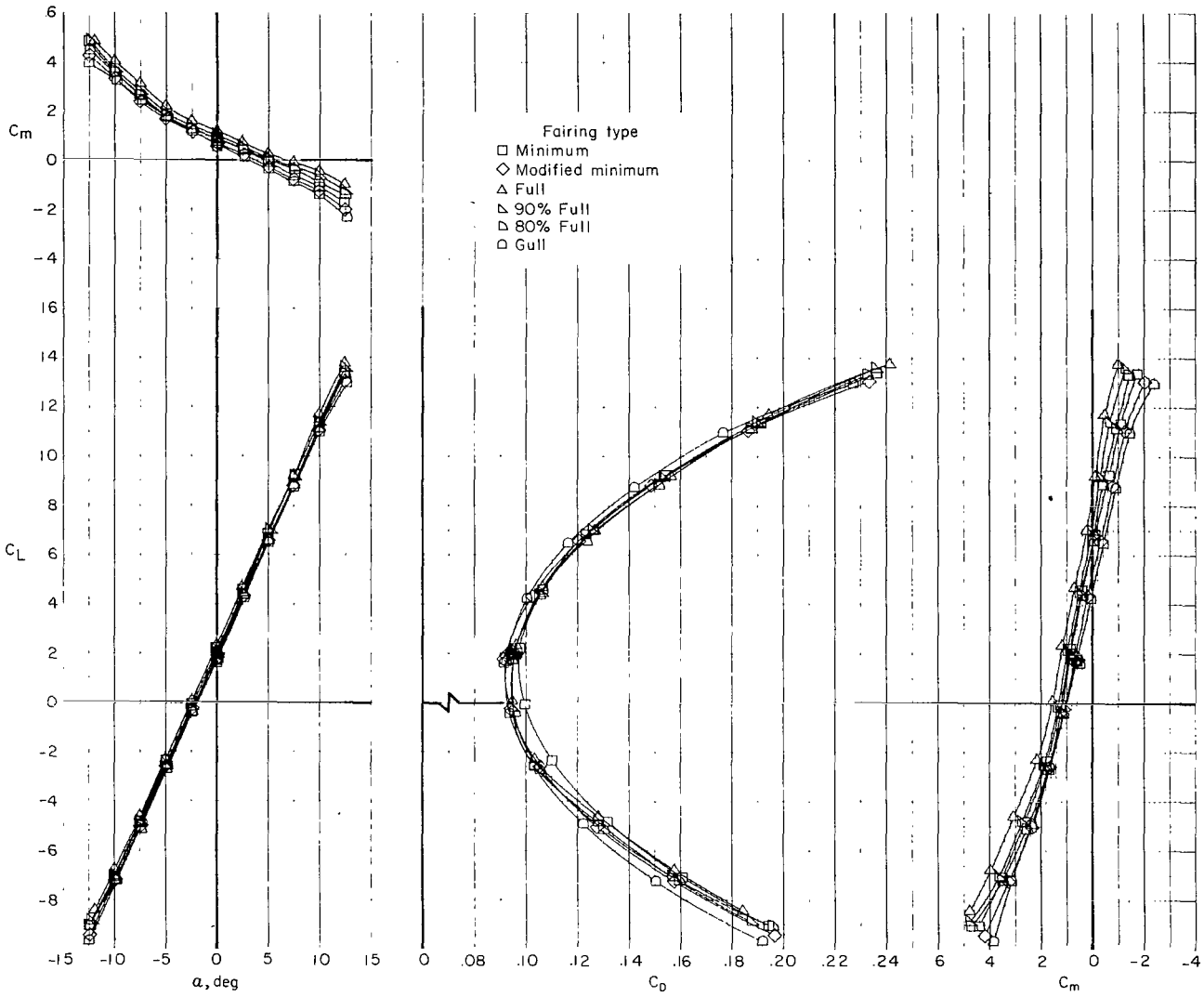

(b) $i_w = 0^o$.

Figure 14.- Continued.

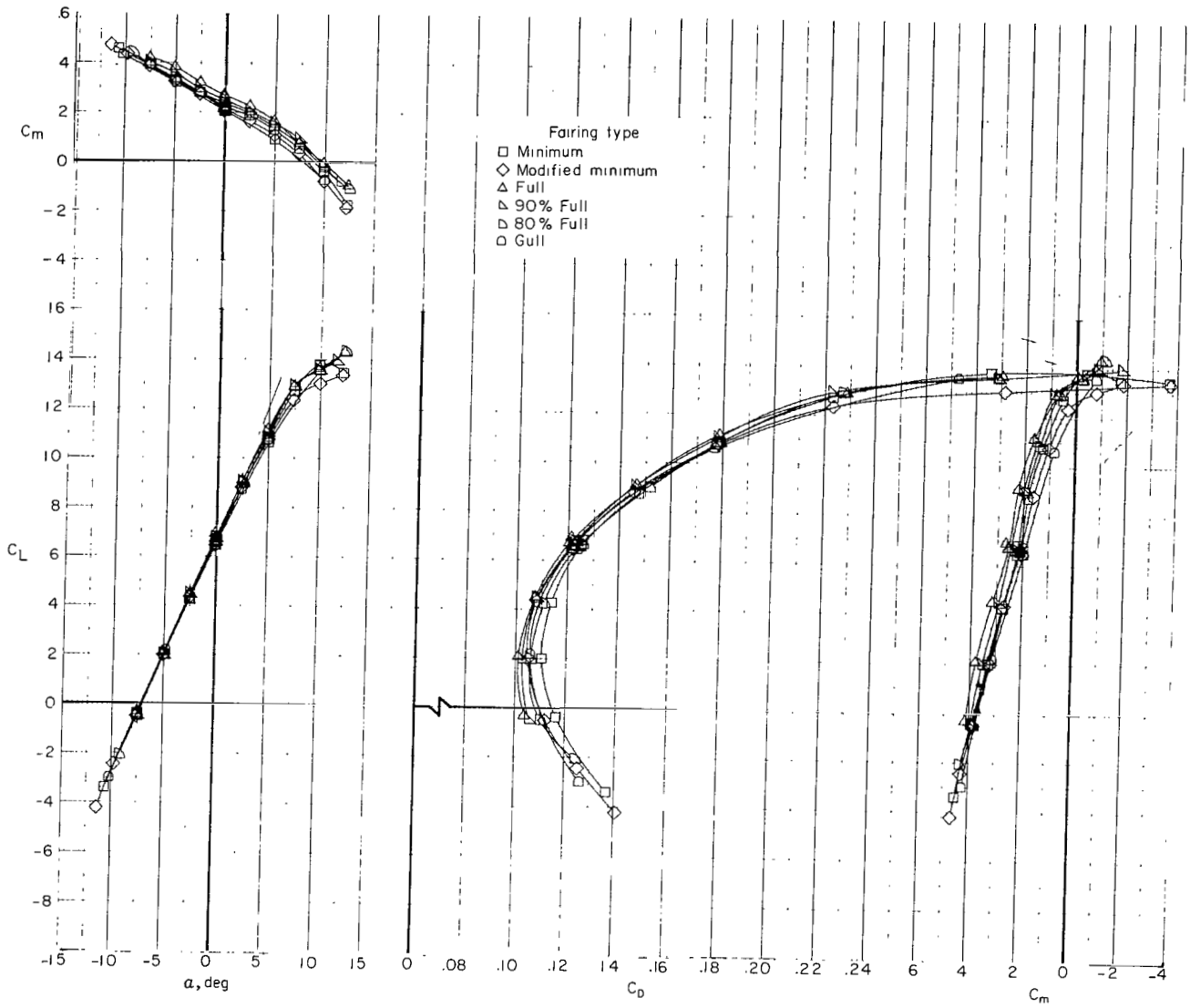

(c) $i_W = 7.5^o$.

Figure 14.- Concluded.

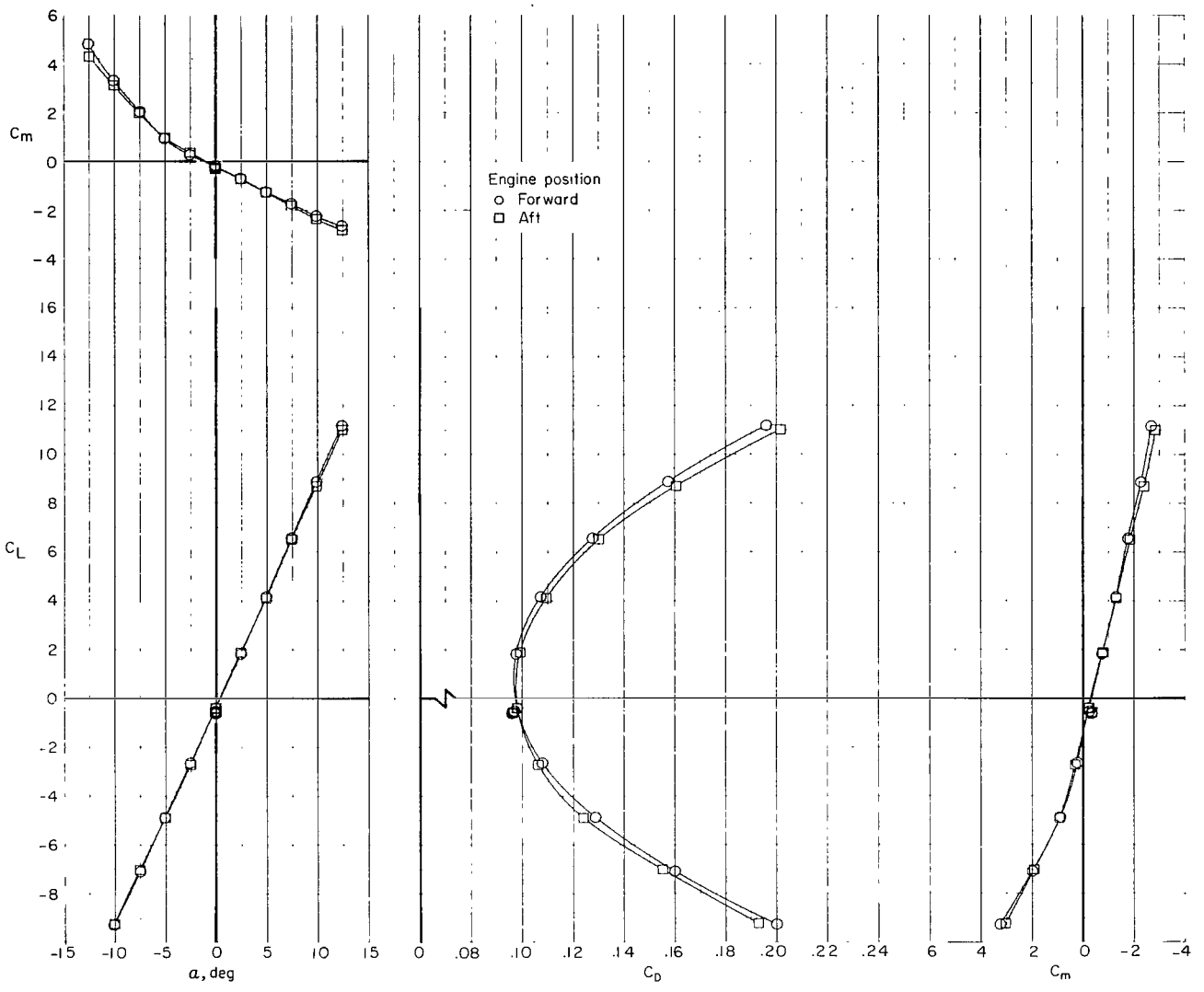

(a) $i_w = -4.5^o$; $\delta_f = 0^o$; windmill thrust.

Figure 15.- Effect of engine-nacelle and pylon-fairing position on longitudinal characteristics of complete configuration with horizontal tails C and E and minimum fairings.

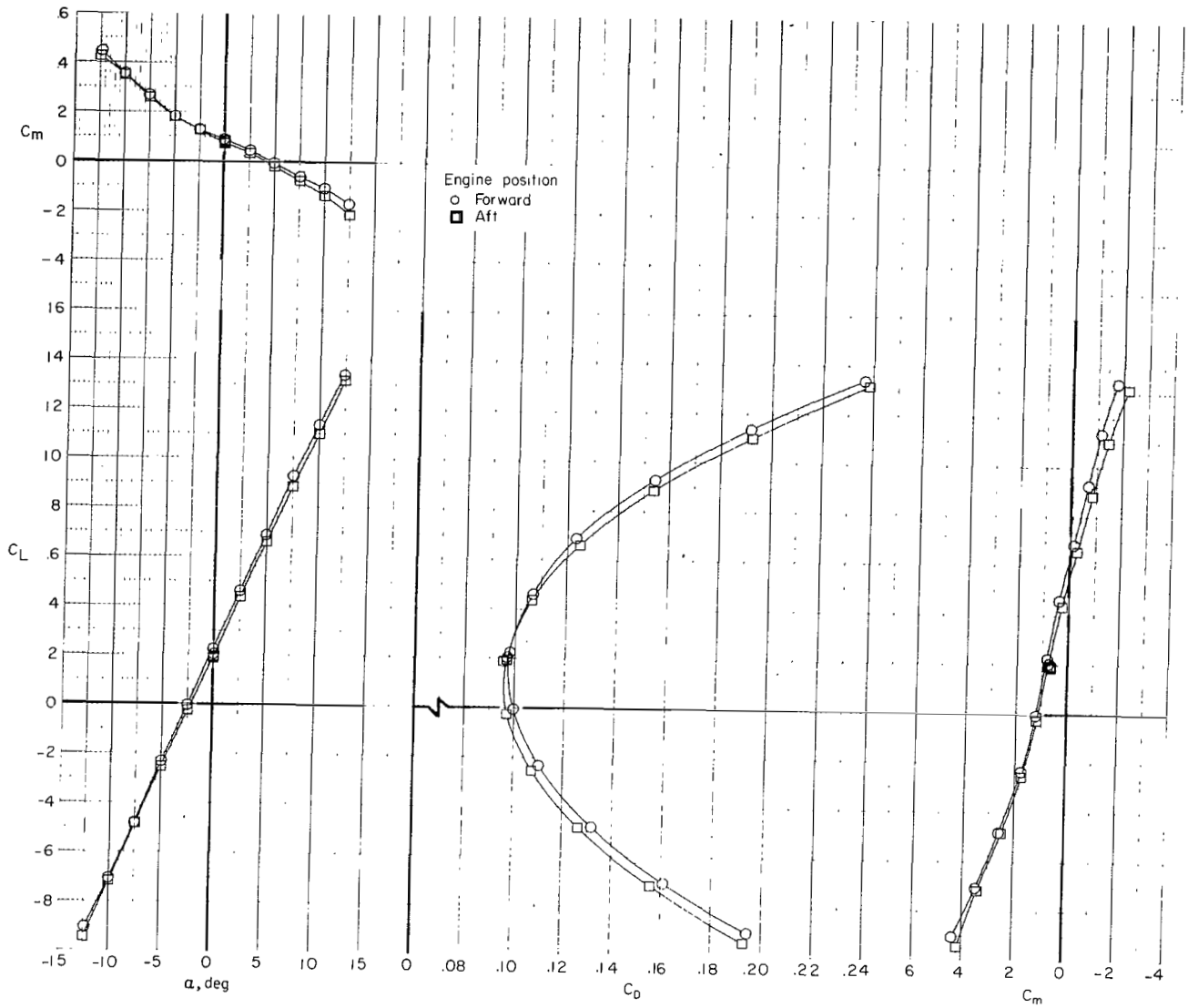

(b) $i_w = 0^o$; $\delta_f = 0^o$; windmill thrust.

Figure 15.- Continued.

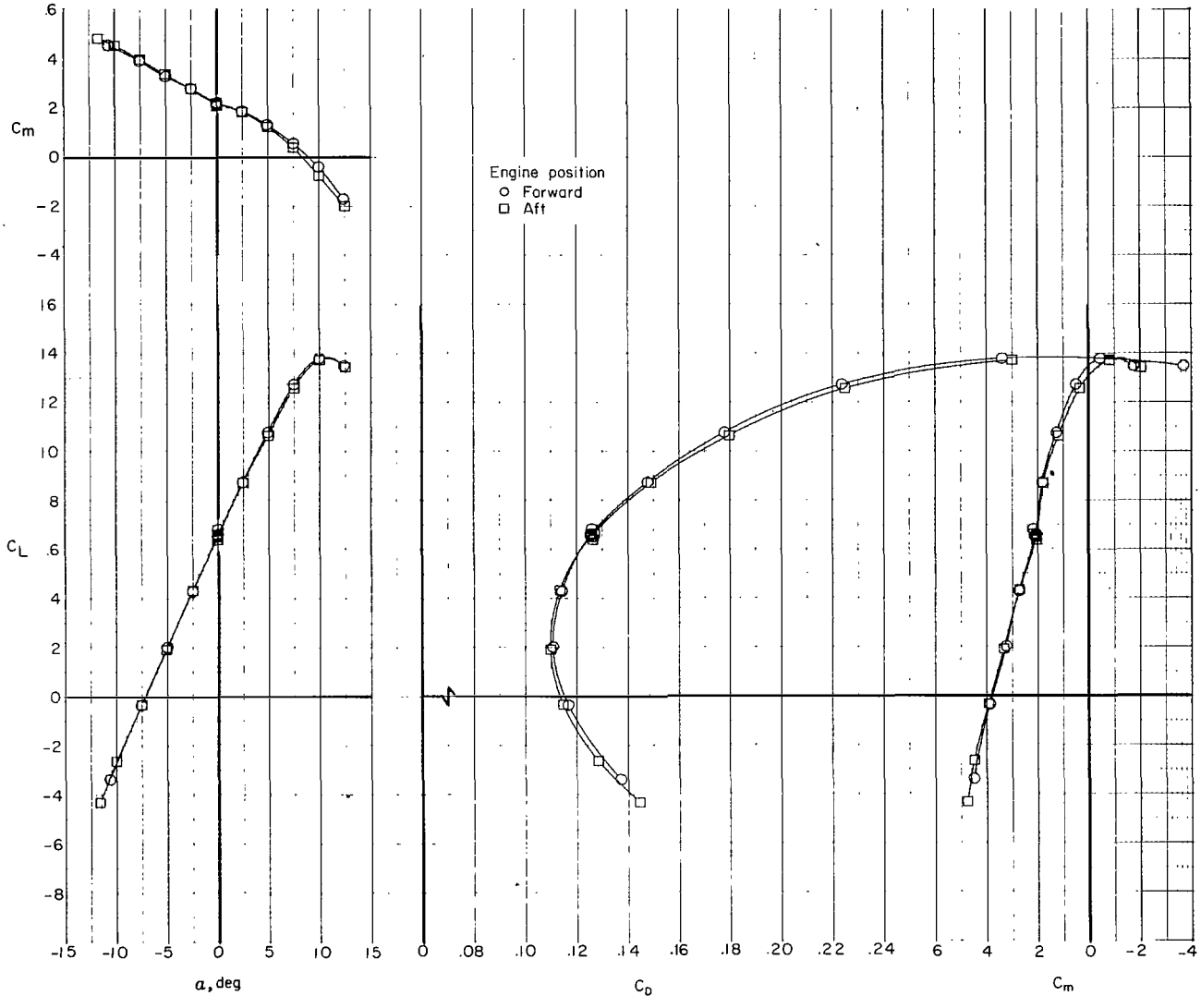

(c) $i_w = 7.5^o$; $\delta_f = 0^o$; windmill thrust.

Figure 15.- Continued.

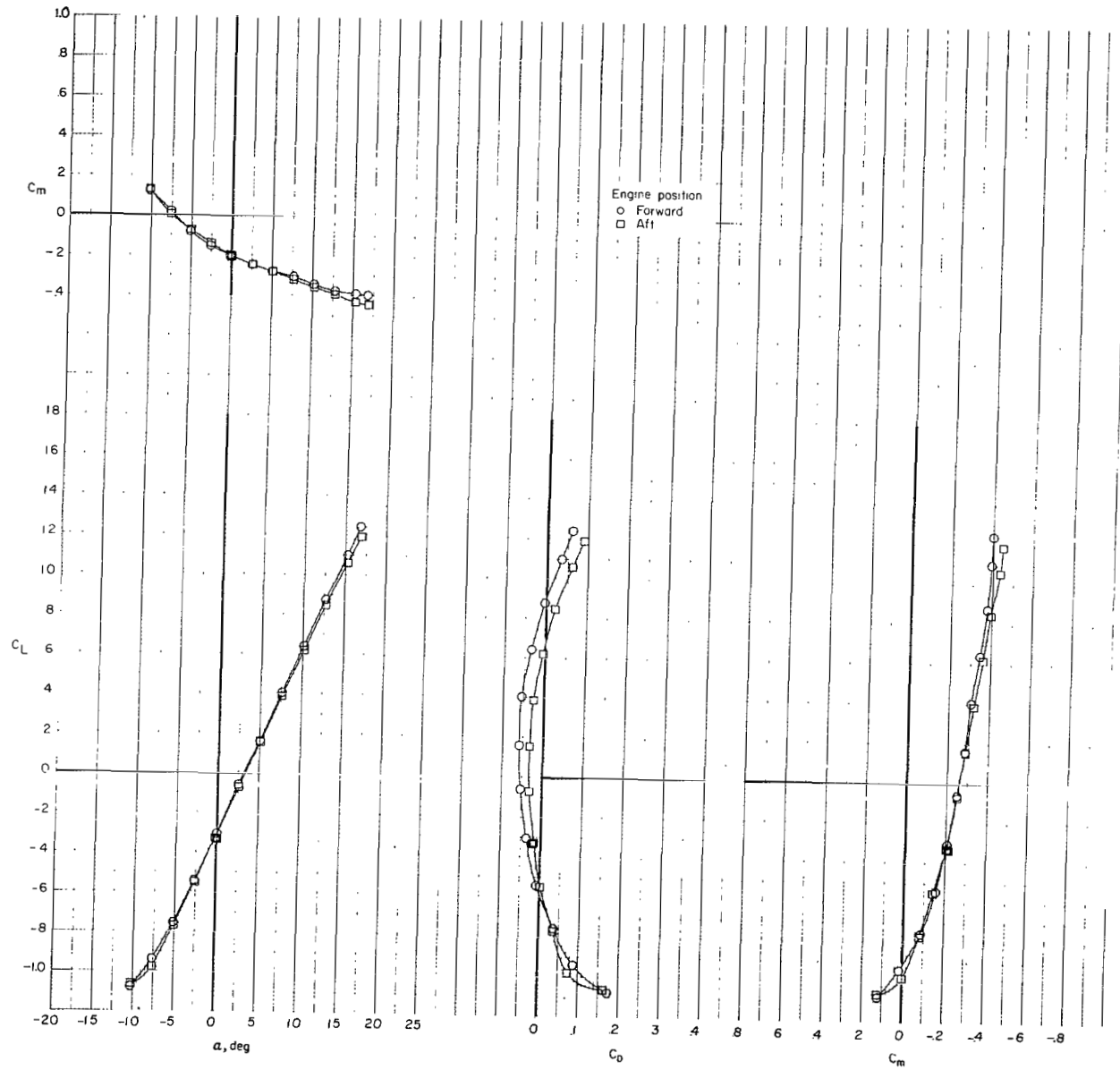

(d) $i_w = -9^o$; $\delta_f = 0^o$; trim thrust.

Figure 15.- Continued.

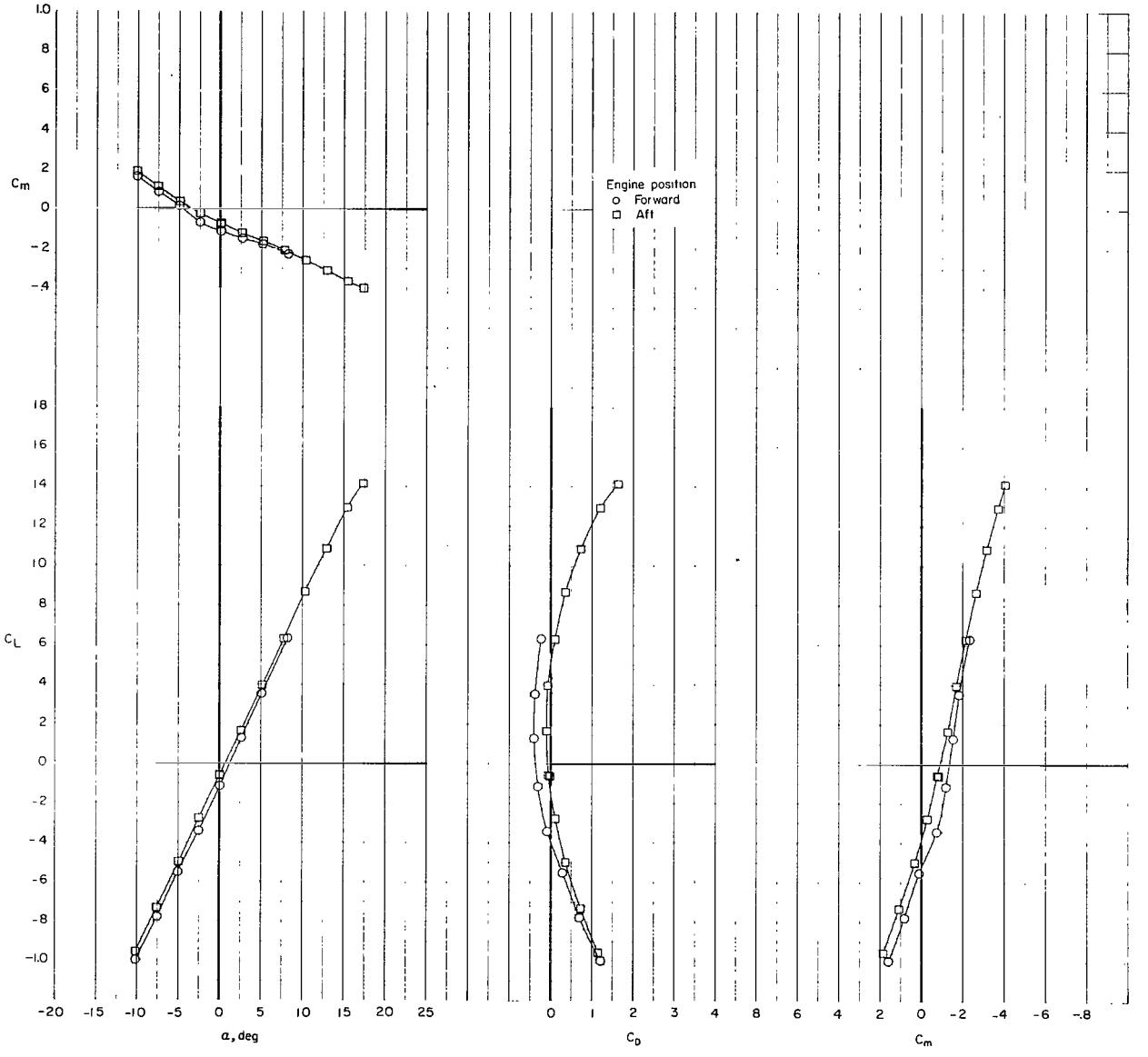

(e) $i_w = -4.5^o$; $\delta_f = 0^o$; trim thrust.

Figure 15.- Continued.

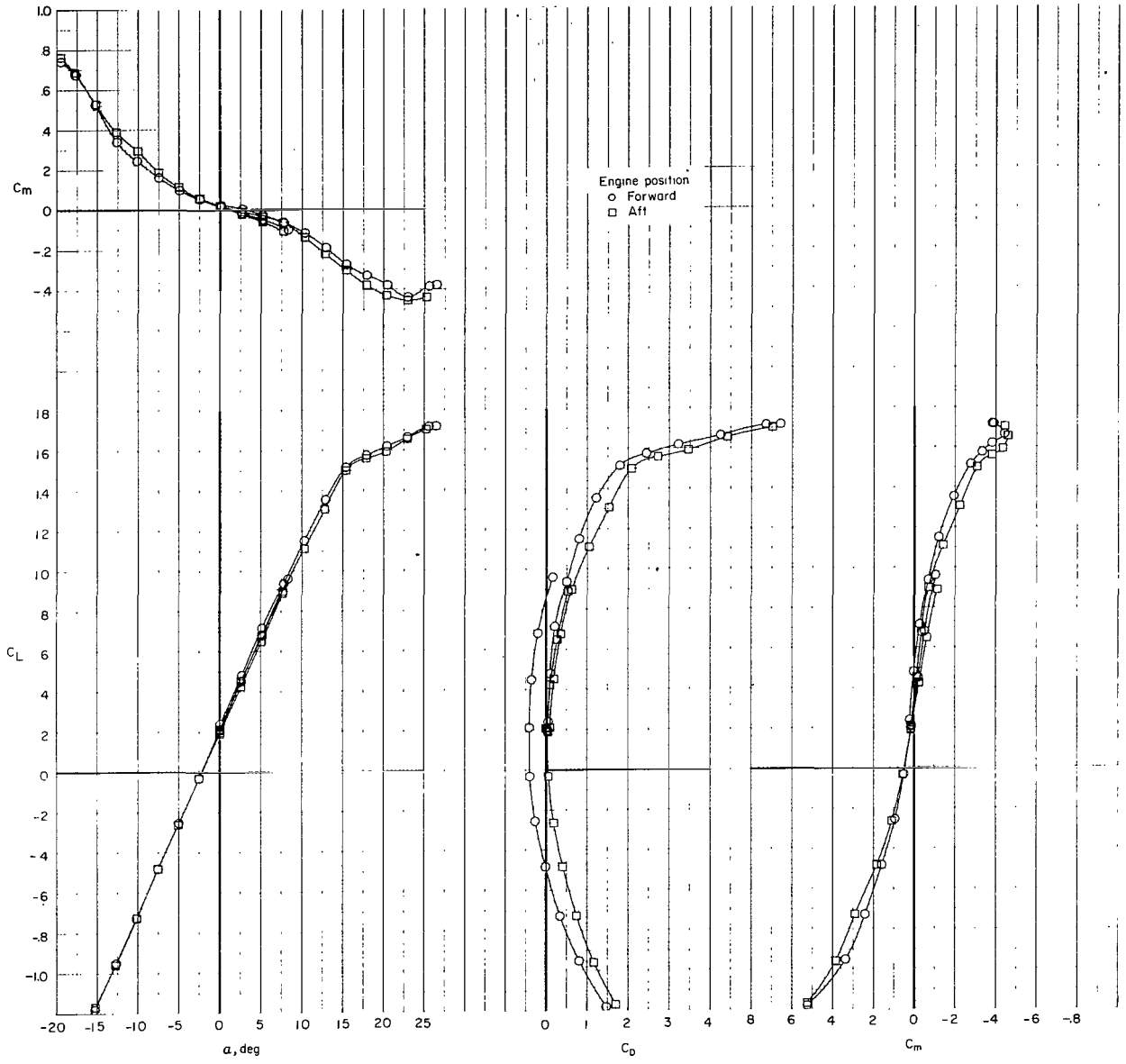

(f) $i_w = 0^o$; $\delta_f = 0^o$; trim thrust.

Figure 15.- Continued.

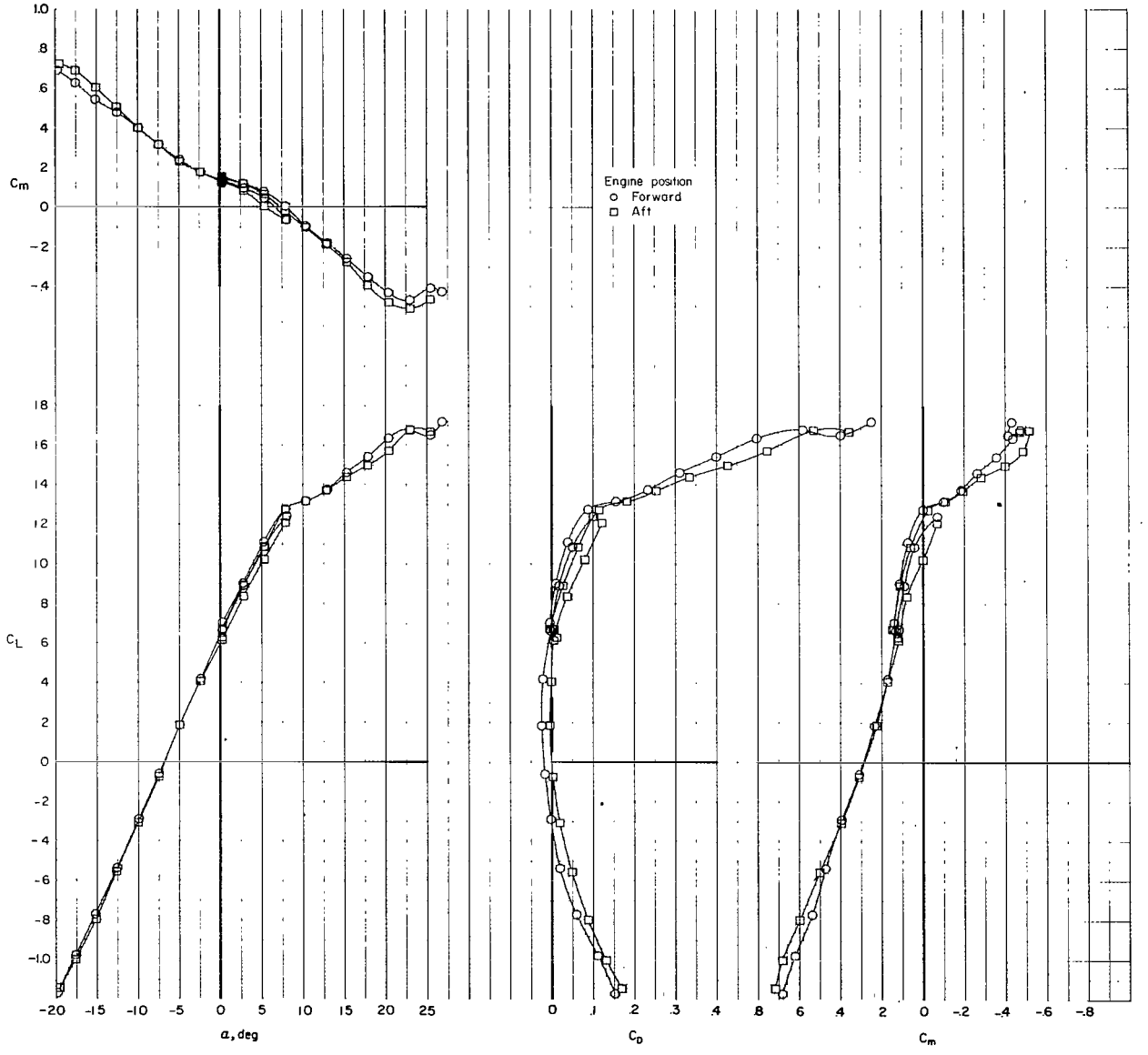

(g) $i_w = 7.5^o$; $\delta_f = 0^o$; trim thrust.

Figure 15.- Continued.

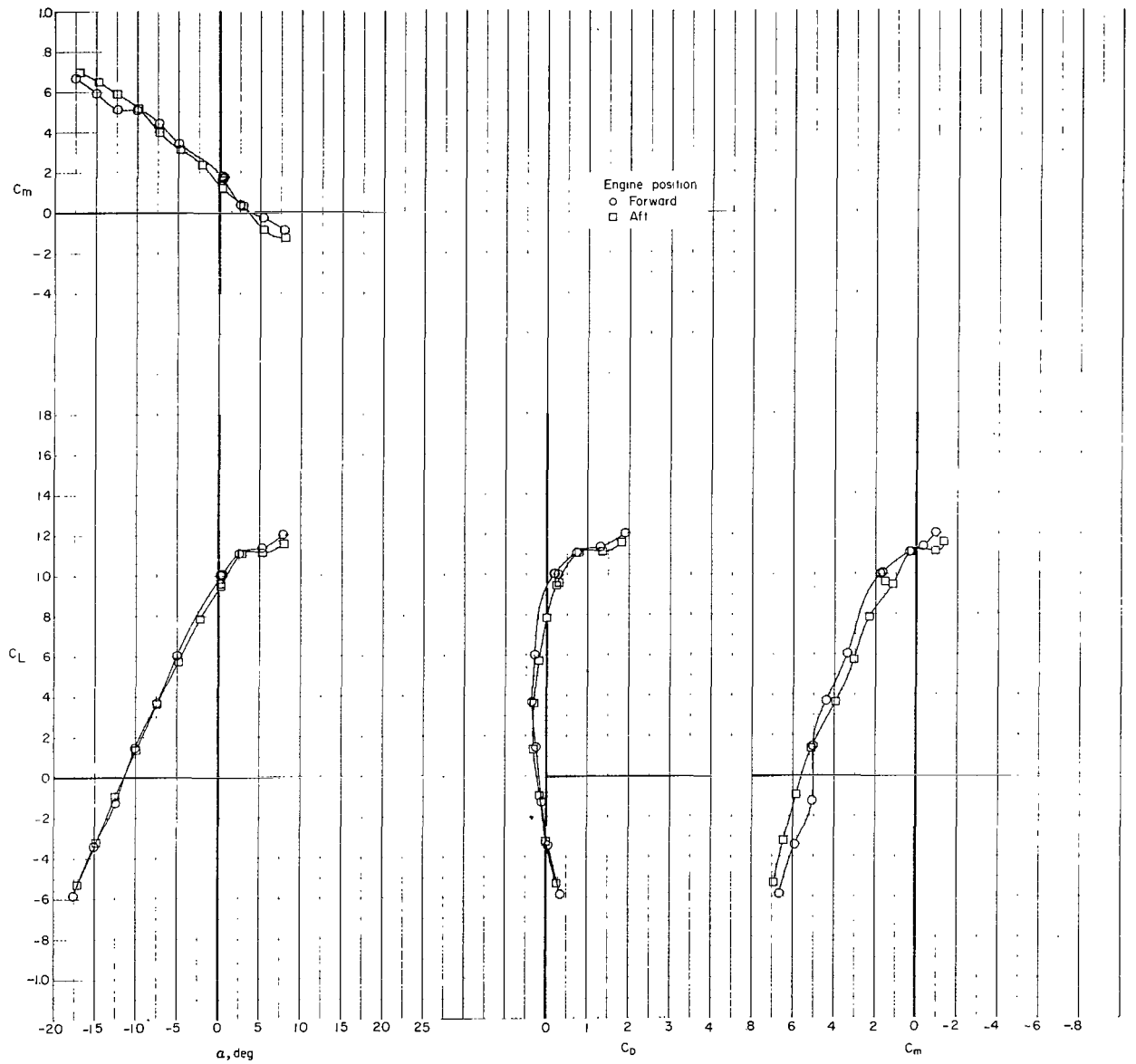

(h) $i_w = 15^o$; $\delta_f = 0^o$; trim thrust.

Figure 15.- Continued.

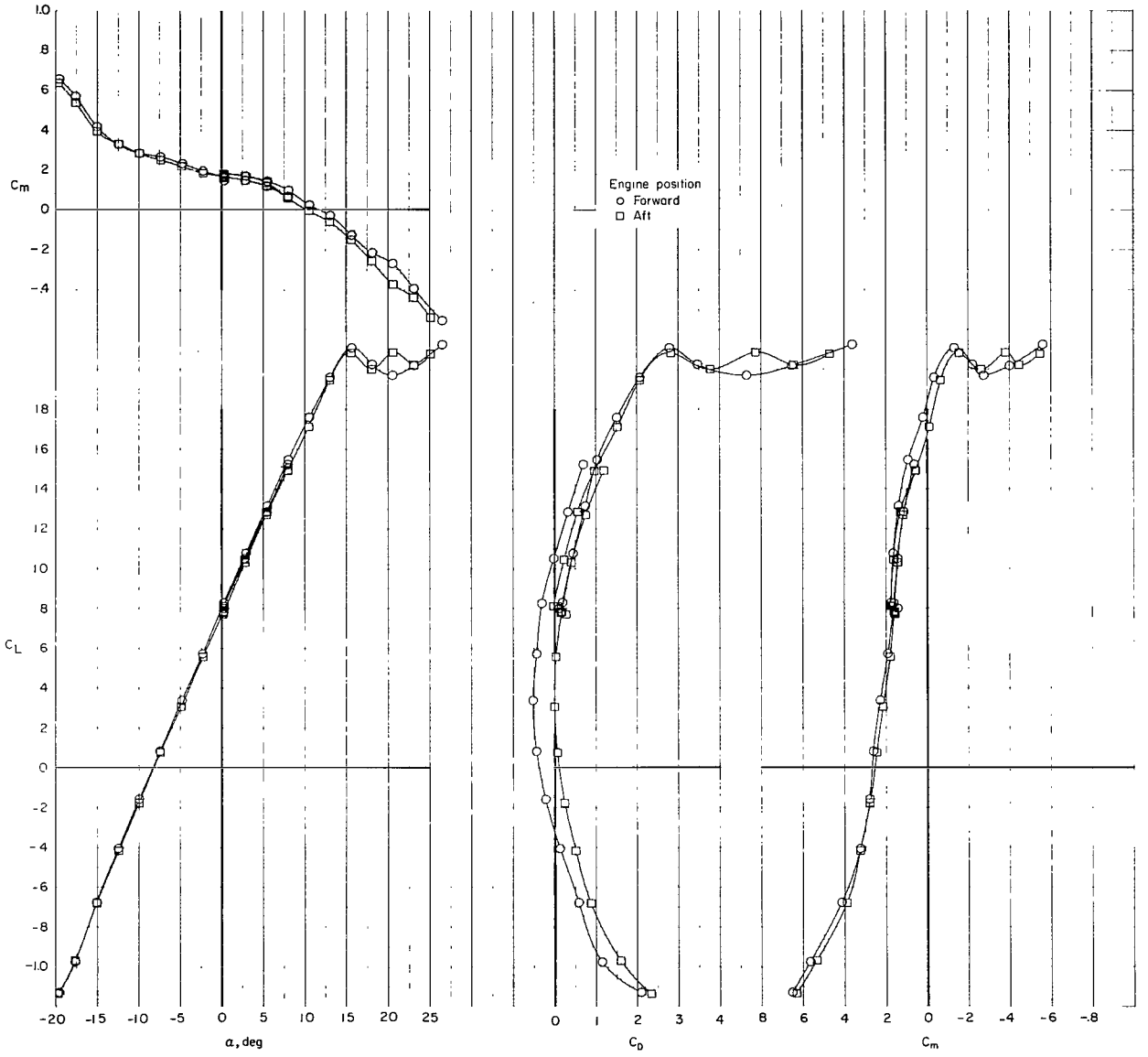

(i) $i_w = 0^o$; $\delta_f = 30^o$; trim thrust.

Figure 15.- Continued.

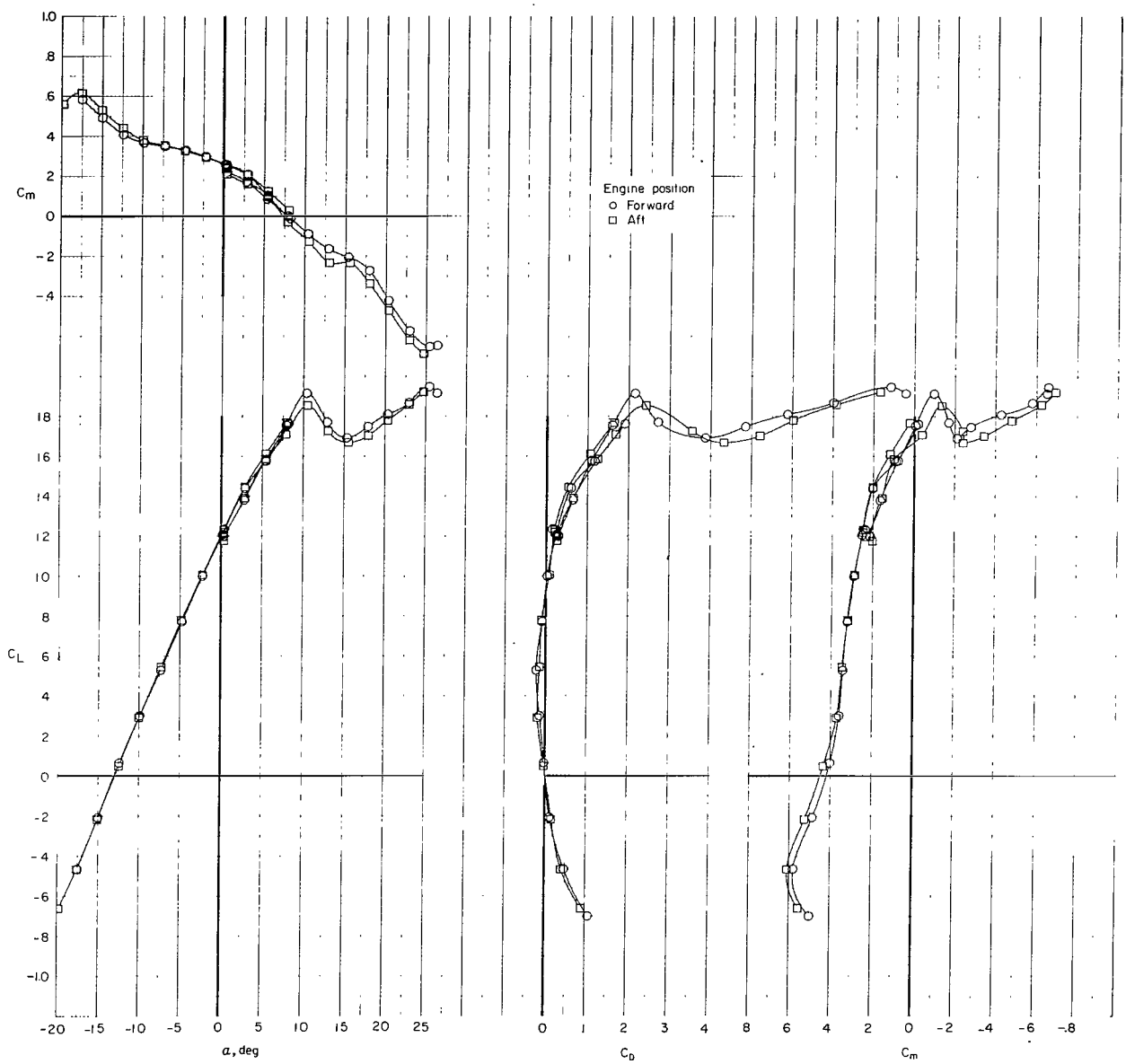

(j) $i_w = 7.5^o$; $\delta_f = 30^o$; trim thrust.

Figure 15.- Continued.

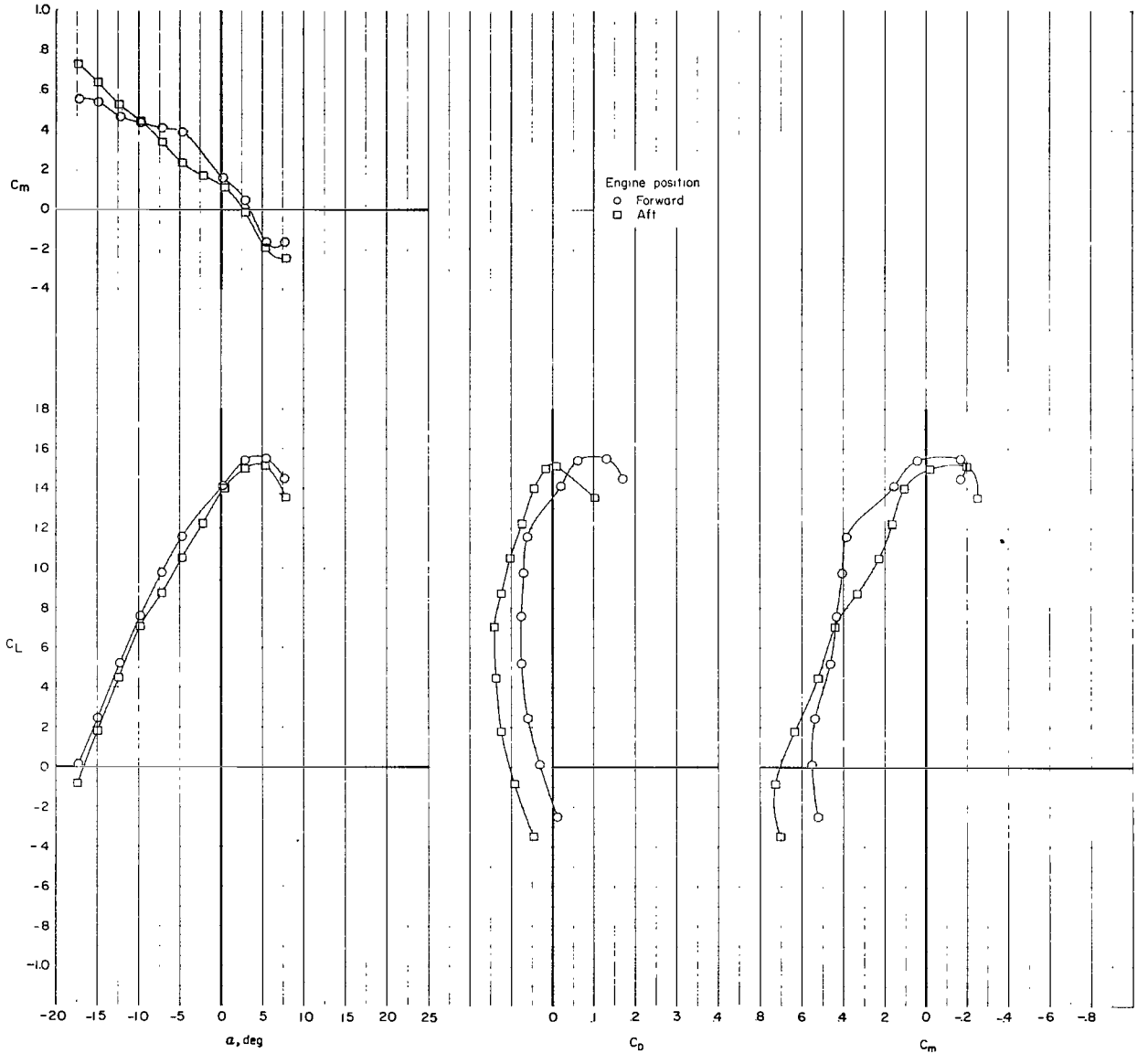

(k) $i_w = 15^o$; $\delta_f = 30^o$; trim thrust.

Figure 15.- Concluded.

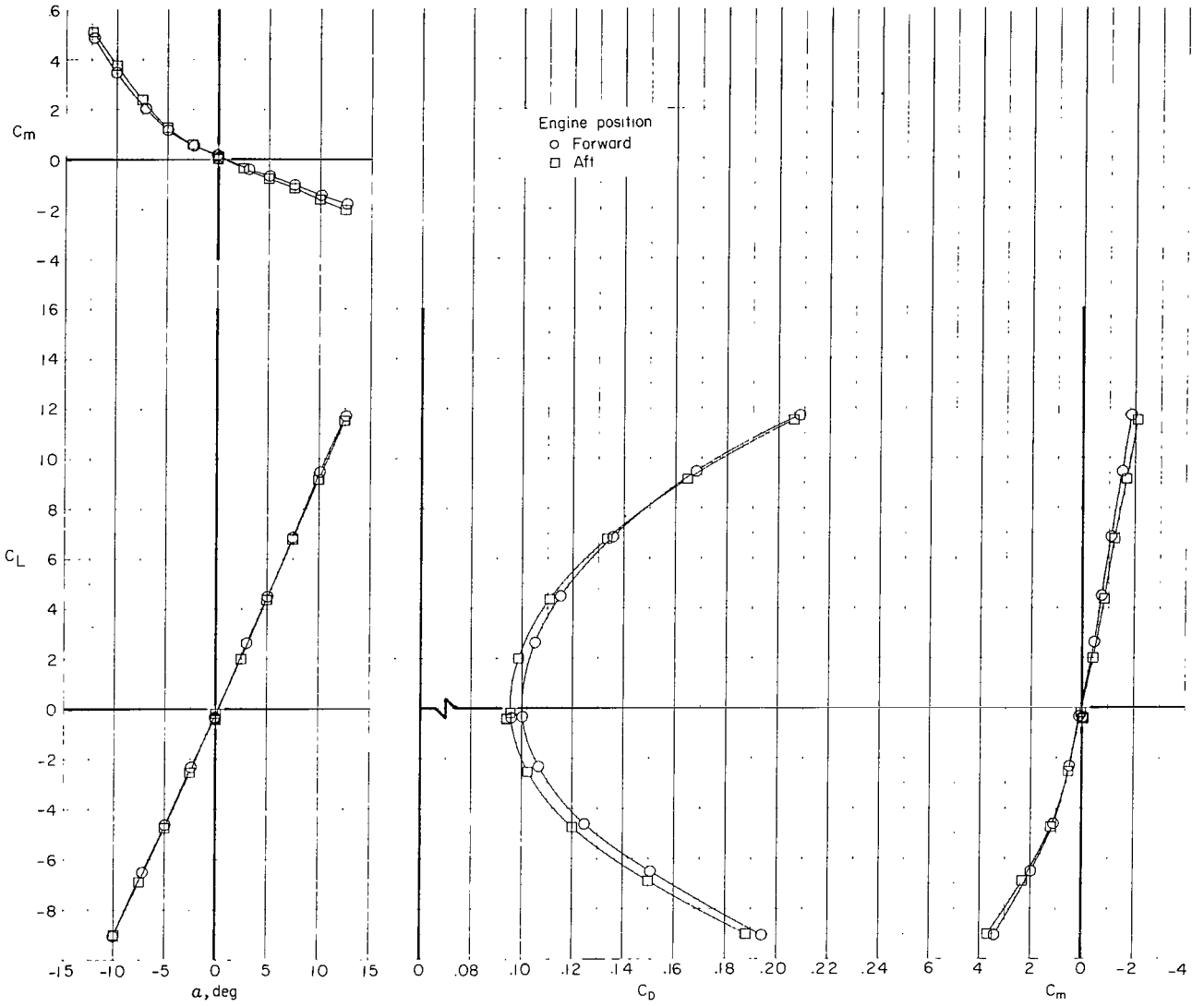

(a) $i_w = -4.5^o$; $\delta_f = 0^o$; windmill thrust.

Figure 16.- Effect of engine position on longitudinal characteristics of complete configuration with horizontal tails C and E and full fairing.

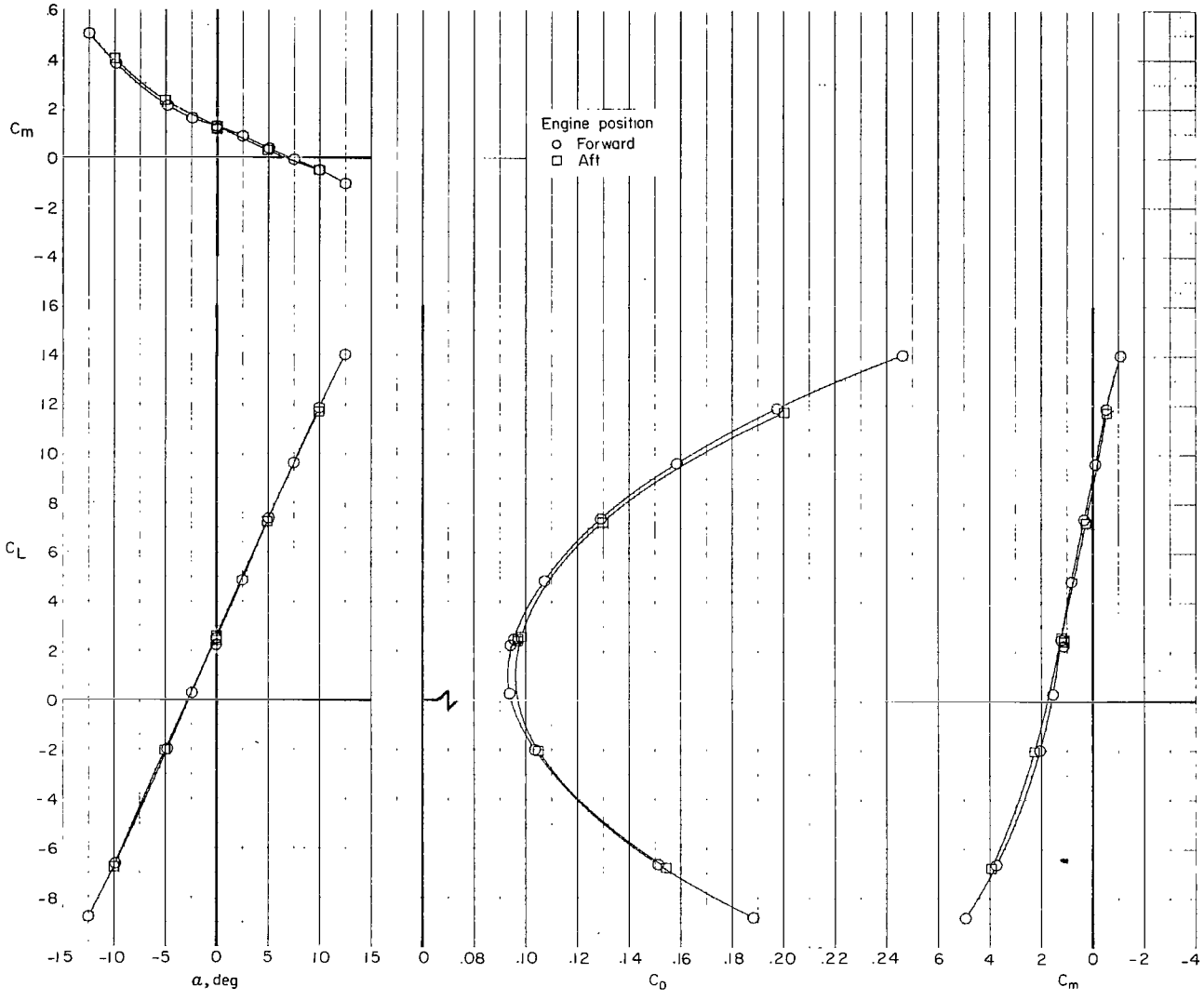

(b) $i_w = 0^o$; $\delta_f = 0^o$; windmill thrust.

Figure 16.- Continued.

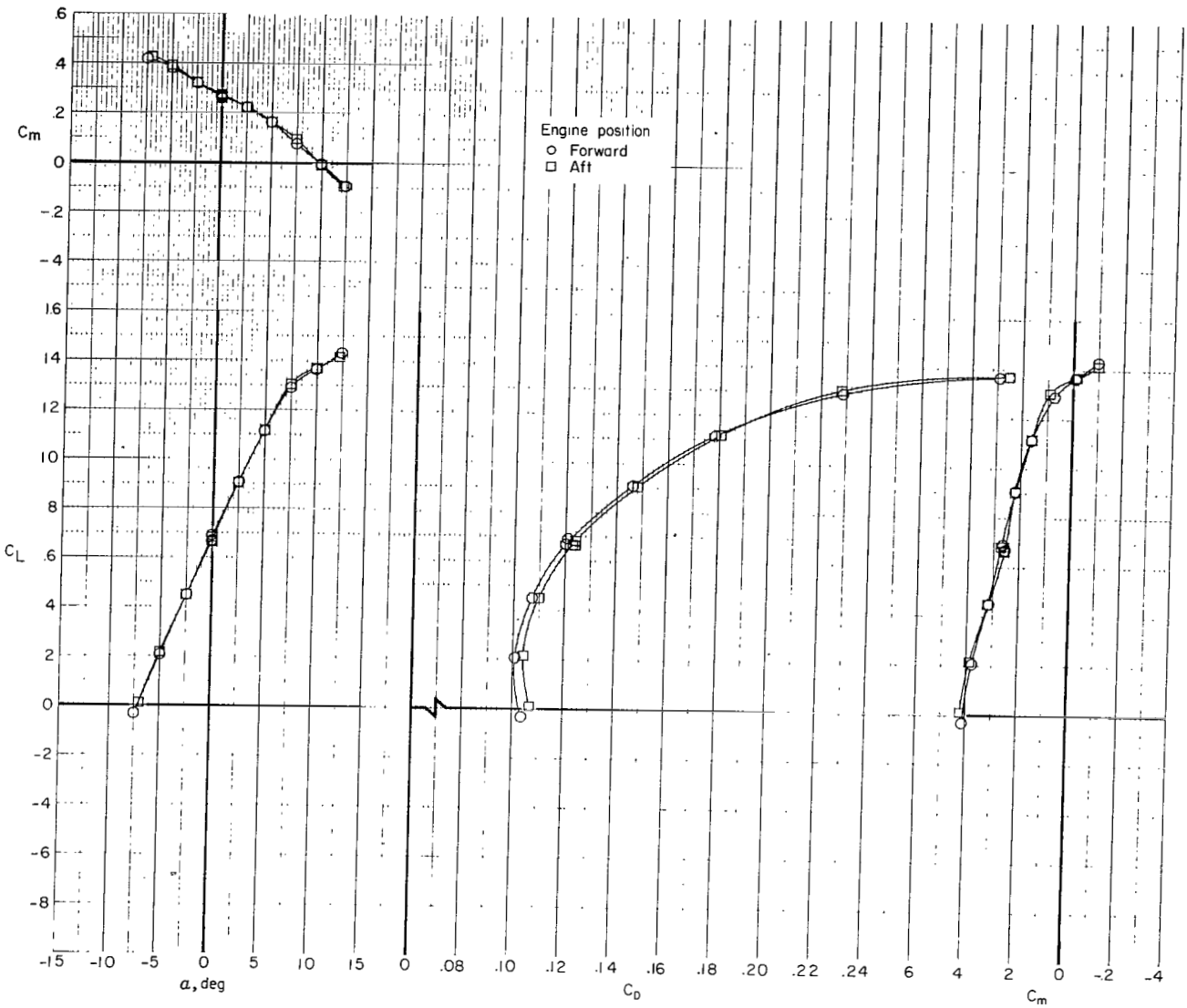

(c) $i_w = 7.5^o$; $\delta_f = 0^o$; windmill thrust.

Figure 16.- Continued.

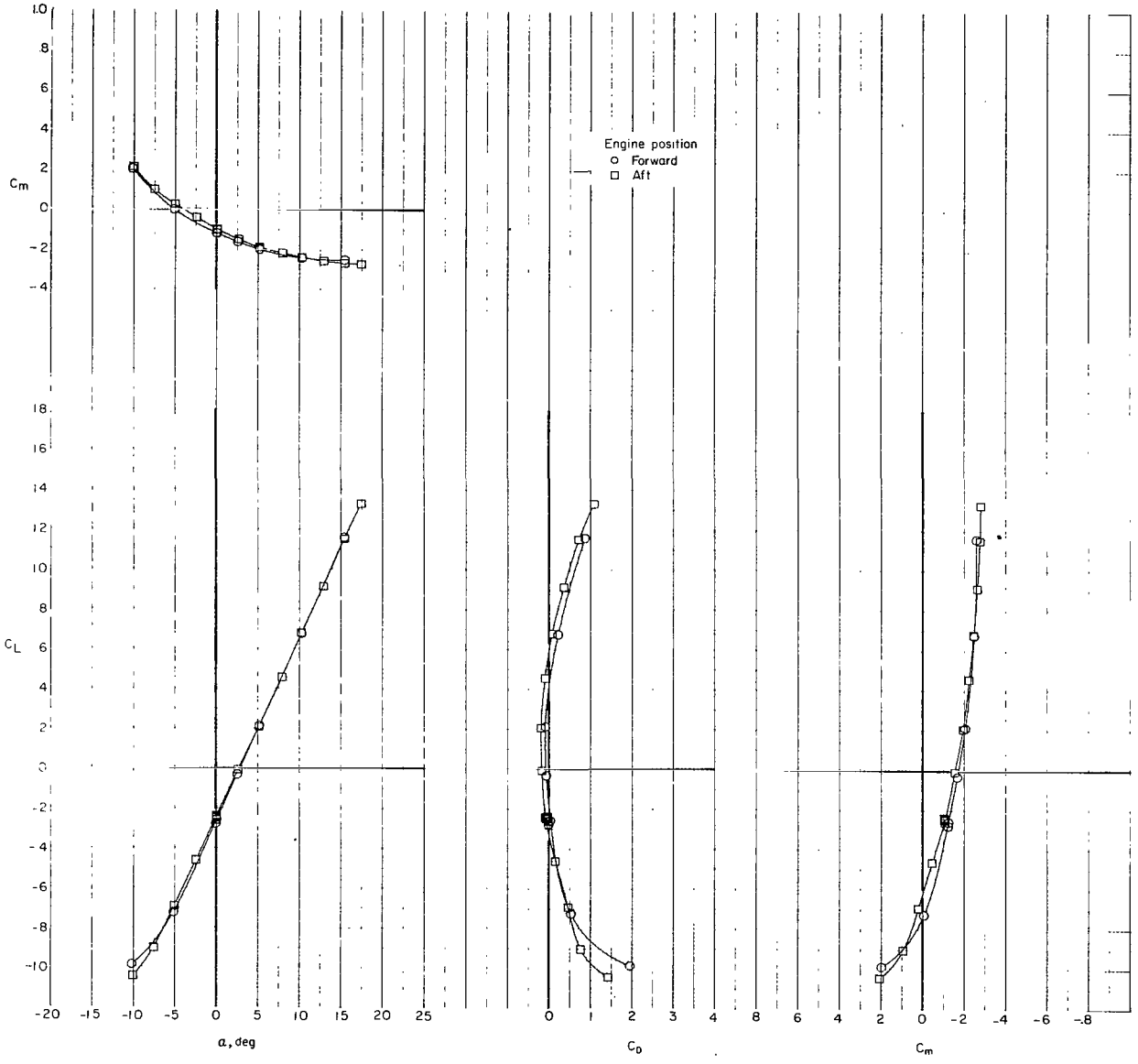

(d) $i_w = -9^o$; $\delta_f = 0^o$; trim thrust.

Figure 16.- Continued.

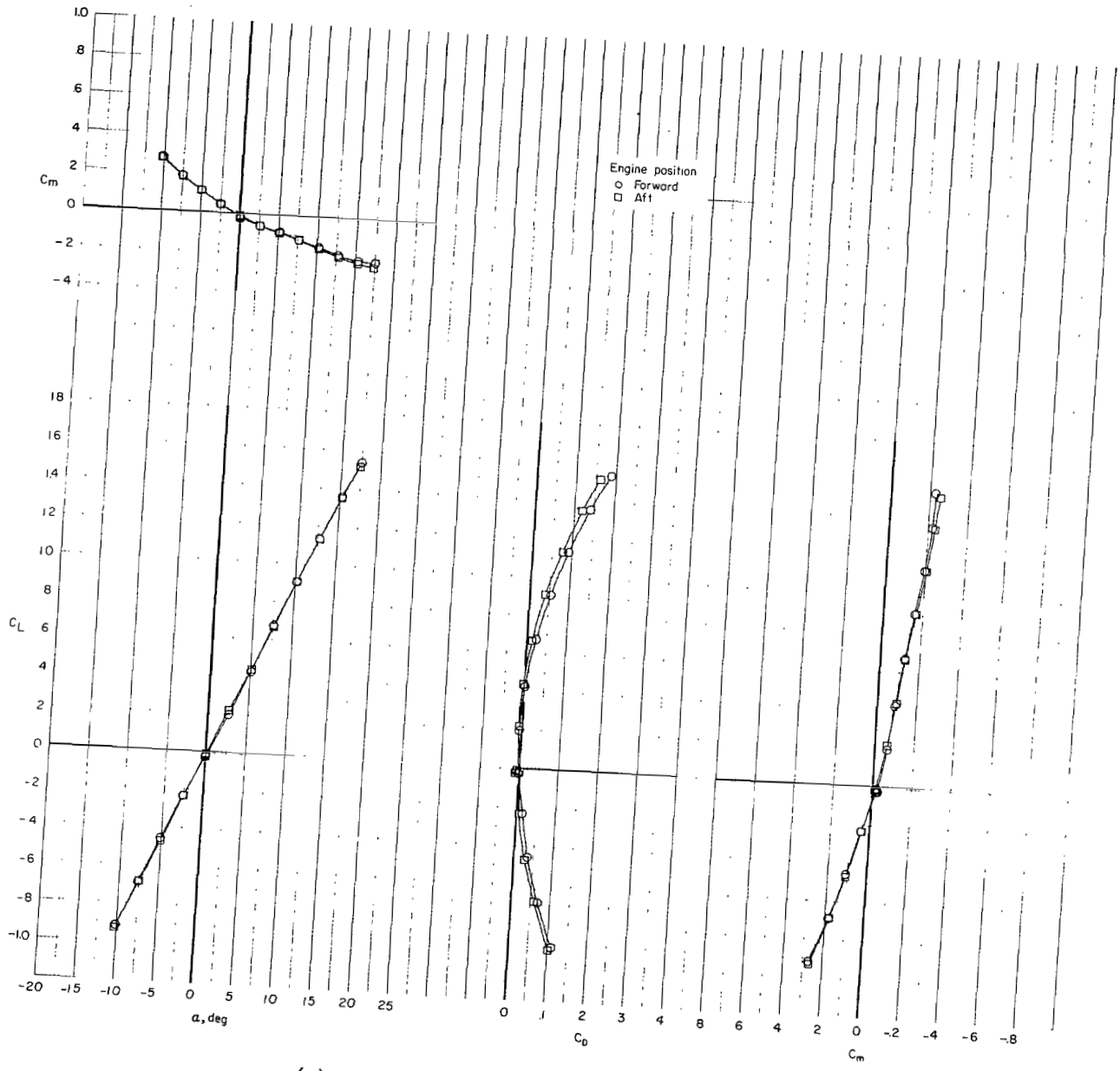

(e) $i_w = -4.5^o$; $\delta_f = 0^o$; trim thrust.

Figure 16.- Continued.

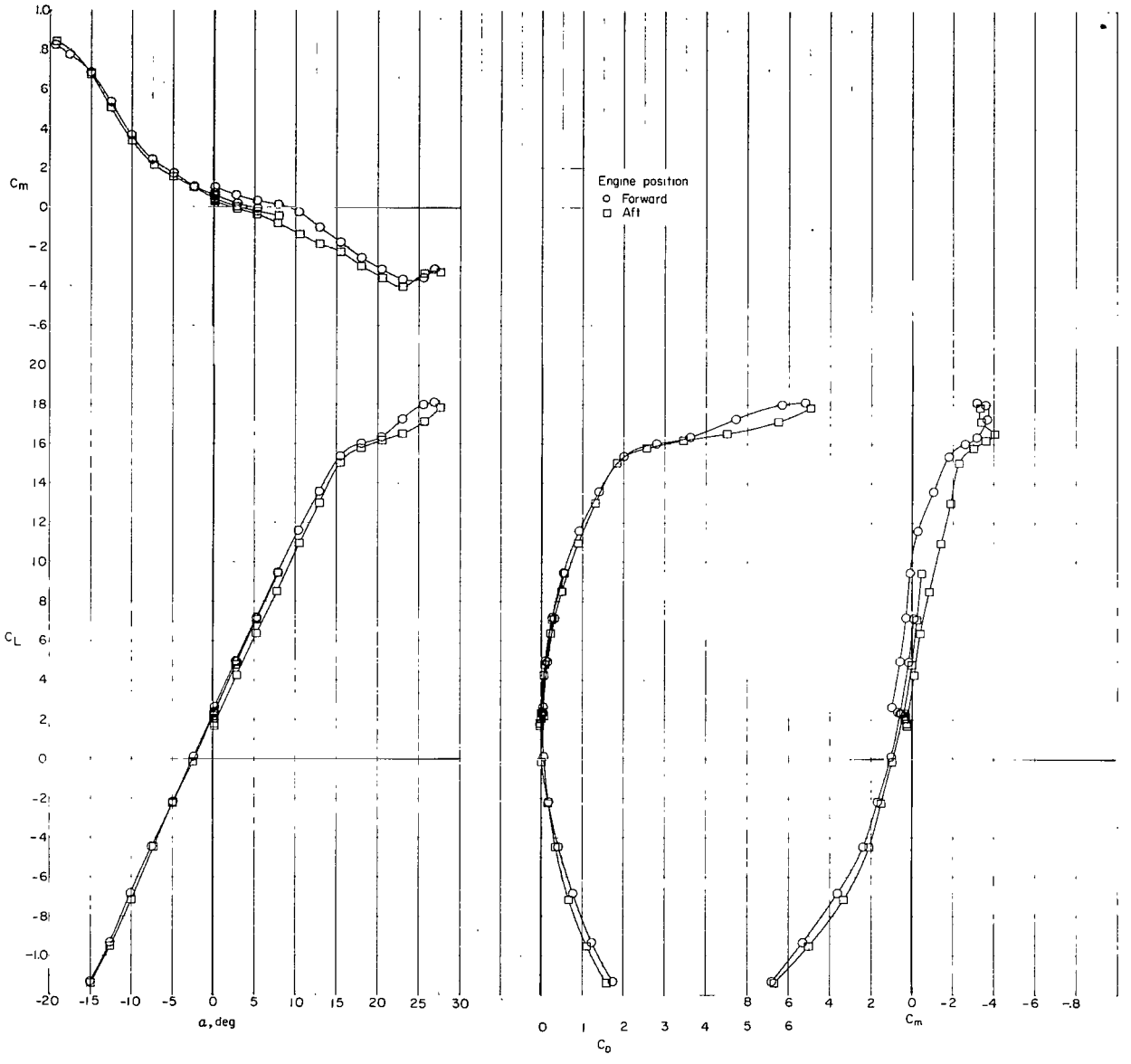

(f) $i_w = 0^o$; $\delta_f = 0^o$; trim thrust.

Figure 16.- Continued.

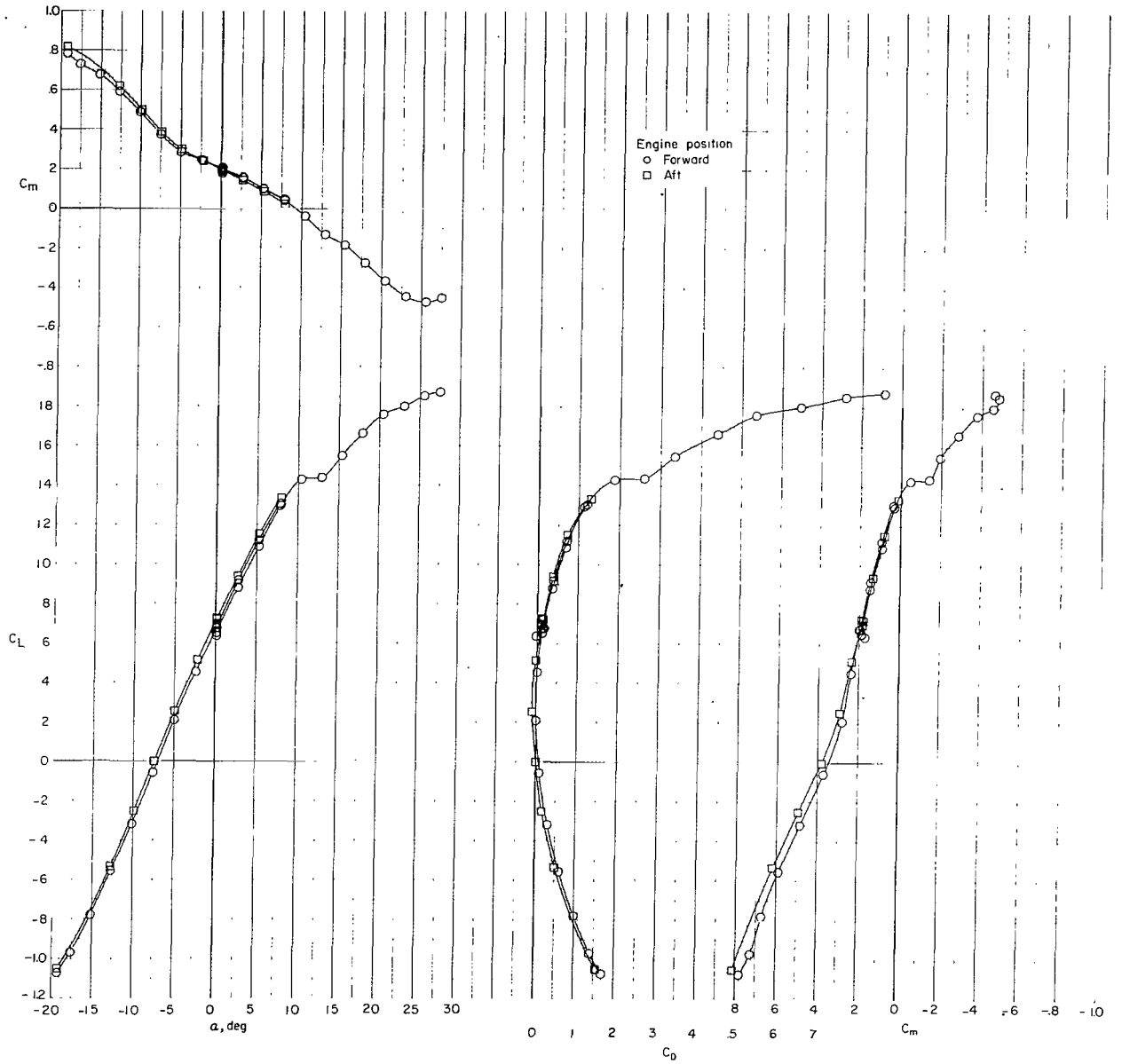

(g) $i_w = 7.5^o$; $\delta_f = 0^o$; trim thrust.

Figure 16.- Continued.

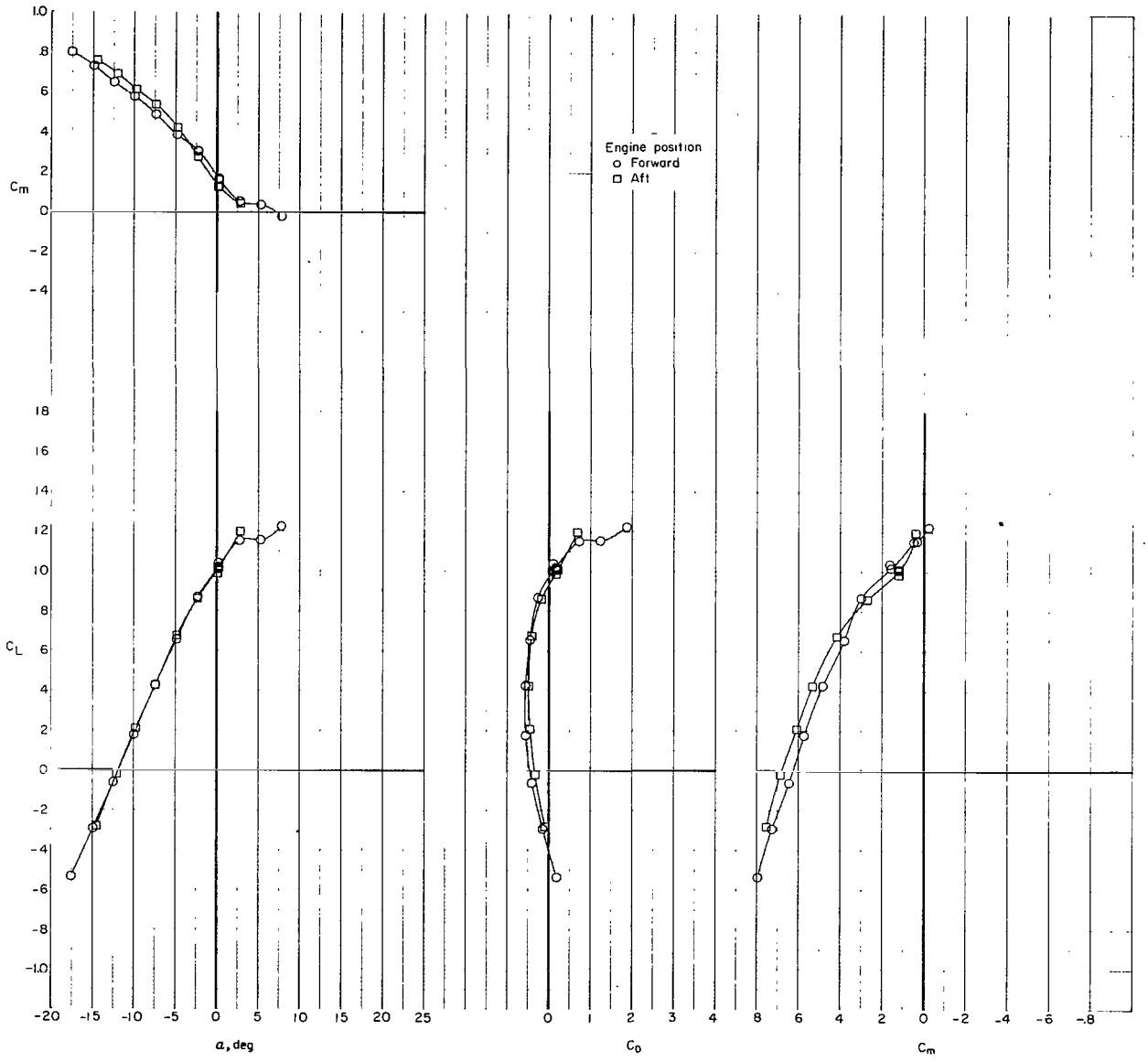

(h) $i_w = 15^o$; $\delta_f = 0^o$; trim thrust.

Figure 16.- Continued.

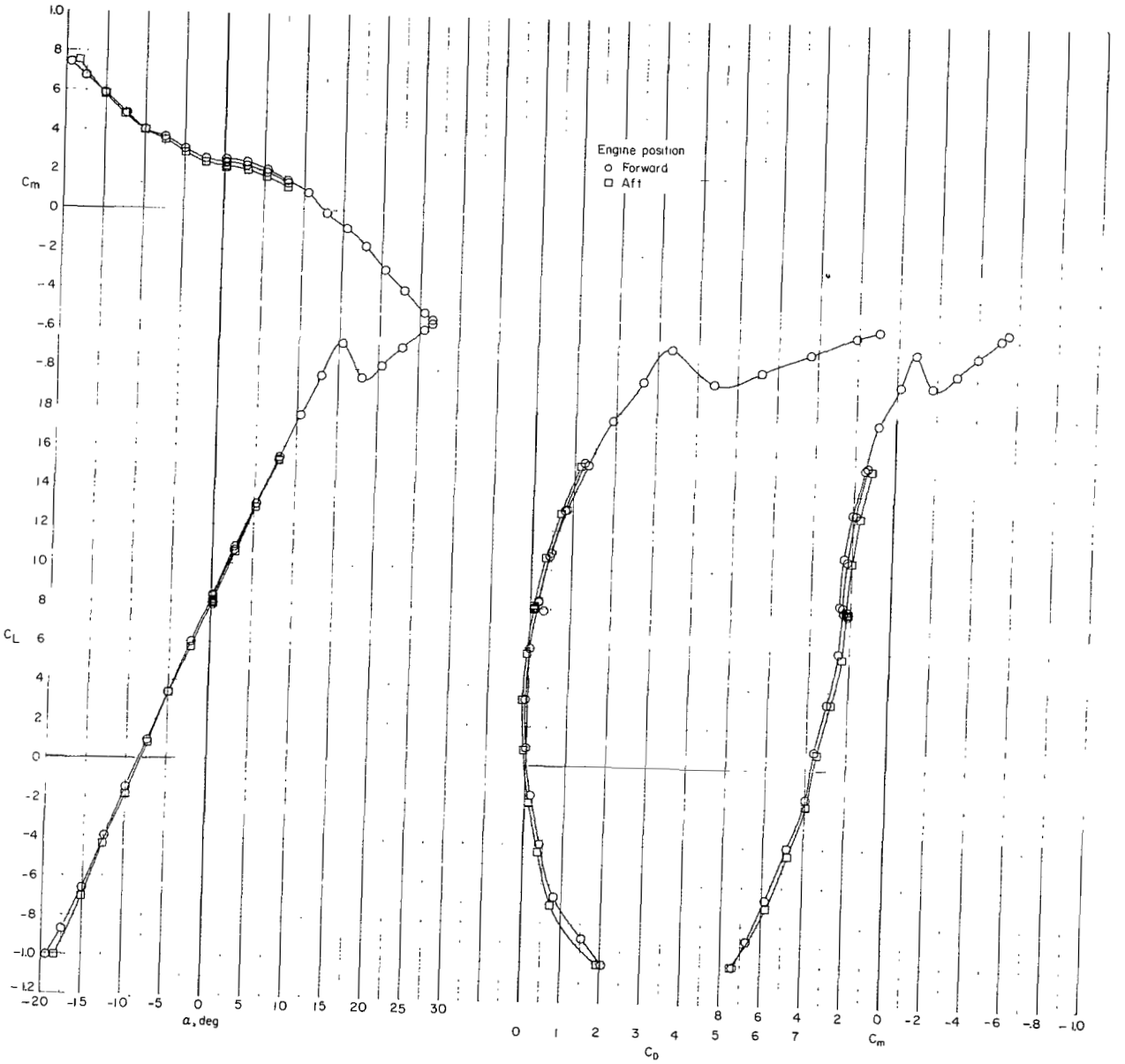

(i) $i_w = 0^o$; $\delta_f = 30^o$; trim thrust.

Figure 16.- Continued.

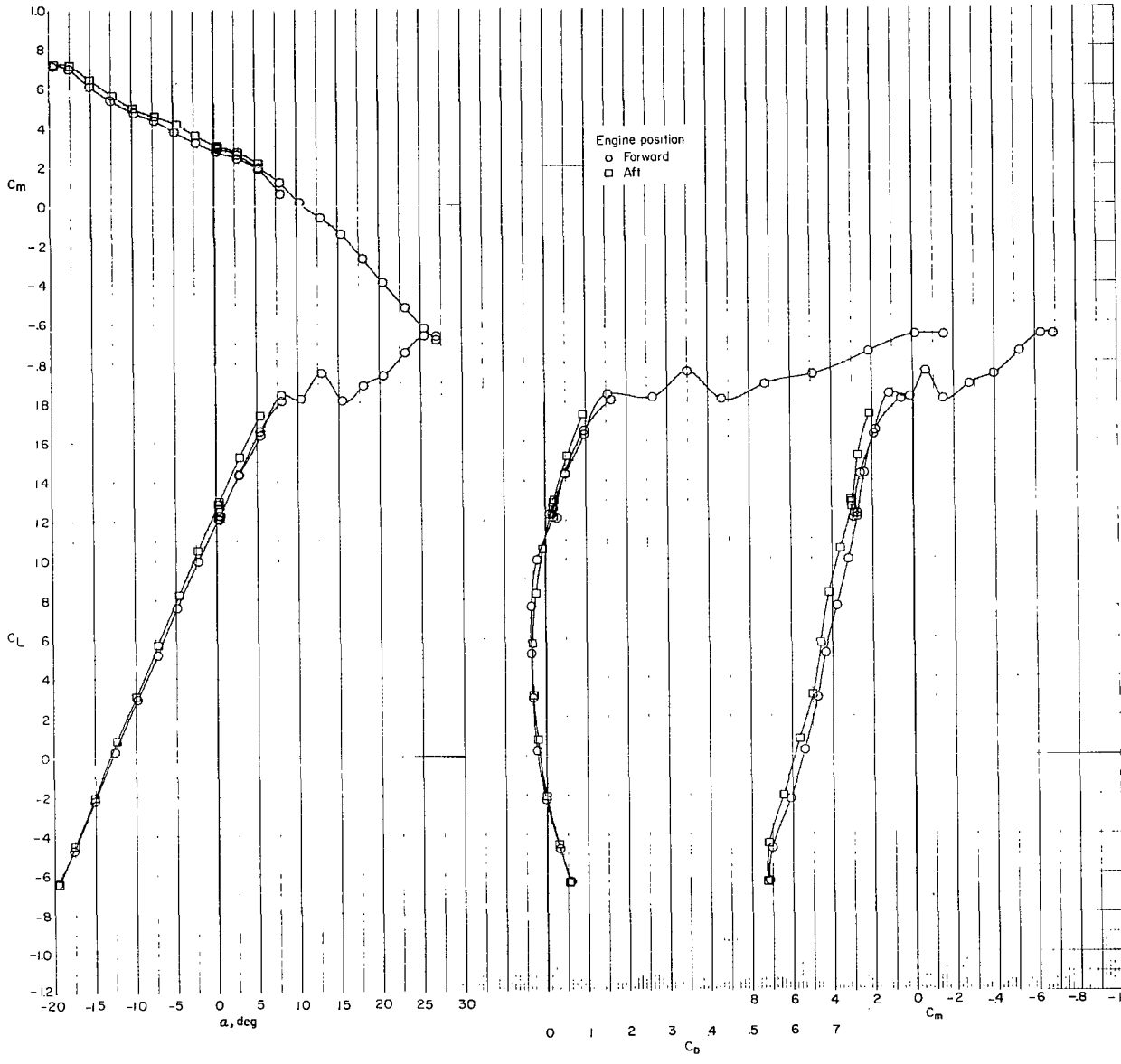

(j) $i_w = 7.5^o$; $\delta_f = 30^o$; trim thrust.

Figure 16.- Continued.

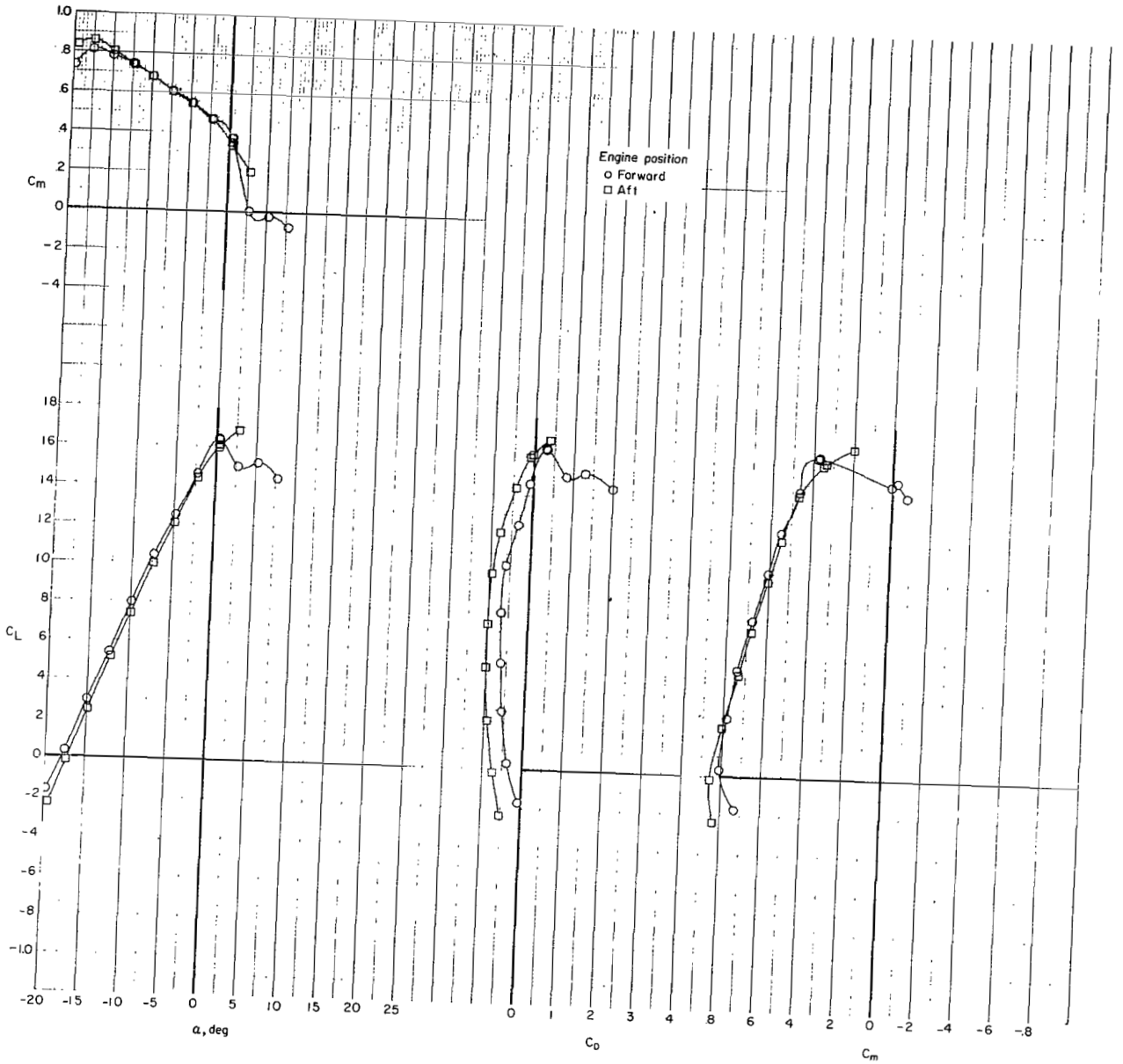

(k) $i_W = 15^o$; $\delta_f = 30^o$; trim thrust.

Figure 16.- Concluded.

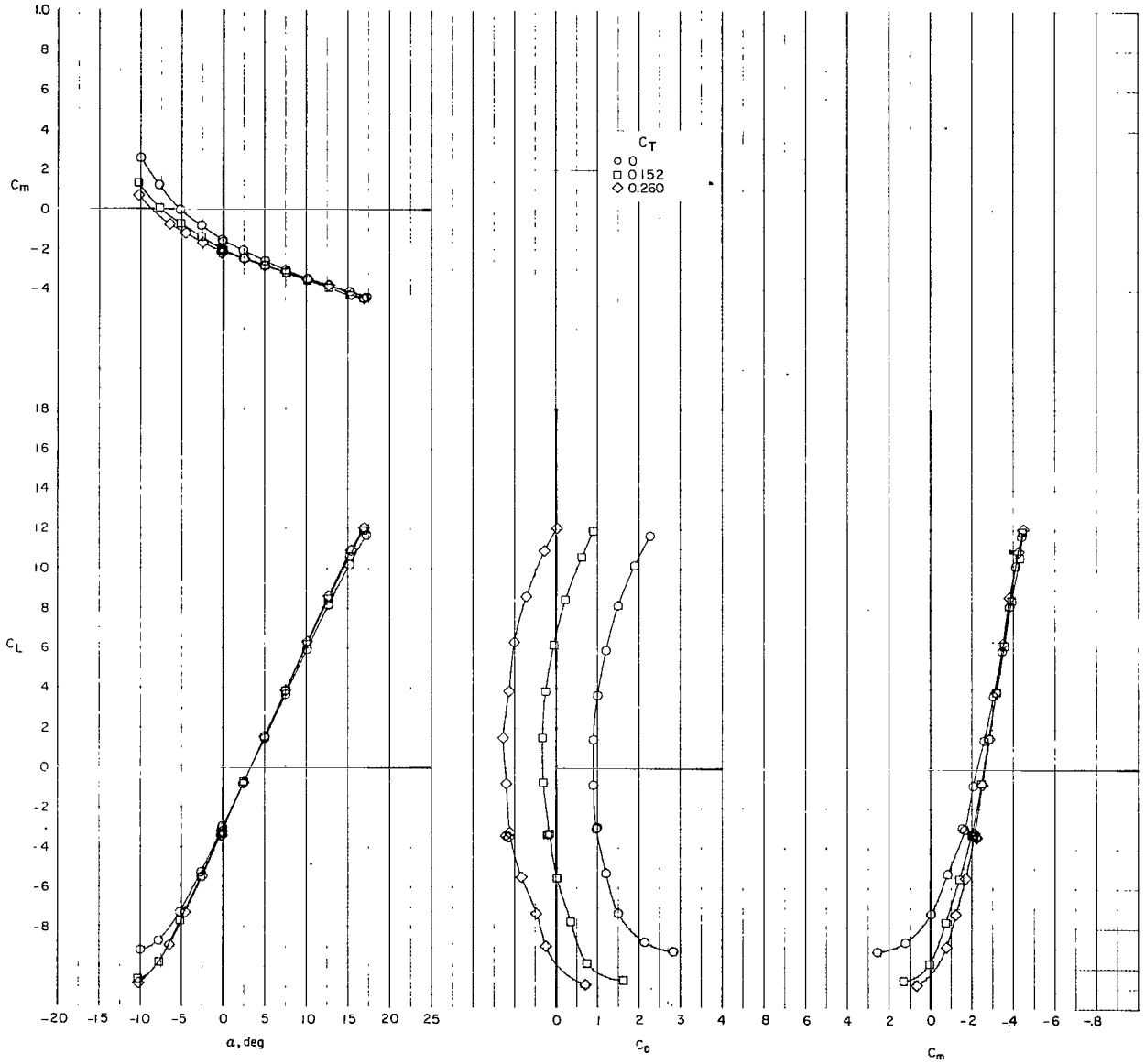

(a) $i_w = -9^o$; $\delta_f = 0^o$.

Figure 17.- Effect of thrust coefficient C_T on longitudinal characteristics of complete configuration with horizontal tails C and E and small-diameter fans with minimum fairings in aft position.

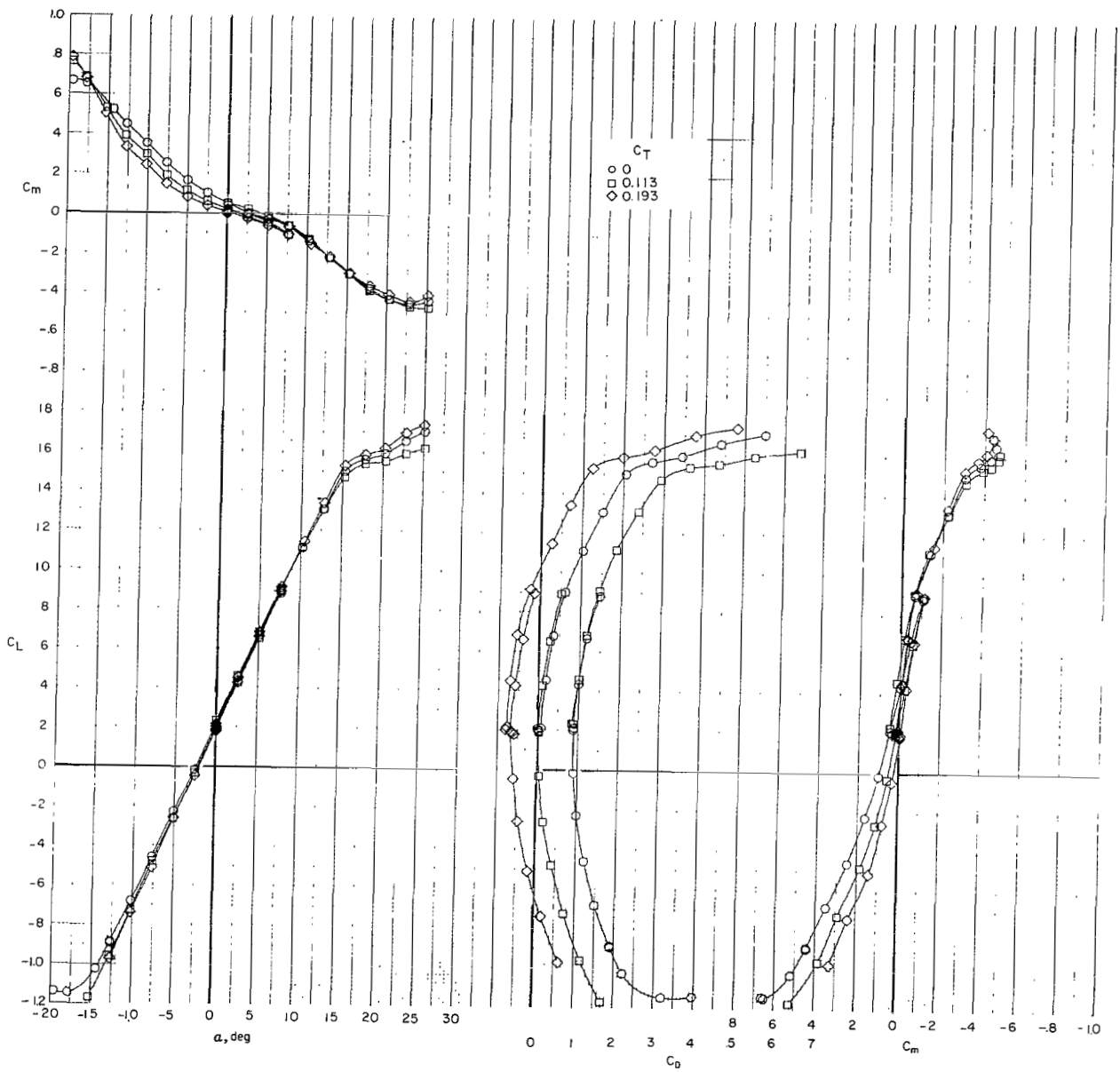

(b) $i_W = 0^O$; $\delta_f = 0^O$.

Figure 17.- Continued.

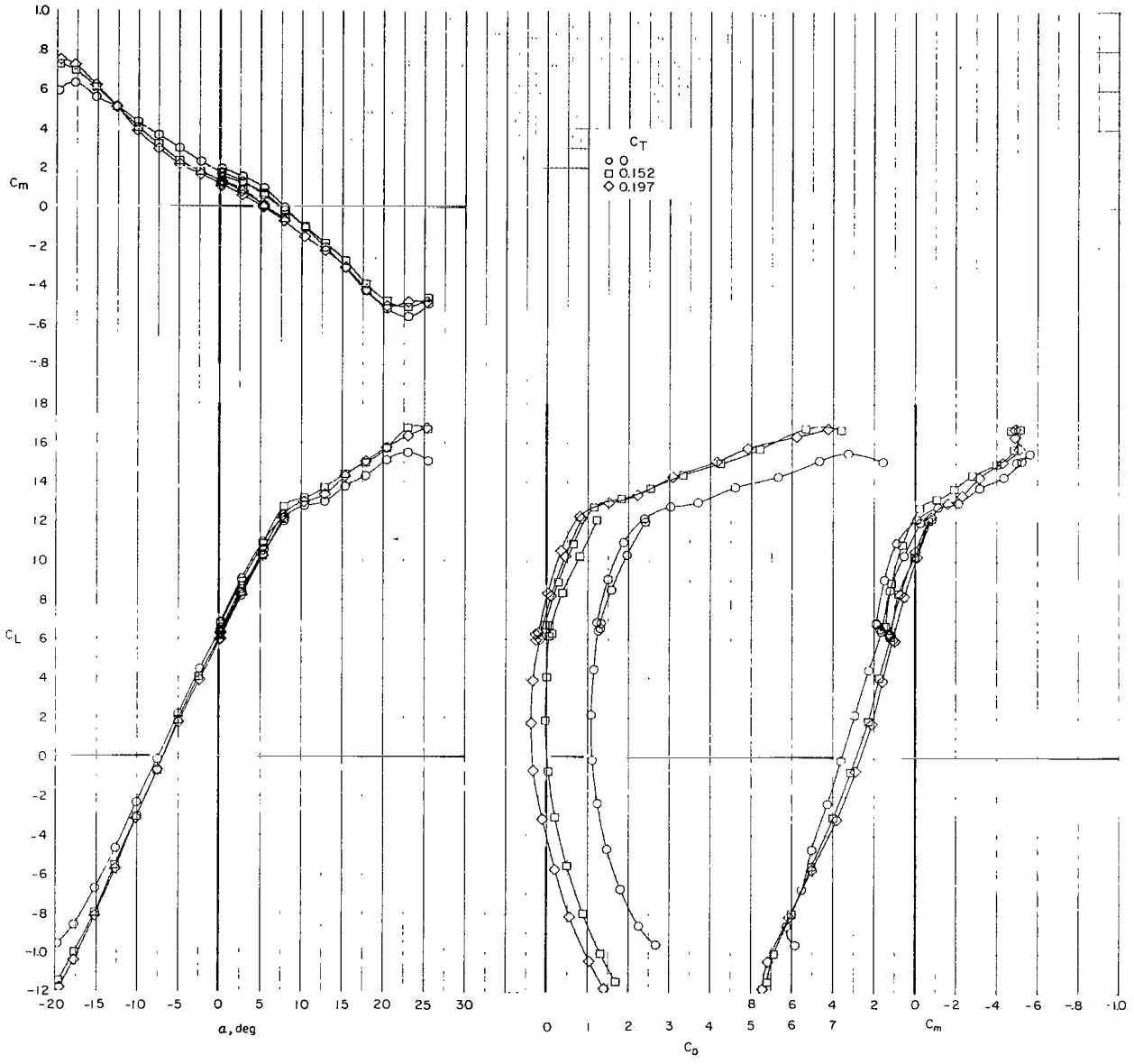

(c) $i_W = 7.5^o$; $\delta_f = 0^o$.

Figure 17.- Continued.

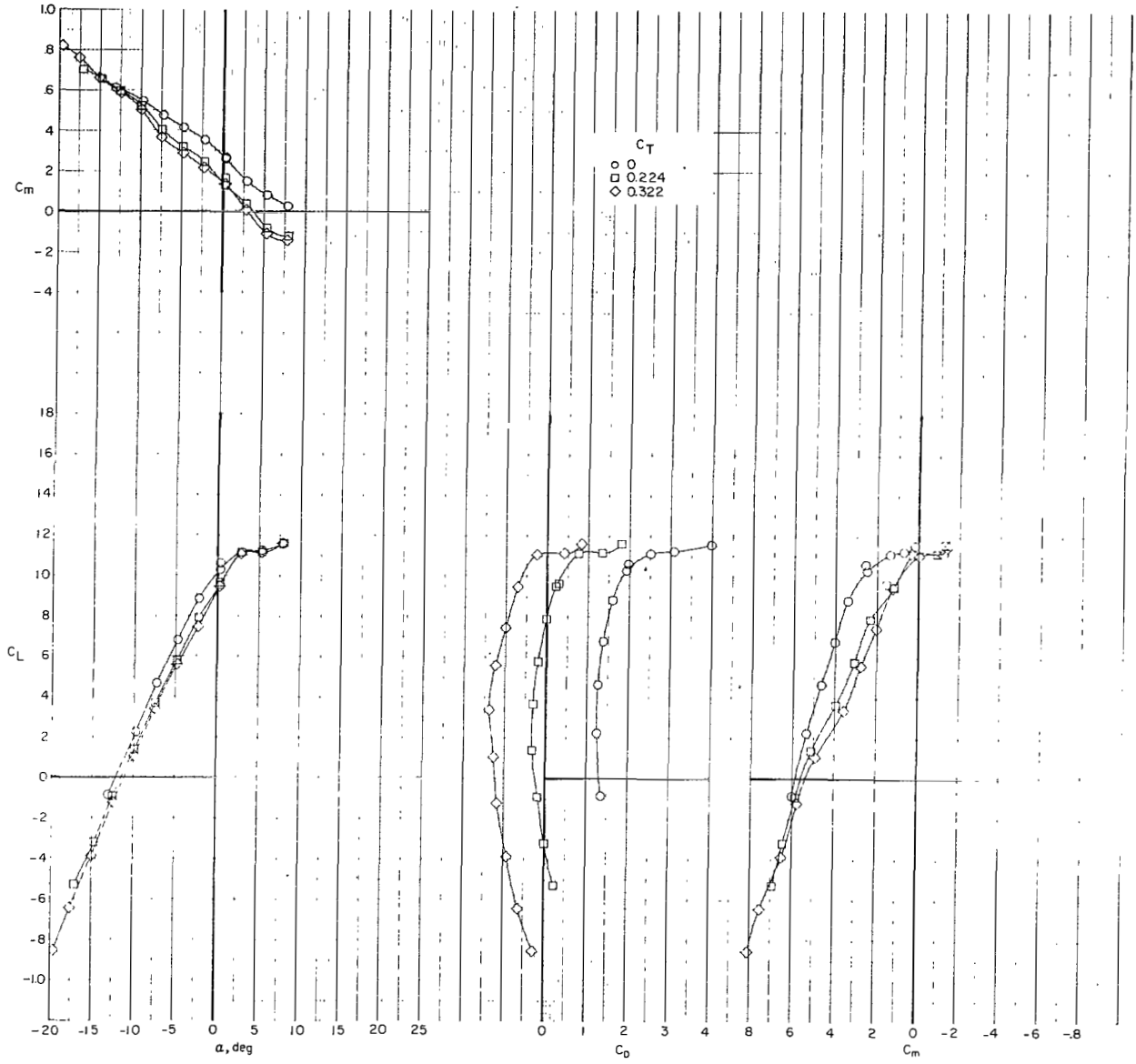

(d) $i_w = 15^o$; $\delta_f = 0^o$.

Figure 17.- Continued.

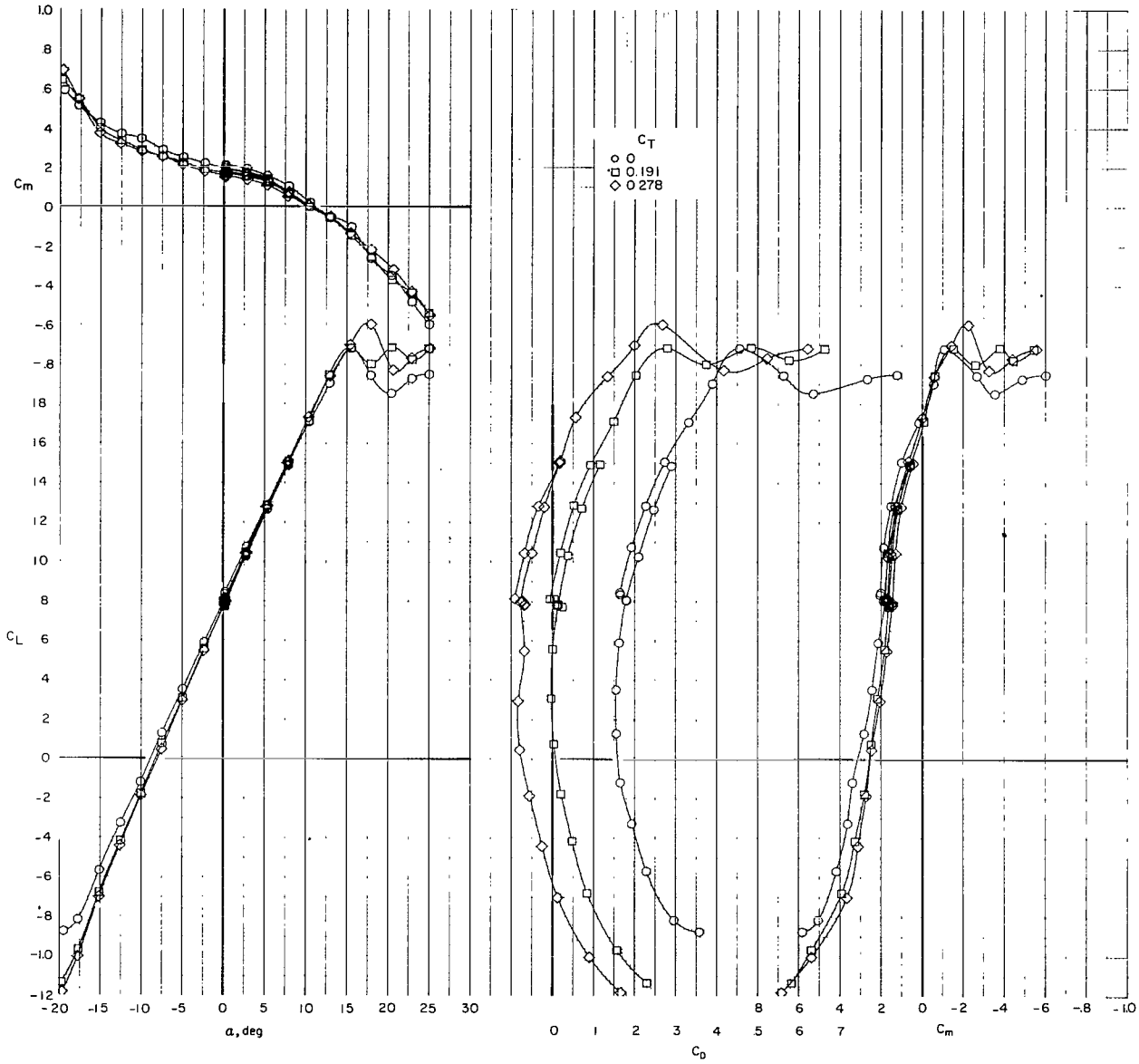

(e) $i_w = 0^o$; $\delta_f = 30^o$.

Figure 17.- Continued.

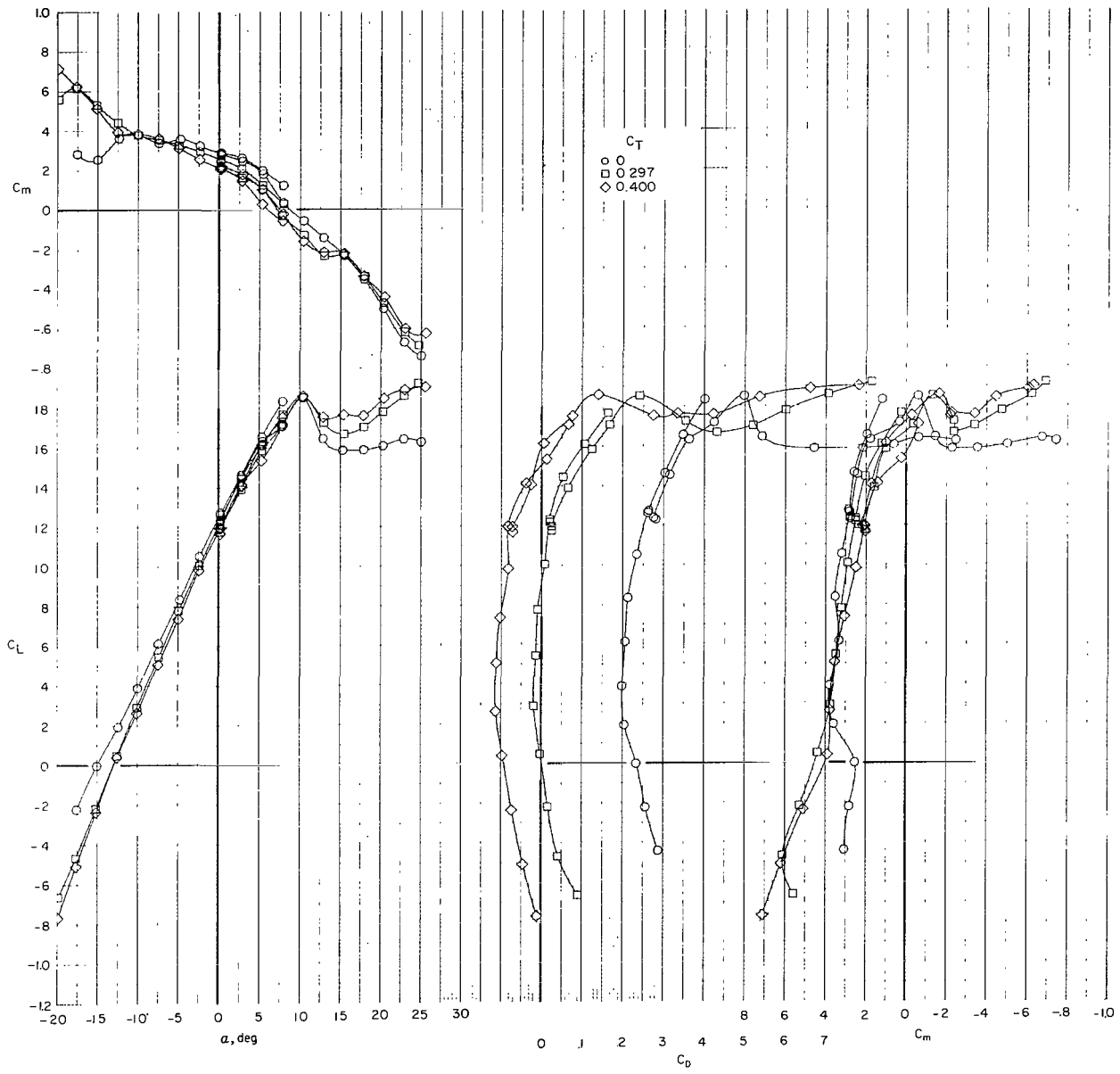

(f) $i_w = 7.5^o$; $\delta_f = 30^o$.

Figure 17.- Continued.

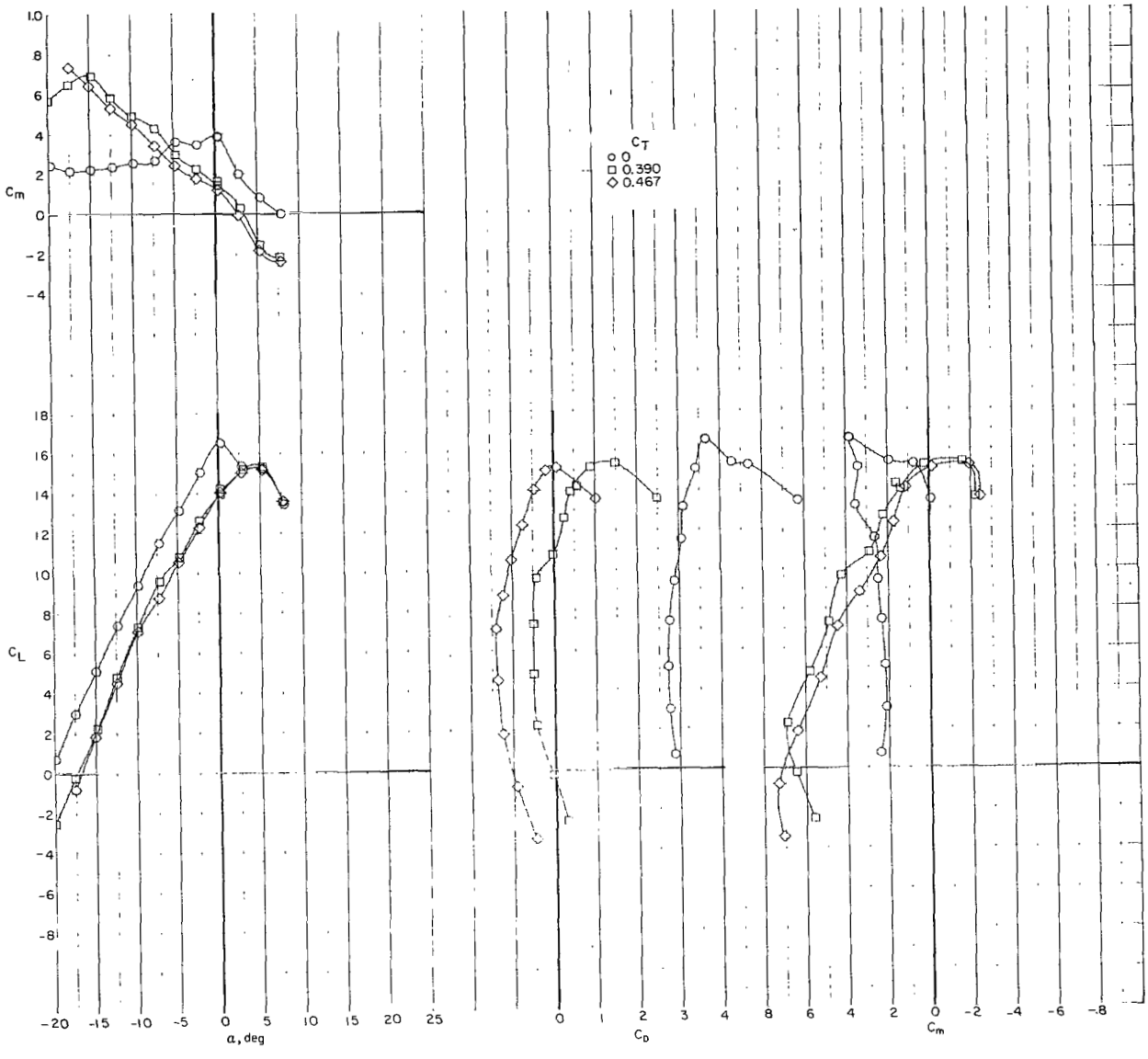

(g) $i_w = 15^o$; $\delta_f = 30^o$.

Figure 17.- Concluded.

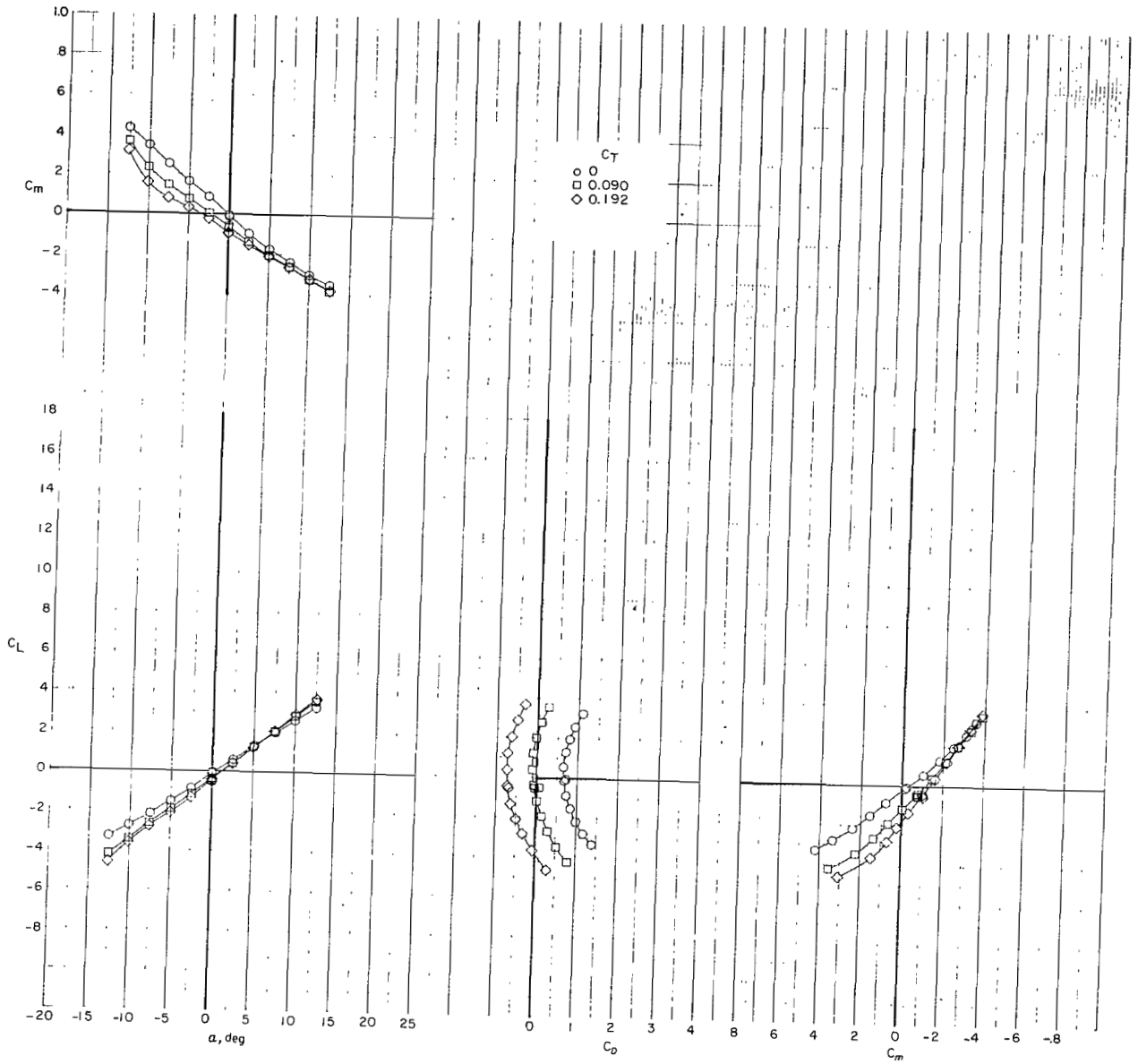

(a) 110-cm (43.33-in.) span lower tail C and T-tail E.

Figure 18.- Effect of thrust coefficient C_T on longitudinal aerodynamic characteristics of configuration with wing removed and small-diameter fans with modified minimum fairings in forward position.

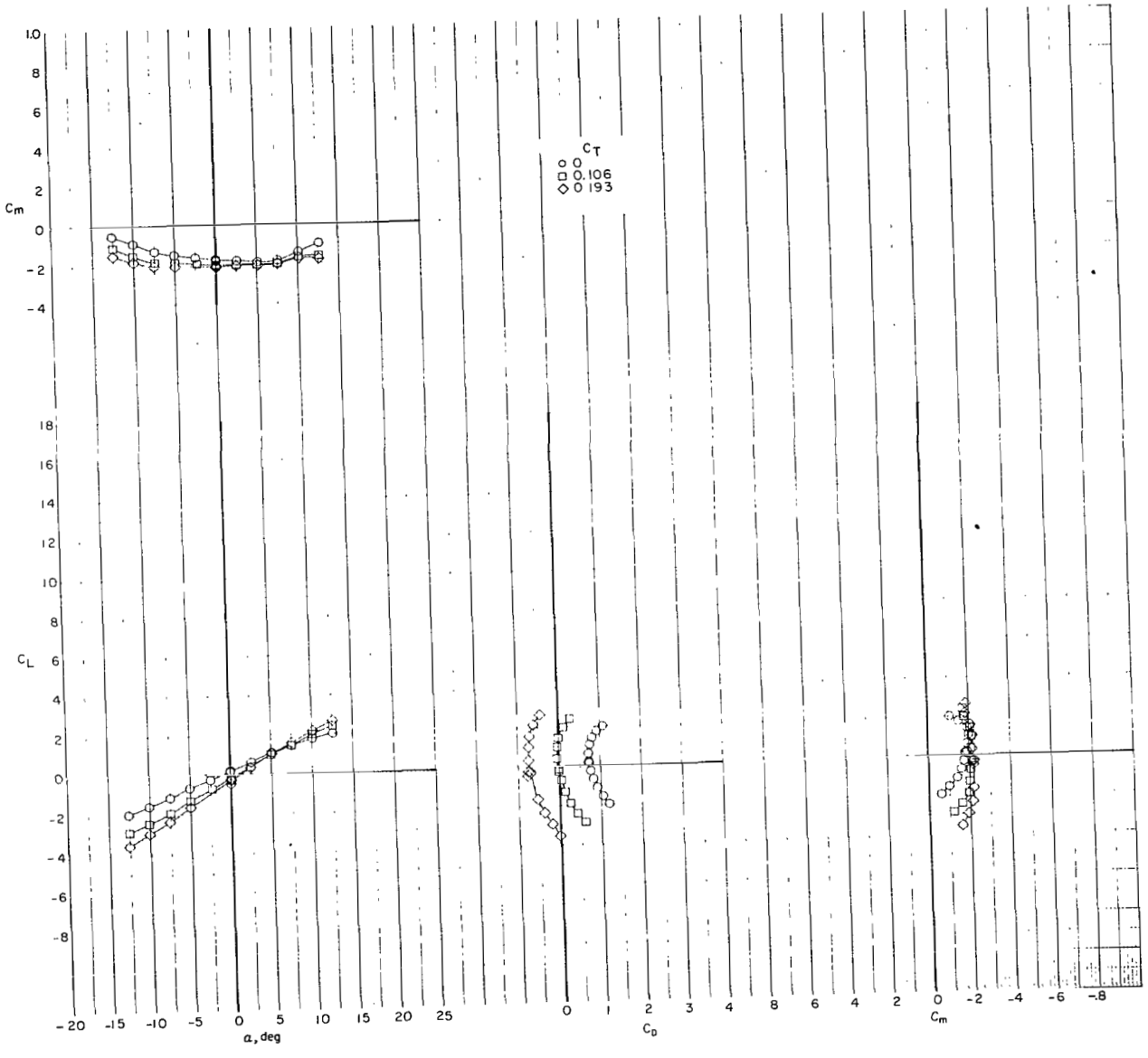

(b) T-tail D.

Figure 18.- Concluded.

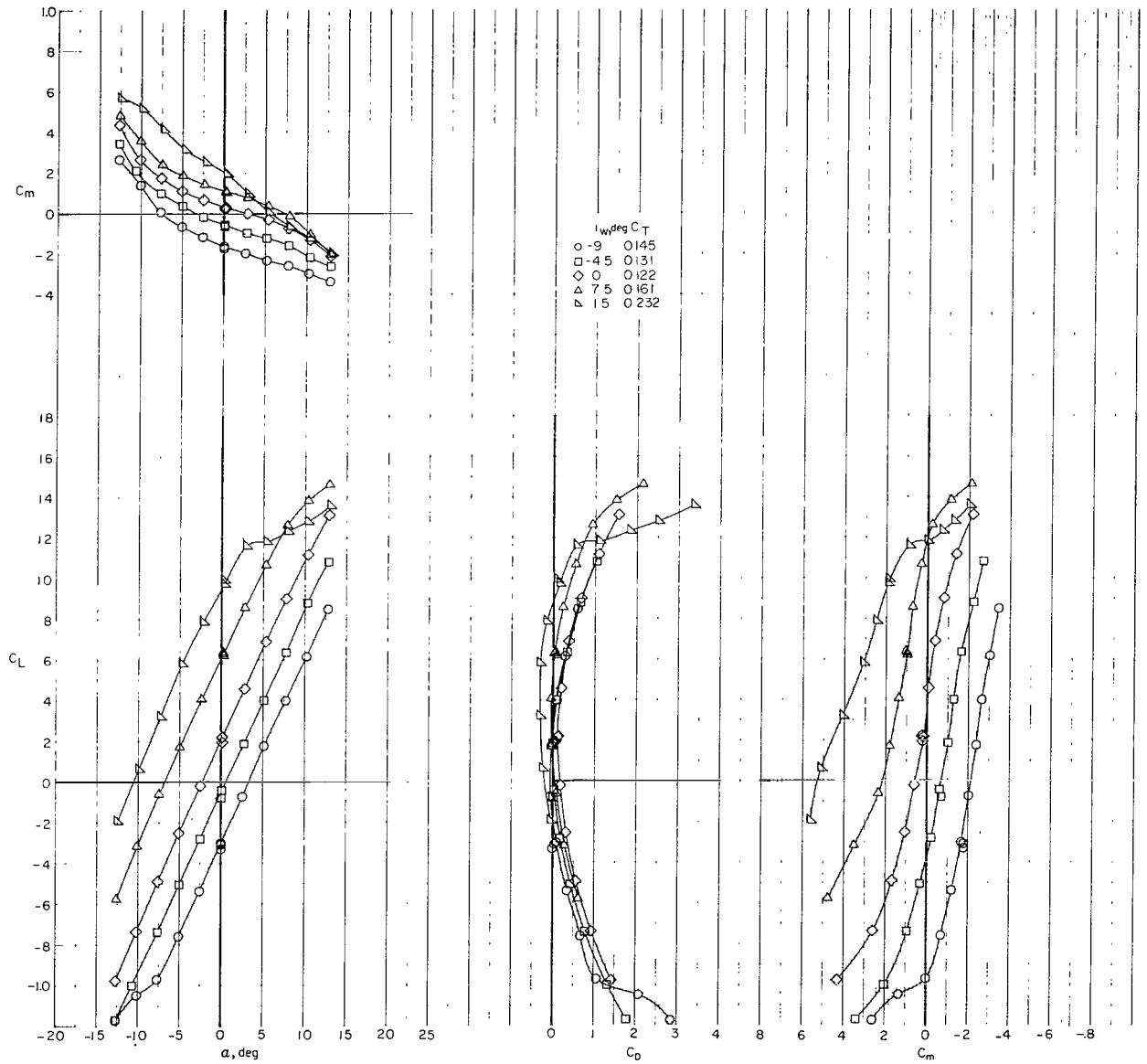

(a) Trim thrust; $\delta_f = 0^o$.

Figure 19.- Effect of wing incidence i_w and flap deflection δ_f on longitudinal characteristics of Phase III baseline configuration.

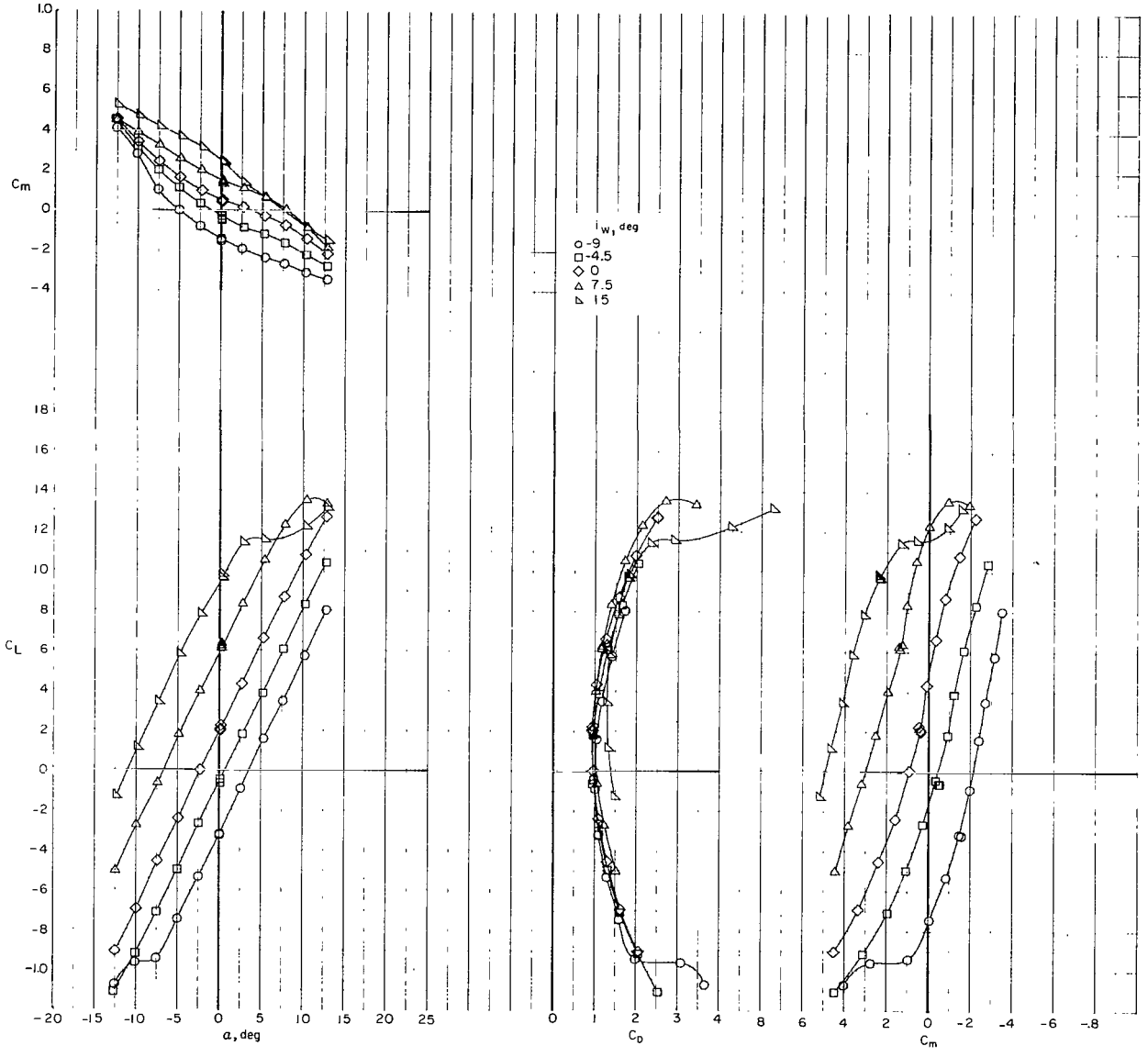

(b) $C_T = 0$; $\delta_f = 0^o$.

Figure 19.- Continued.

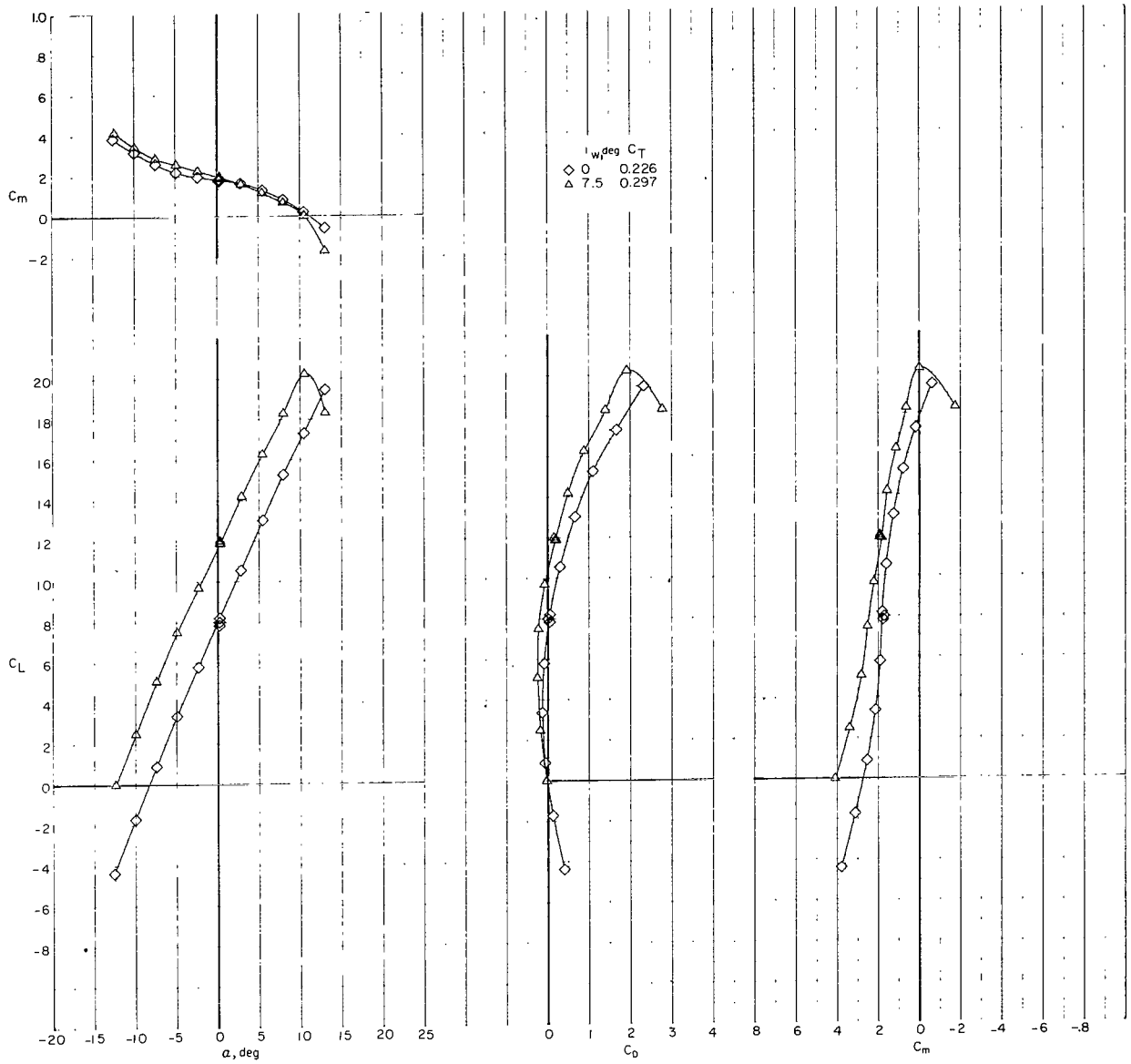

(c) Trim thrust; $\delta_f = 30^o$.

Figure 19.- Continued.

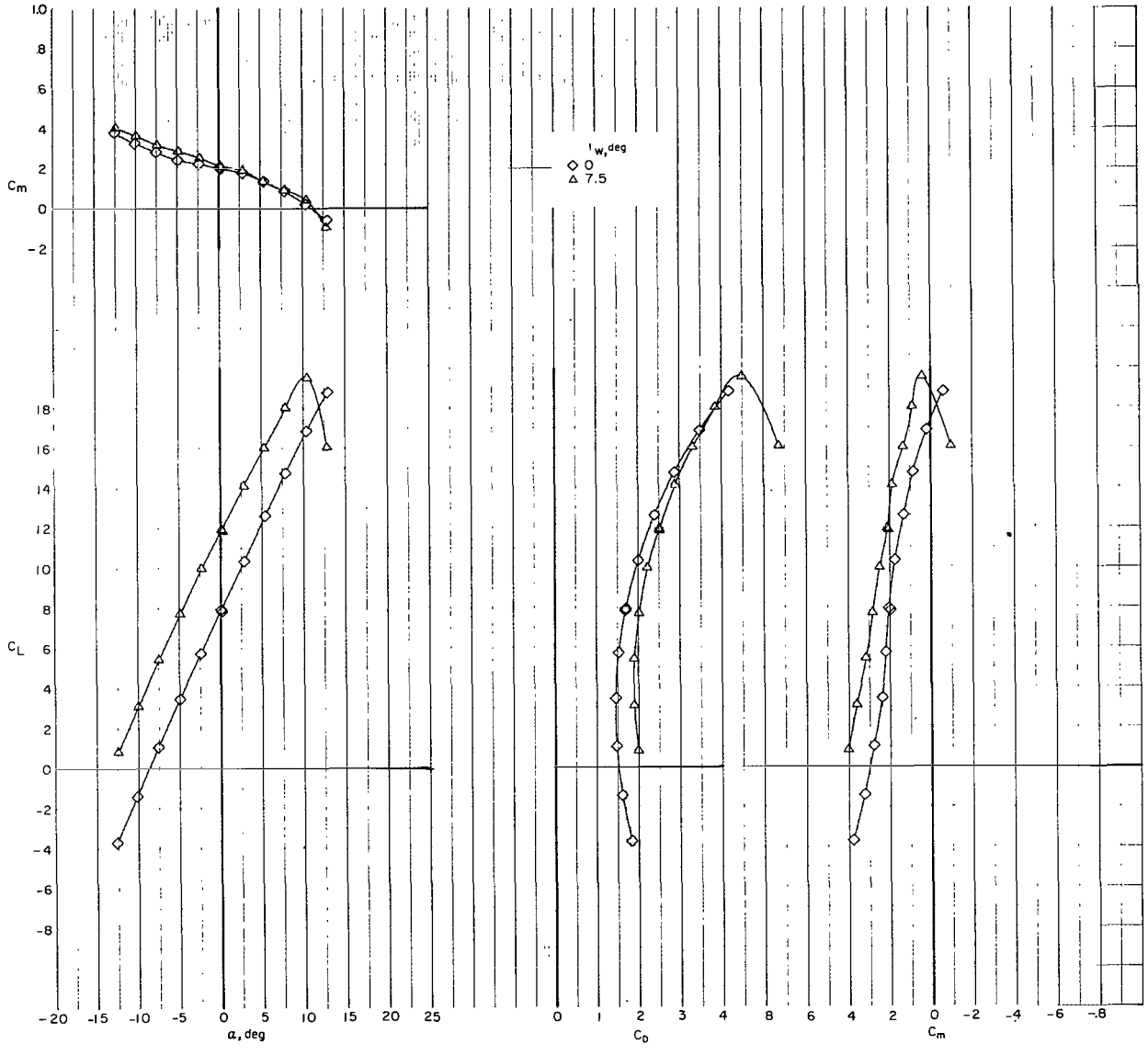

(d) $C_T = 0$; $\delta_f = 30^o$.

Figure 19.- Concluded.

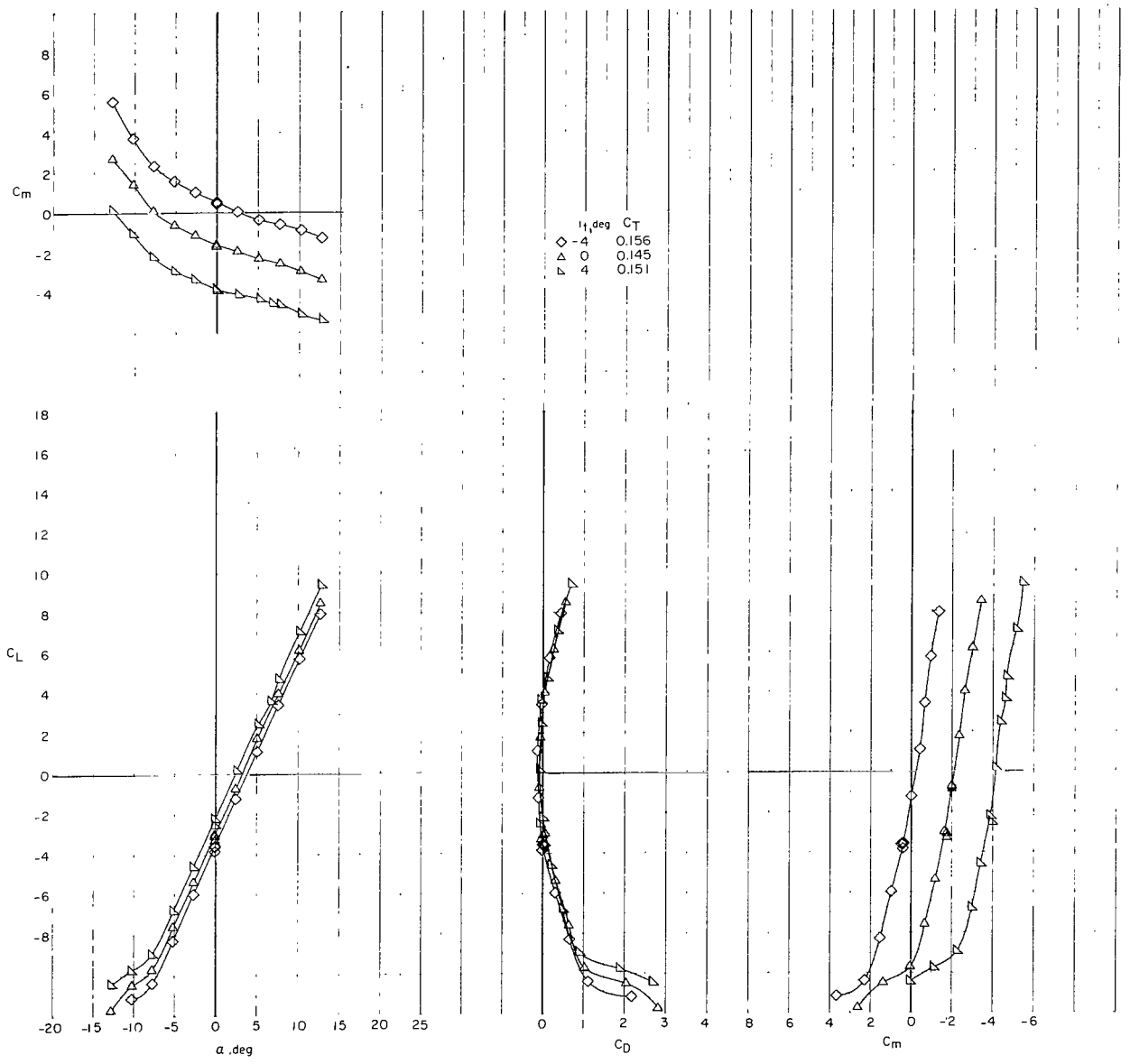

(a) Trim thrust; $i_w = -9^o$; $\delta_f = 0^o$.

Figure 20.- Effect of lower horizontal-tail incidence i_t on longitudinal characteristics of Phase III baseline configuration.

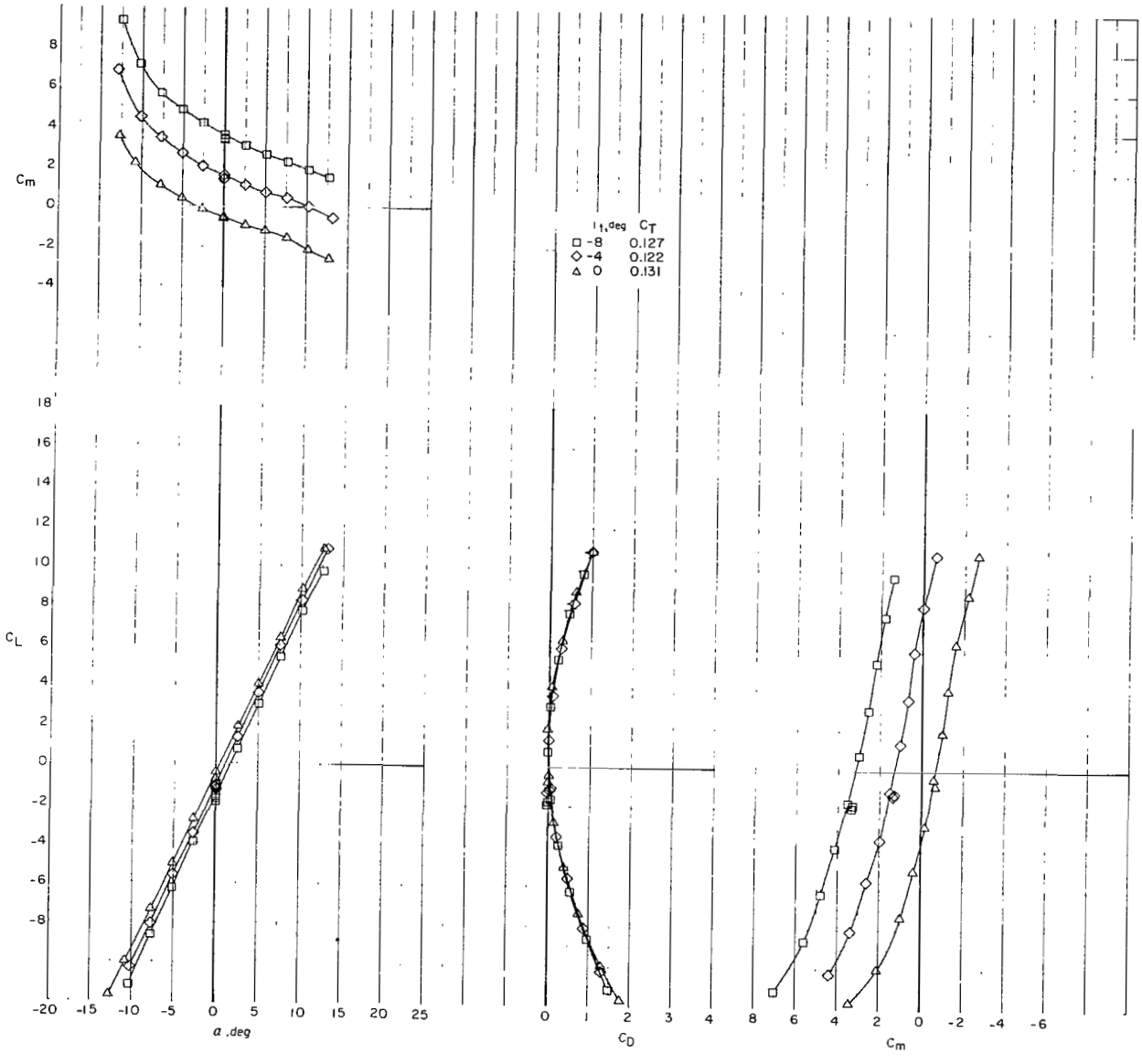

(b) Trim thrust; $i_w = -4.5^o$; $\delta_f = 0^o$.

Figure 20.- Continued.

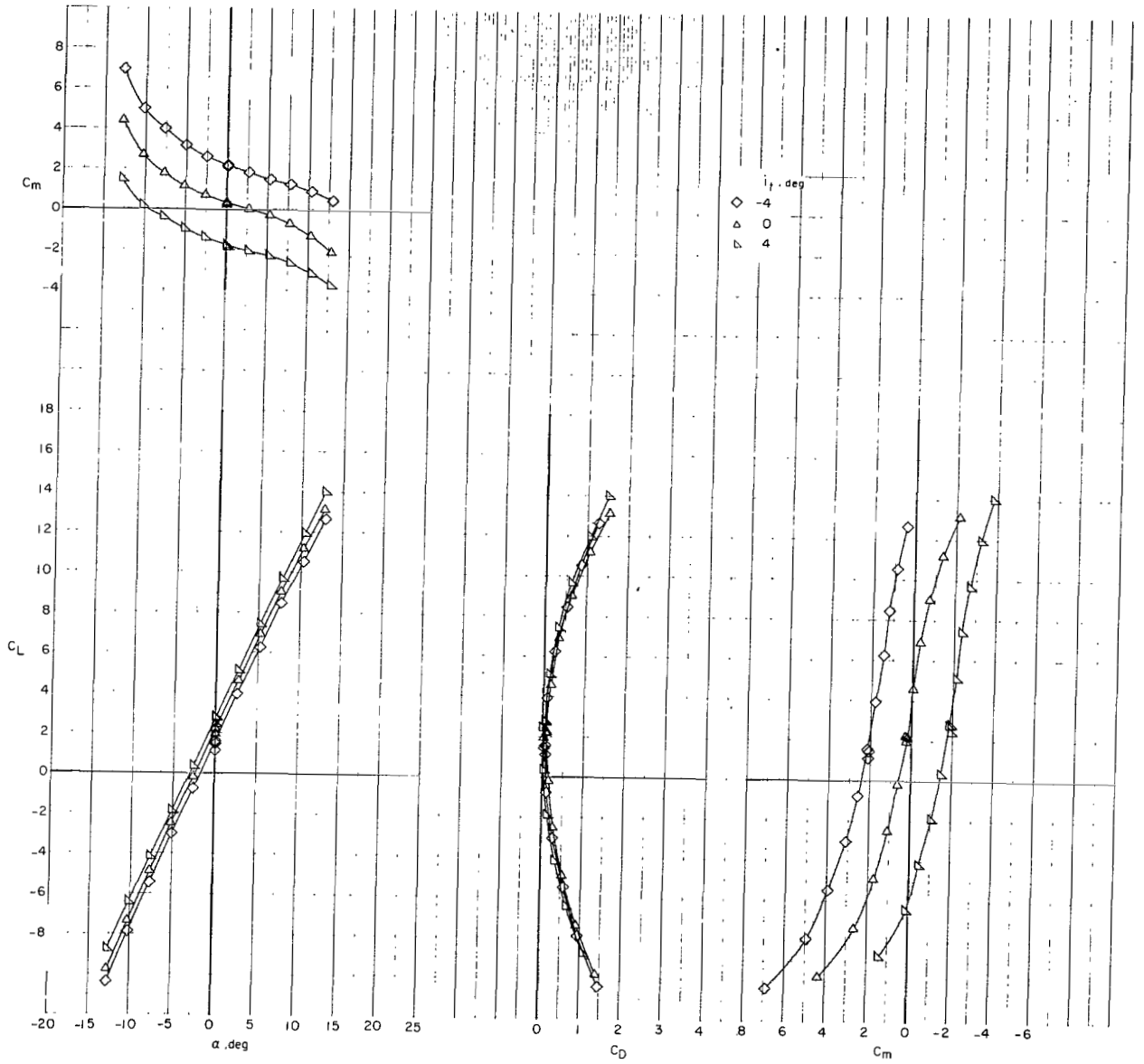

(c) Trim thrust; $i_w = 0^o$; $\delta_f = 0^o$.

Figure 20.- Continued.

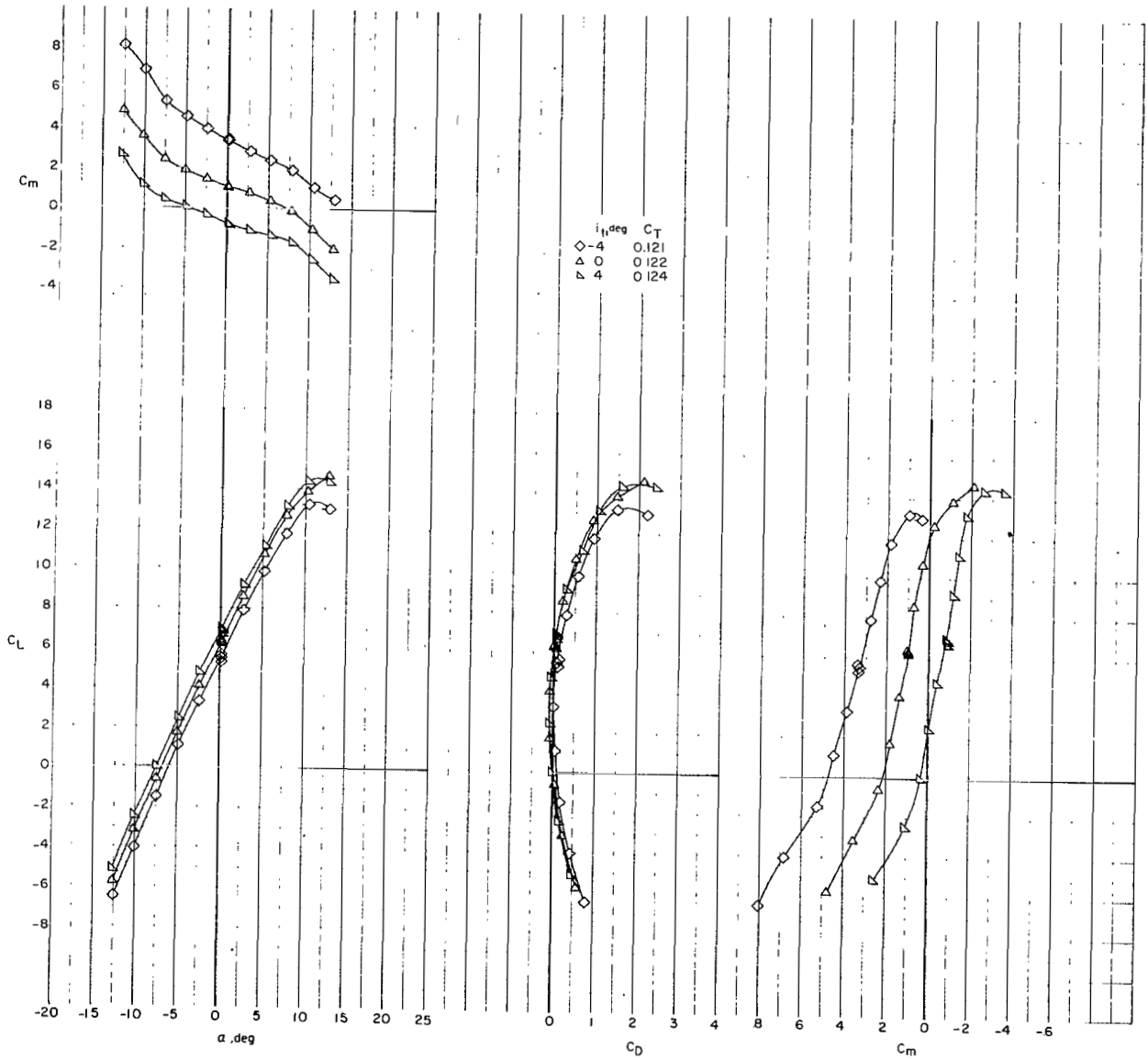

(d) Trim thrust; $i_w = 7.5^o$; $\delta_f = 0^o$.

Figure 20.- Continued.

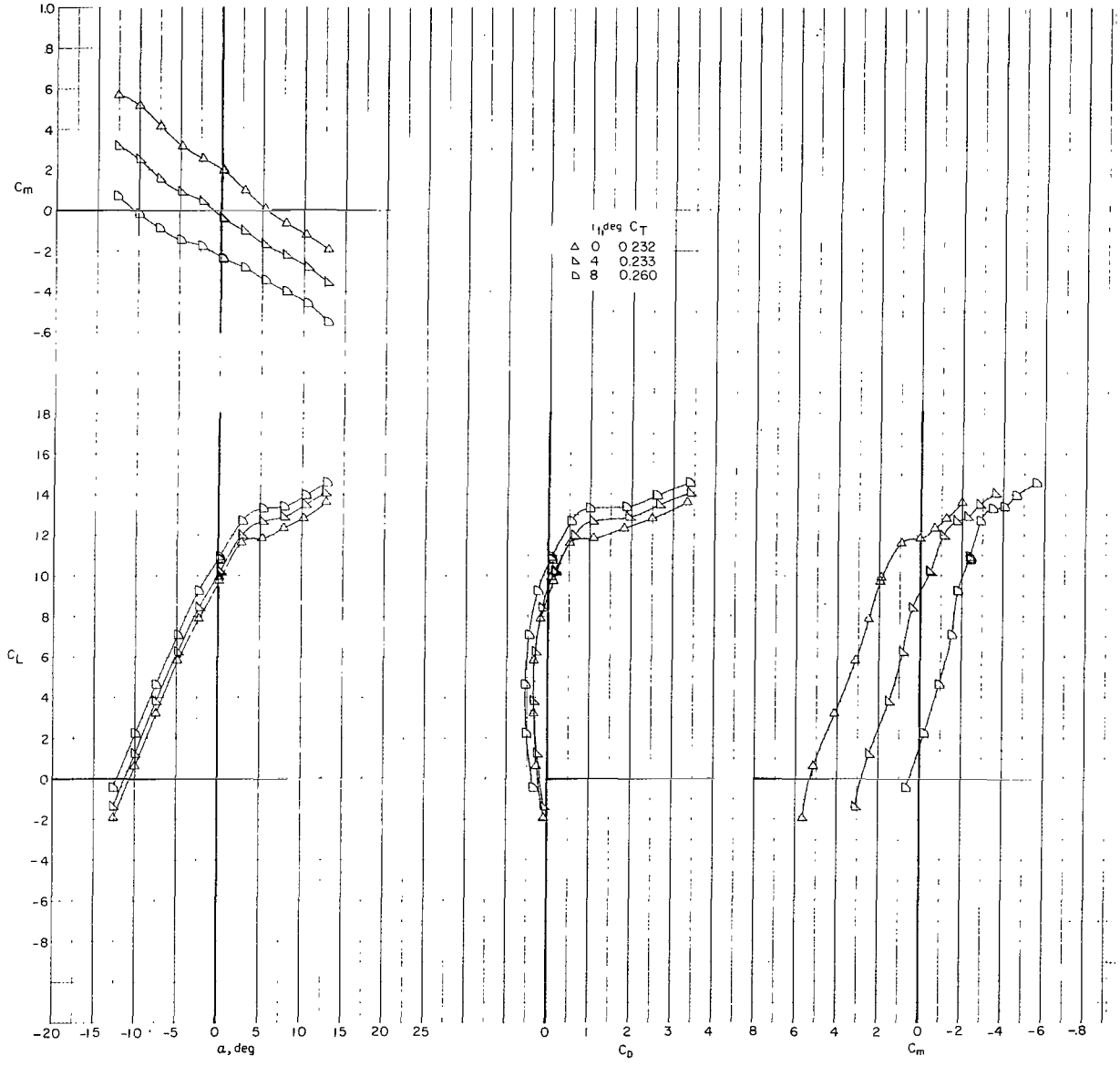

(e) Trim thrust; $i_w = 15^o$; $\delta_f = 0^o$.

Figure 20.- Continued.

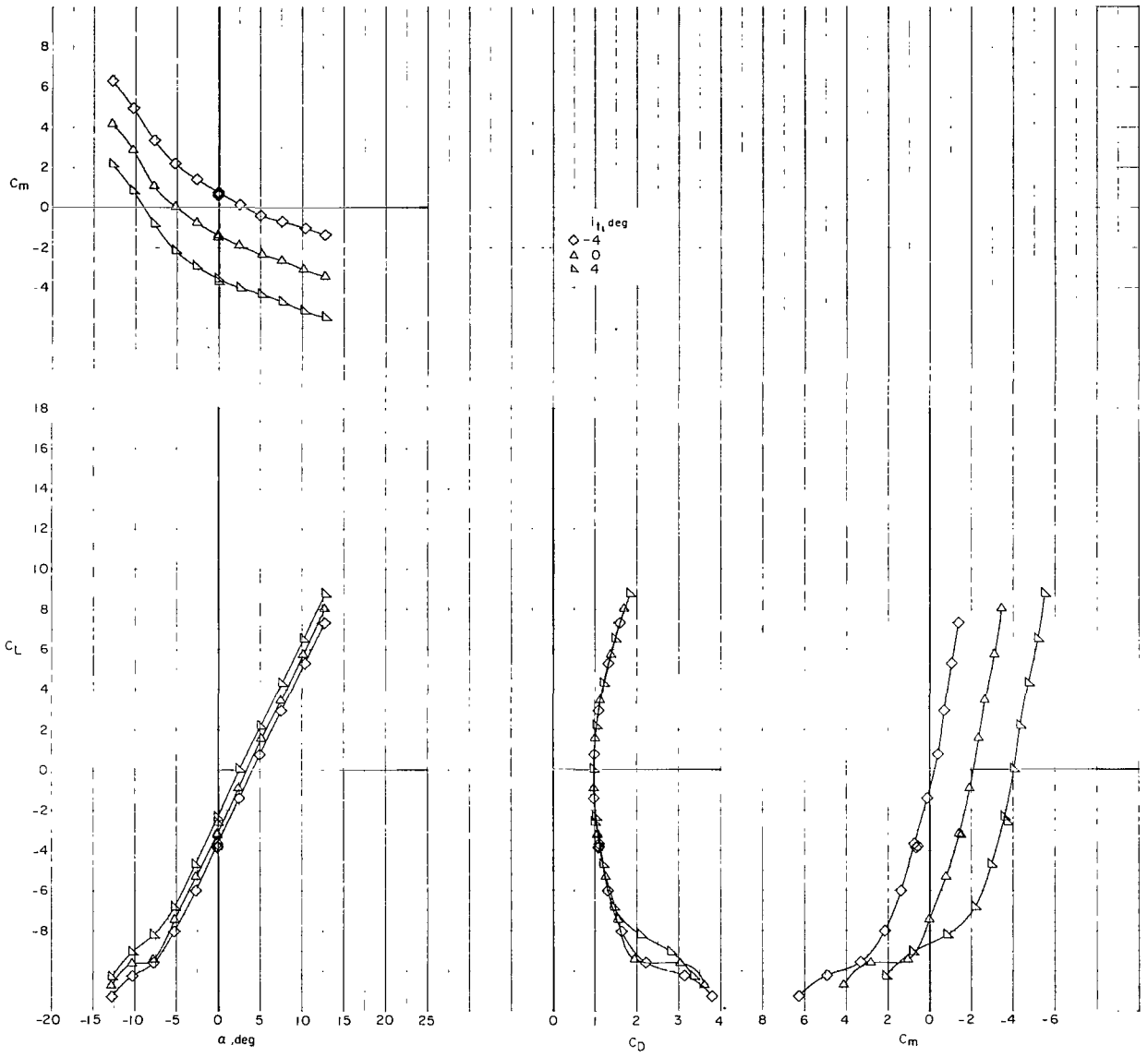

(f) $C_T = 0$; $i_w = -9^o$; $\delta_f = 0^o$.

Figure 20.- Continued.

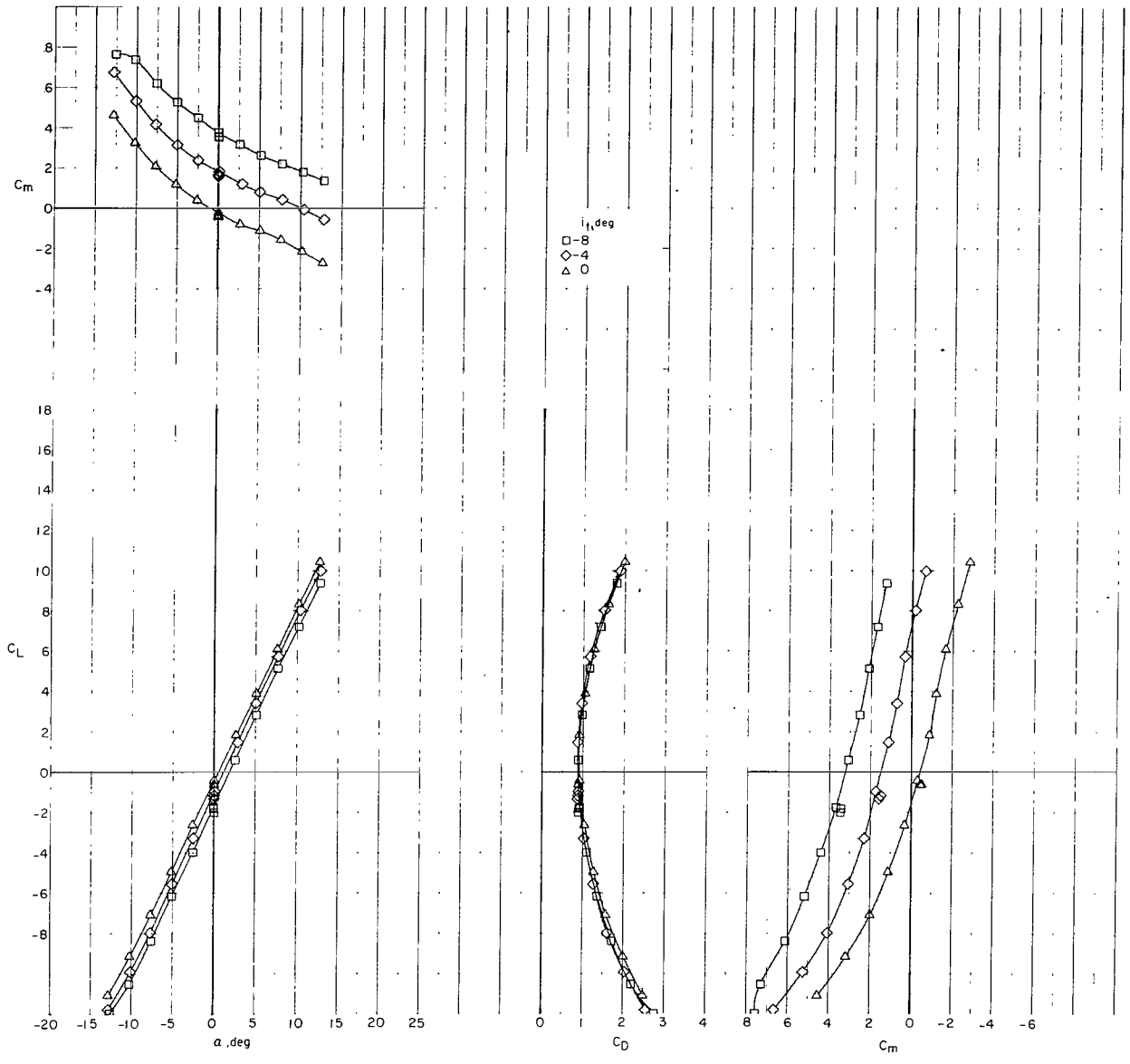

(g) $C_T = 0$; $i_w = -4.5^o$; $\delta_f = 0^o$.

Figure 20.- Continued.

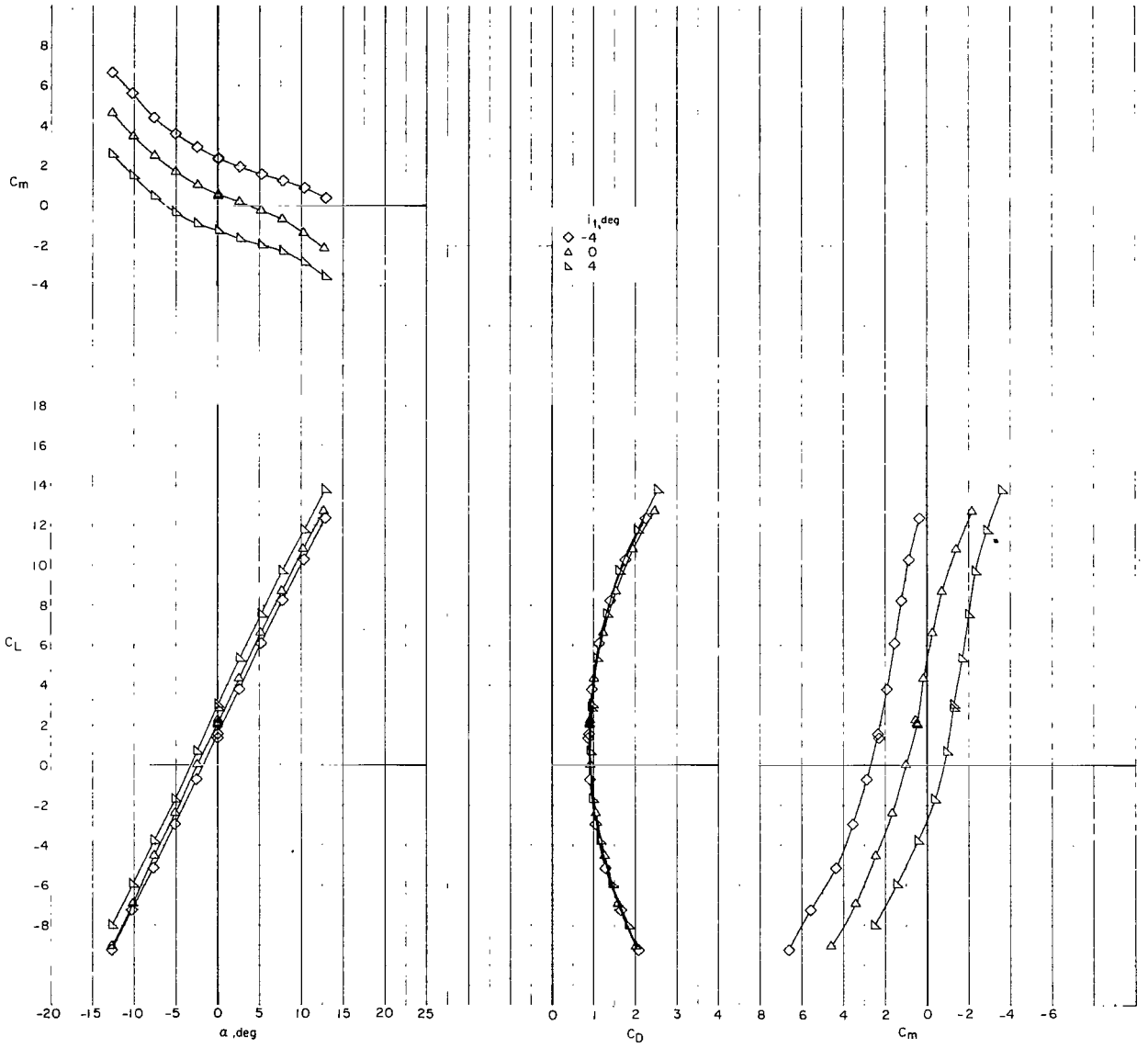

(h) $C_T = 0$; $i_w = 0^o$; $\delta_f = 0^o$.

Figure 20.- Continued.

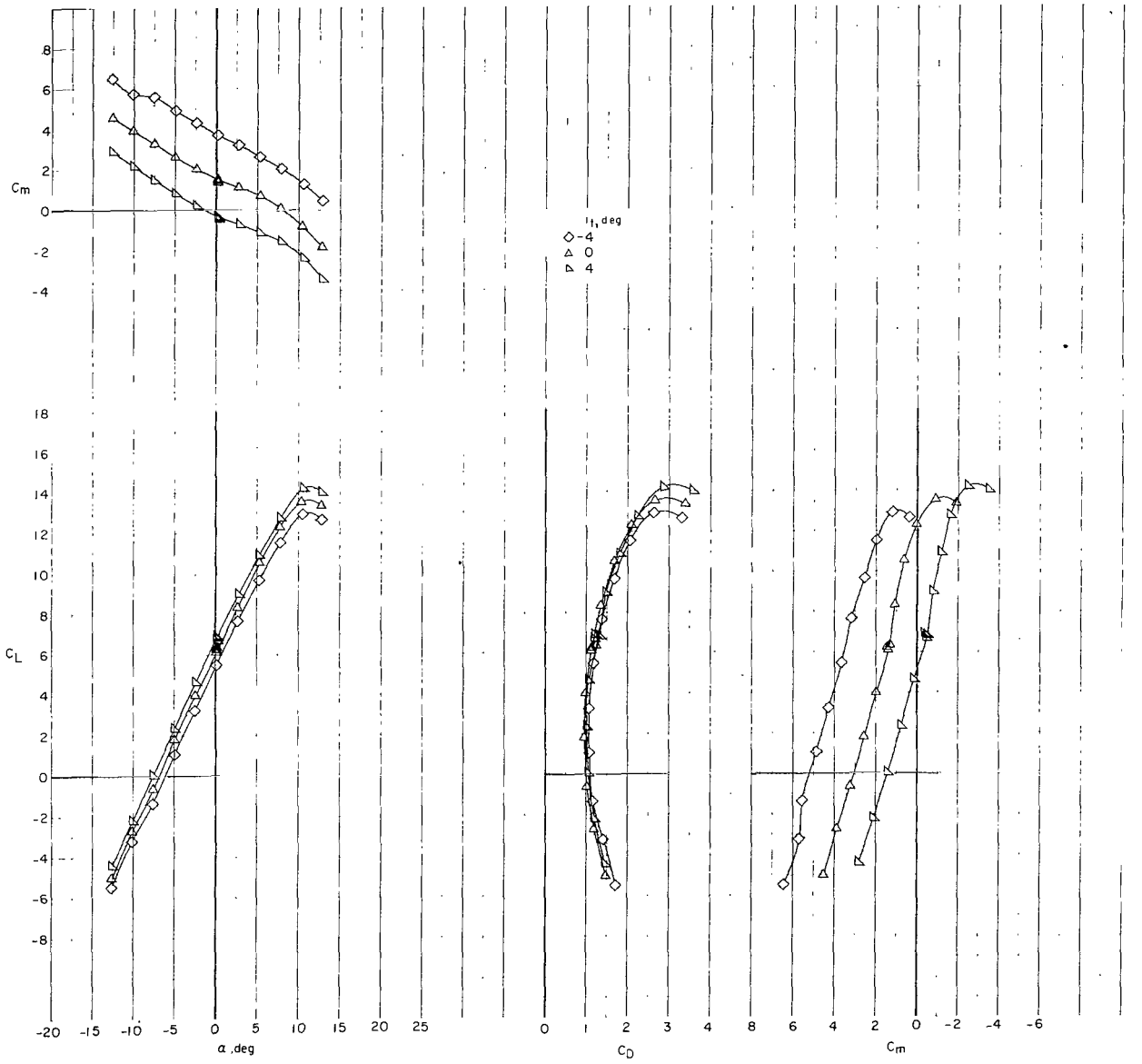

(i) $C_T = 0$; $i_w = 7.5^o$; $\delta_f = 0^o$.

Figure 20.- Continued.

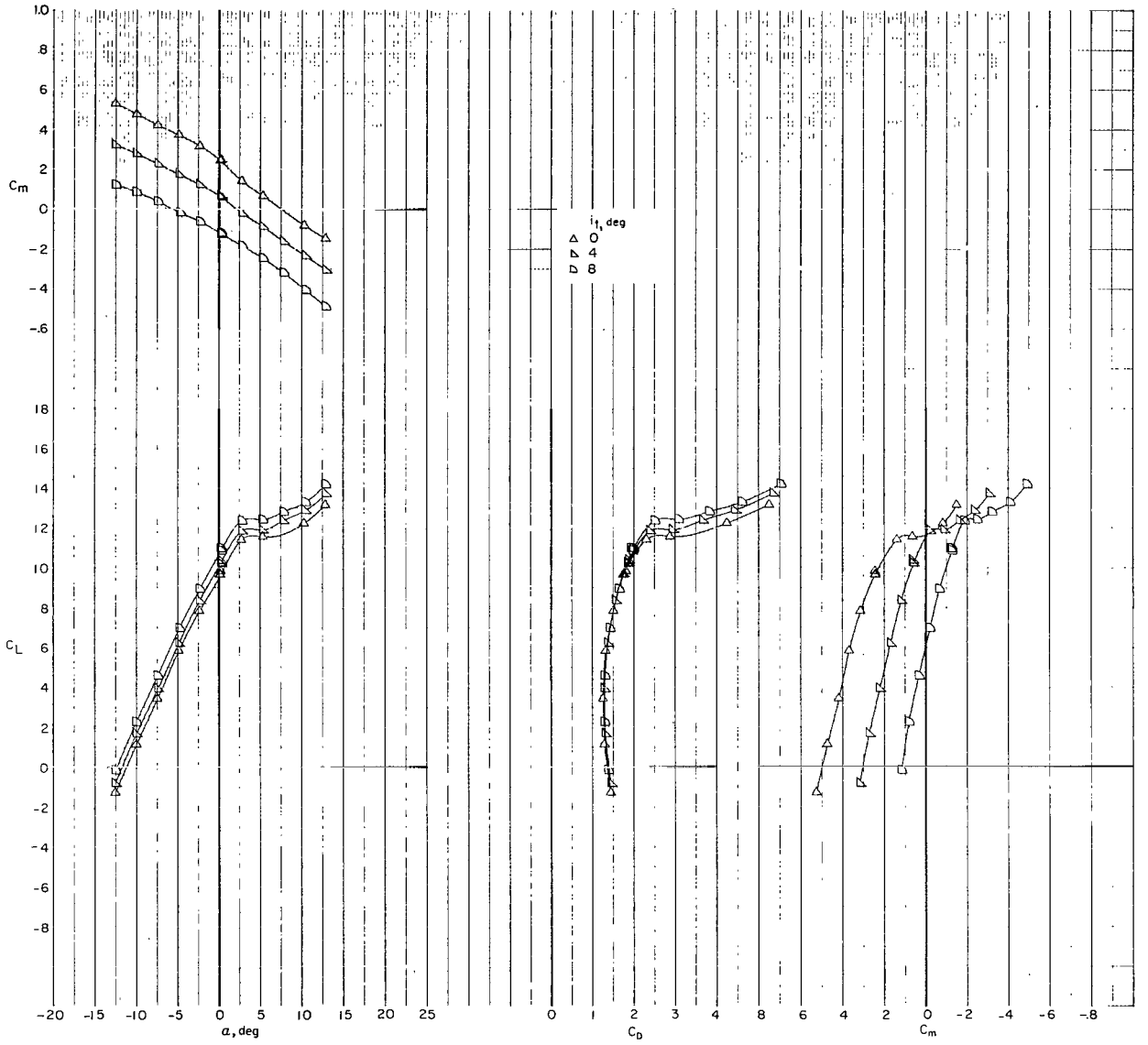

(j) $C_T = 0$; $i_w = 15^o$; $\delta_f = 0^o$.

Figure 20.- Continued.

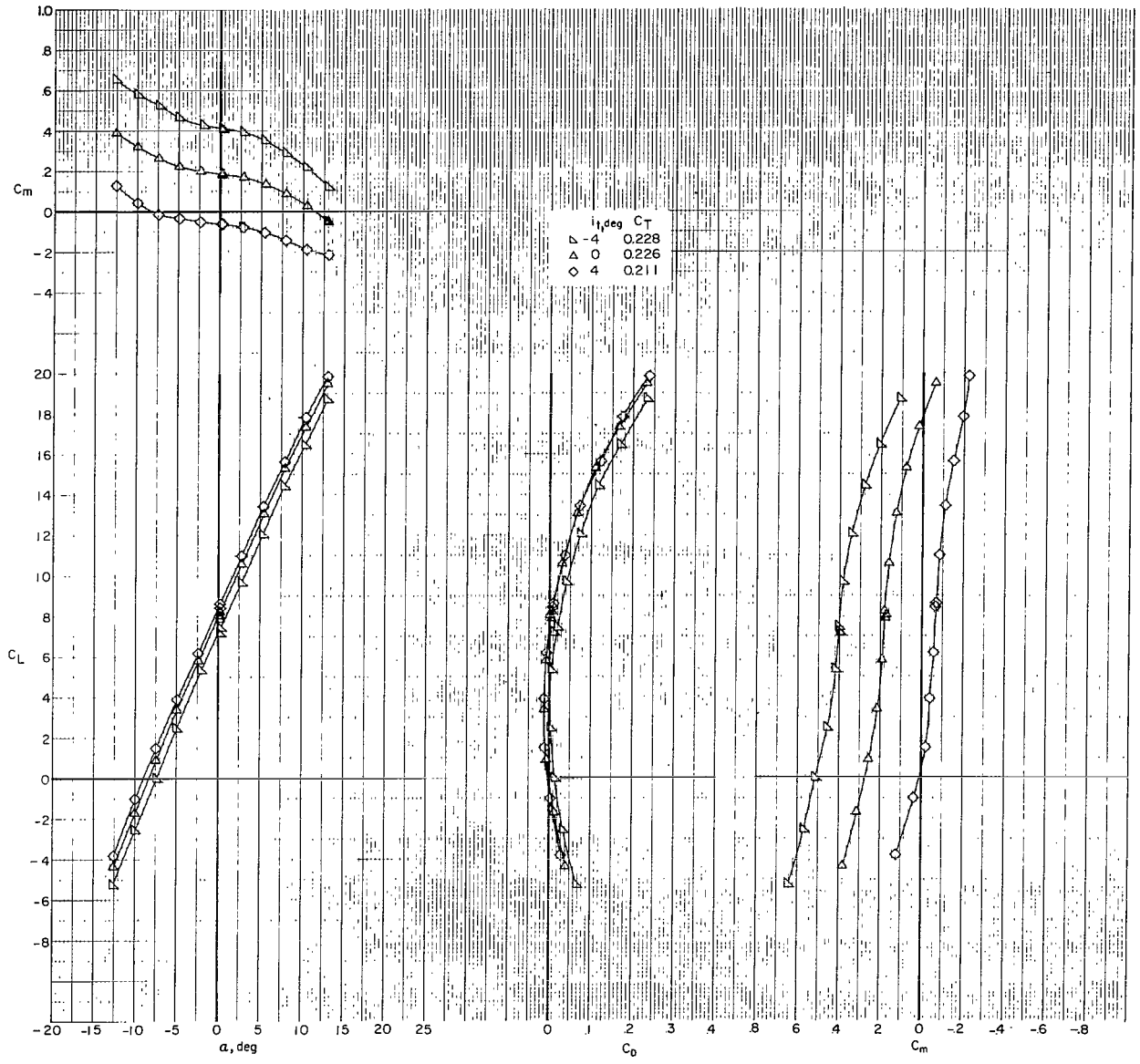

(k) Trim thrust; $i_W = 0^O$; $\delta_f = 30^O$.

Figure 20.- Continued.

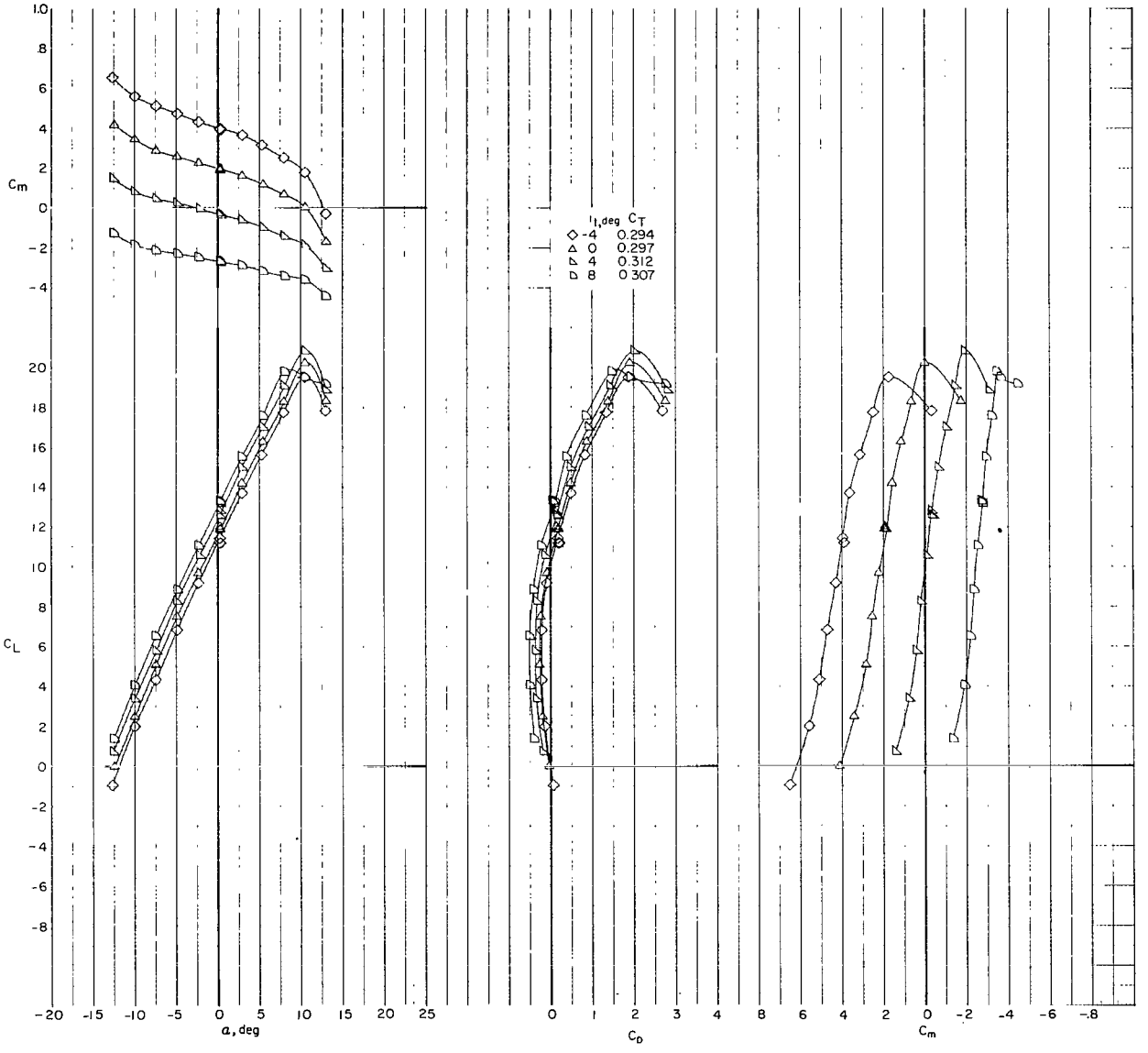

(l) Trim thrust; $i_w = 7.5^o$; $\delta_f = 30^o$.

Figure 20.- Continued.

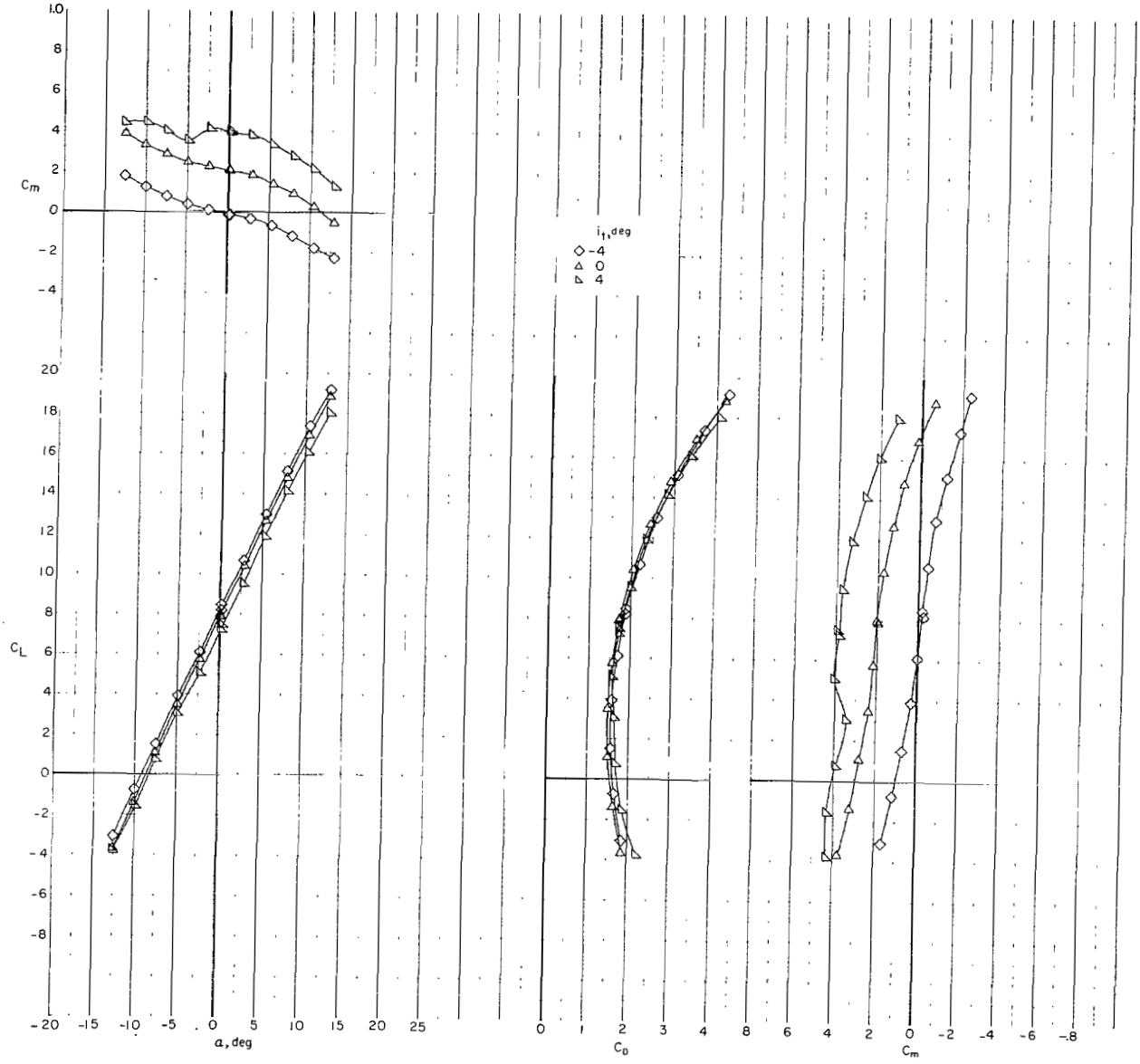

(m) $C_T = 0$; $i_w = 0^o$; $\delta_f = 30^o$.

Figure 20.- Continued.

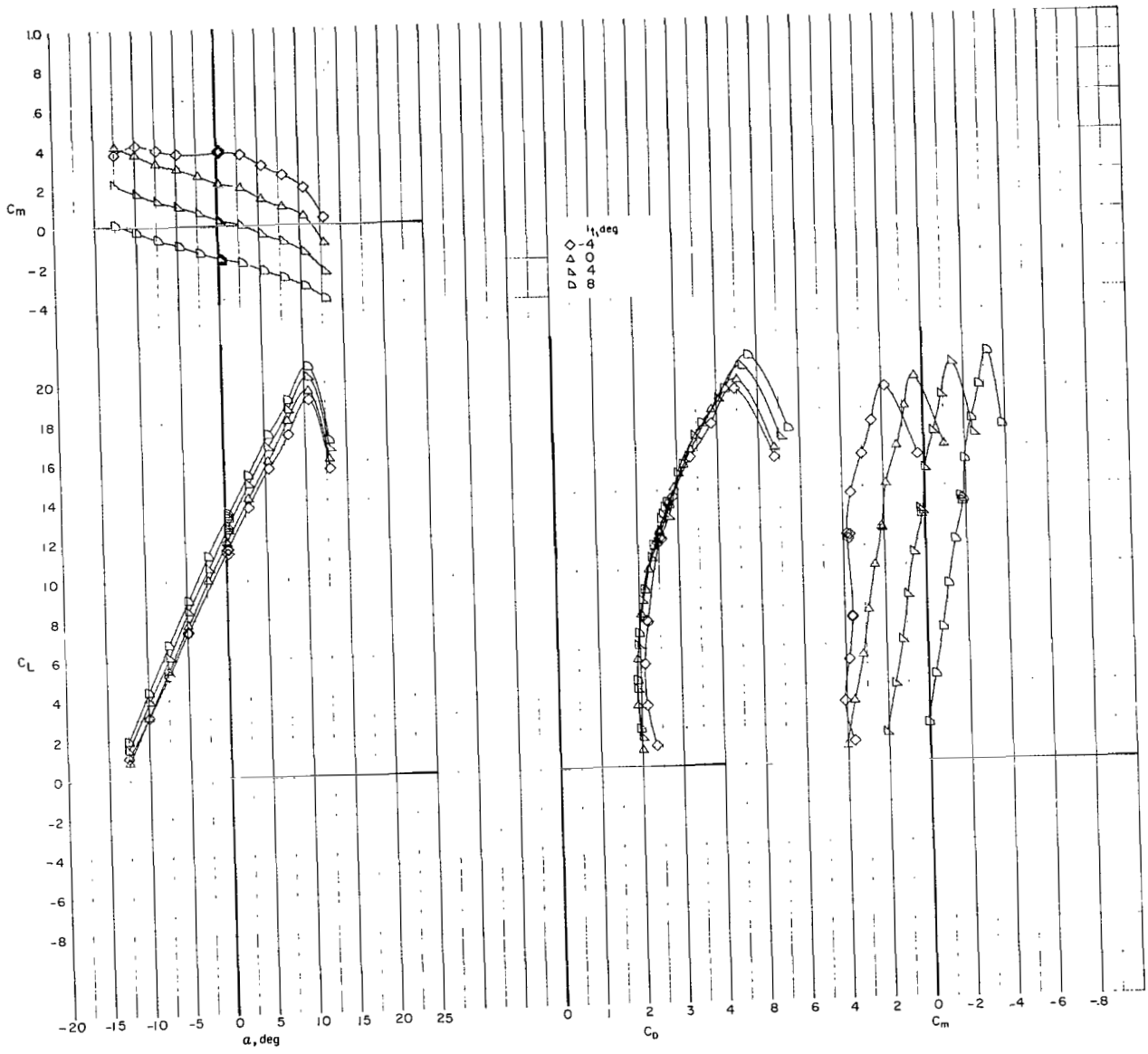

(n) $C_T = 0$; $i_w = 7.5^o$; $\delta_f = 30^o$.

Figure 20.- Concluded.

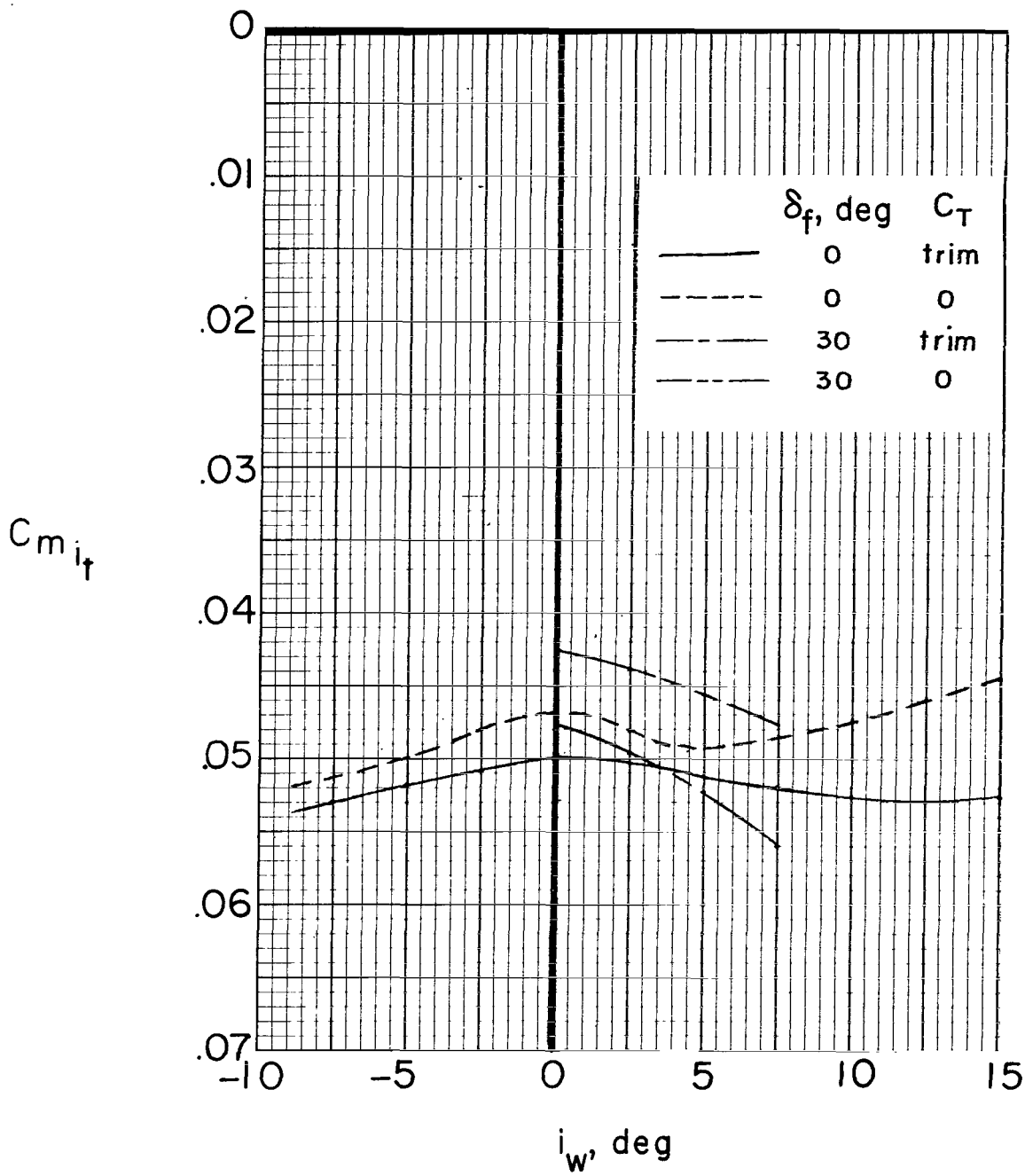

Figure 21.- Variation of $C_{m_{i_t}}$ with i_w for Phase III baseline configuration.

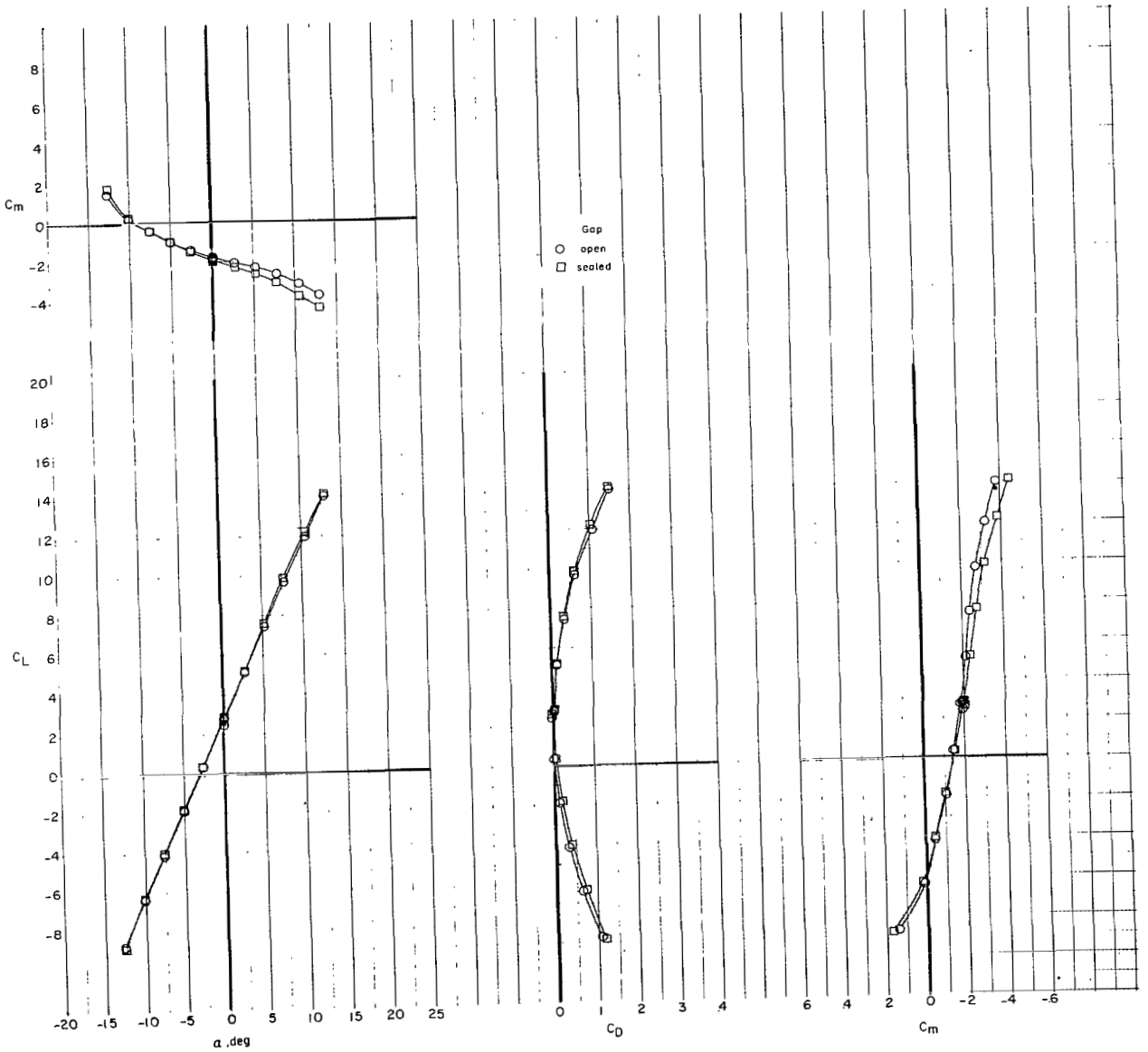

(a) $i_w = 0^o$; $i_t = 4^o$.

Figure 22.- Effect of sealing gap in horizontal-tail—fuselage junction on longitudinal characteristics of Phase III baseline configuration. Trim thrust.

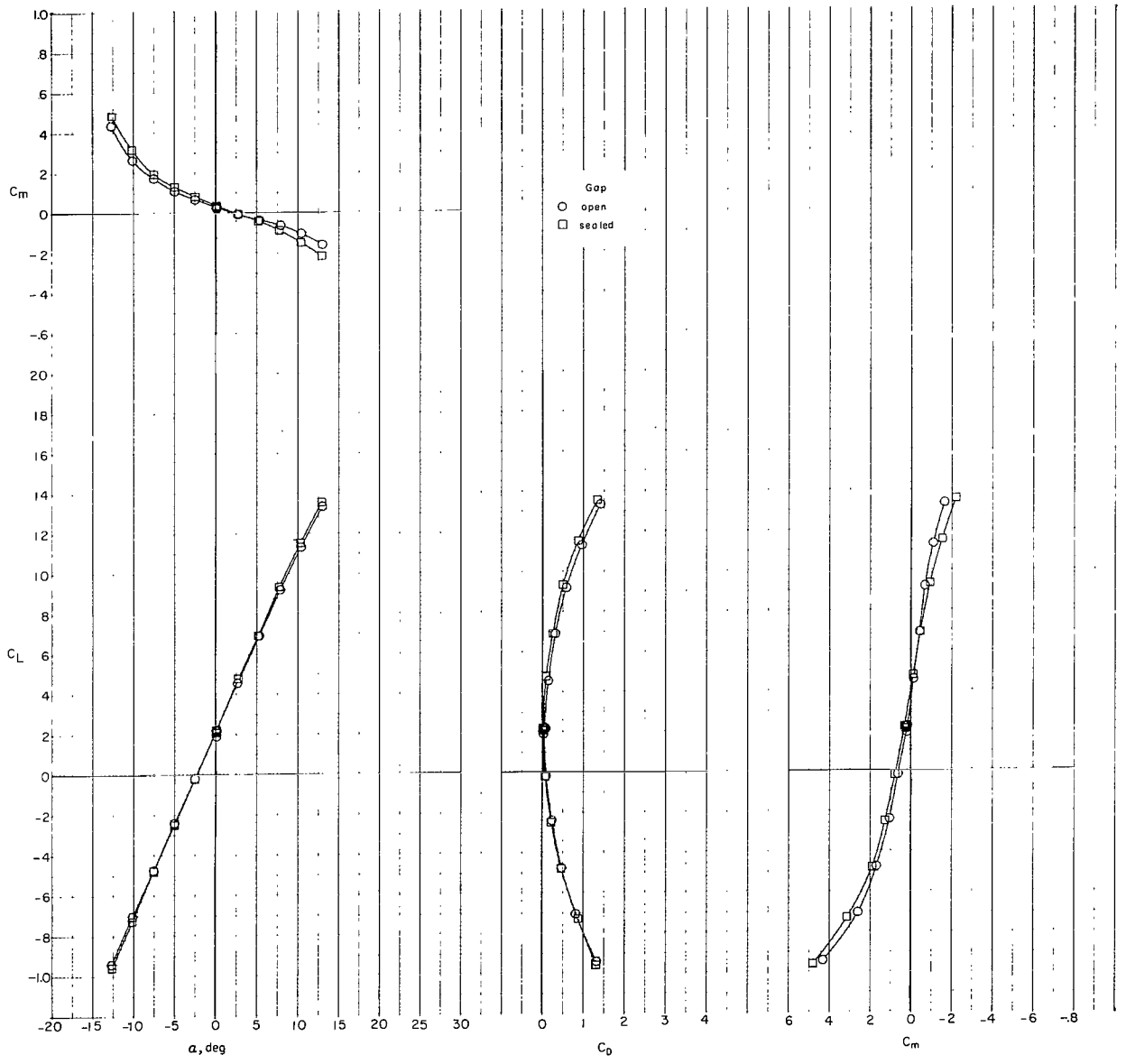

(b) $i_w = 0^o$; $i_t = 0^o$.

Figure 22.- Continued.

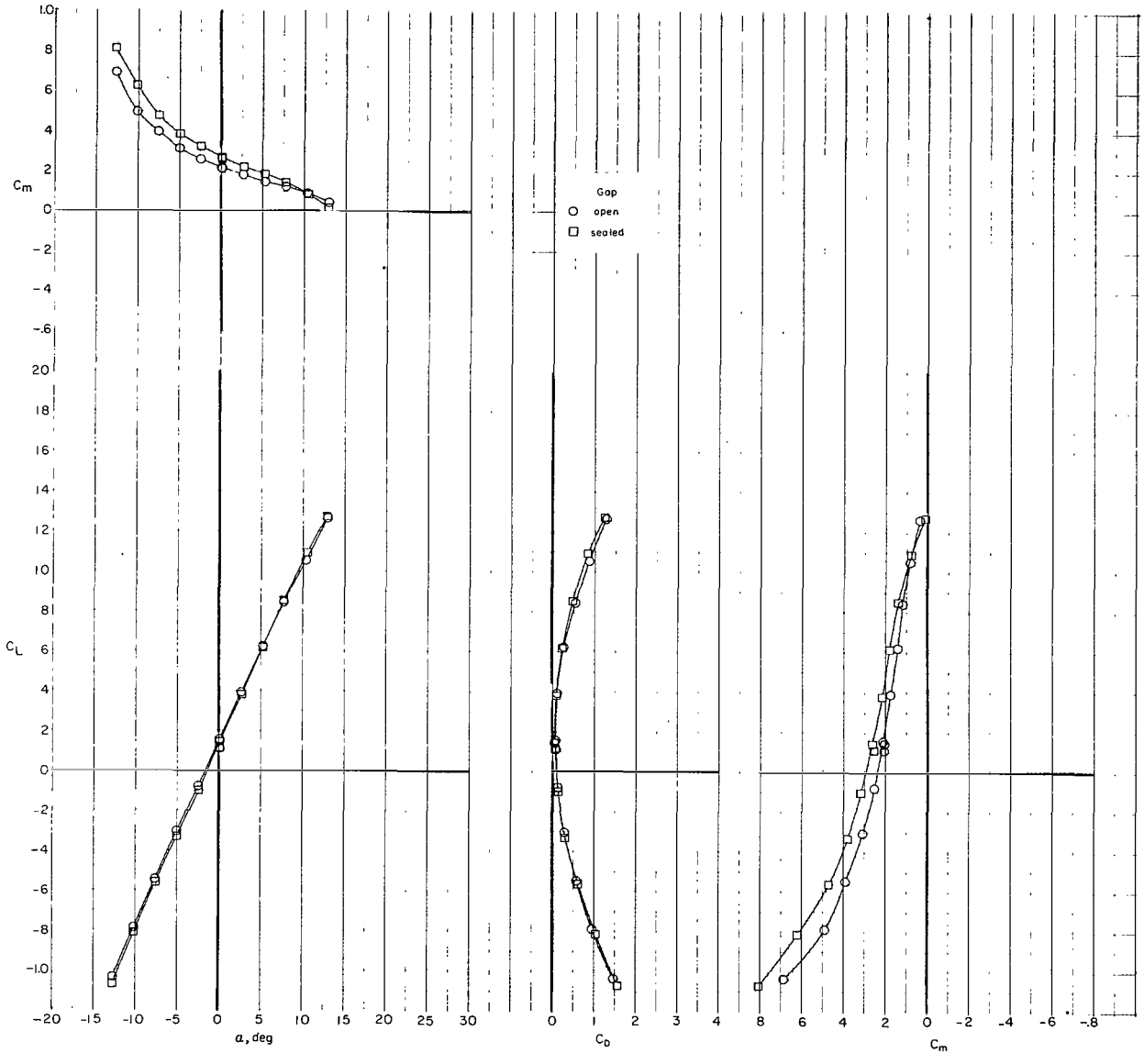

(c) $i_w = 0^o$; $i_t = -4^o$.

Figure 22.- Concluded.

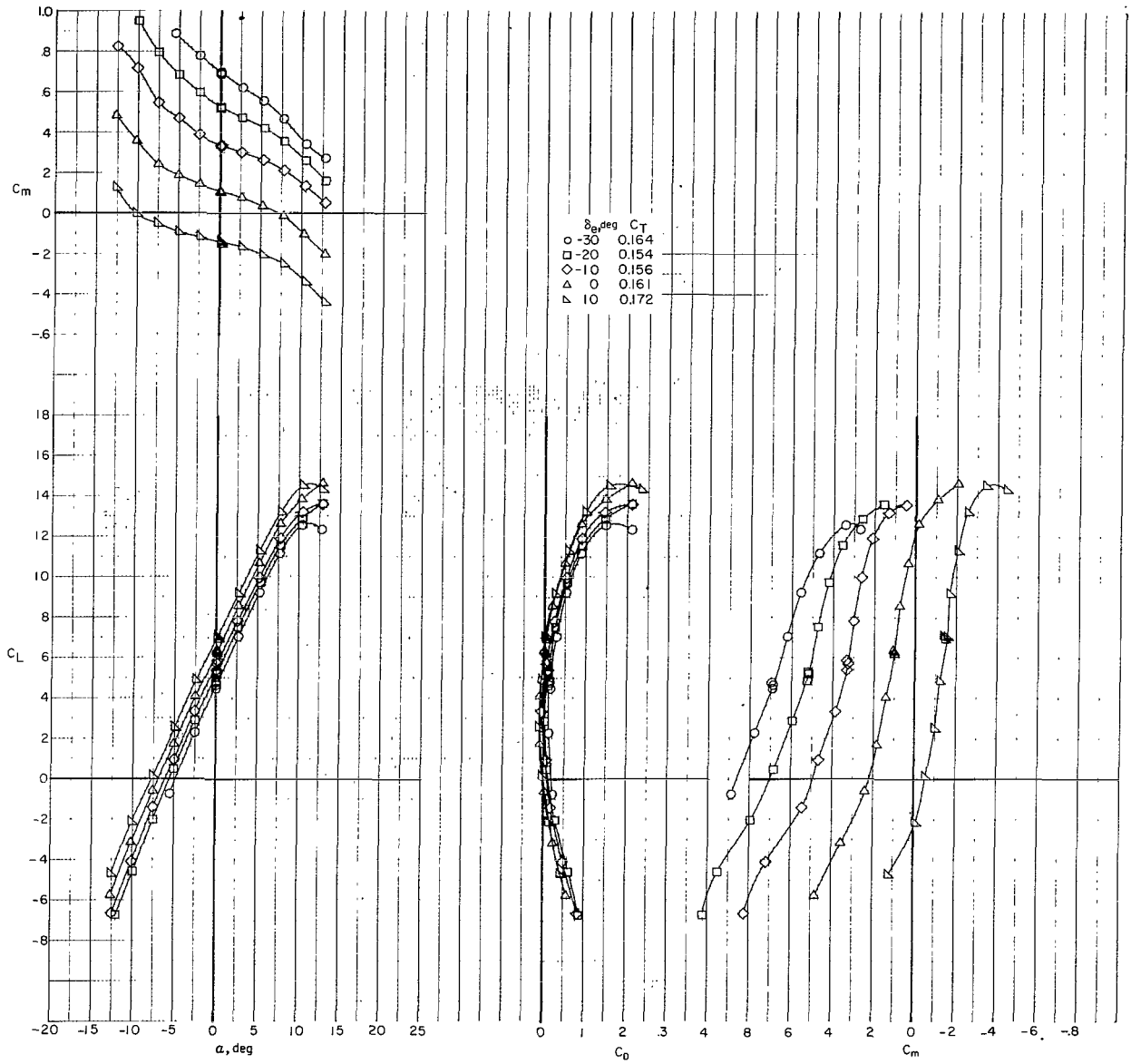

(a) Trim thrust; $\delta_f = 0^o$; $i_t = 0^o$.

Figure 23.- Effect of elevator deflection δ_e on longitudinal characteristics of Phase III baseline configuration. $i_w = 7.5^o$.

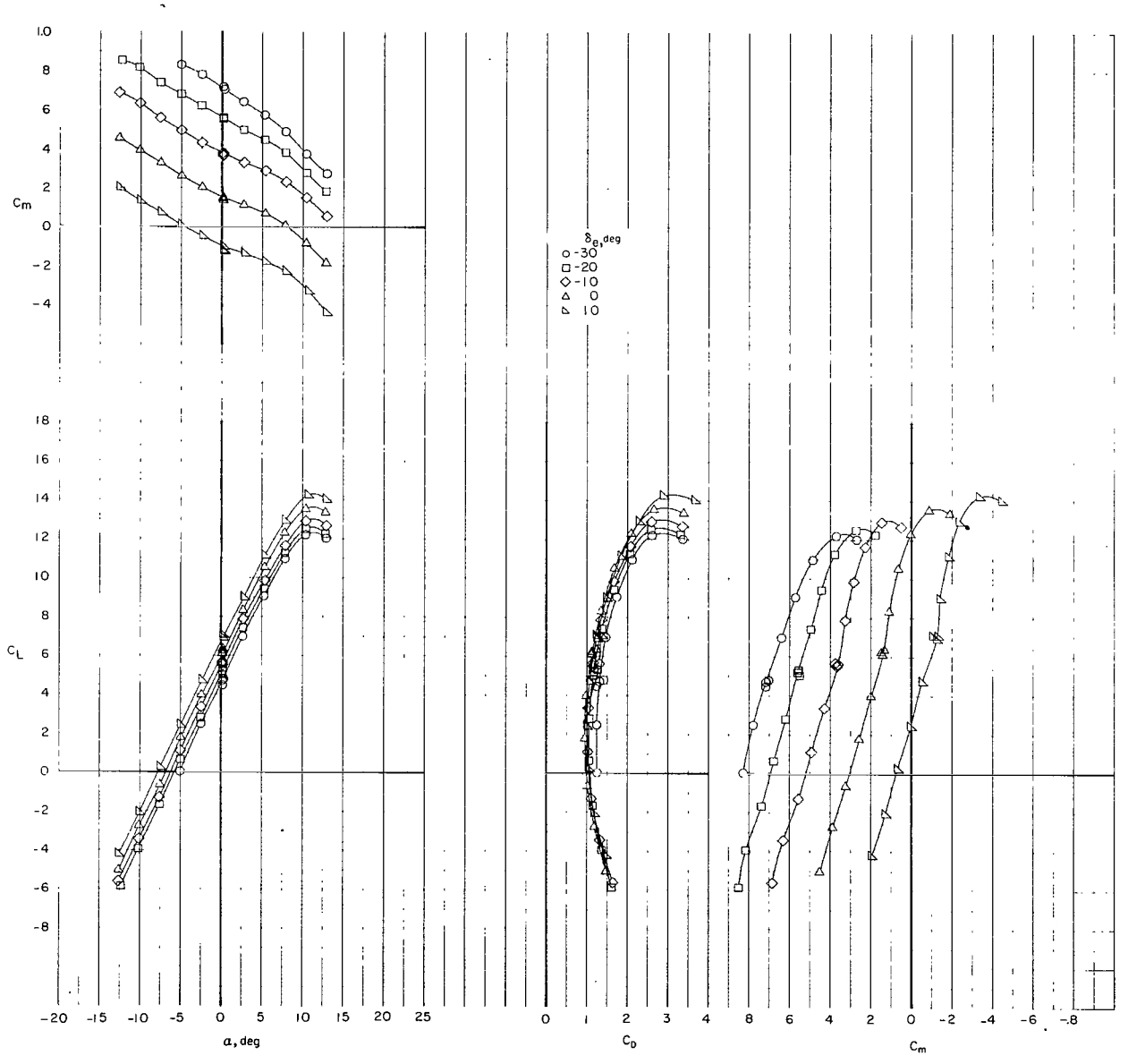

(b) $C_T = 0$; $\delta_f = 0^o$; $i_t = 0^o$.

Figure 23.- Continued.

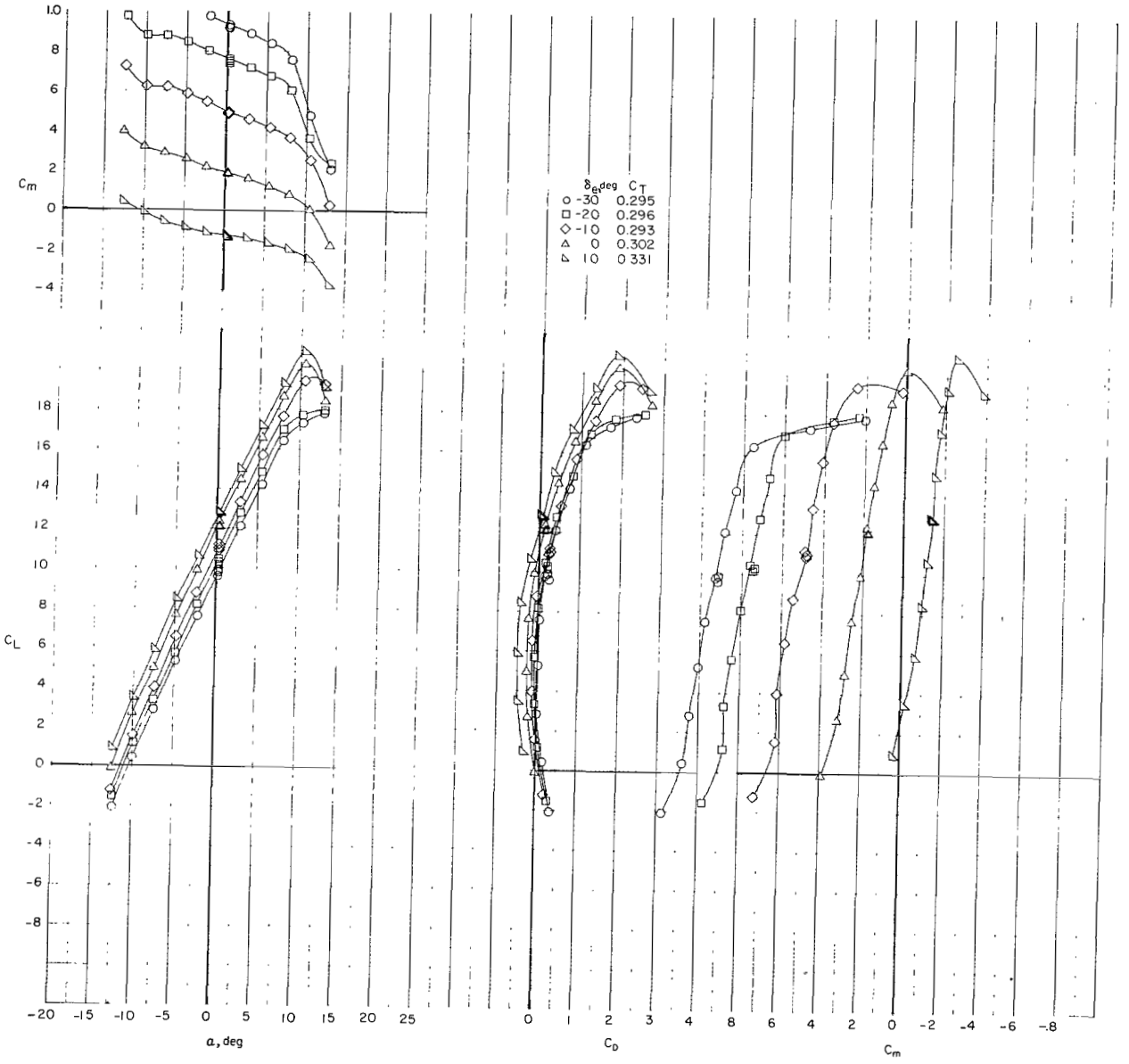

(c) Trim thrust; $\delta_f = 30^o$; $i_t = 0^o$.

Figure 23.- Continued.

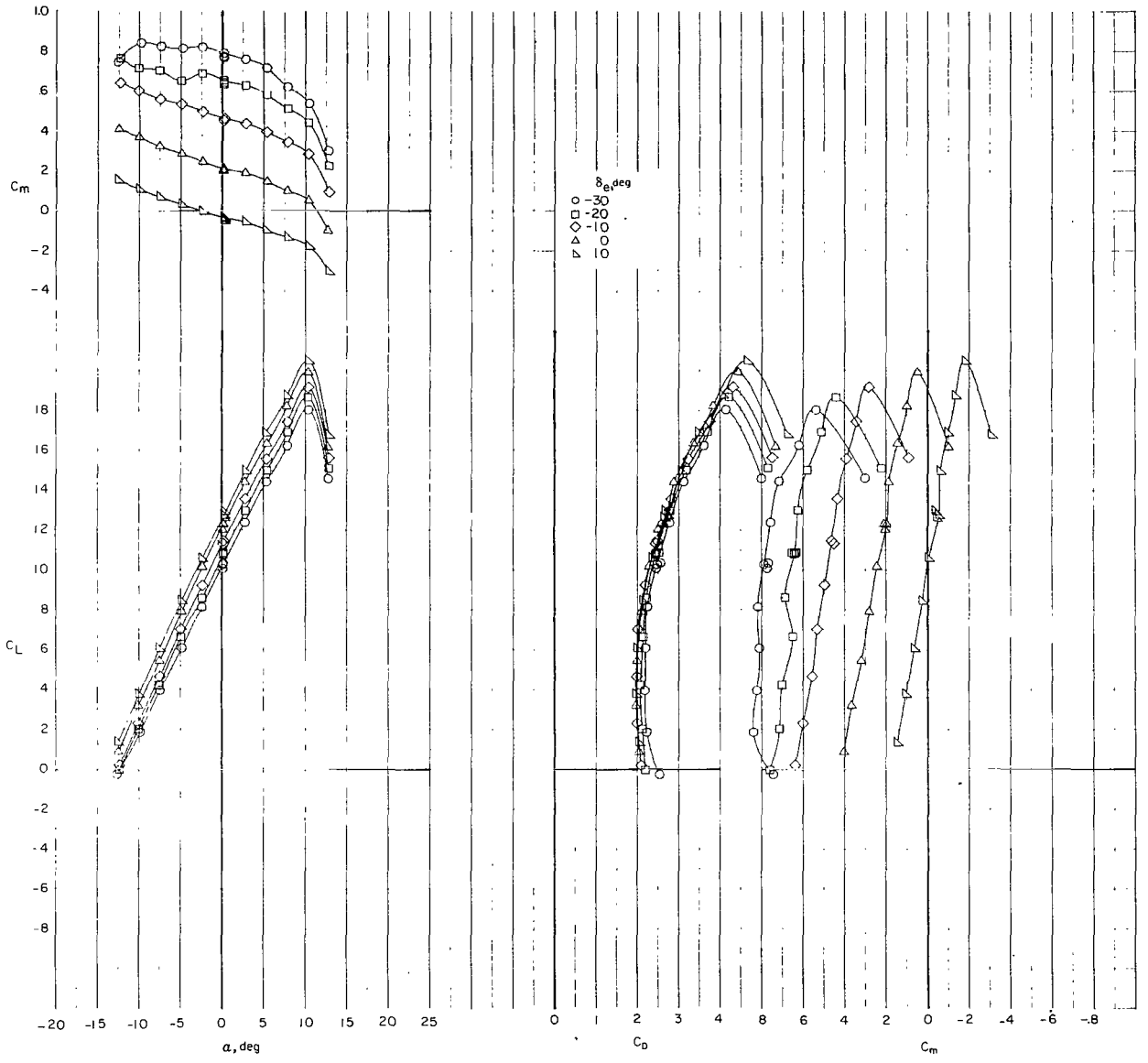

(d) $C_T = 0$; $\delta_f = 30^o$; $i_t = 0^o$.

Figure 23.- Continued.

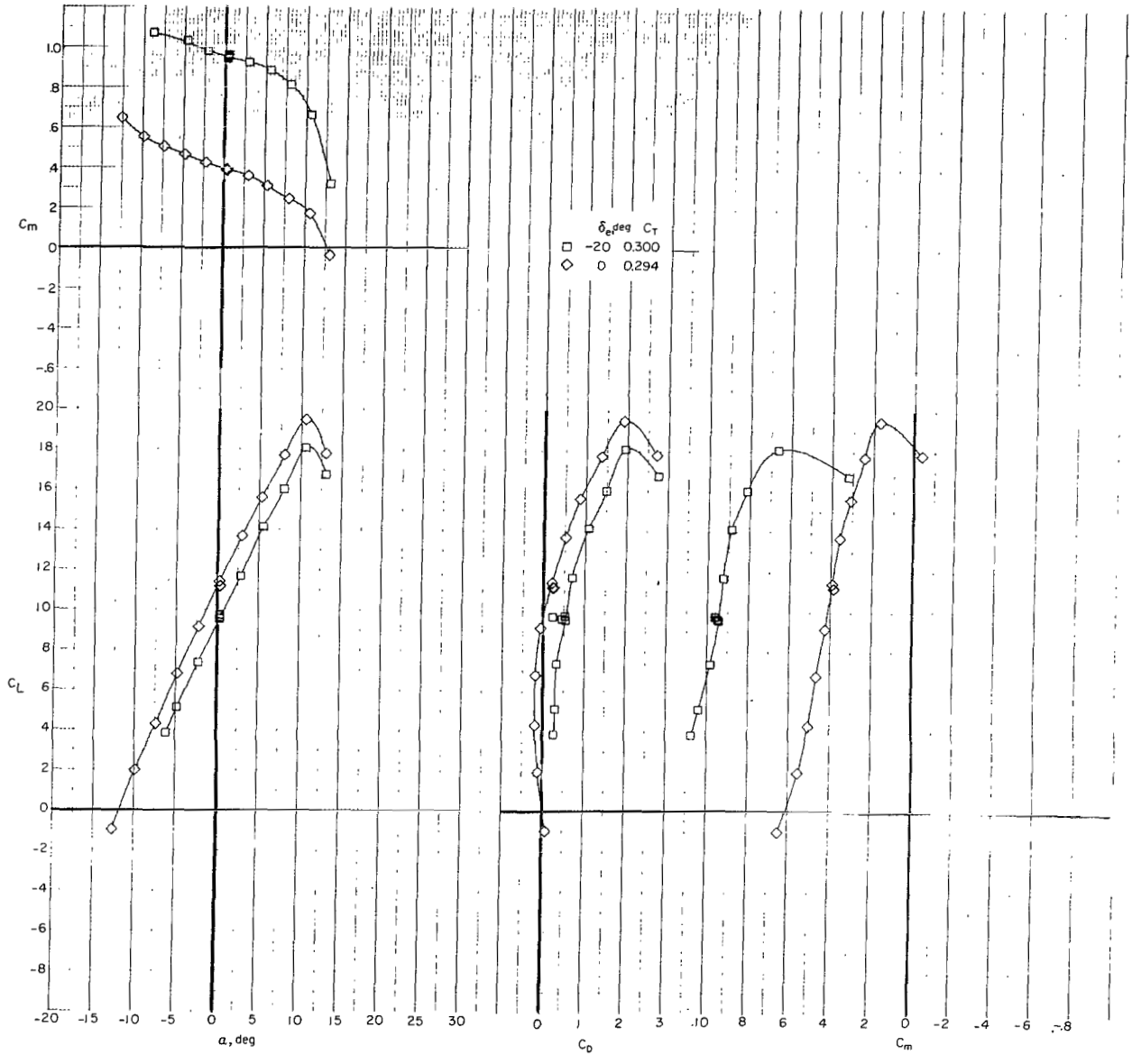

(e) Trim thrust; $\delta_f = 30^o$; $i_t = -4^o$.

Figure 23.- Continued.

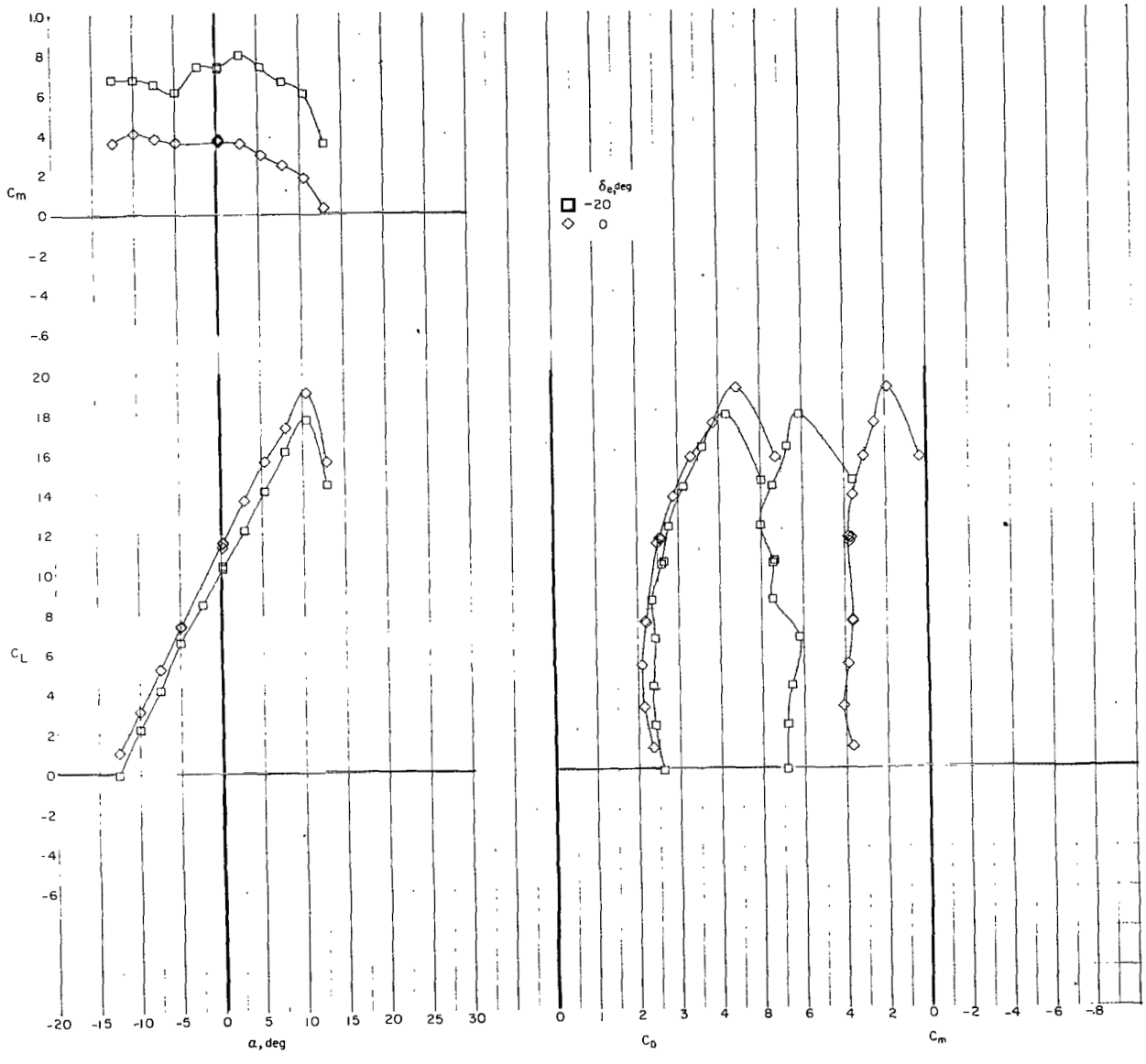

(f) $C_T = 0$; $\delta_f = 30^o$; $i_t = -4^o$.

Figure 23.- Concluded.

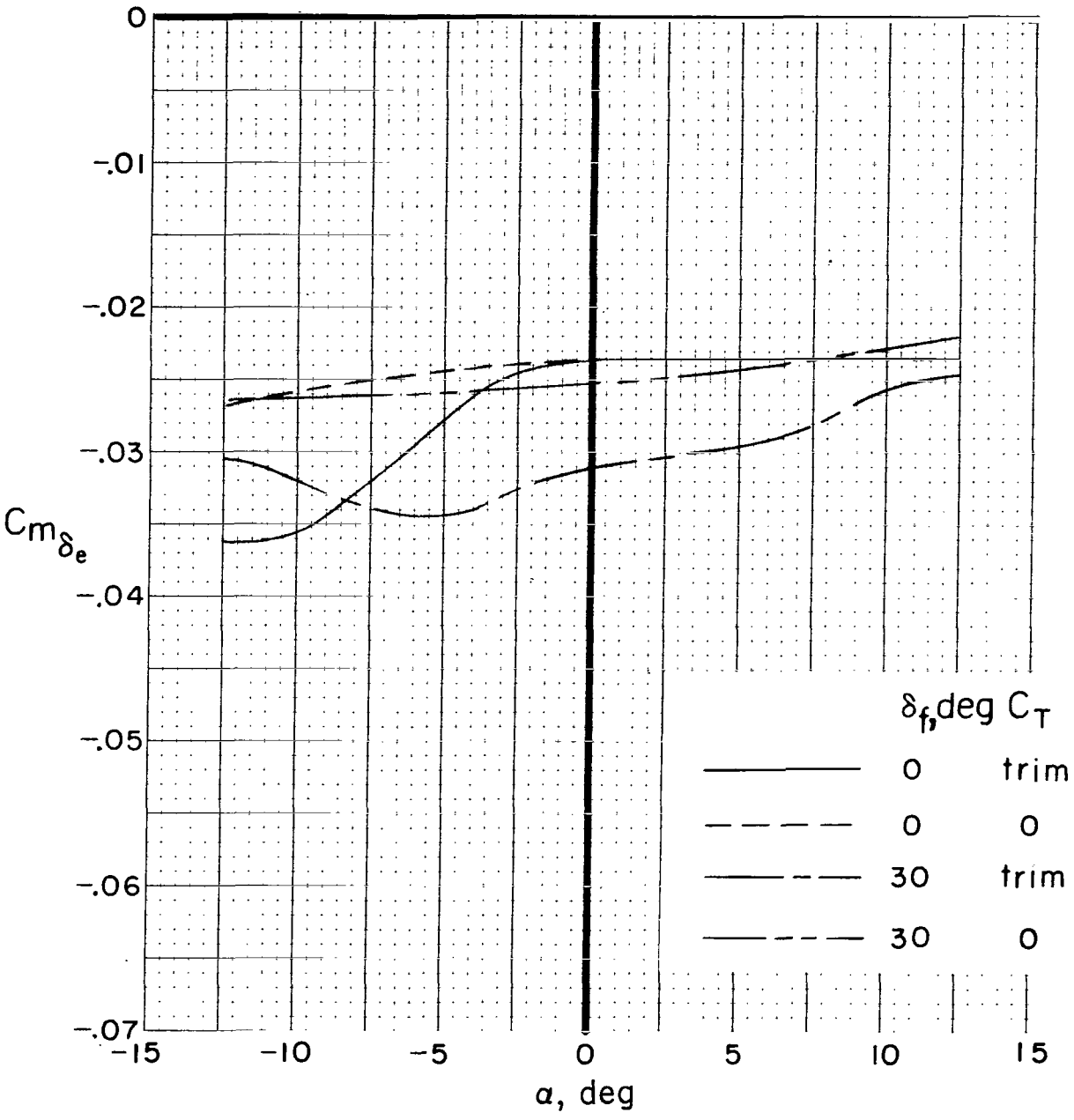

(a) $i_t = 0^o$.

Figure 24.- Variation of Cm_{δ_e} with α for Phase III baseline configuration. $i_w = 7.5^o$.

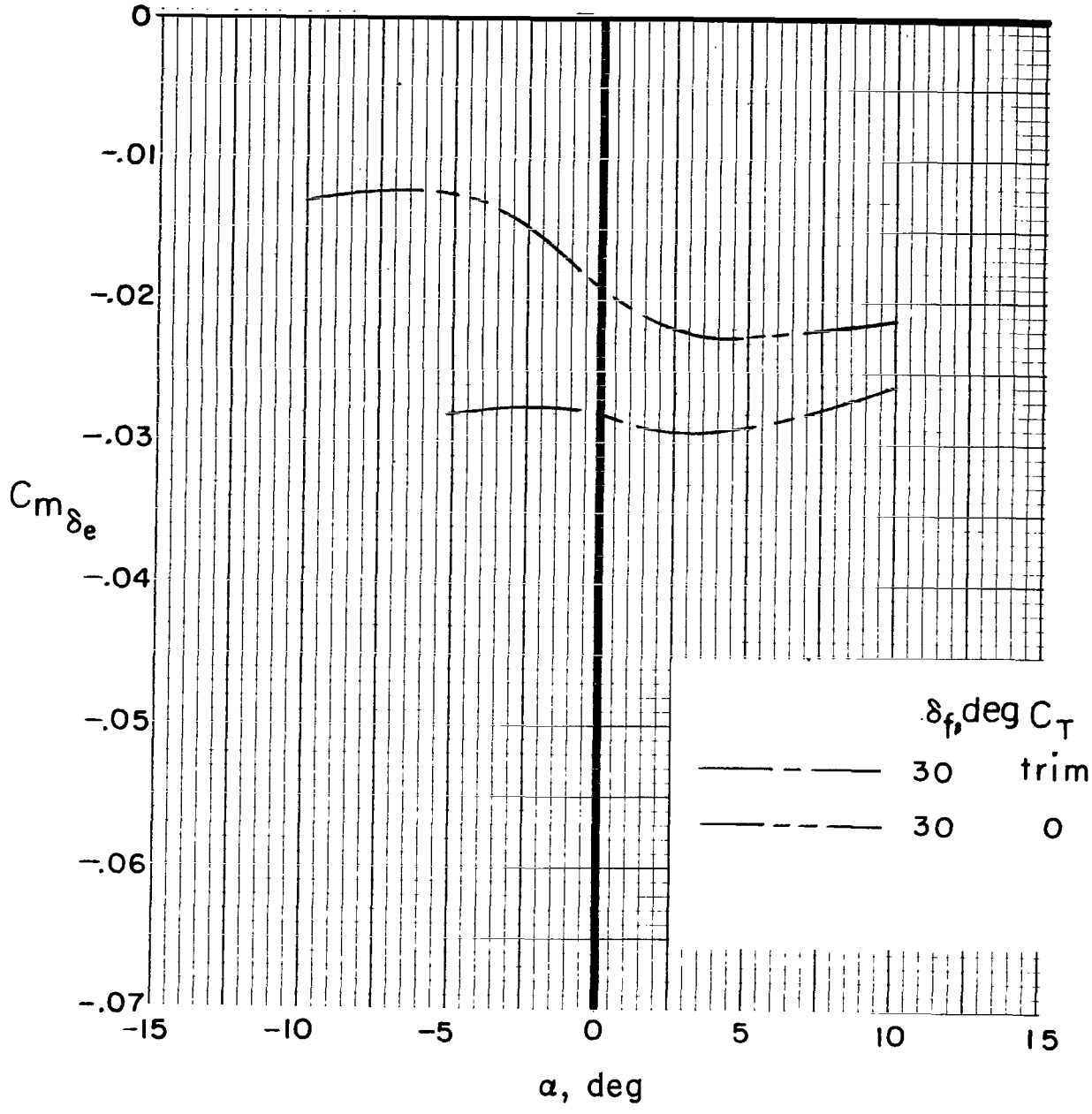

(b) $i_t = -4^o$.

Figure 24.- Concluded.

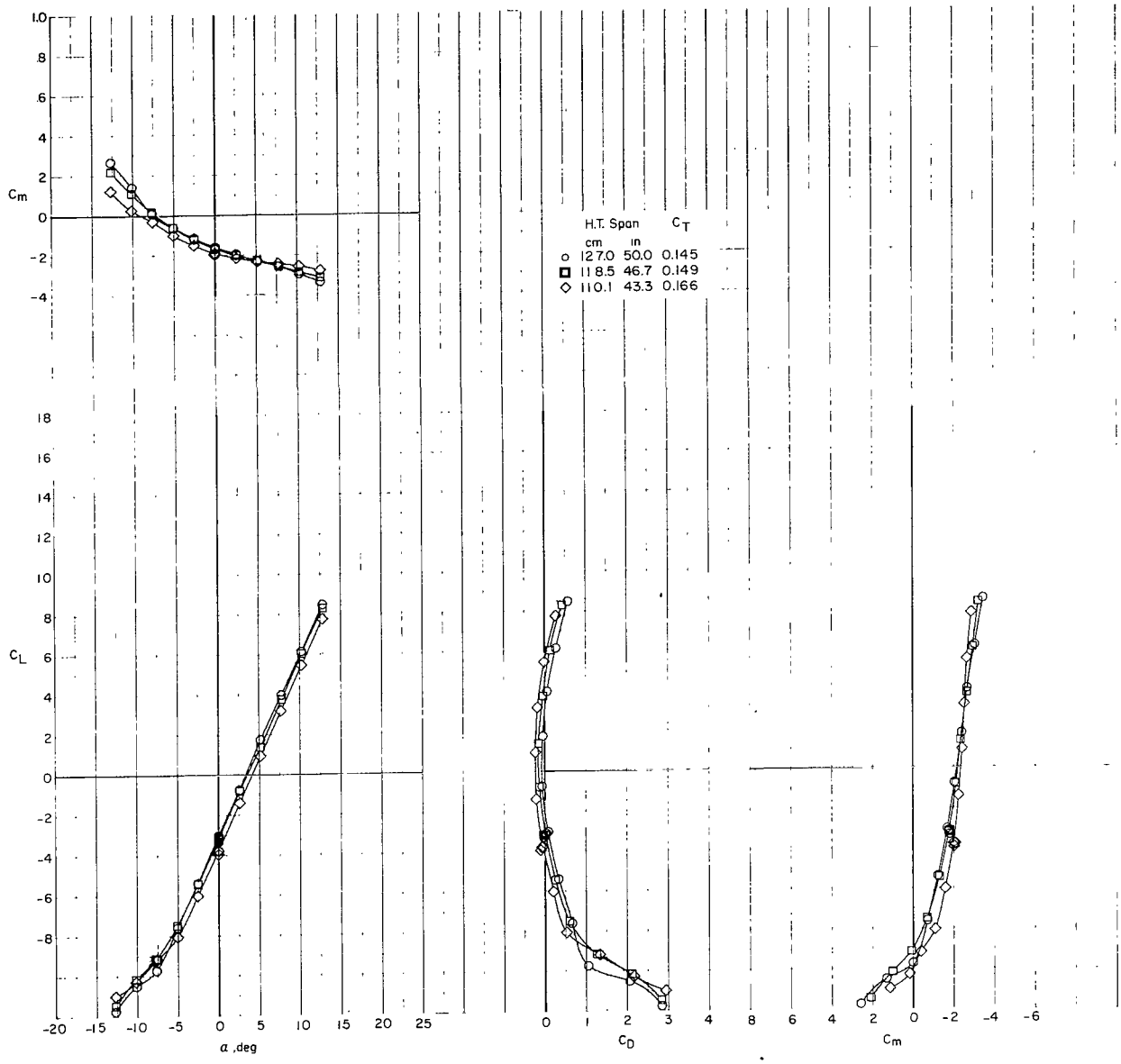

(a) $i_w = -9^o$; $\delta_f = 0^o$.

Figure 25.- Effect of lower horizontal-tail (H.T.) span on longitudinal characteristics of Phase III baseline configuration. Trim thrust.

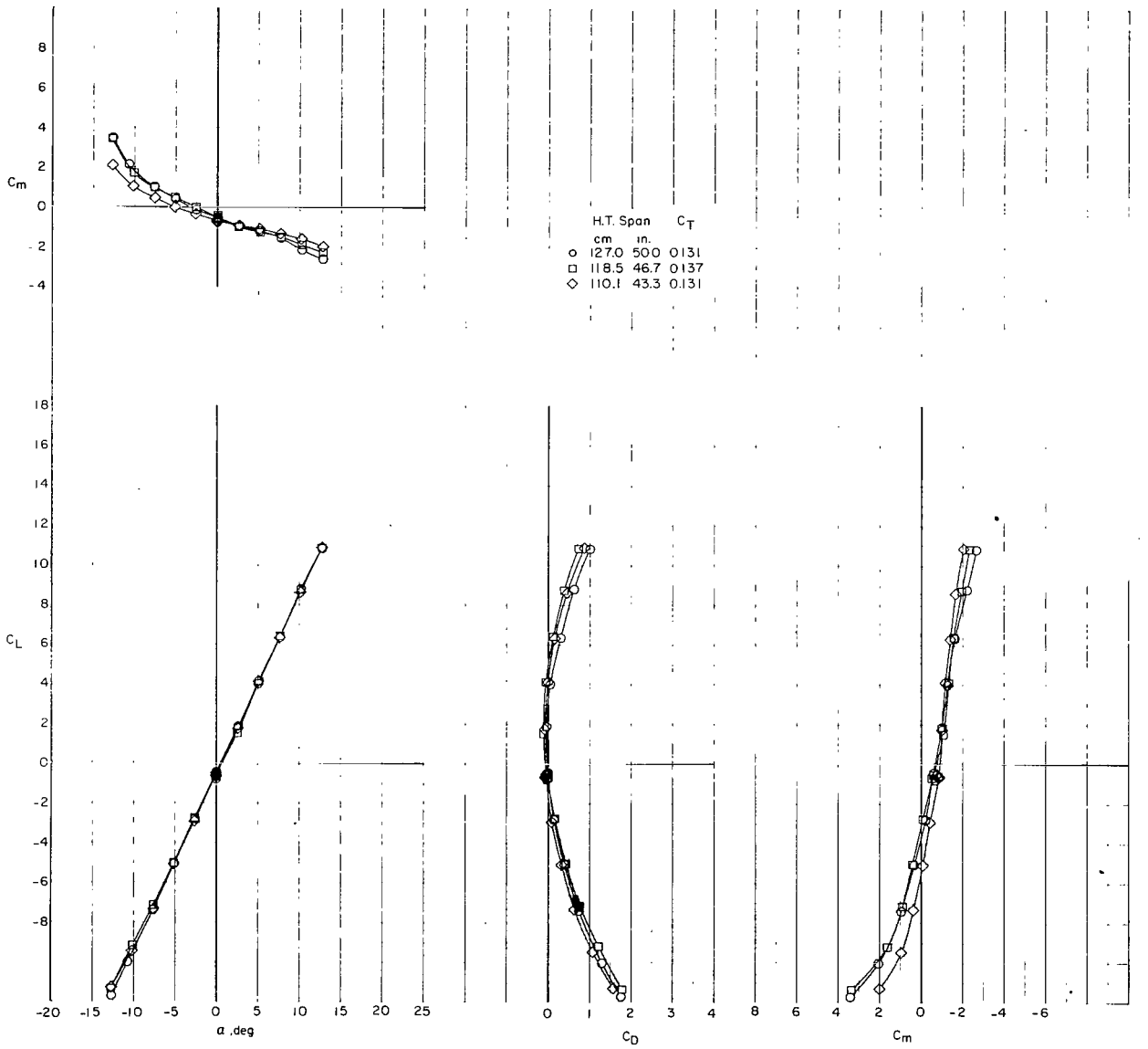

(b) $i_w = -4.5^o$; $\delta_f = 0^o$.

Figure 25.- Continued.

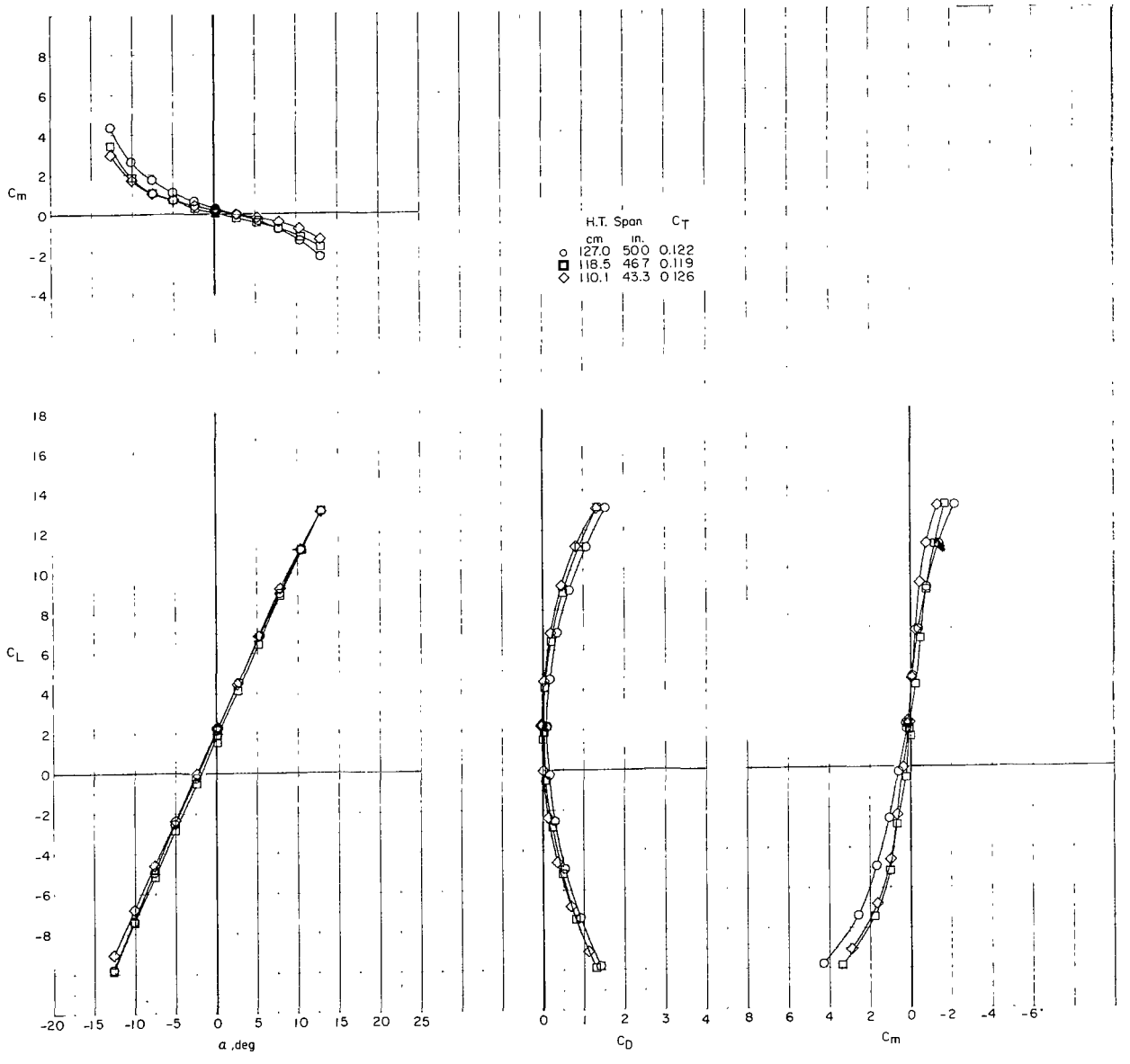

(c) $i_w = 0^o$; $\delta_f = 0^o$.

Figure 25.- Continued.

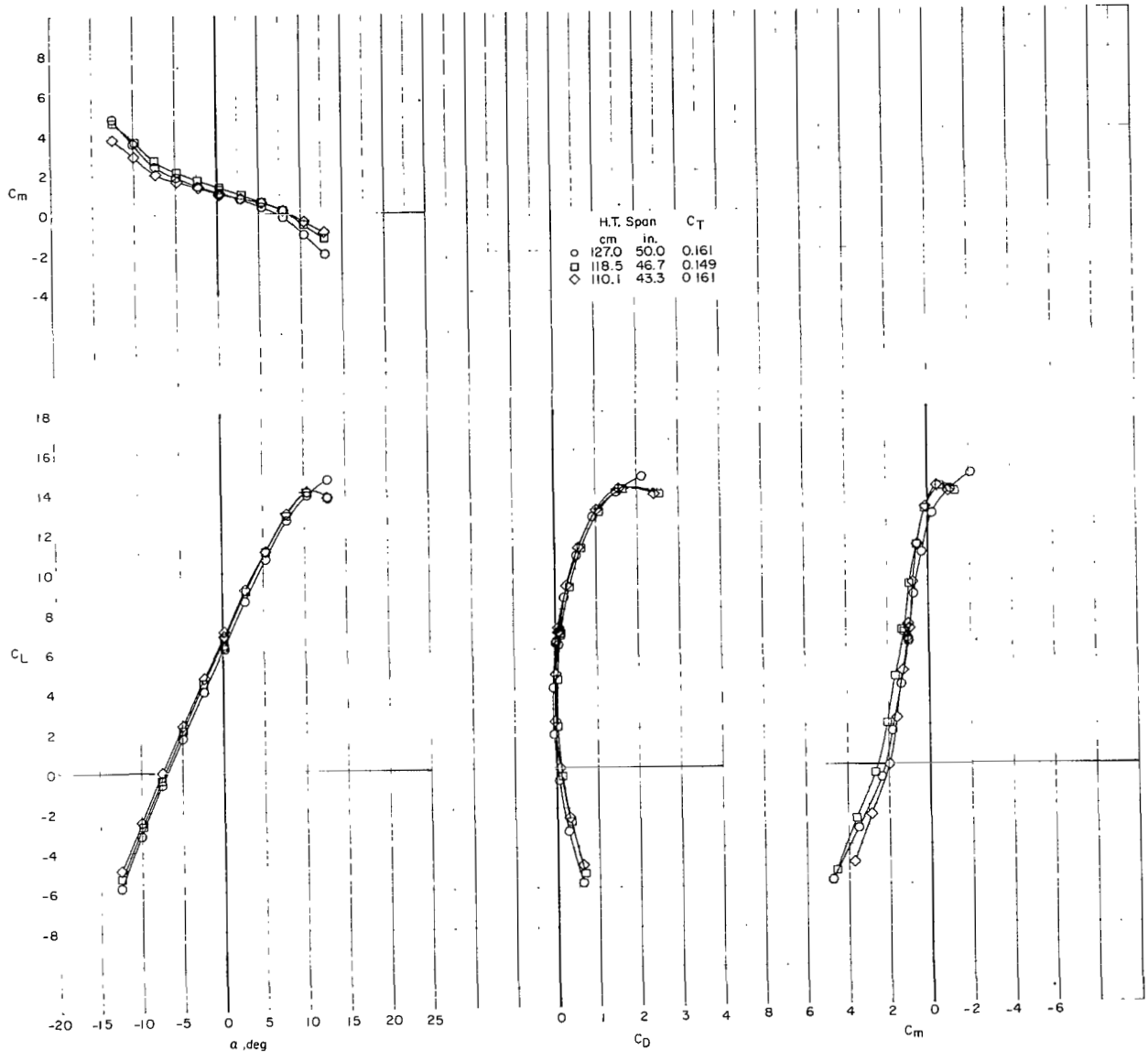

(d) $i_w = 7.5^o$; $\delta_f = 0^o$.

Figure 25.- Continued.

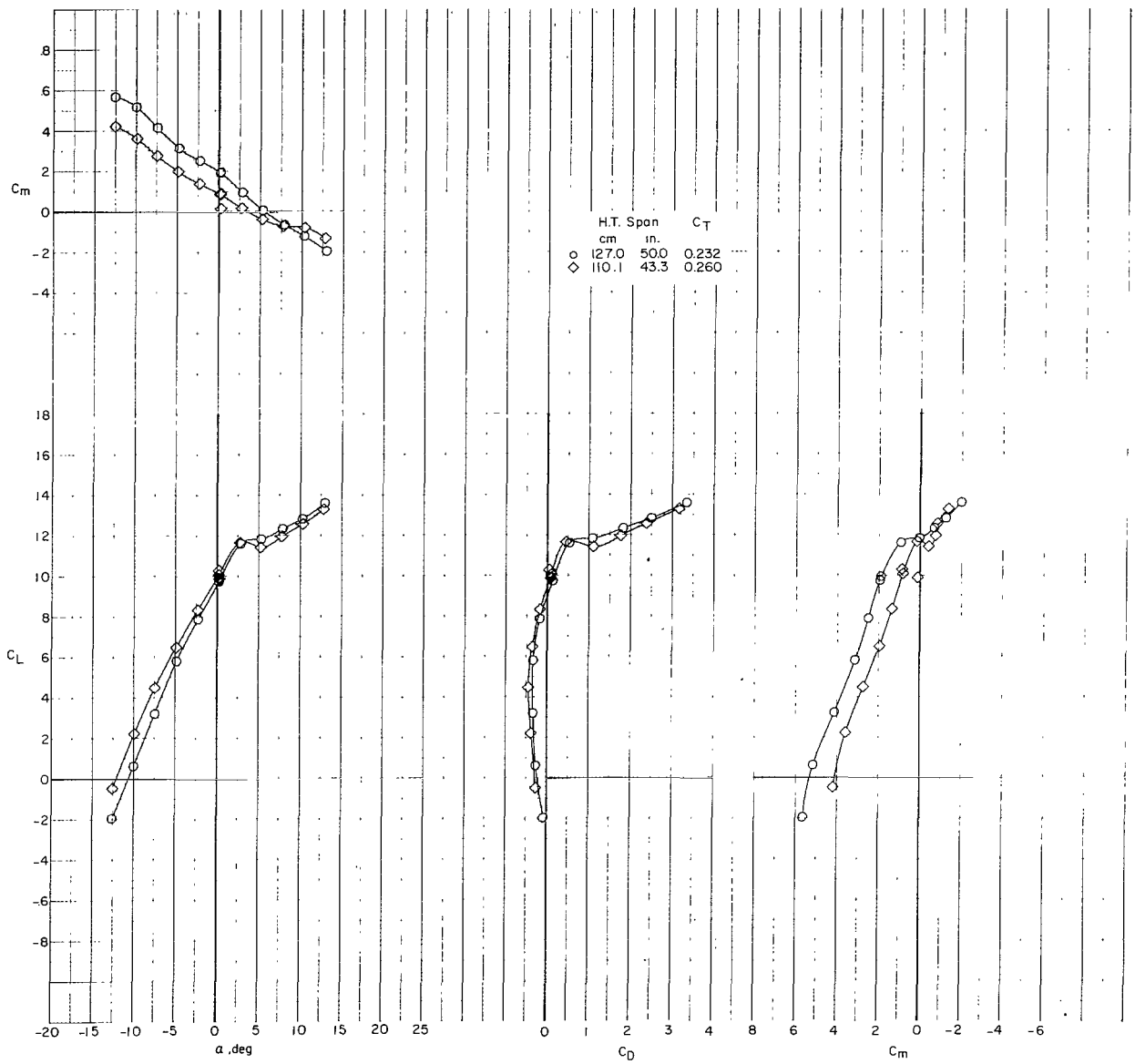

(e) $i_w = 15^o$; $\delta_f = 0^o$.

Figure 25.- Continued.

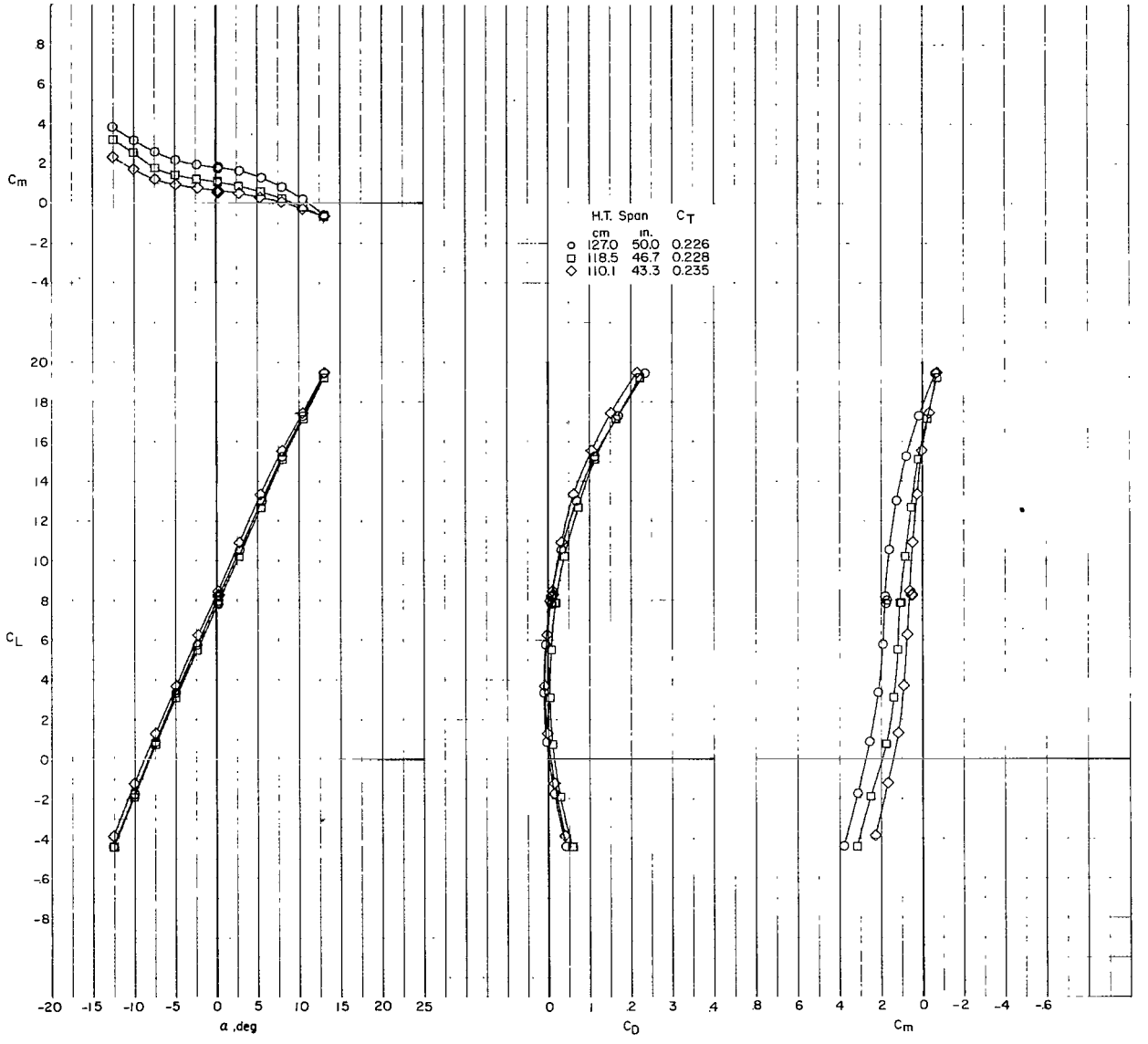

(f) $i_w = 0^o$; $\delta_f = 30^o$.

Figure 25.- Continued.

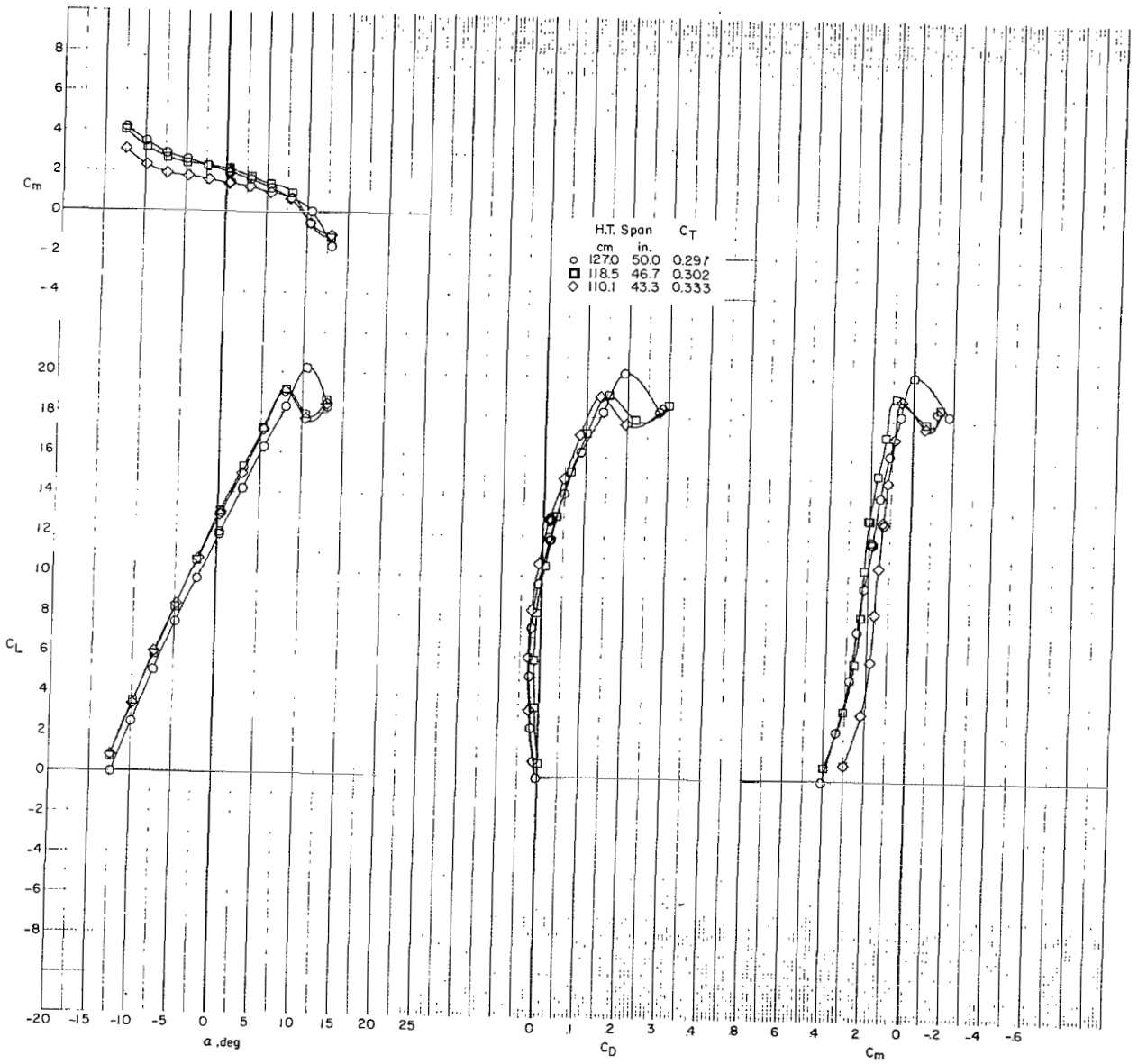

(g) $i_w = 7.5^o$; $\delta_f = 30^o$.

Figure 25.- Concluded.

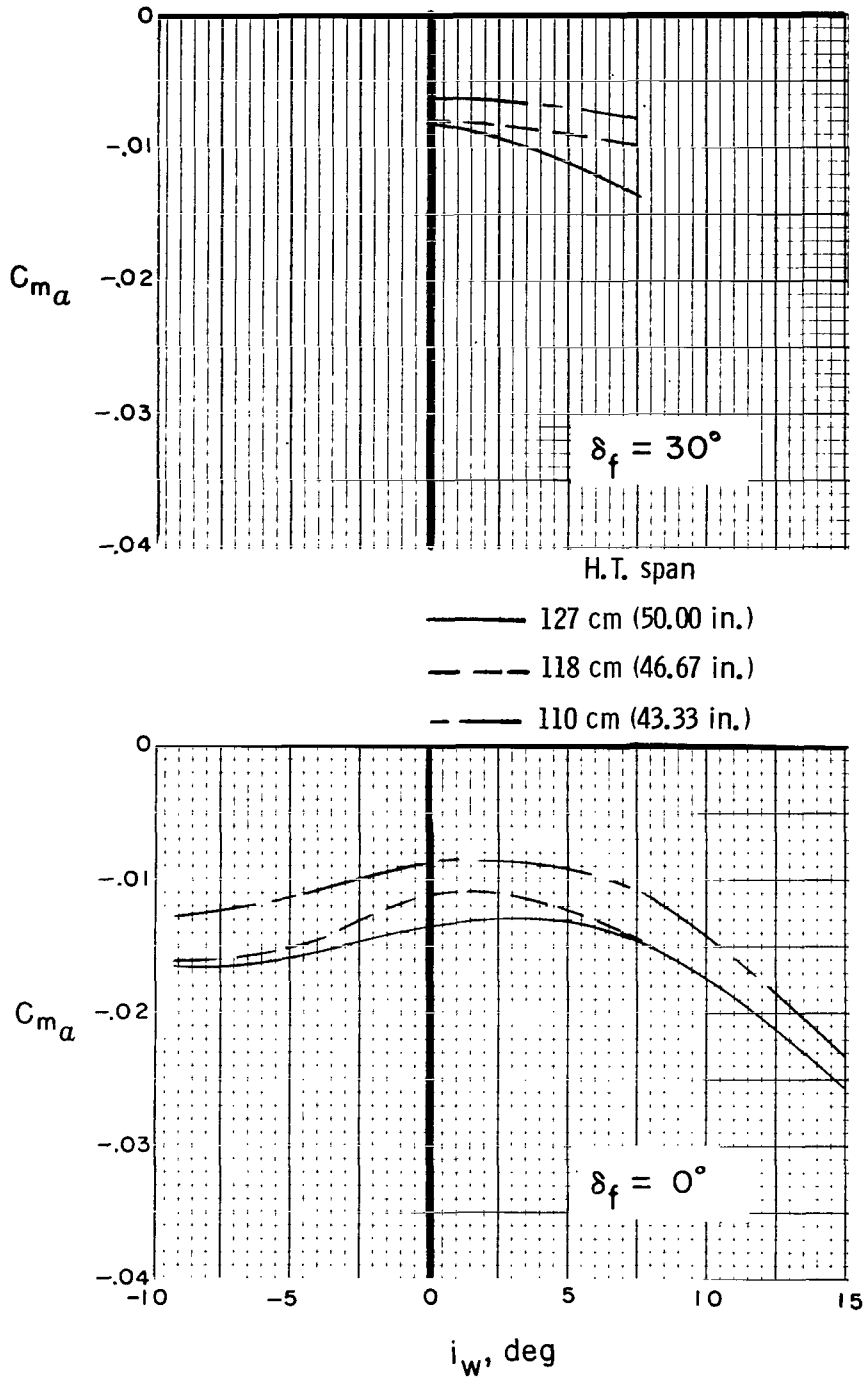

Figure 26.- Effect of lower horizontal-tail span on C_{m_α} for Phase III baseline configuration. Trim thrust.

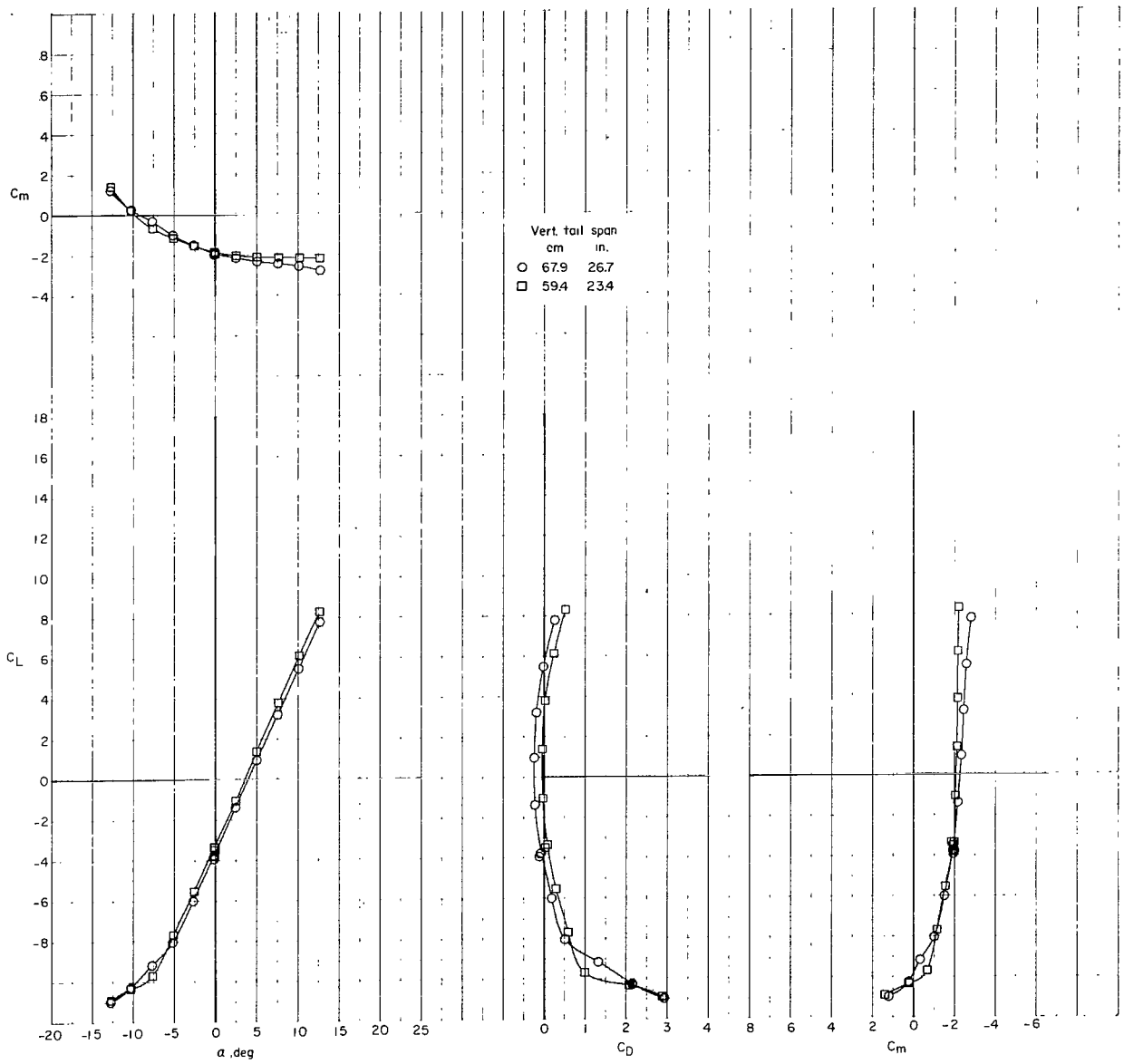

(a) $i_w = -9^o$; $\delta_f = 0^o$.

Figure 27.- Effect of vertical-tail span on longitudinal characteristics of Phase III baseline configuration with 118-cm (46.67-in.) span lower tail C. Trim thrust.

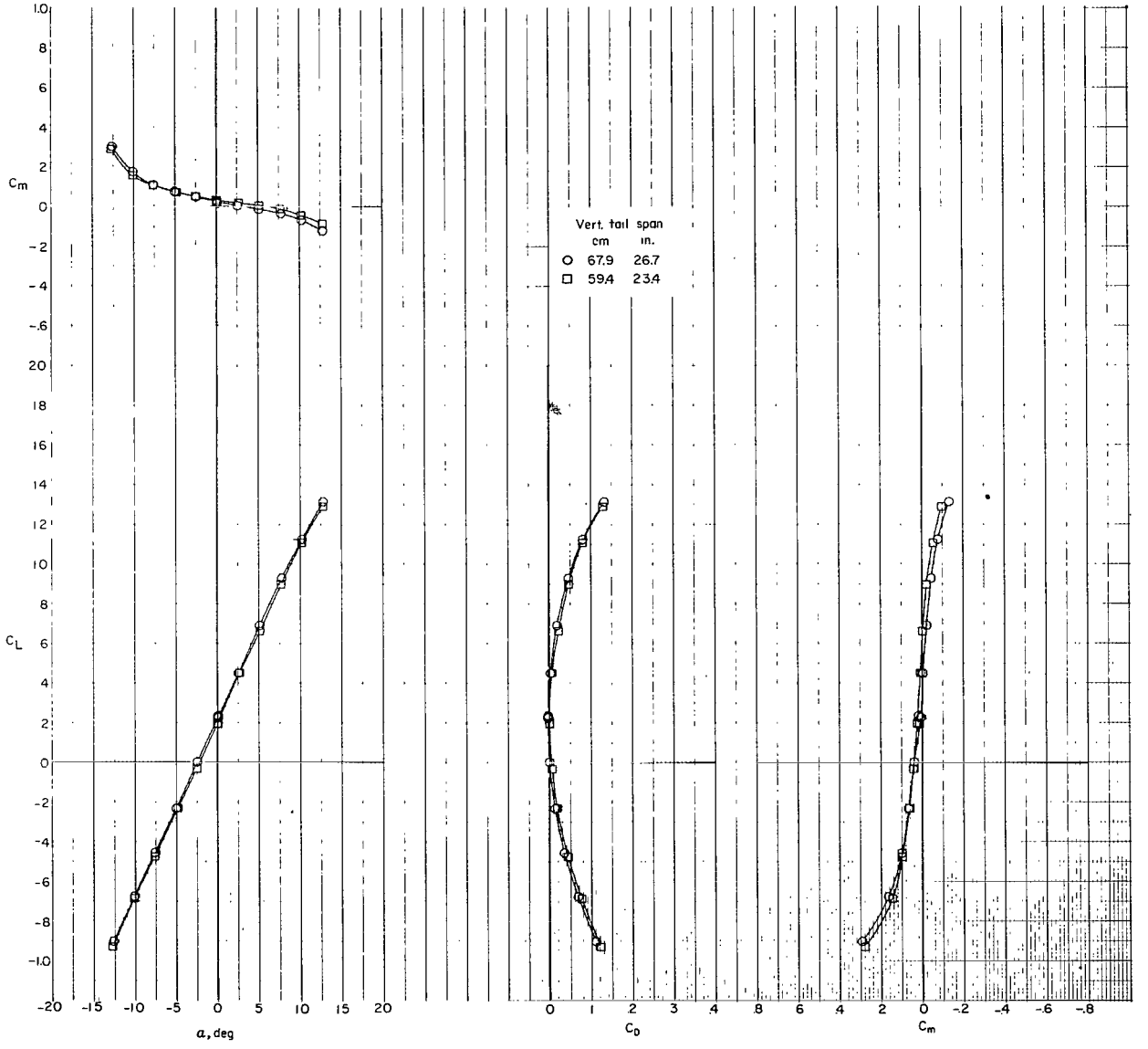

(b) $i_w = 0^o$; $\delta_f = 0^o$.

Figure 27.- Continued.

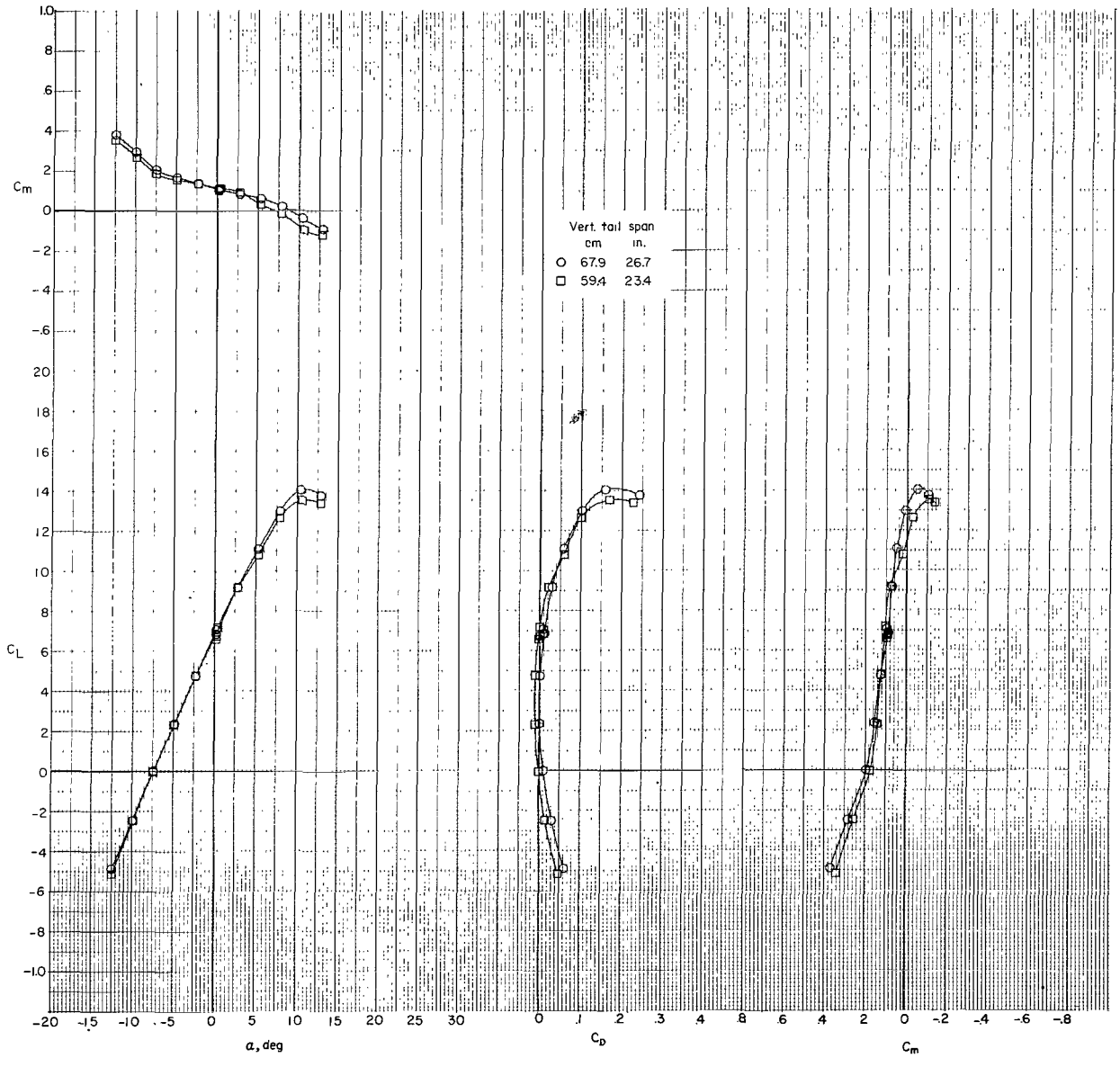

(c) $i_w = 7.5^o$; $\delta_f = 0^o$.

Figure 27.- Continued.

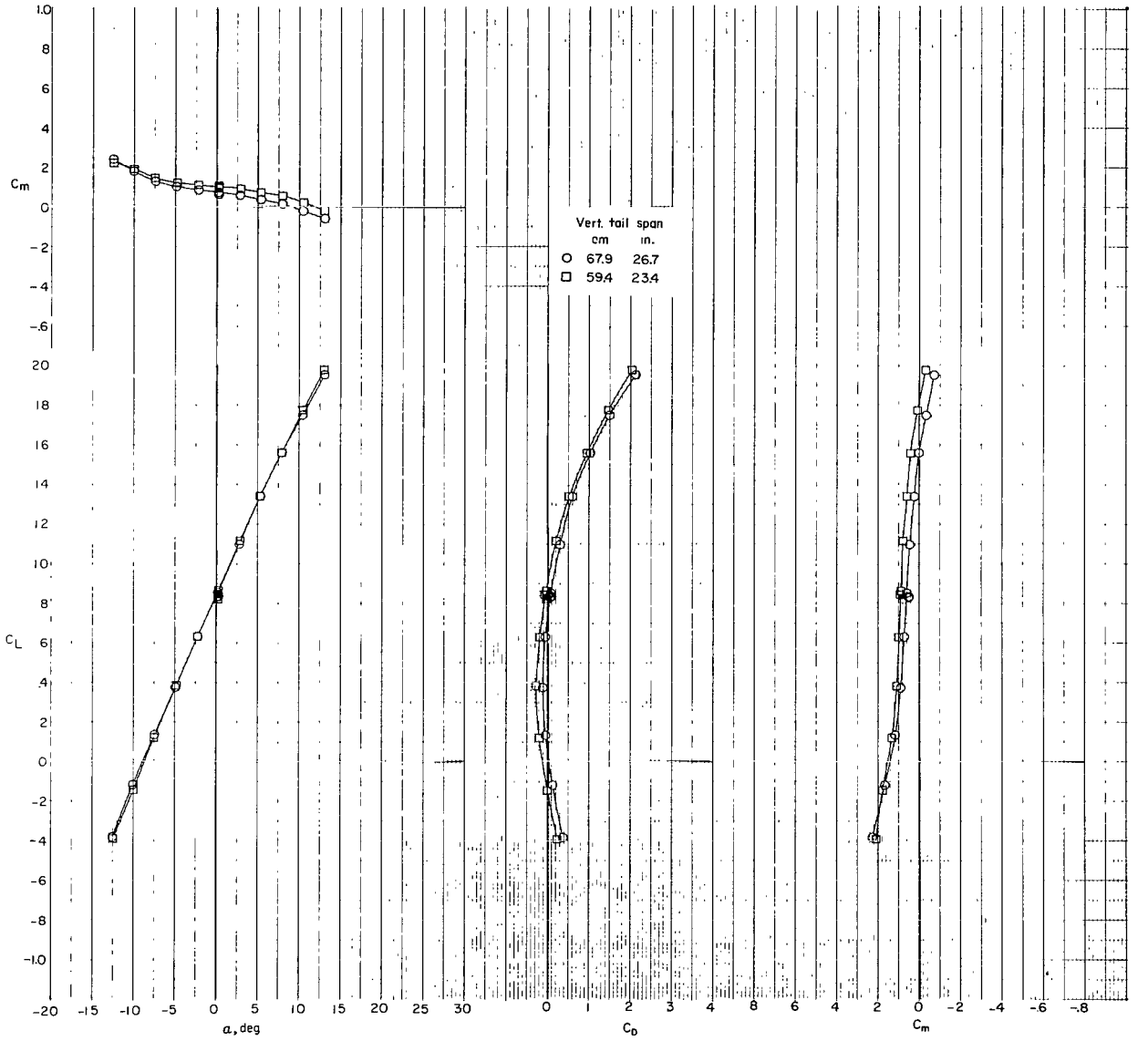

(d) $i_w = 0^o$; $\delta_f = 30^o$.

Figure 27.- Continued.

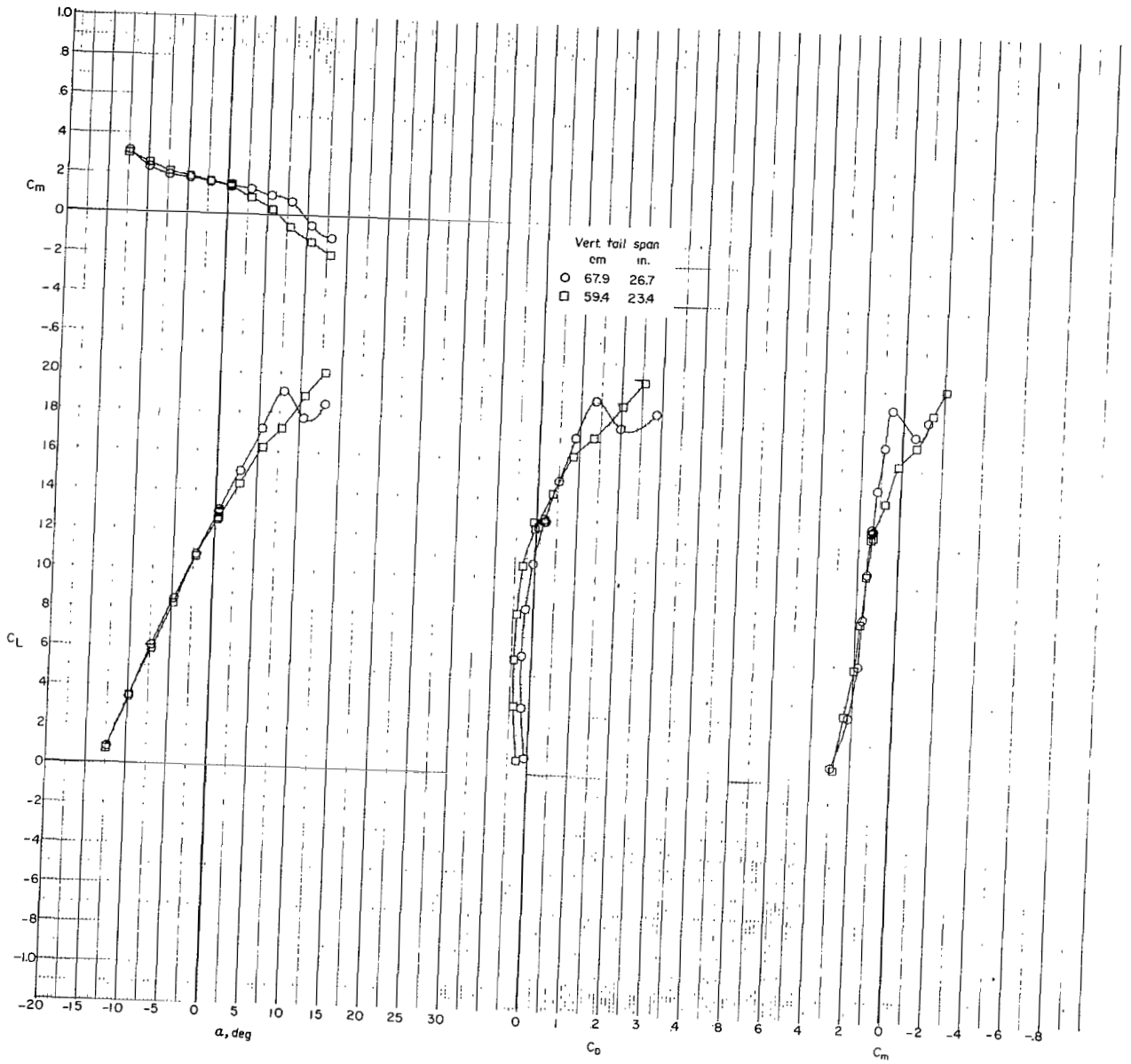

(e) $i_w = 7.5^o$; $\delta_f = 30^o$.

Figure 27.- Continued.

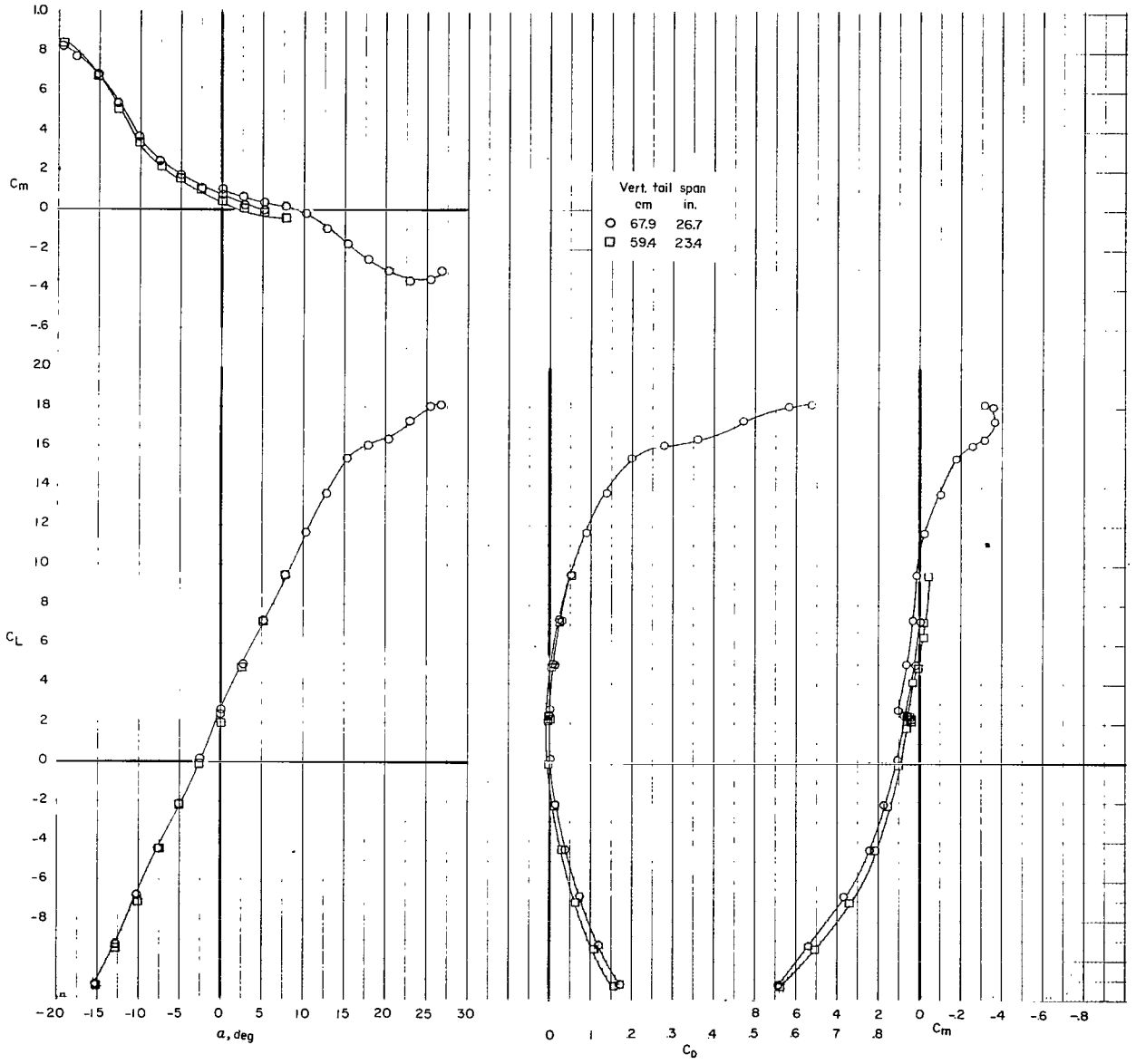

(f) $i_w = 0^o$; $\delta_f = 0^o$.

Figure 27.- Concluded.

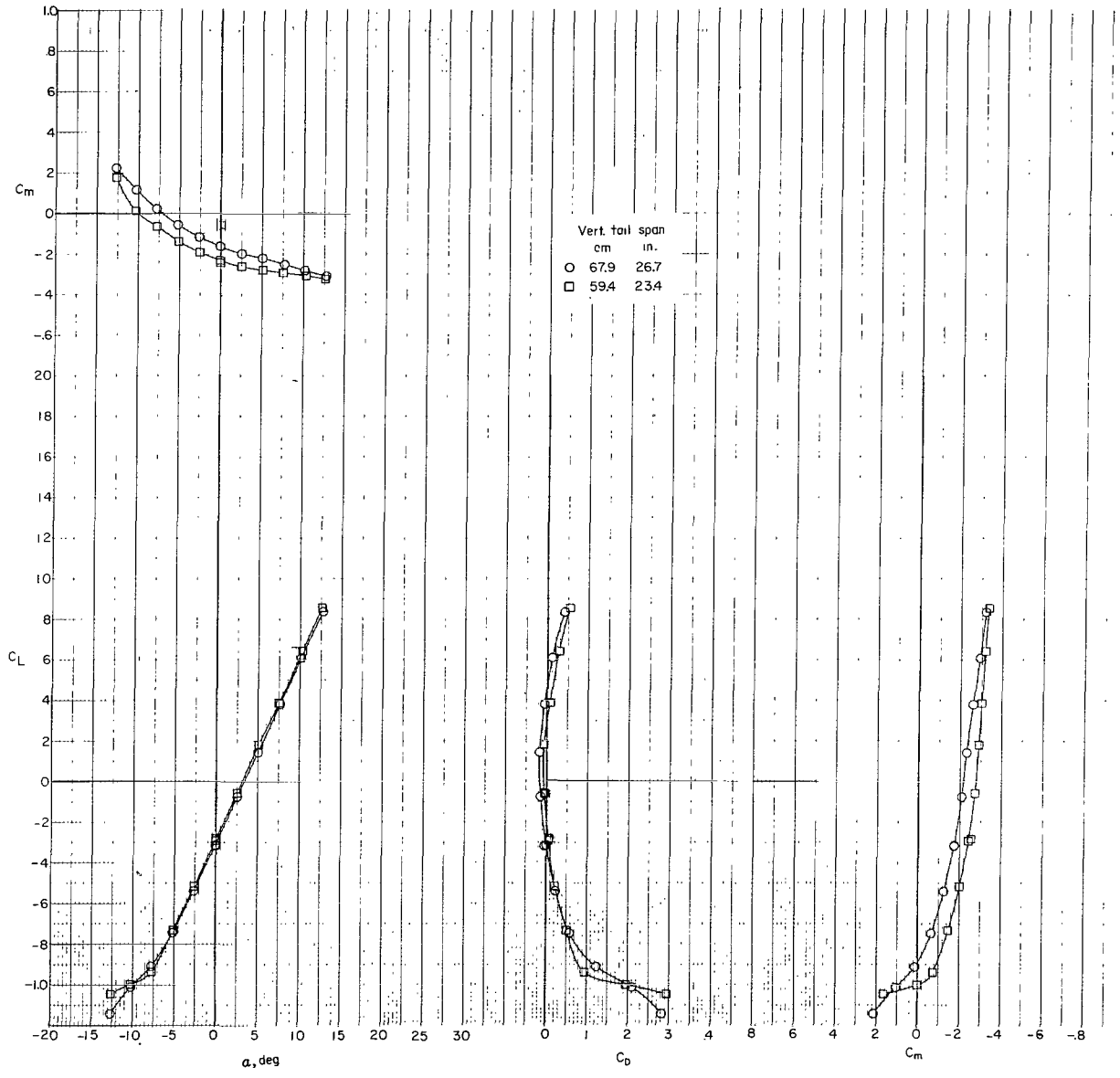

(a) $i_w = -9^o$; $\delta_f = 0^o$.

Figure 28.- Effect of vertical-tail span on longitudinal characteristics of Phase III baseline configuration with 110-cm (43.33-in.) span lower tail C. Trim thrust.

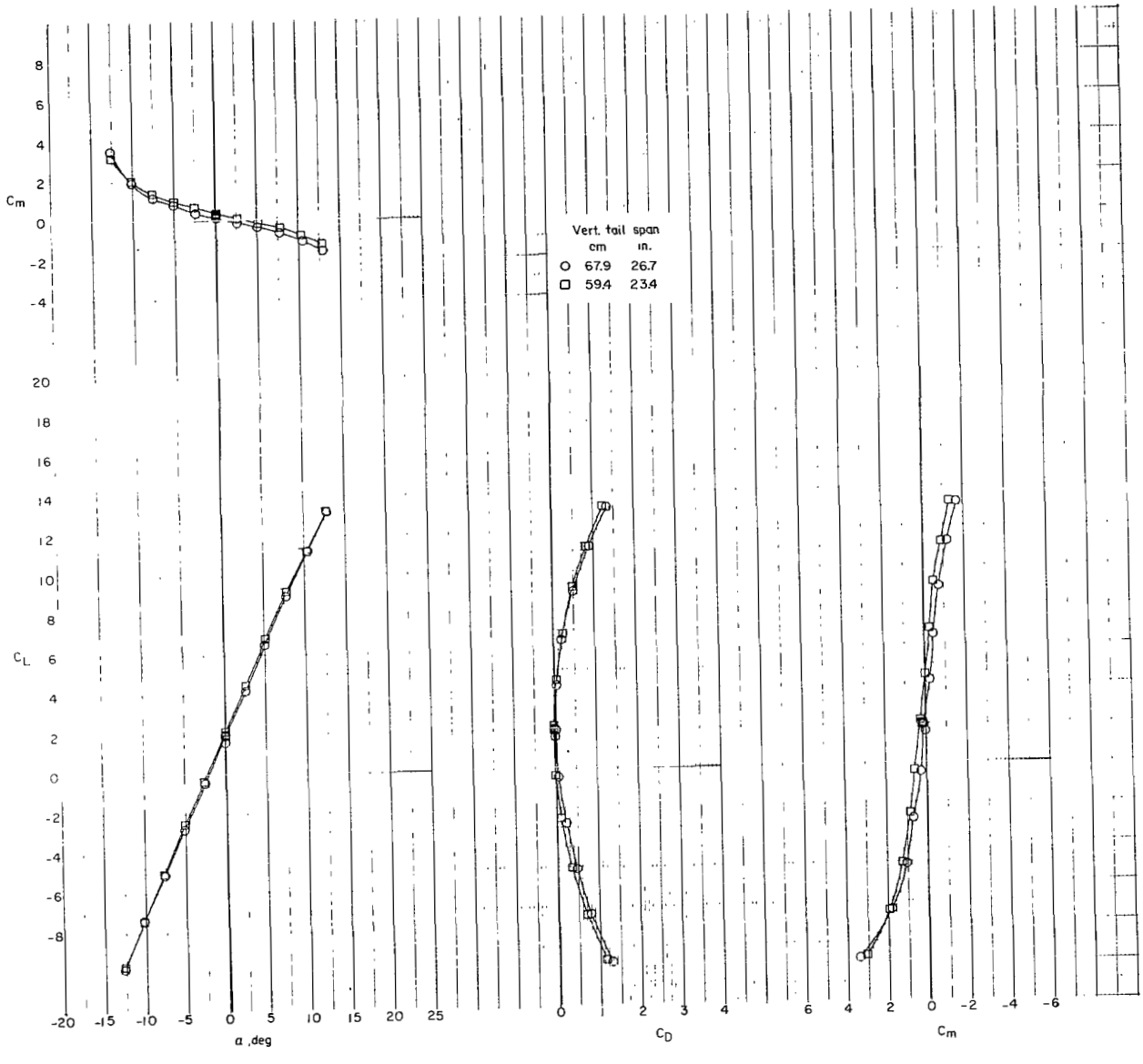

(b) $i_w = 0^o$; $\delta_f = 0^o$.

Figure 28.- Continued.

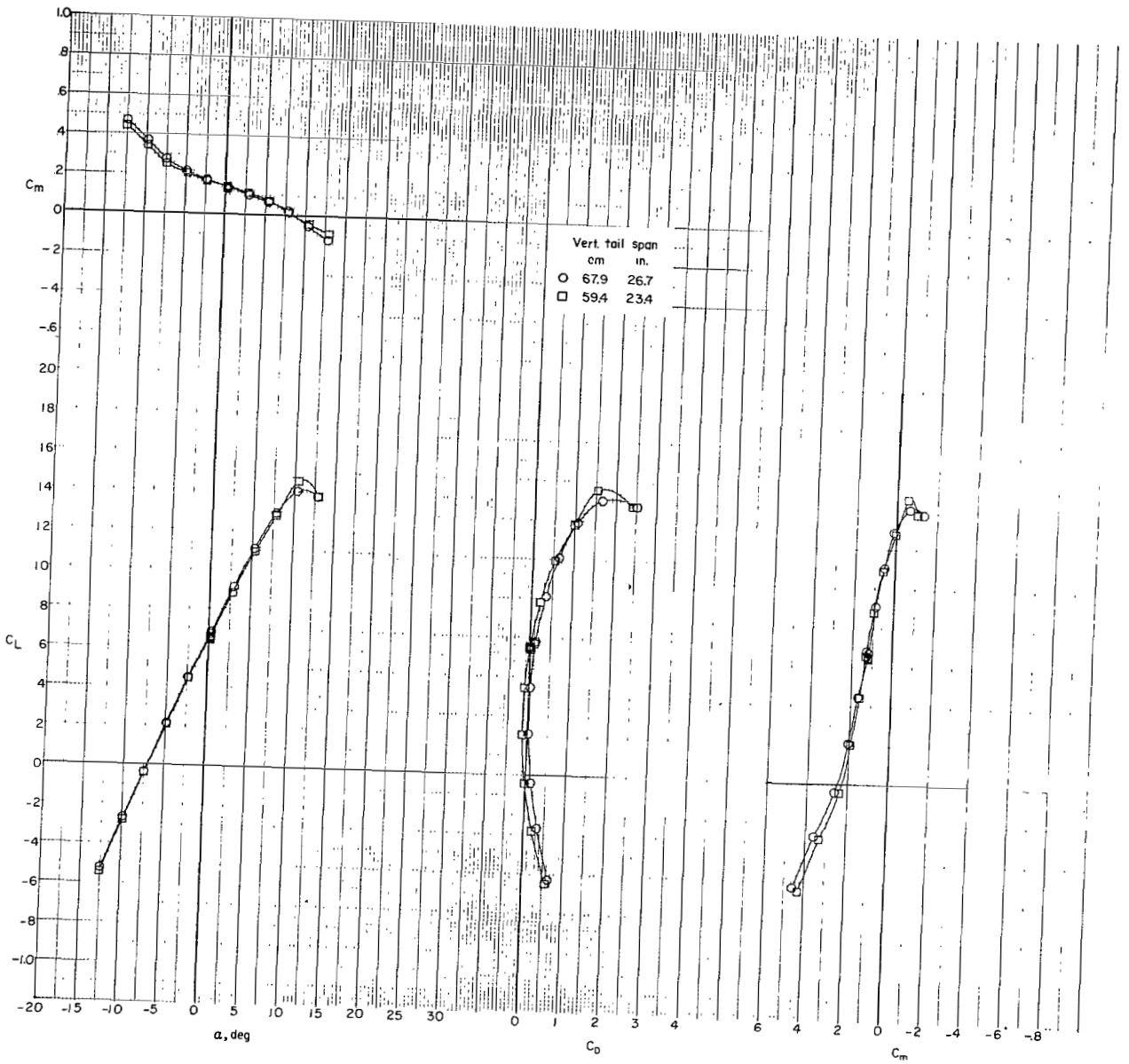

(c) $i_w = 7.5^o$; $\delta_f = 0^o$.

Figure 28.- Continued.

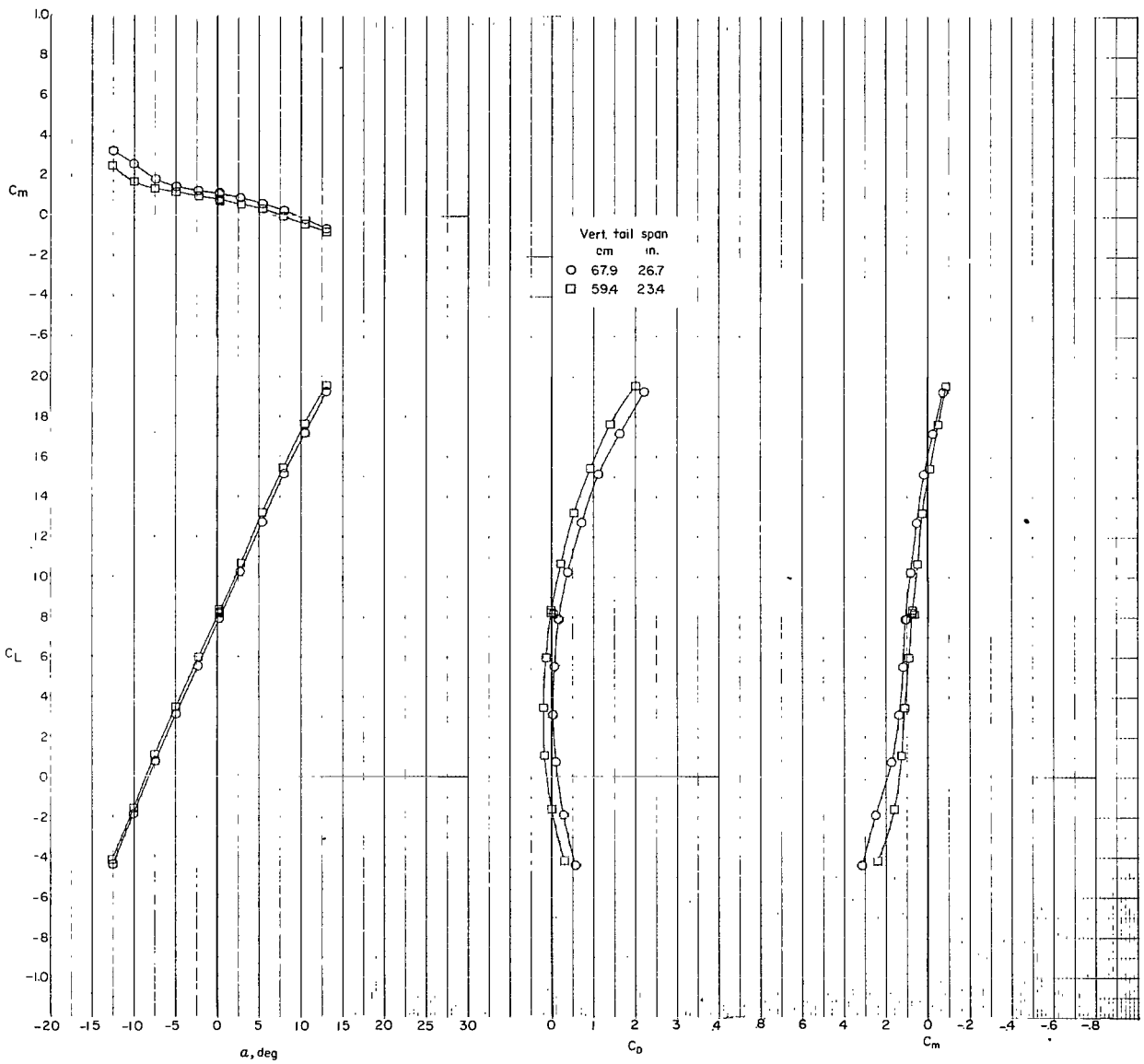

(d) $i_w = 0^o$; $\delta_f = 30^o$.

Figure 28.- Continued.

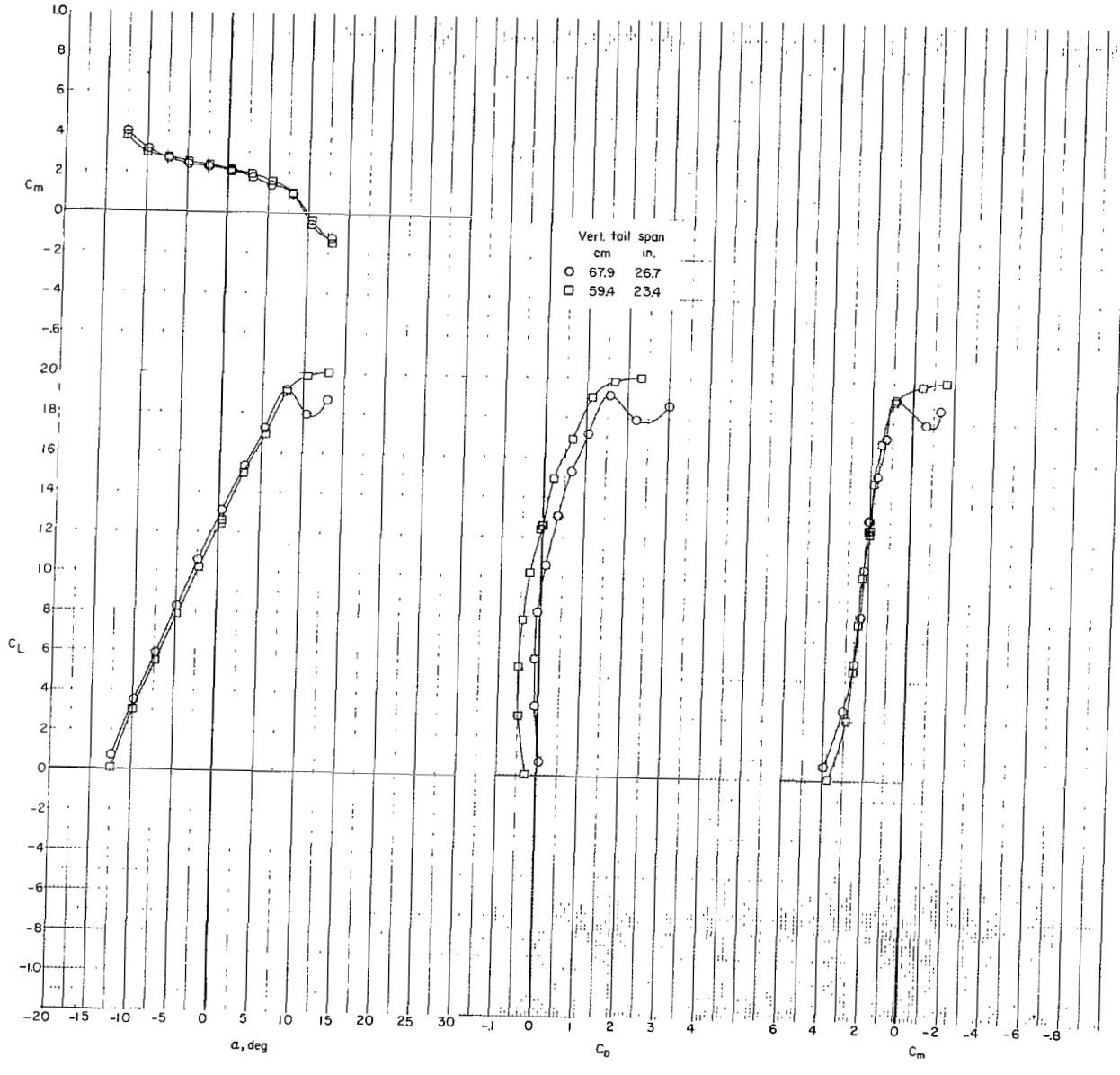

(e) $i_w = 7.5^o$; $\delta_f = 30^o$.

Figure 28.- Concluded.

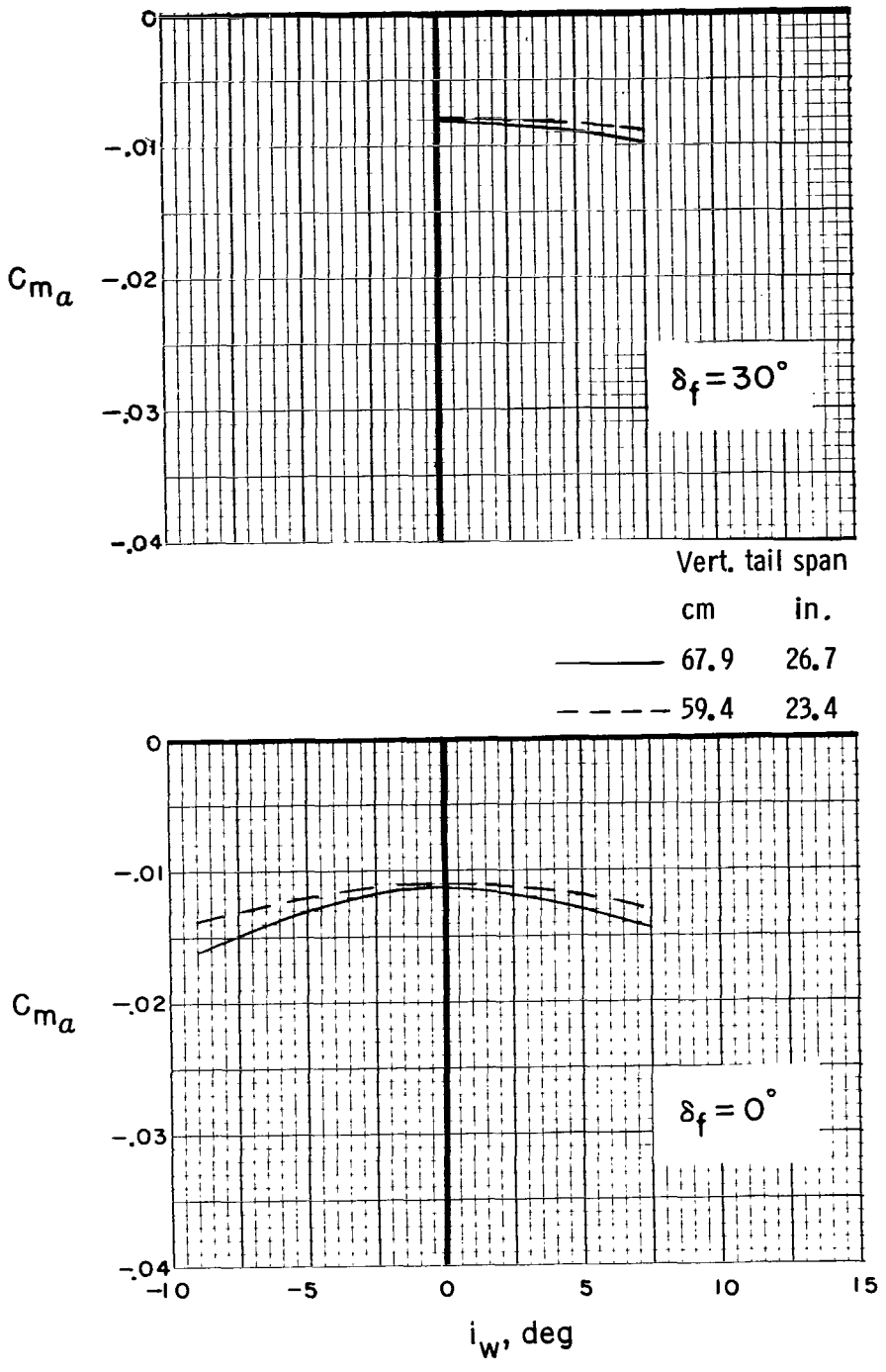

(a) 118-cm (46.67-in.) lower tail C.

Figure 29.- Effect of vertical-tail span on C_{m_α} for Phase III baseline configuration with two reduced-span lower tails C. $i_t = 0^o$.

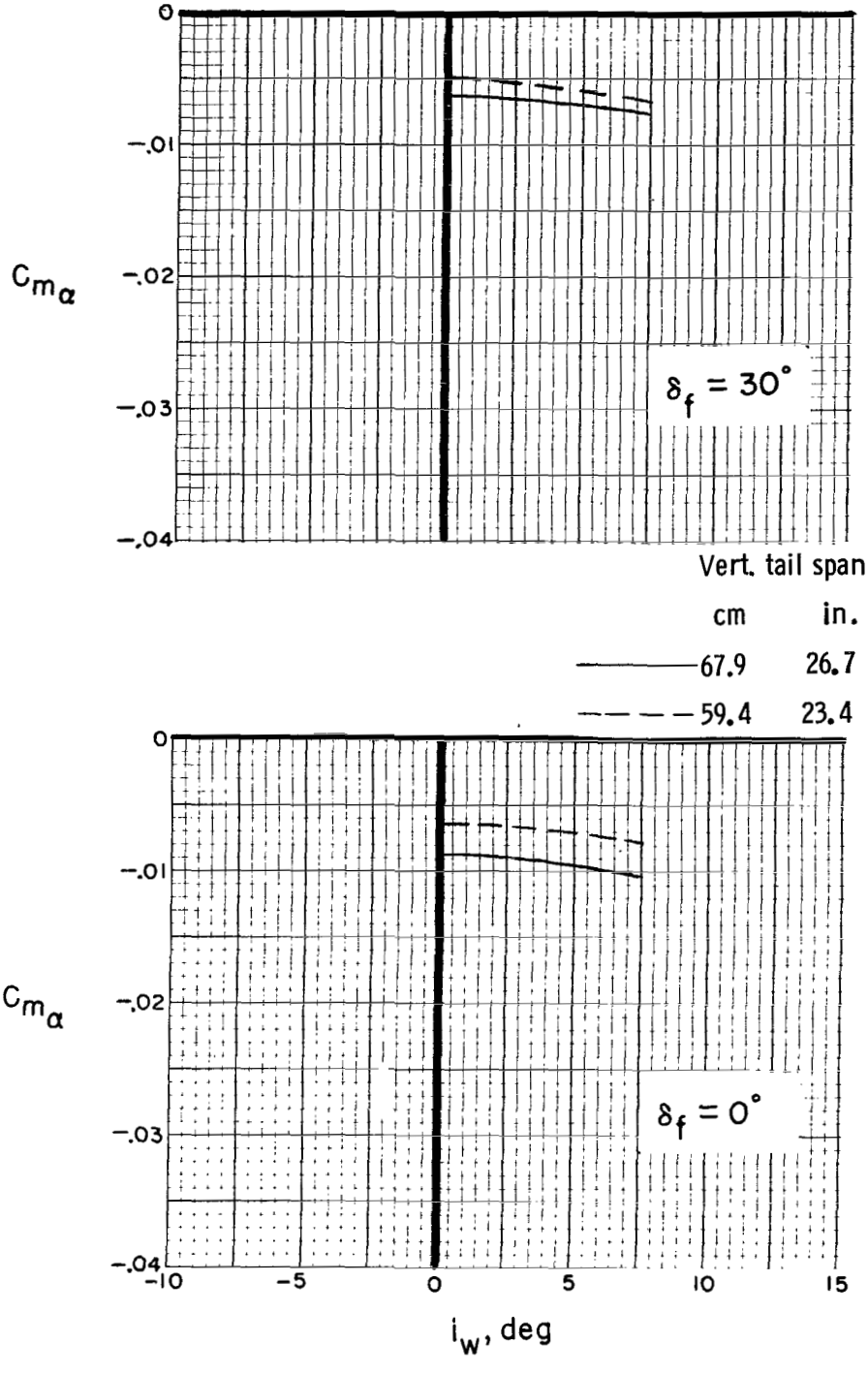

(b) 110-cm (43.33-in.) lower tail C.

Figure 29.- Concluded.

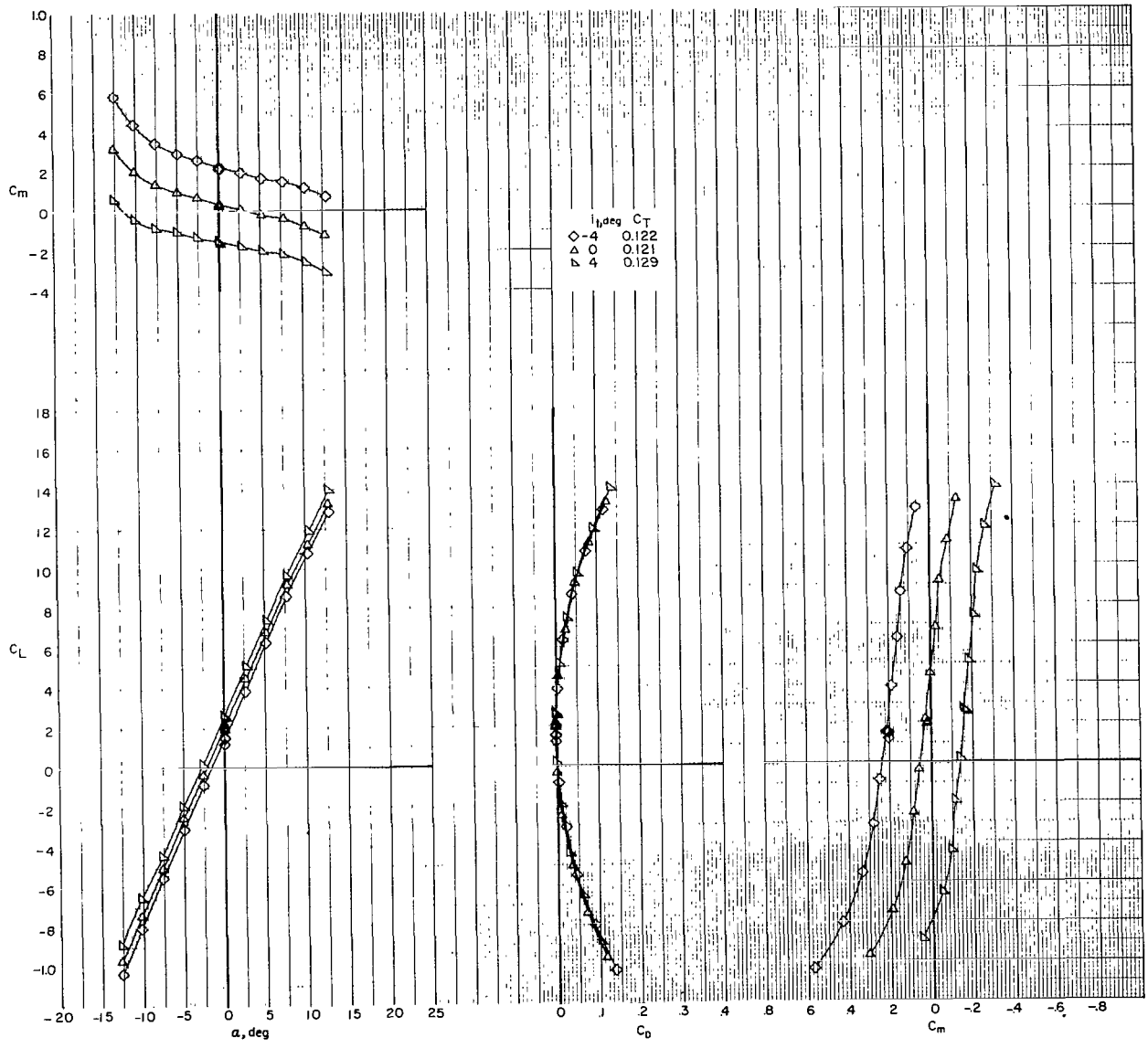

(a) 118-cm (46.67-in.) span lower tail C.

Figure 30.- Effect of i_t on longitudinal characteristics of Phase III baseline configuration with two reduced-span lower tails C. Trim thrust; $\delta_f = 0^o$.

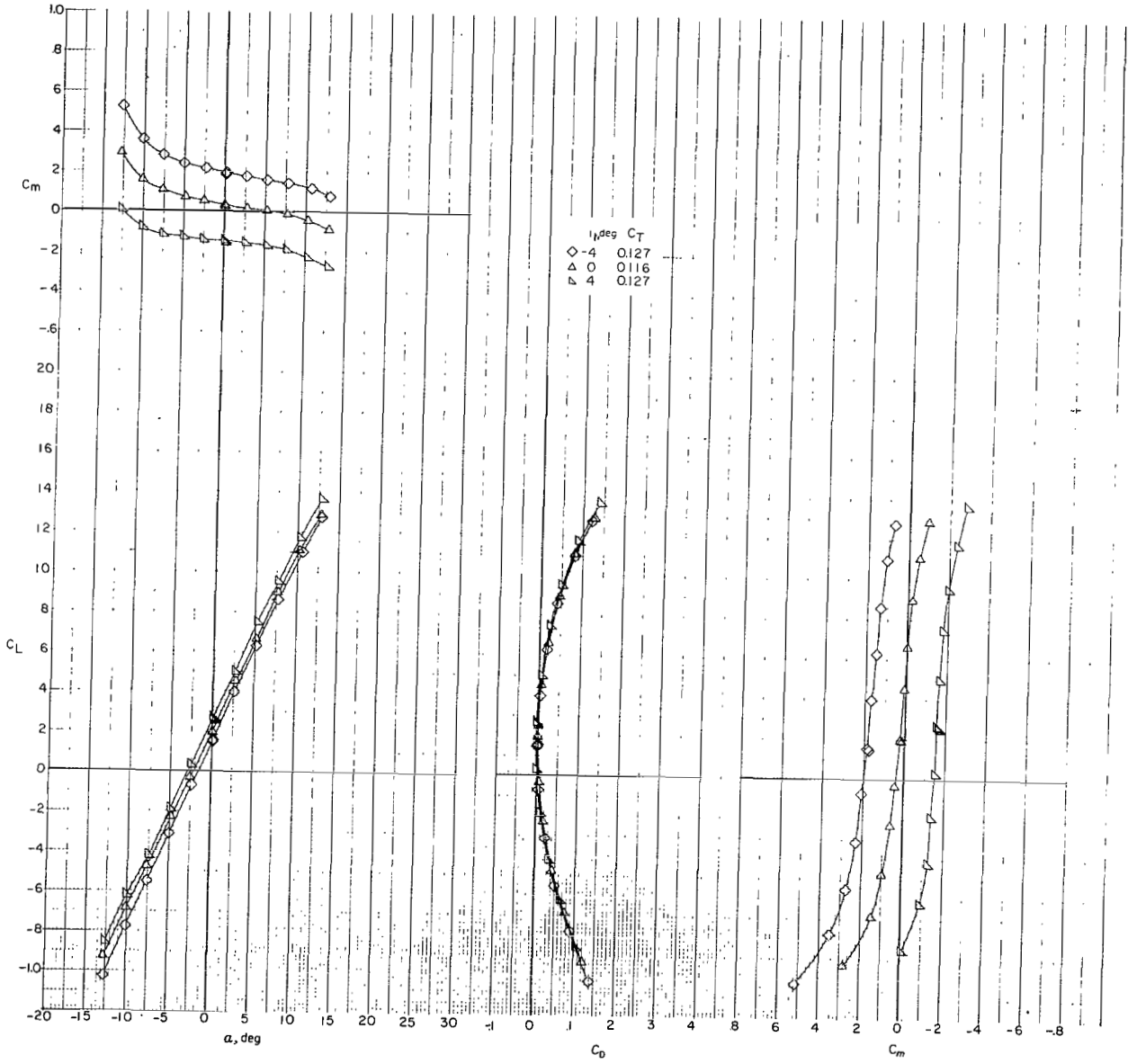

(b) 110-cm (43.33-in.) span lower tail C.

Figure 30.- Concluded.

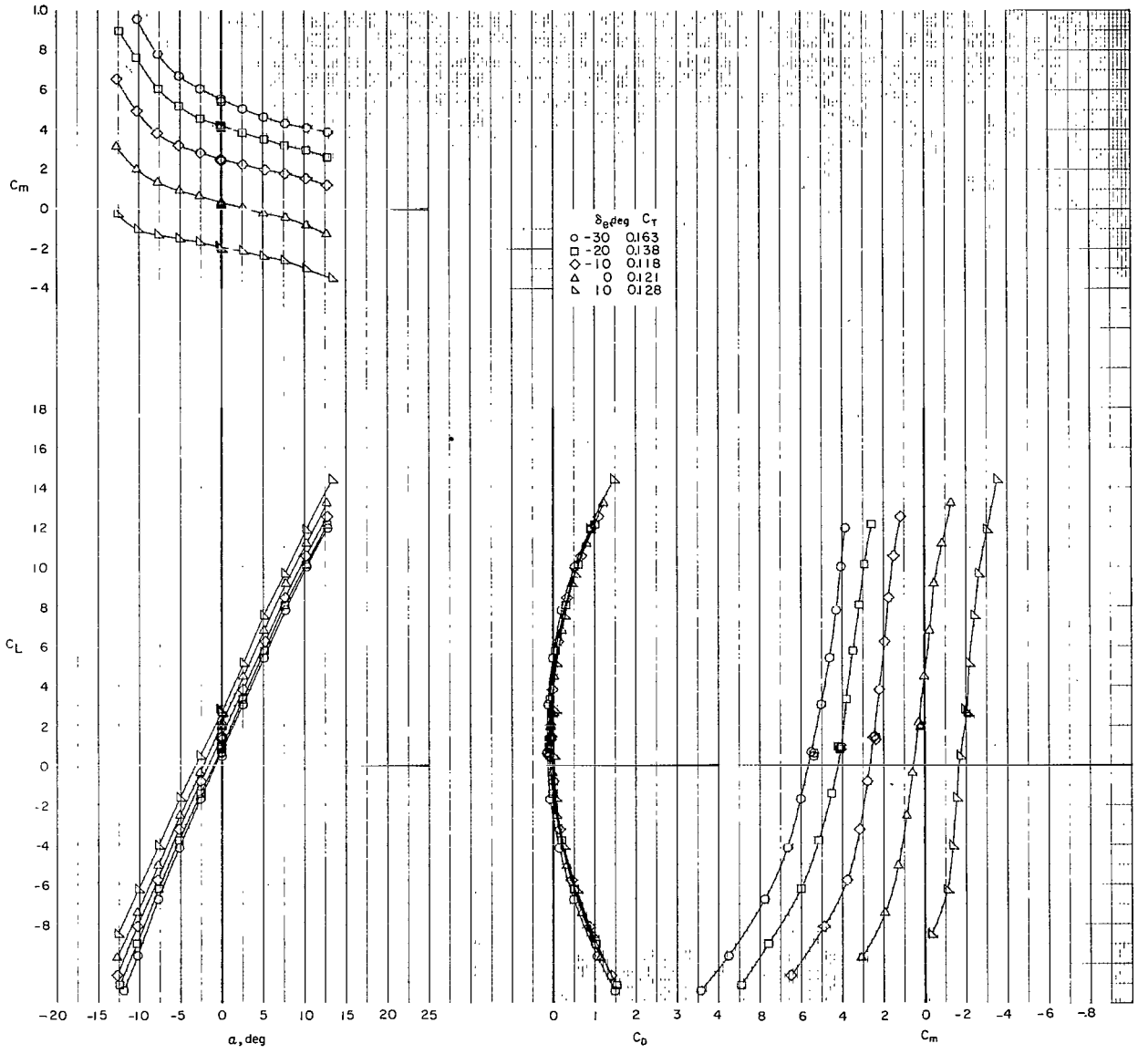

(a) 118-cm (46.67-in.) span lower tail C.

Figure 31.- Effect of δ_e on longitudinal characteristics of Phase III baseline configuration with reduced-span lower tail C and reduced vertical tail. Trim thrust; $\delta_f = 0^o$.

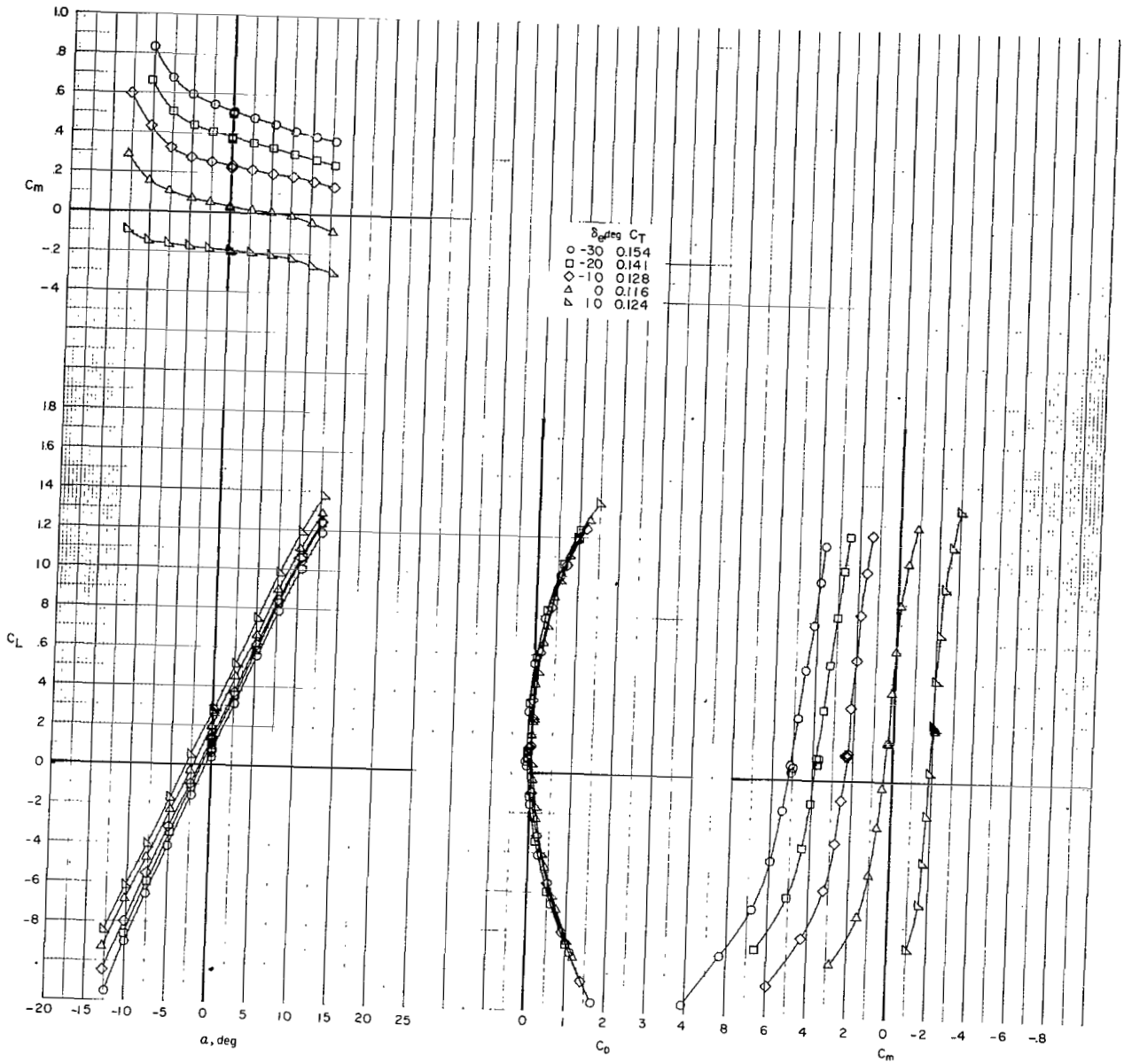

(b) 110-cm (43.33-in.) span lower tail C.

Figure 31.- Concluded.

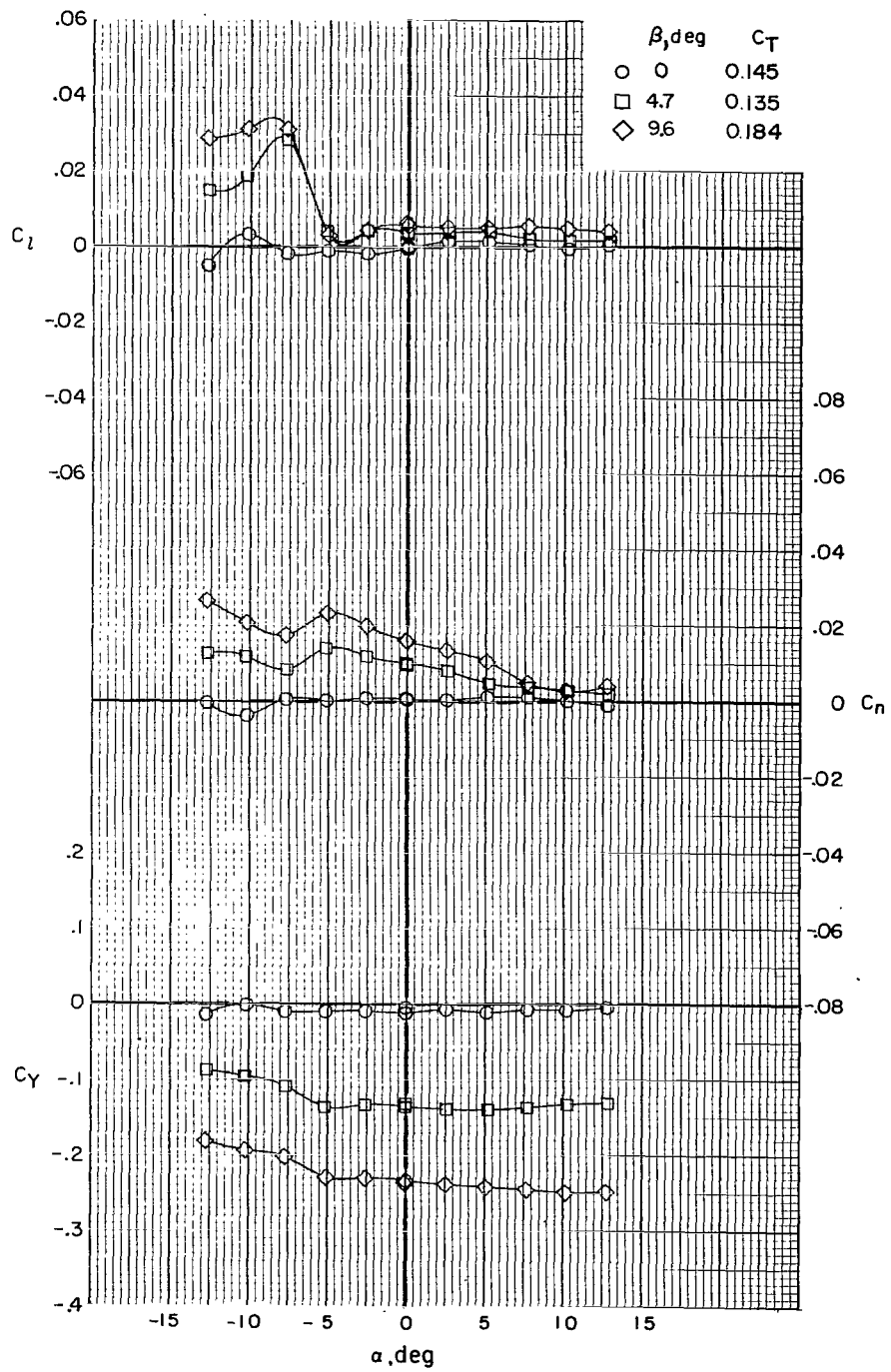

(a) Trim thrust; i_w -9°; $\delta_f = 0°$.

Figure 32.- Effect of β on lateral-directional characteristics of Phase III baseline configuration.

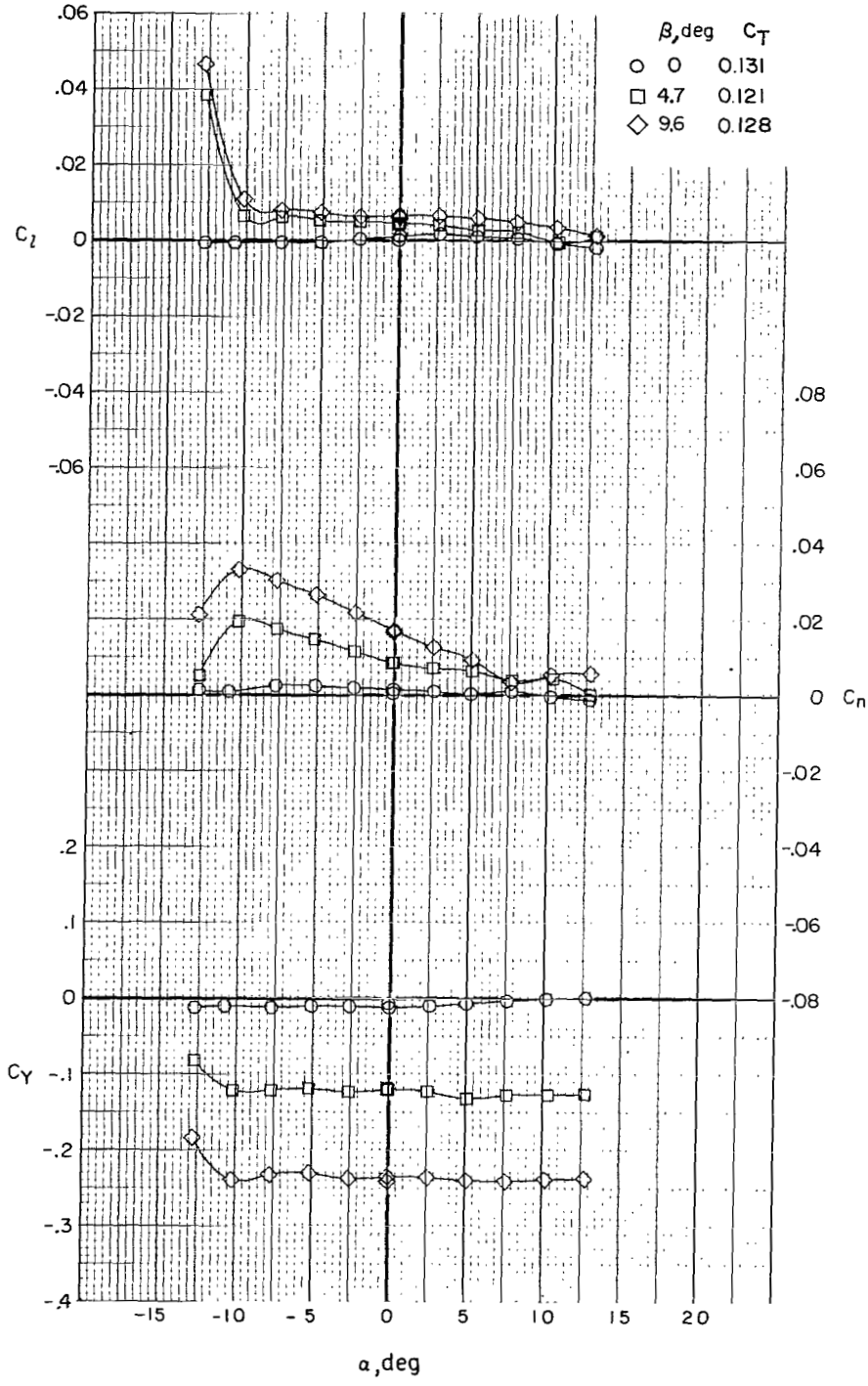

(b) Trim thrust; $i_W = -4.5^o$; $\delta_f = 0^o$.

Figure 32.- Continued.

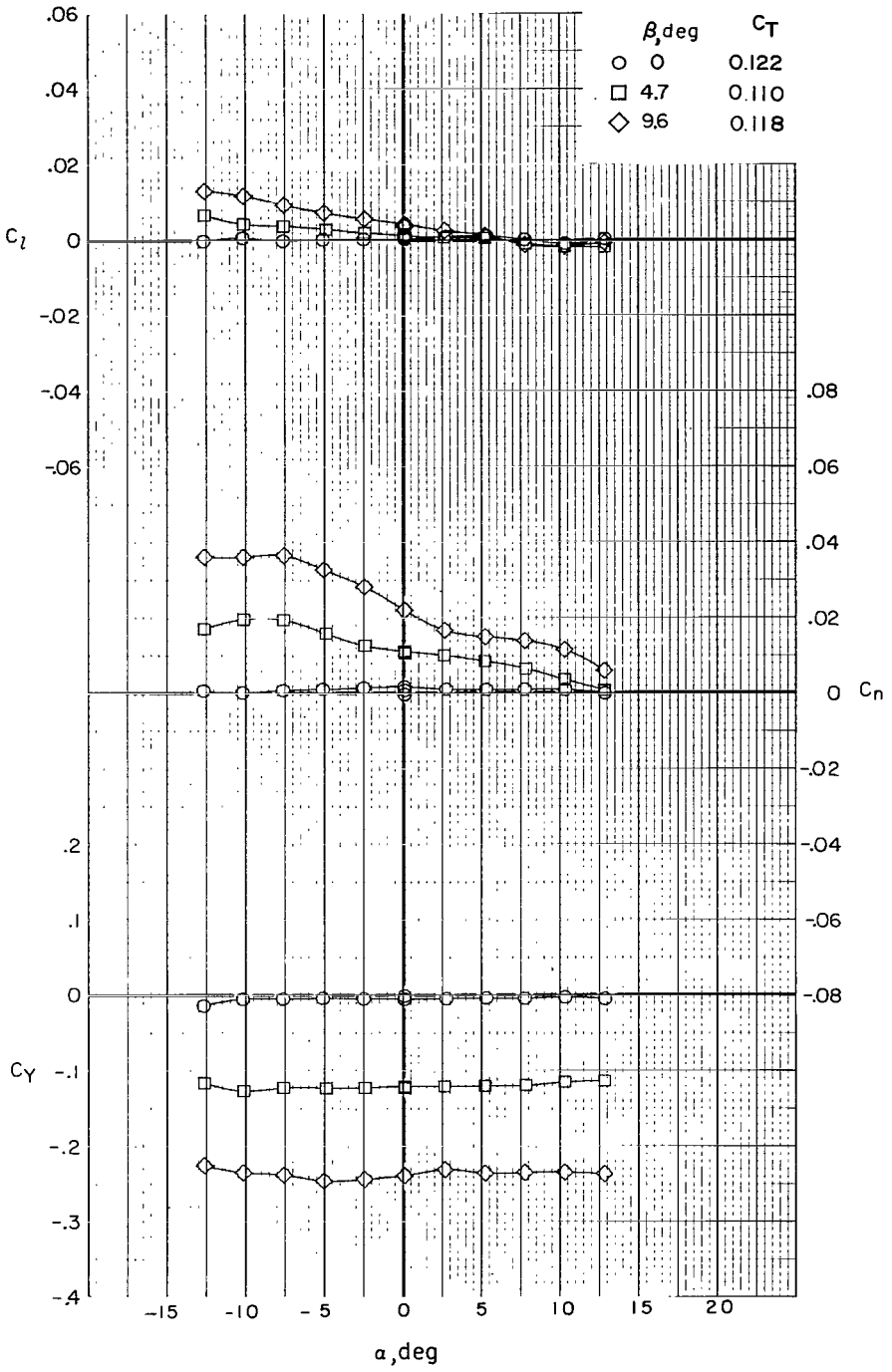

(c) Trim thrust; $i_w = 0^o$; $\delta_f = 0^o$.

Figure 32.- Continued.

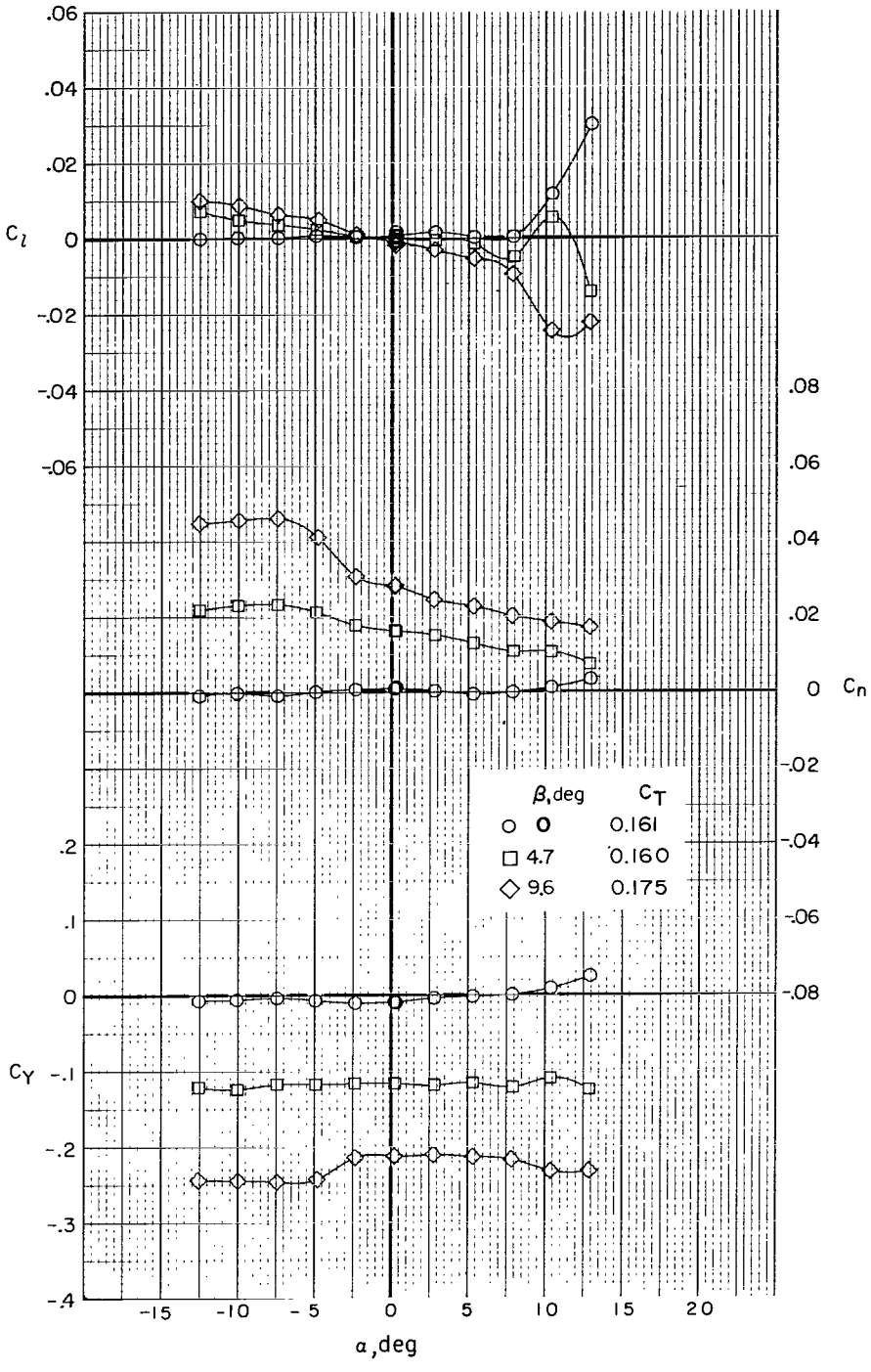

(d) Trim thrust; $i_w = 7.5^o$; $\delta_f = 0^o$.

Figure 32.- Continued.

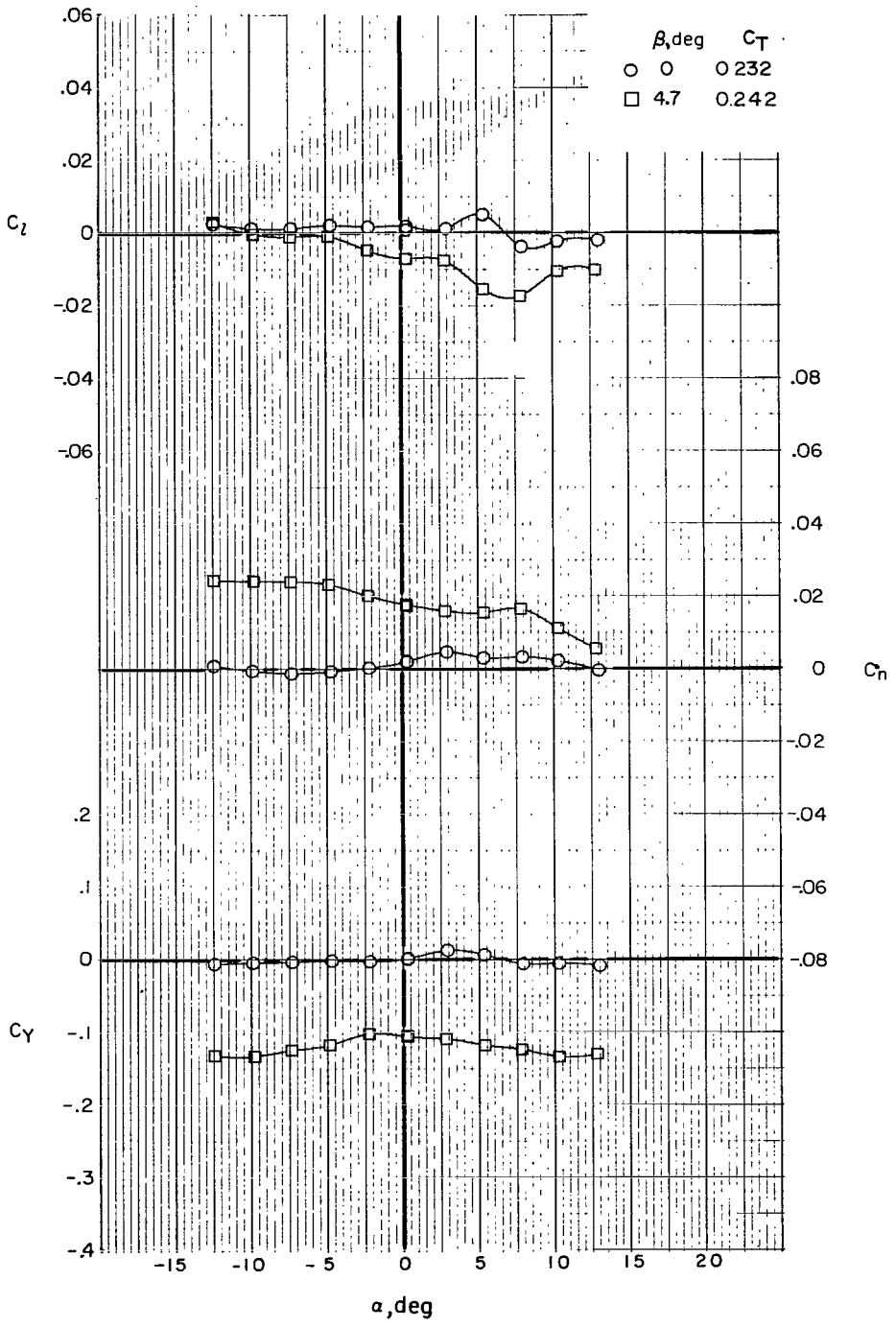

(e) Trim thrust; $i_w = 15^o$; $\delta_f = 0^o$.

Figure 32.- Continued.

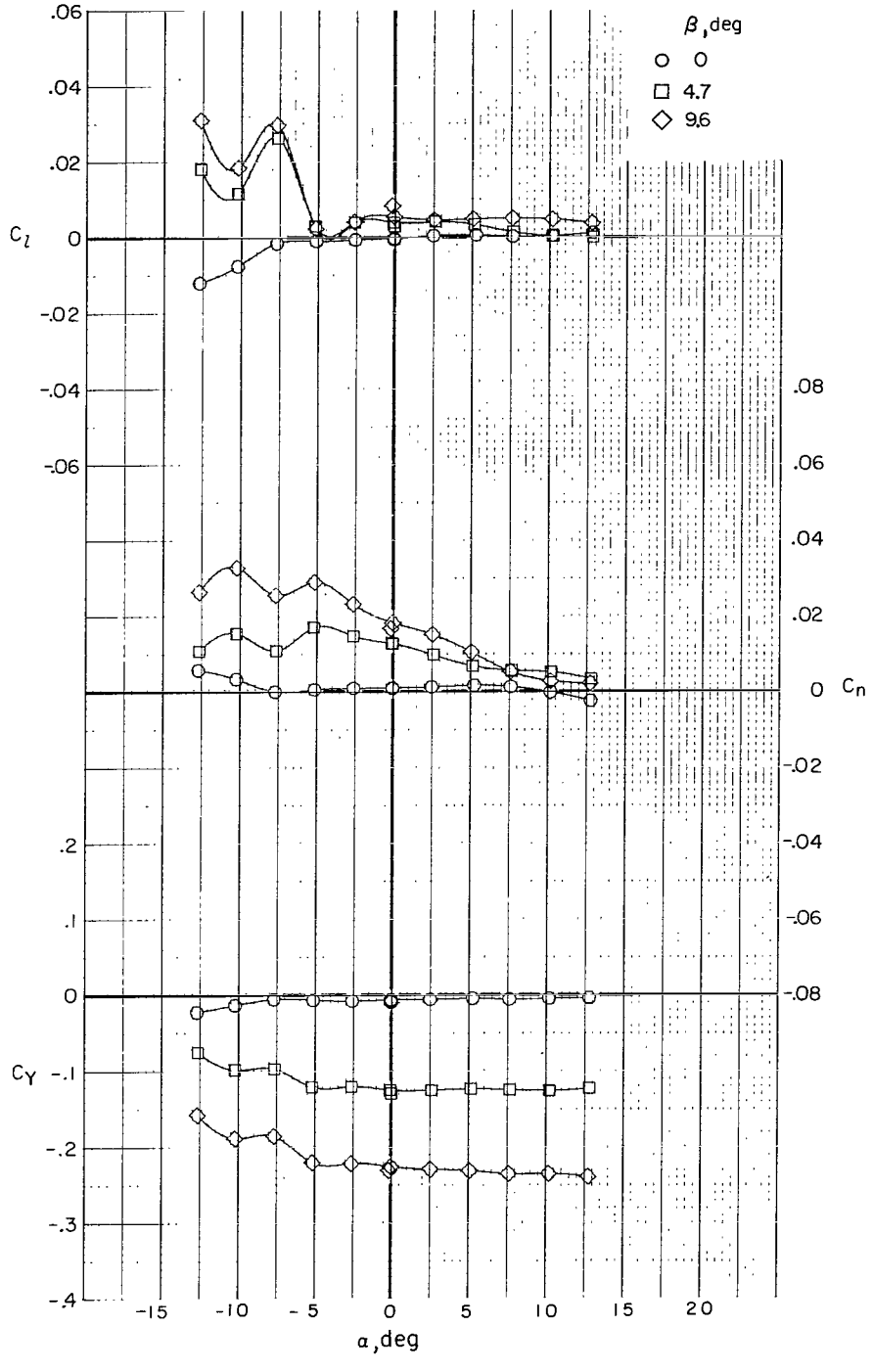

(f) $C_T = 0$; $i_w = -9^o$; $\delta_f = 0^o$.

Figure 32.- Continued.

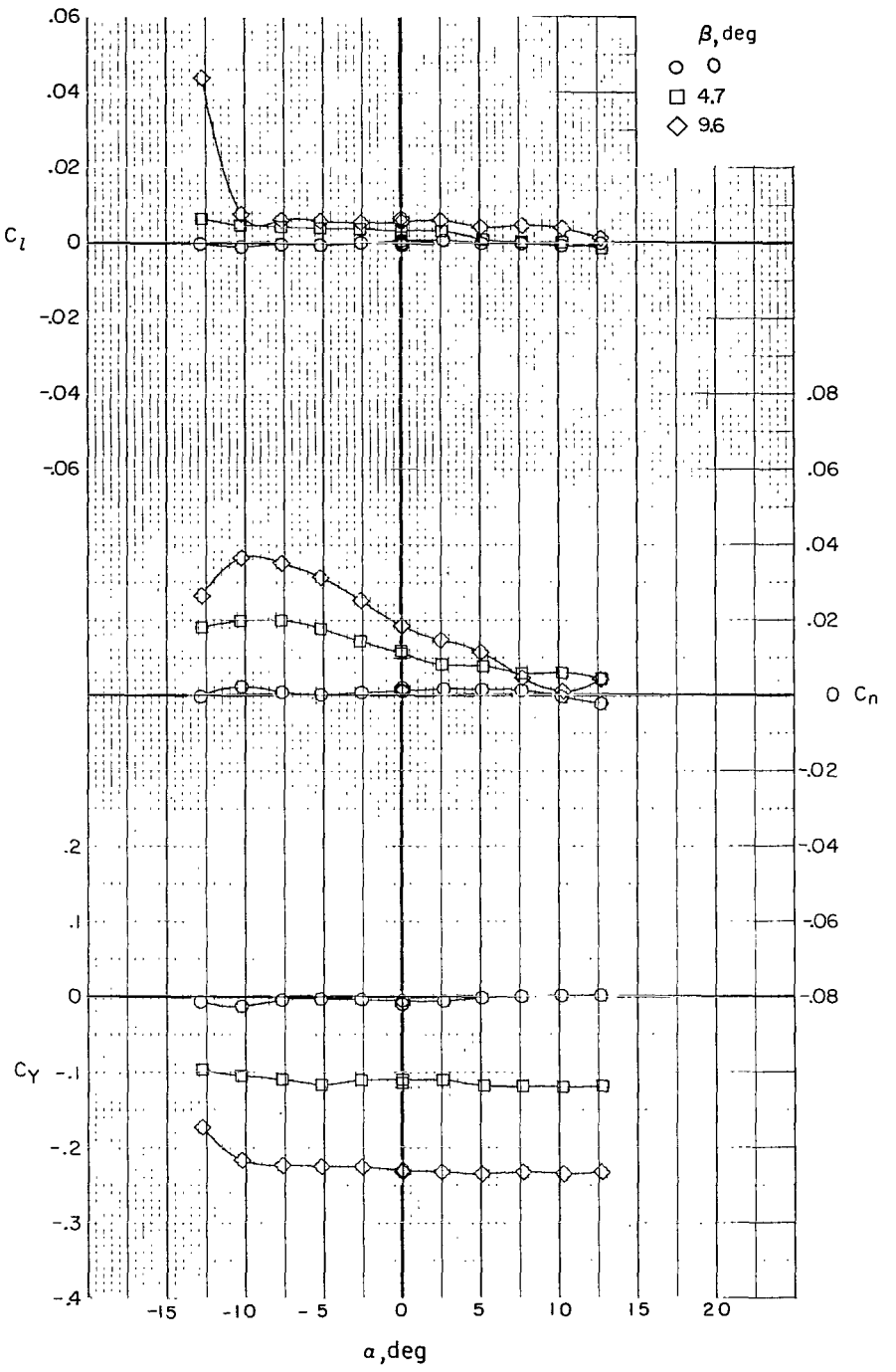

(g) $C_T = 0$; $i_w = -4.5^o$; $\delta_f = 0^o$.

Figure 32.- Continued.

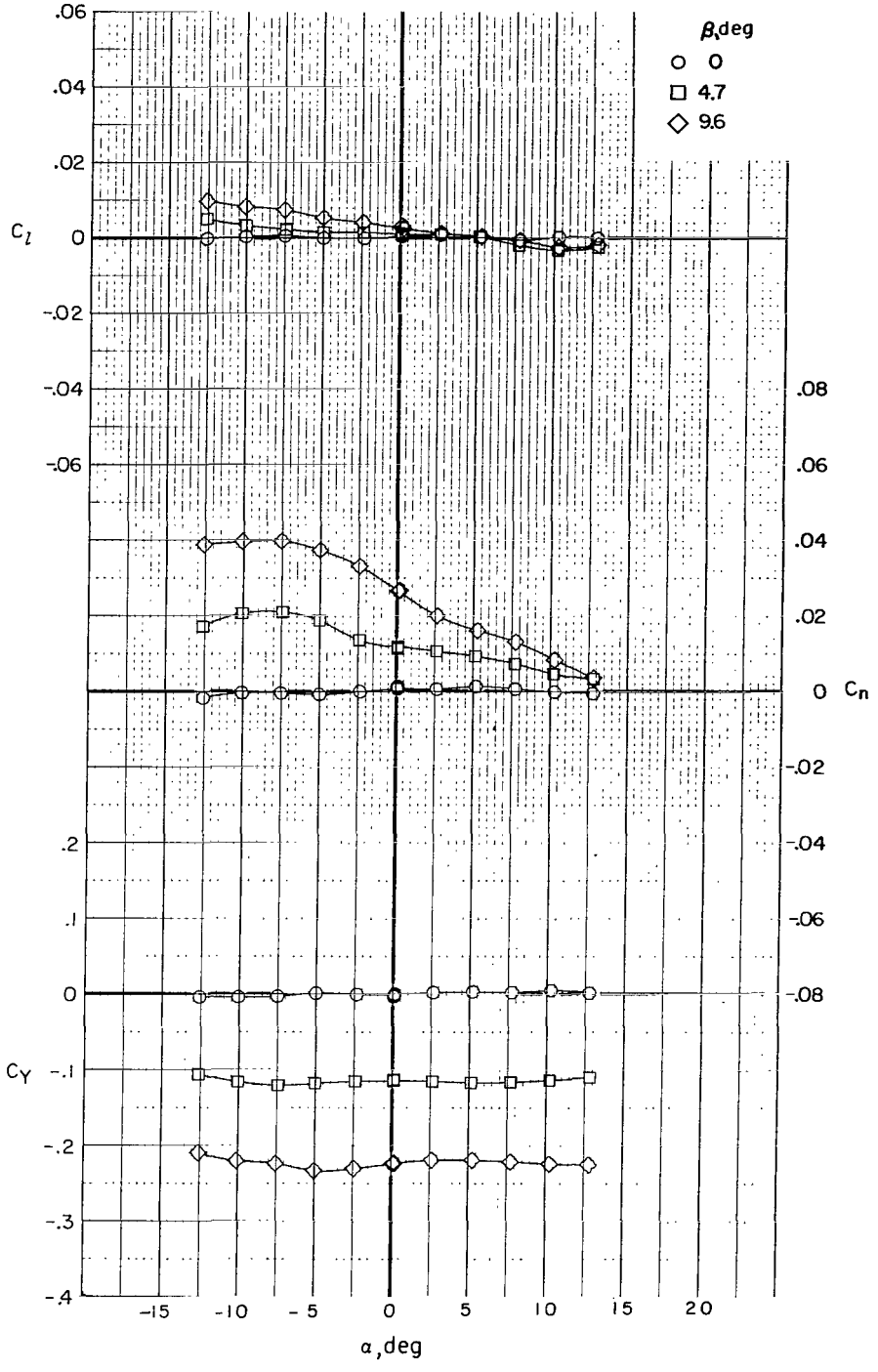

(h) $C_T = 0$; $i_w = 0^o$; $\delta_f = 0^o$.

Figure 32.- Continued.

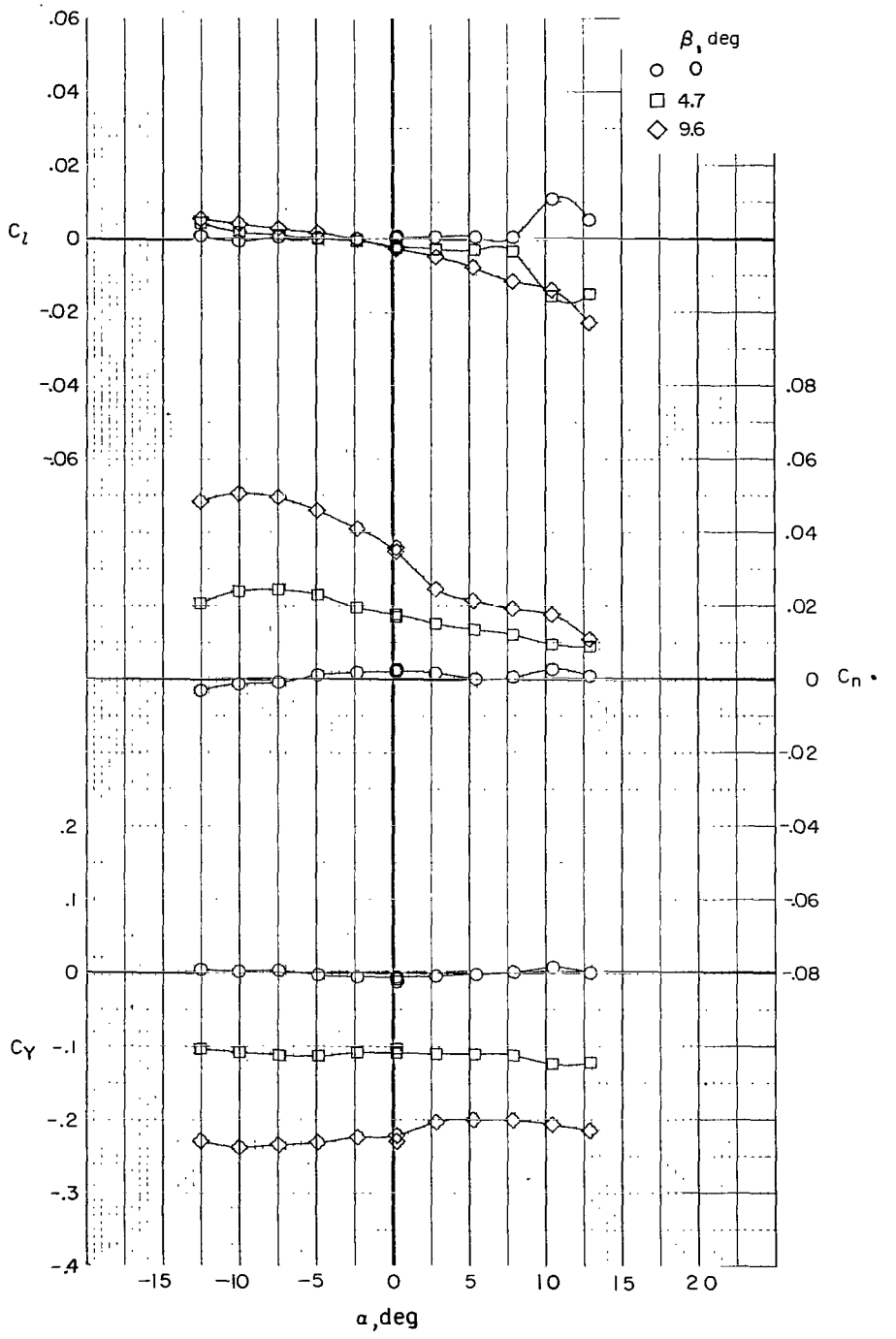

(i) $C_T = 0$; $i_w = 7.5^o$; $\delta_f = 0^o$.

Figure 32.- Continued.

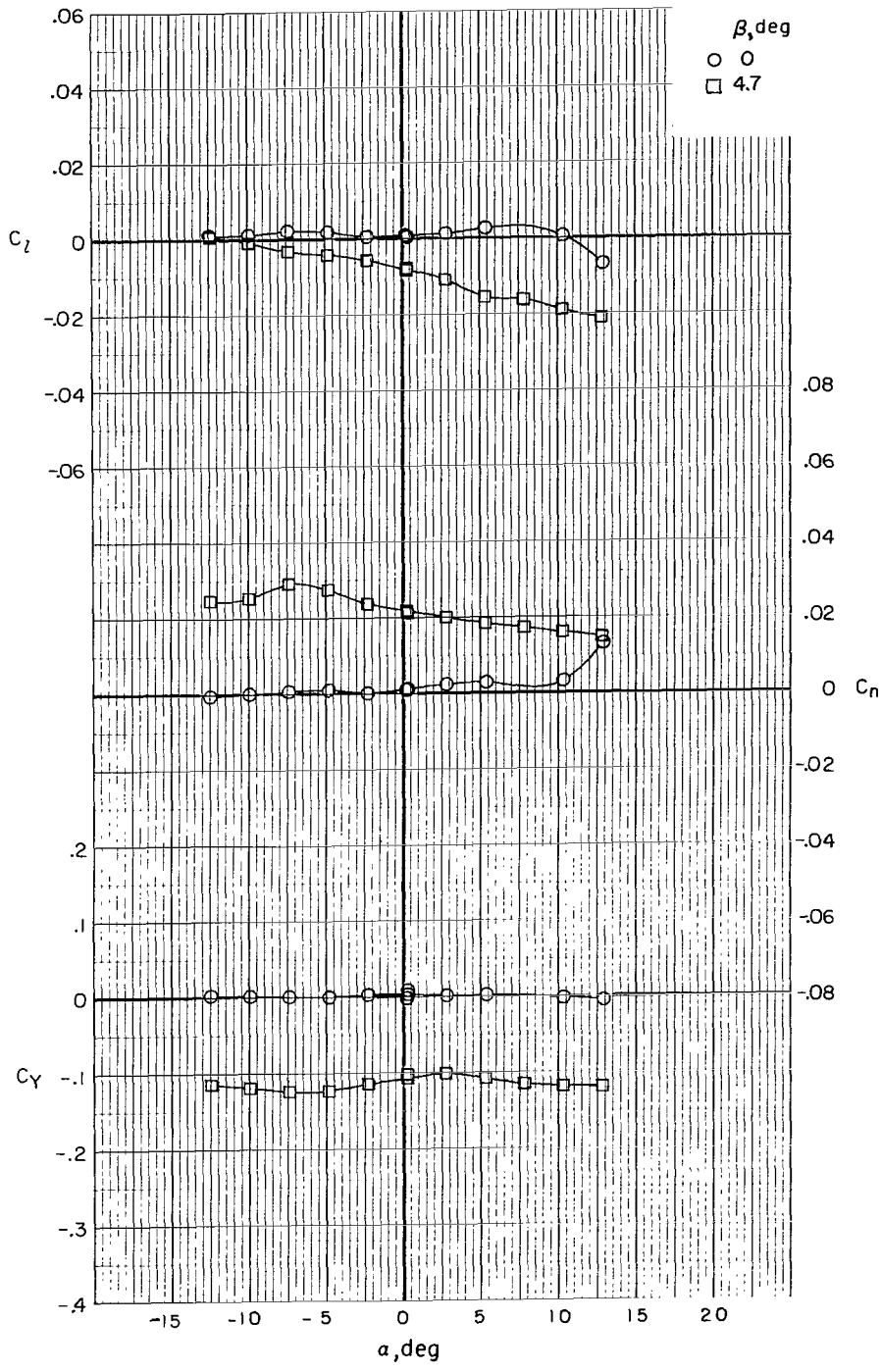

(j) $C_T = 0$; $i_w = 15^o$; $\delta_f = 0^o$.

Figure 32.- Continued.

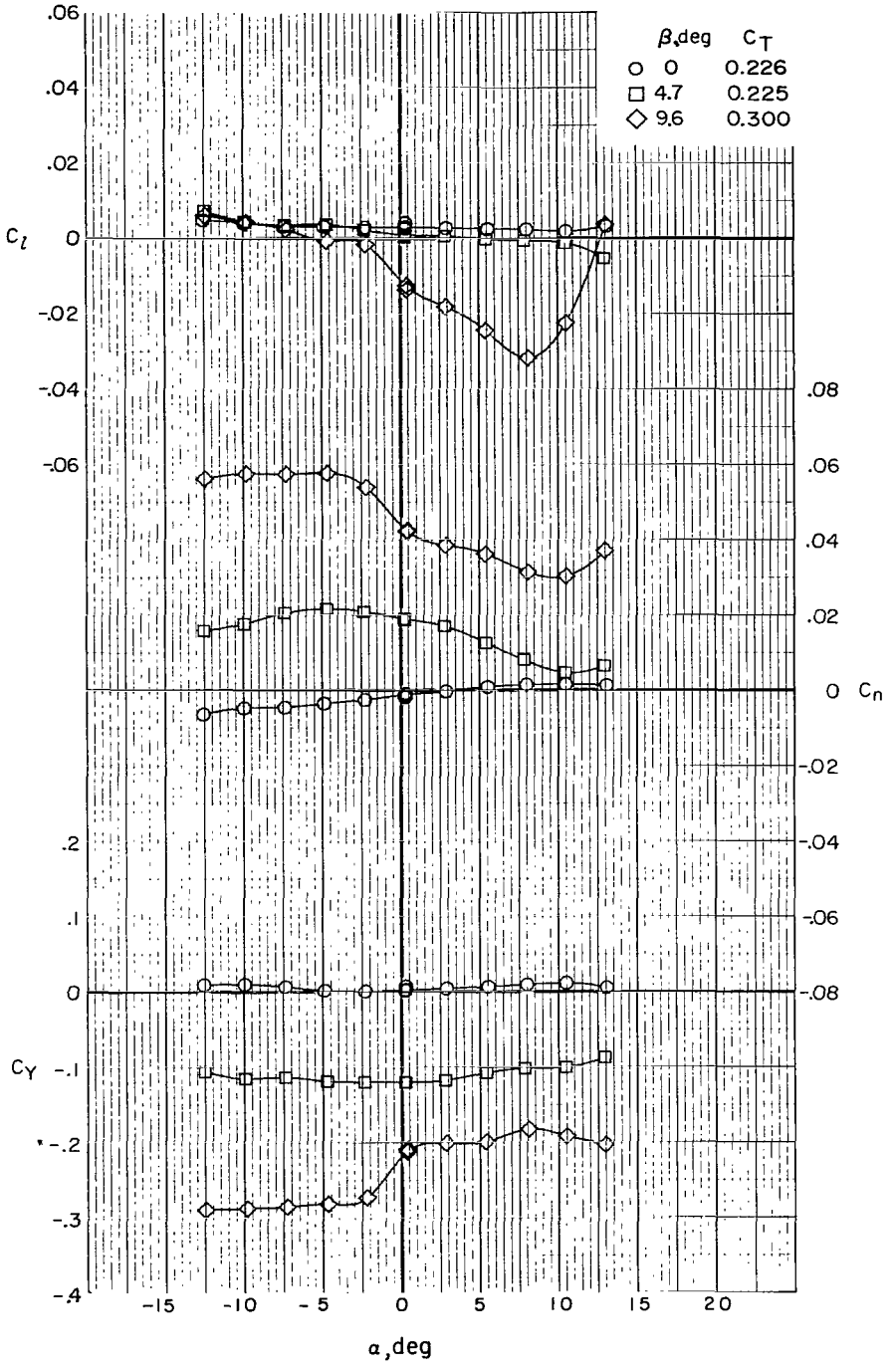

(k) Trim thrust; $i_w = 0^o$; $\delta_f = 30^o$.

Figure 32.- Continued.

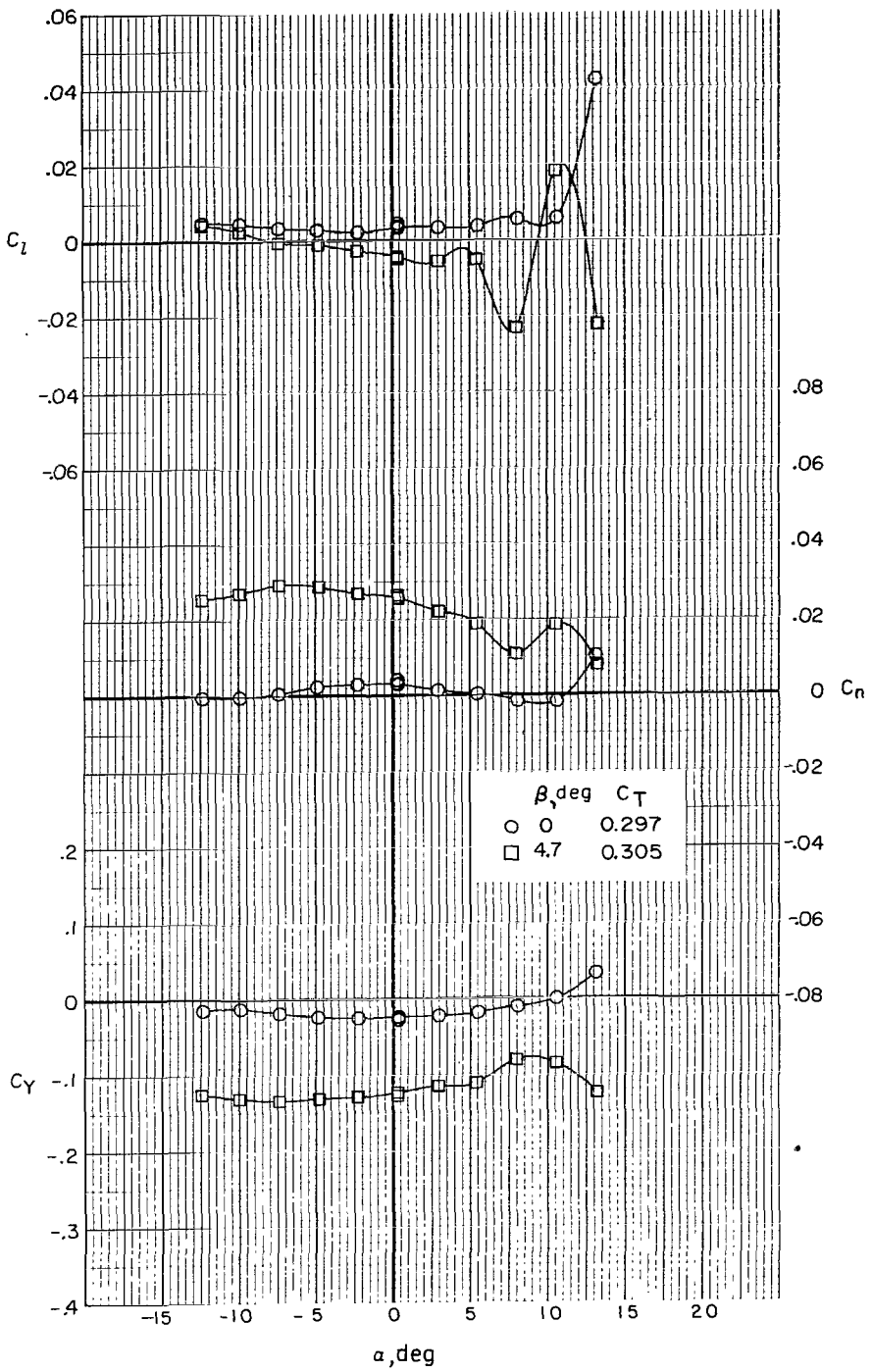

(l) Trim thrust; $i_w = 7.5^o$; $\delta_f = 30^o$.

Figure 32.- Continued.

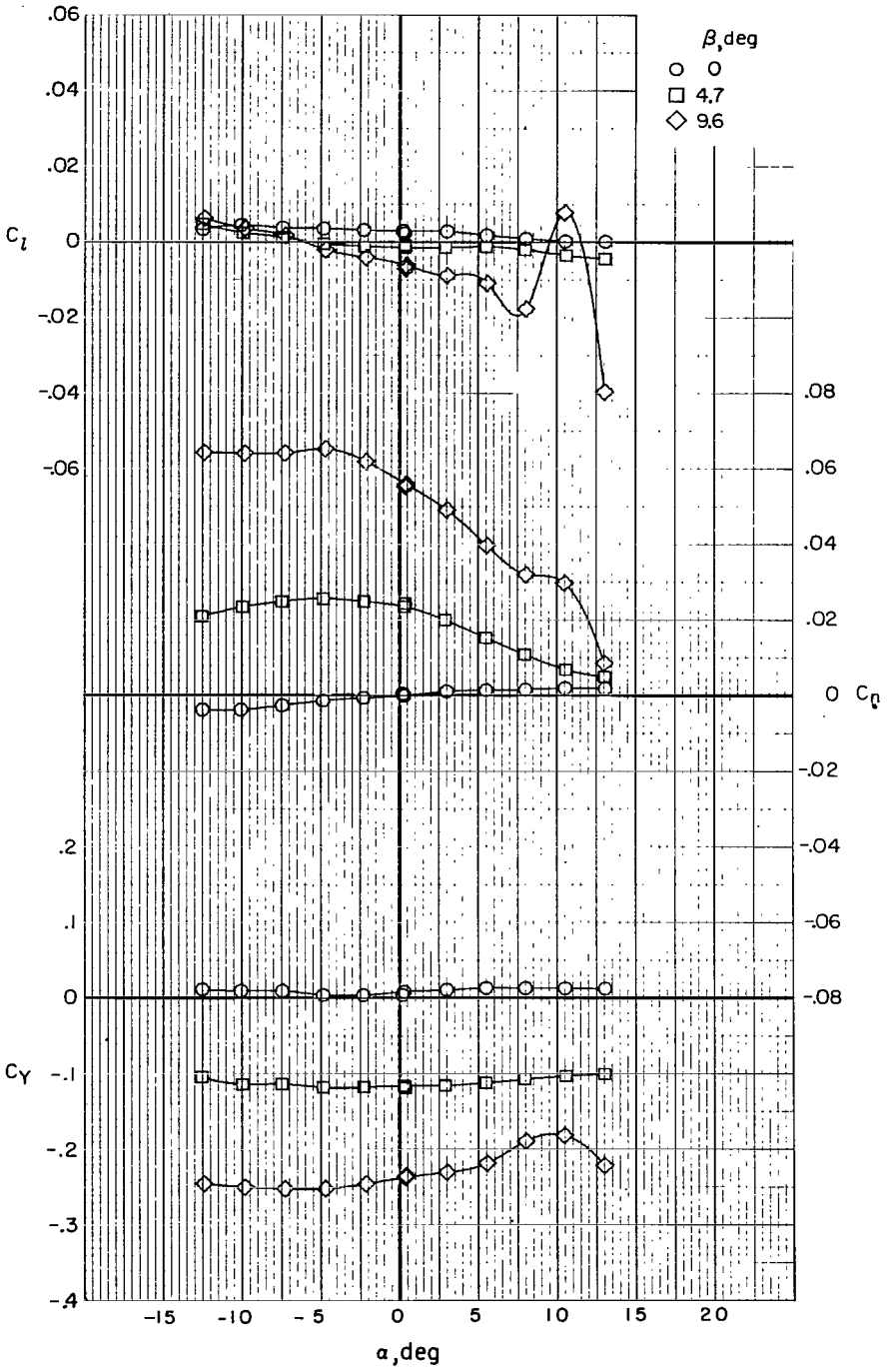

(m) $C_T = 0$; $i_w = 0^o$; $\delta_f = 30^o$.

Figure 32.- Continued.

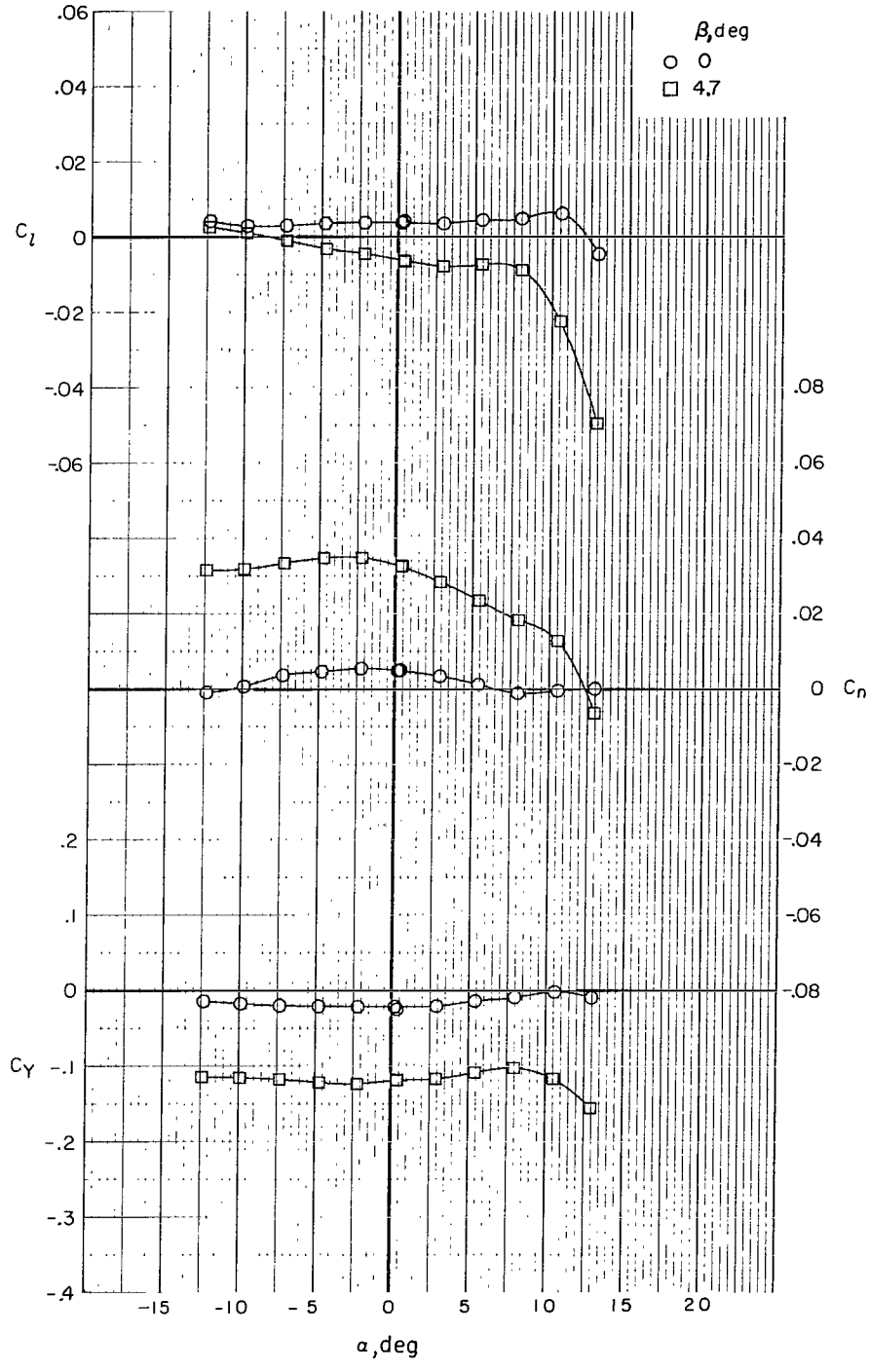

(n) $C_T = 0$; $i_w = 7.5^o$; $\delta_f = 30^o$.

Figure 32.- Concluded.

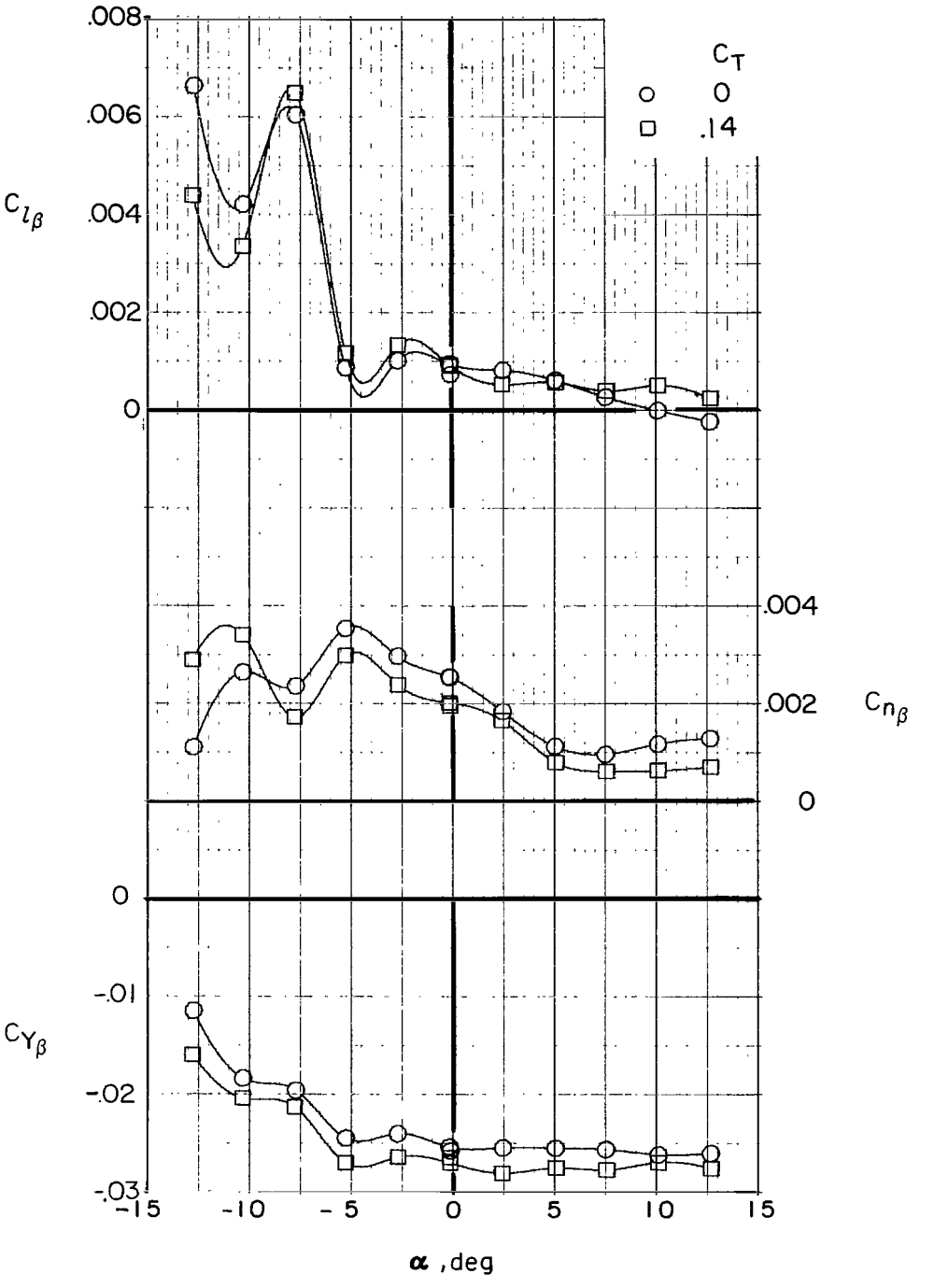

(a) $i_w = -9^o$; $\delta_f = 0^o$.

Figure 33.- Effect of C_T on lateral-directional stability derivatives of Phase III baseline configuration.

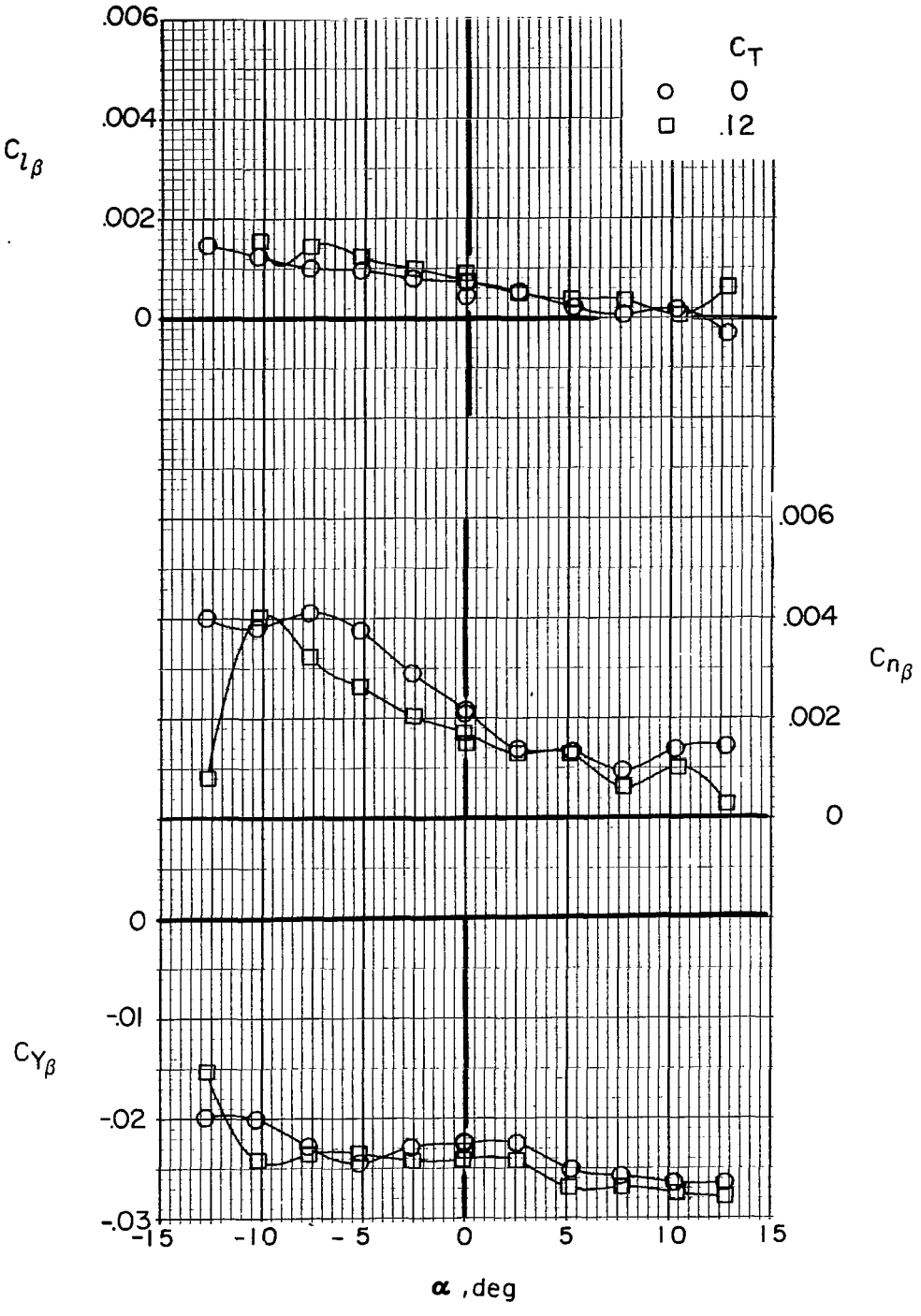

(b) $i_w = -4.5^o$; $\delta_f = 0^o$.

Figure 33.- Continued.

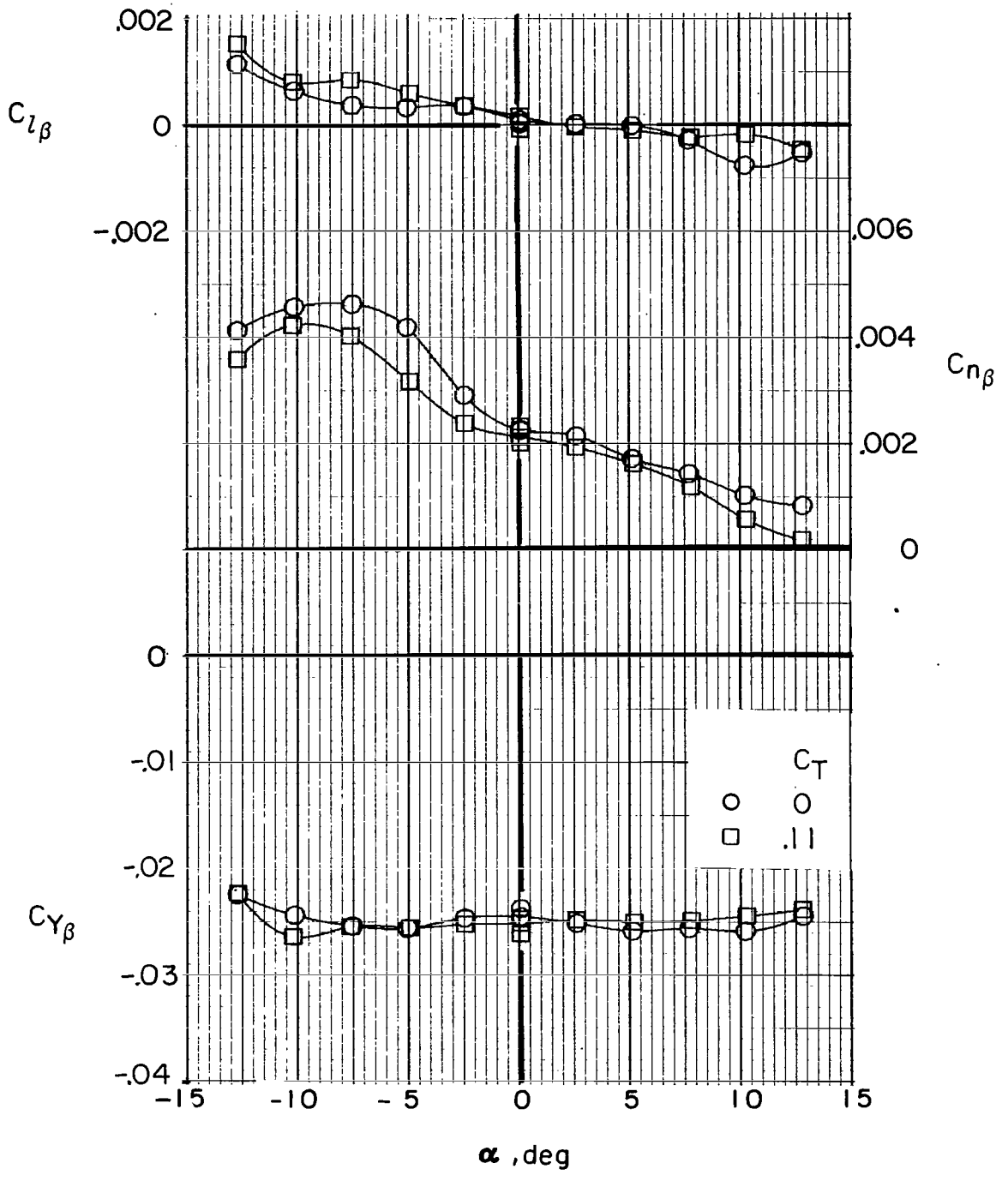

(c) $i_w = 0^o$; $\delta_f = 0^o$.

Figure 33.- Continued.

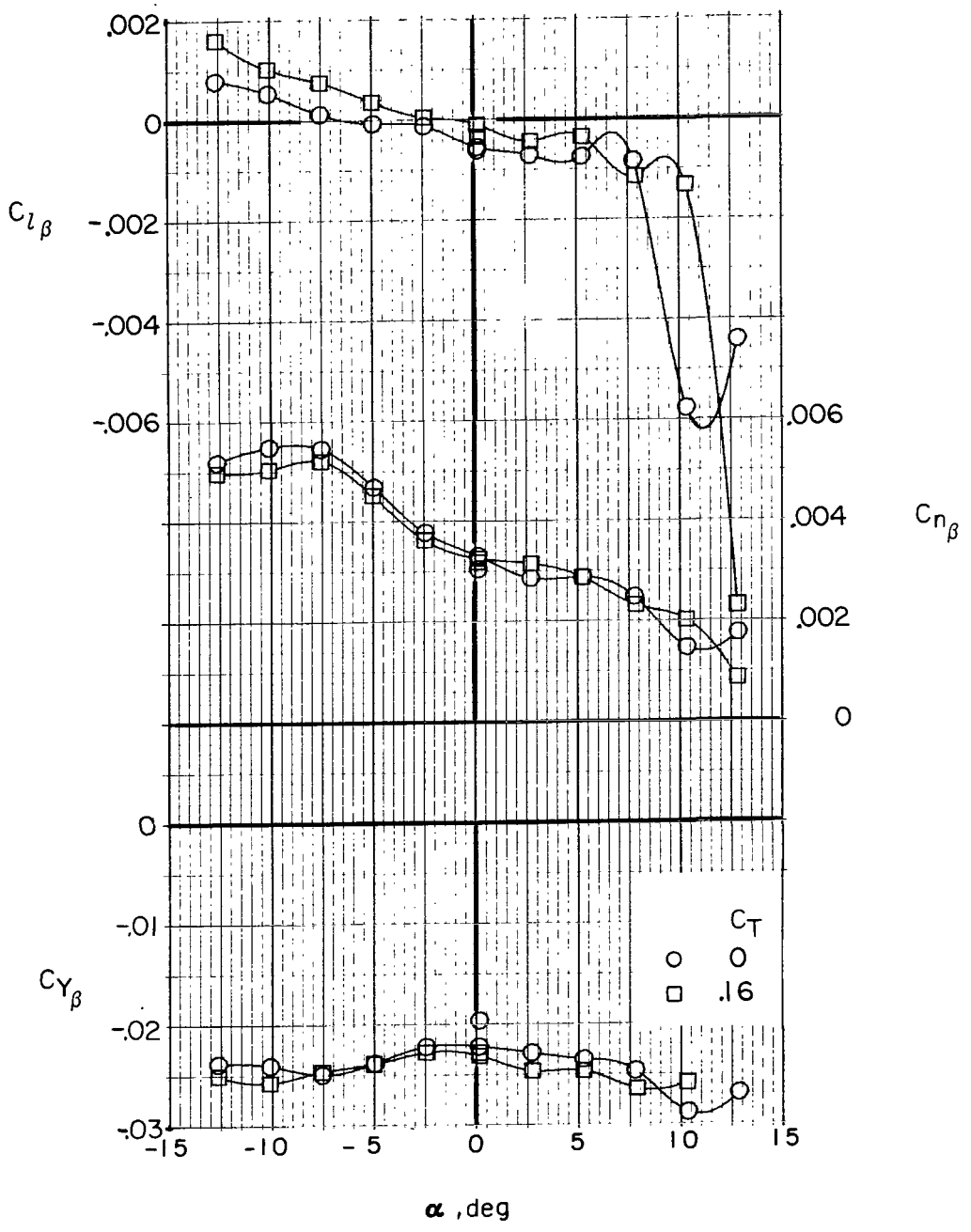

(d) $i_w = 7.5^o$; $\delta_f = 0^o$.

Figure 33.- Continued.

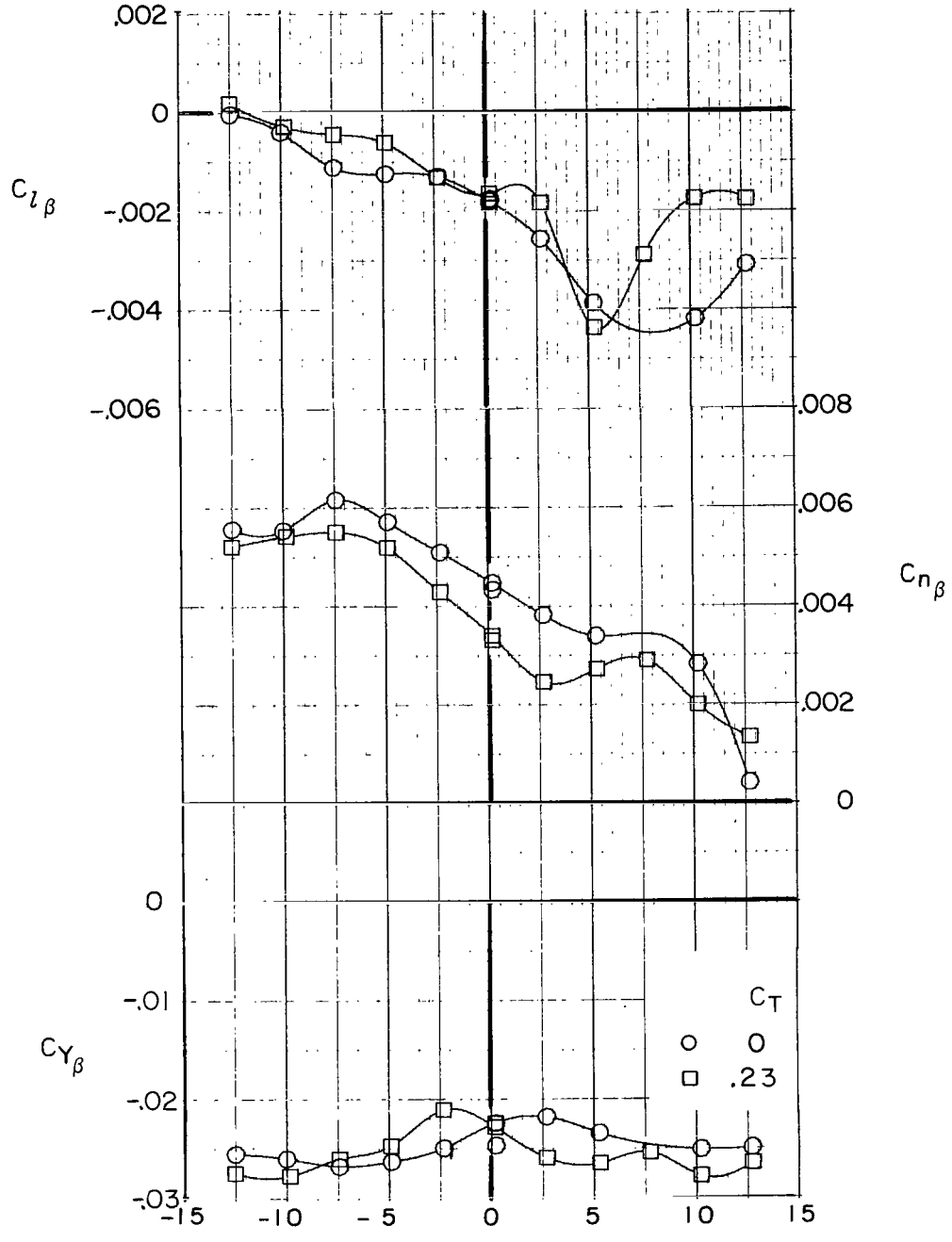

(e) $i_w = 15^o$; $\delta_f = 0^o$.

Figure 33.- Continued.

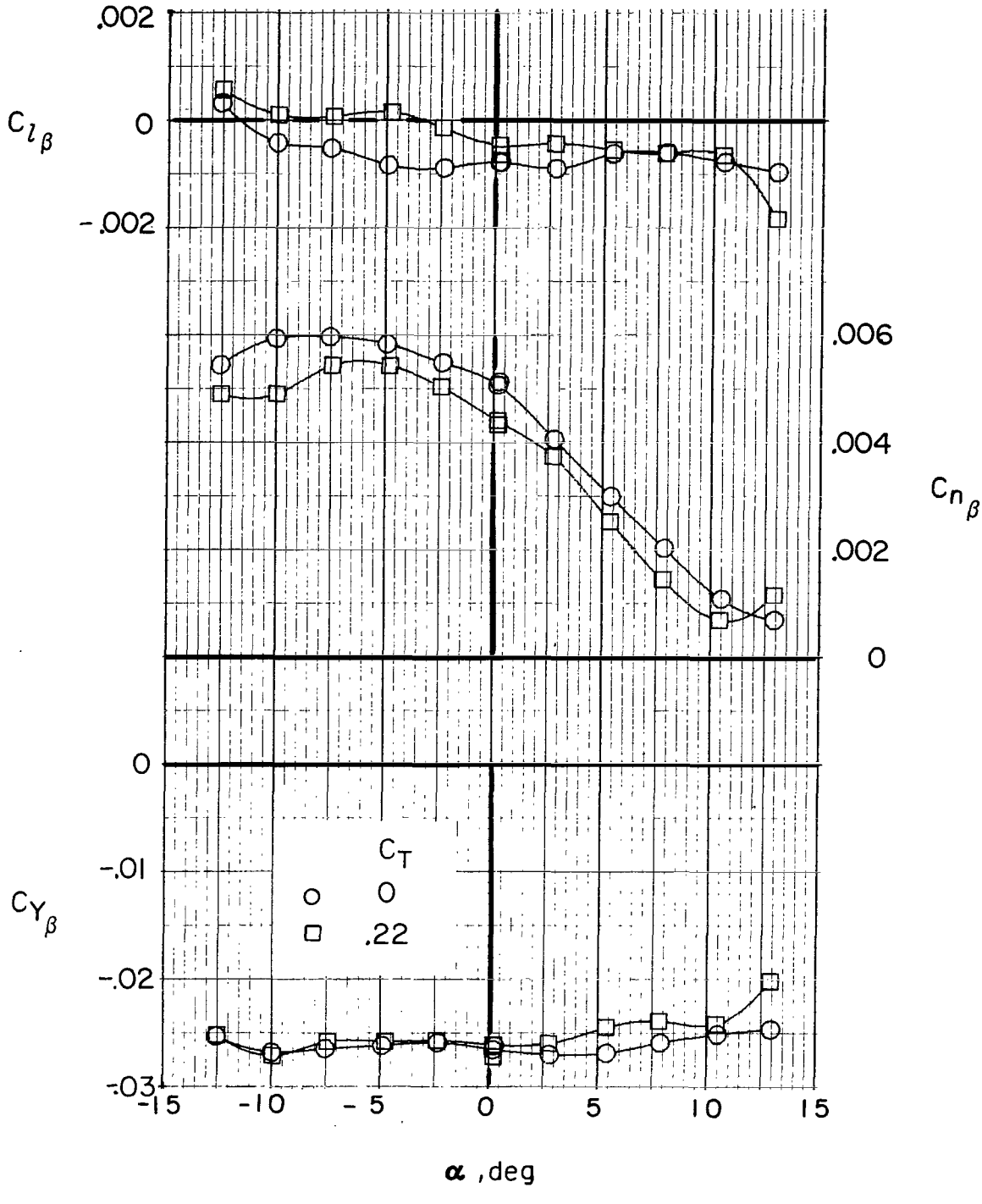

(f) $i_W = 0^o$; $\delta_f = 30^o$.

Figure 33.- Continued.

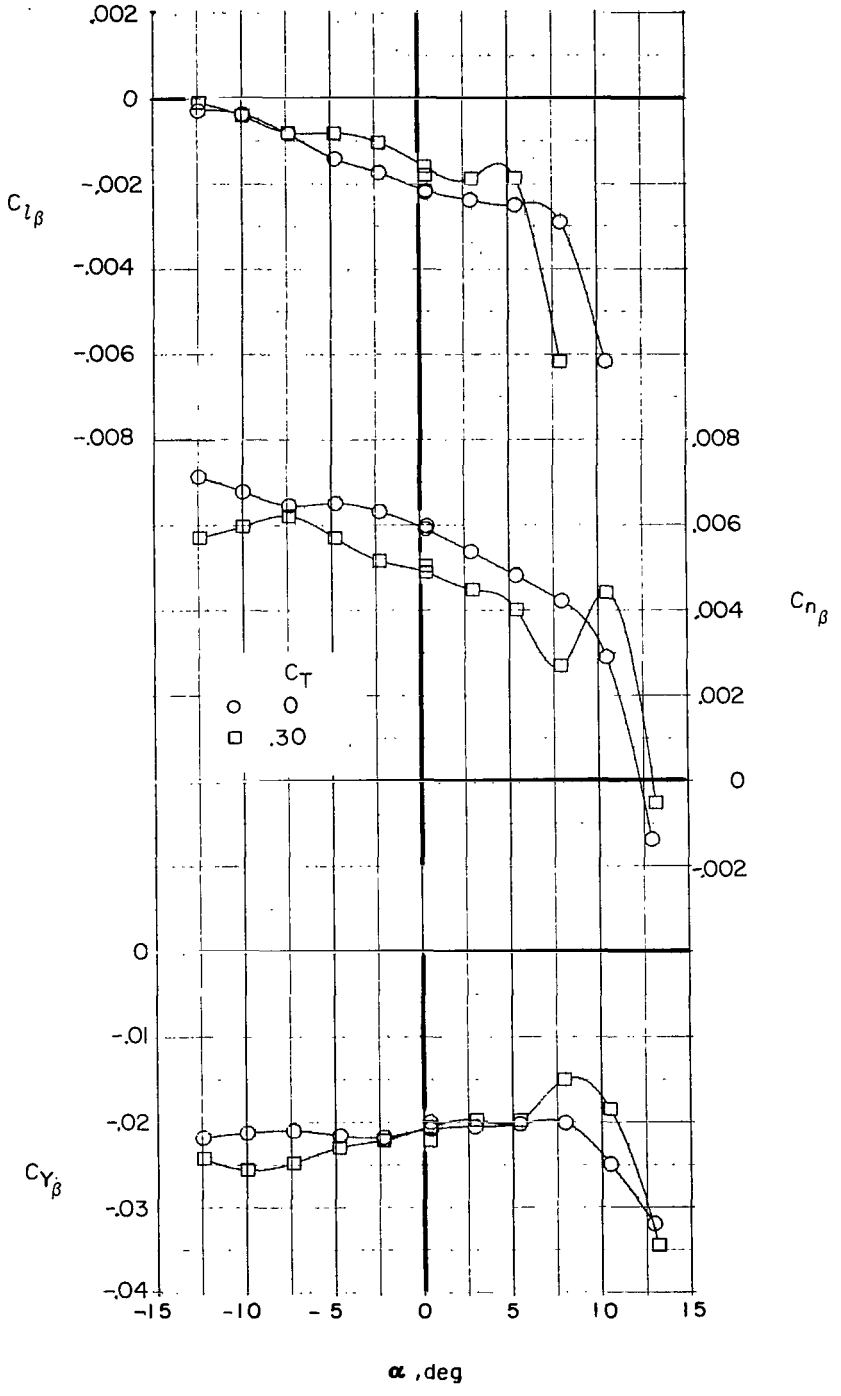

(g) $i_w = 7.5^o$; $\delta_f = 30^o$.

Figure 33.- Concluded.

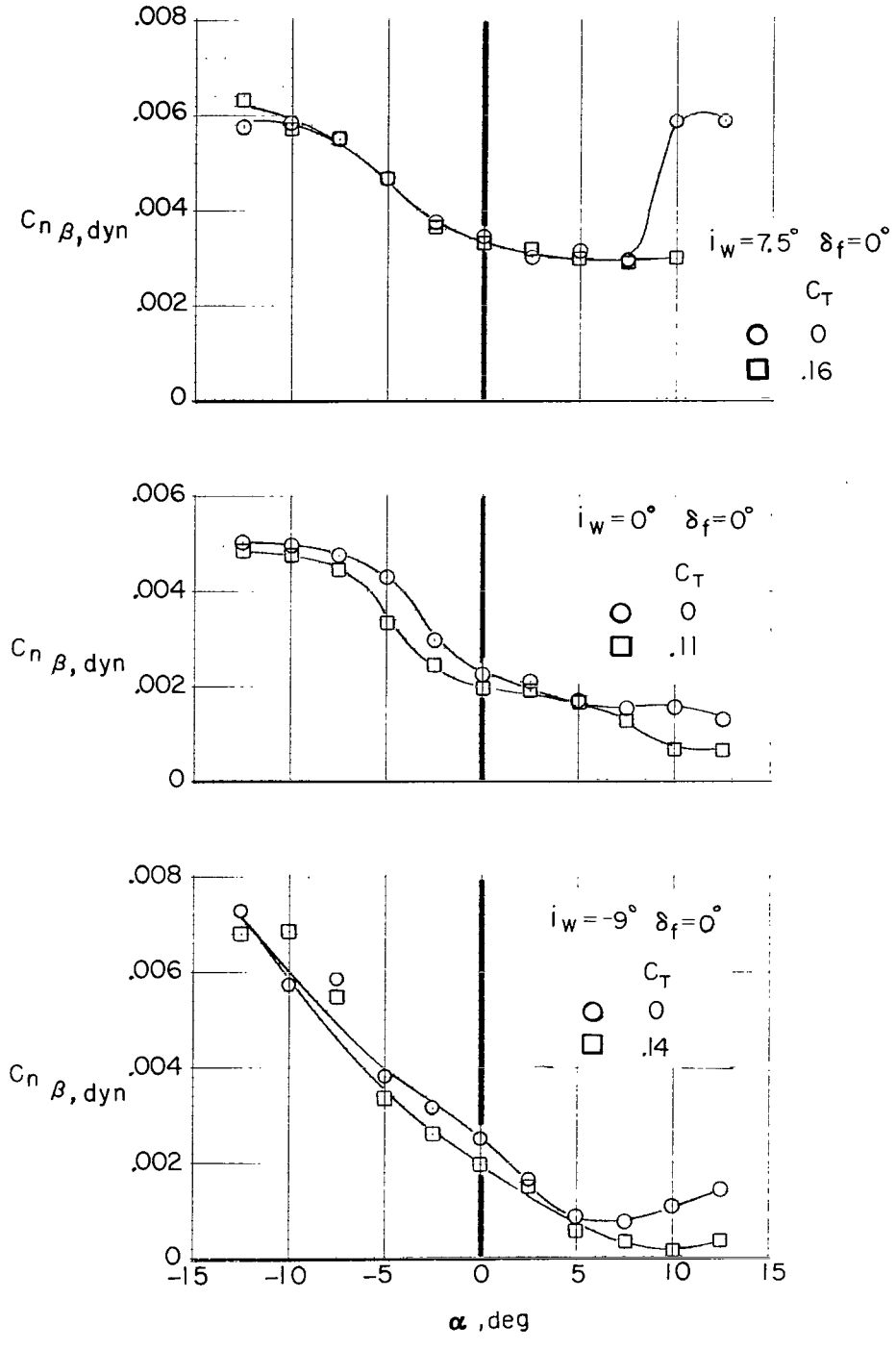

Figure 34.- Effect of C_T on dynamic directional-stability derivative of Phase III baseline configuration.

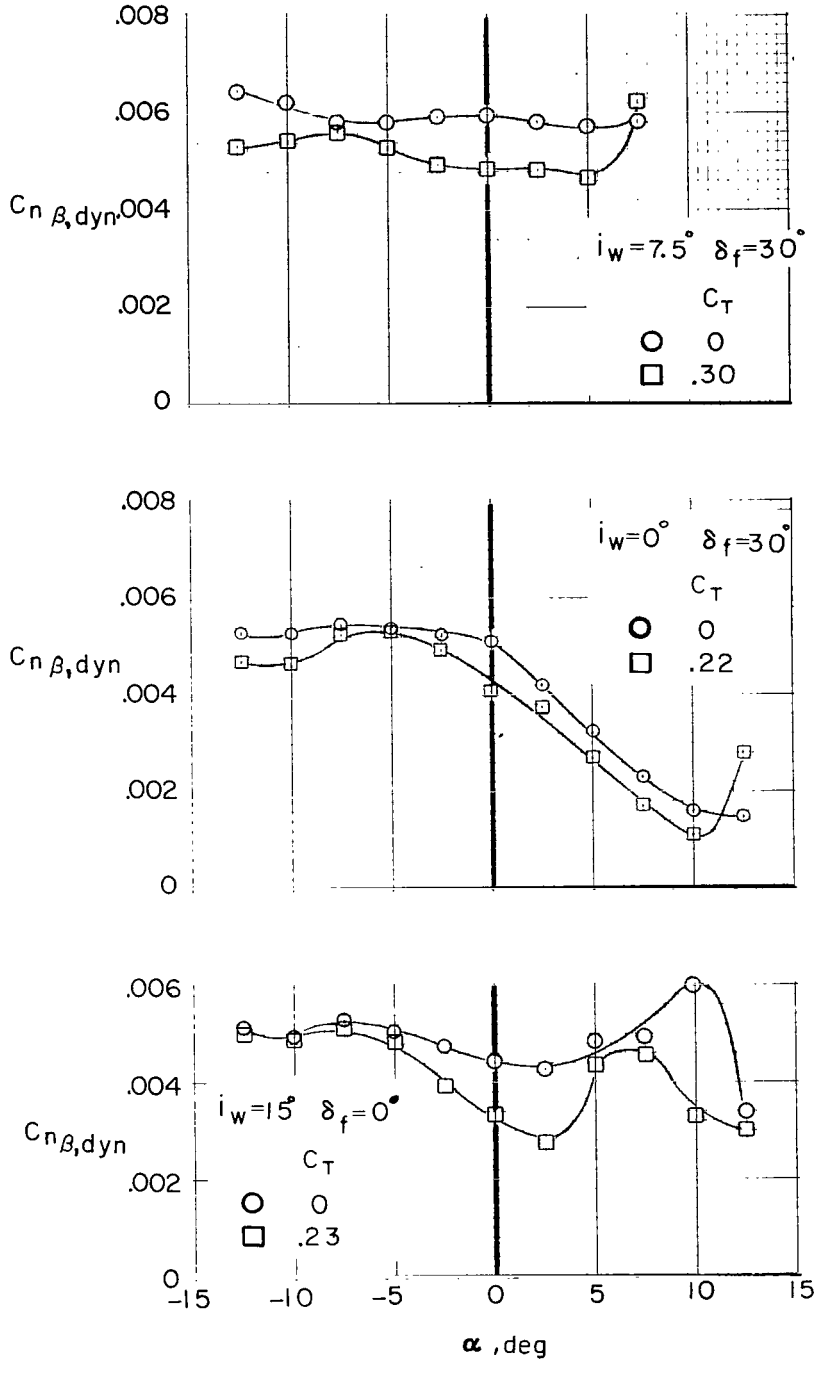

Figure 34.- Concluded.

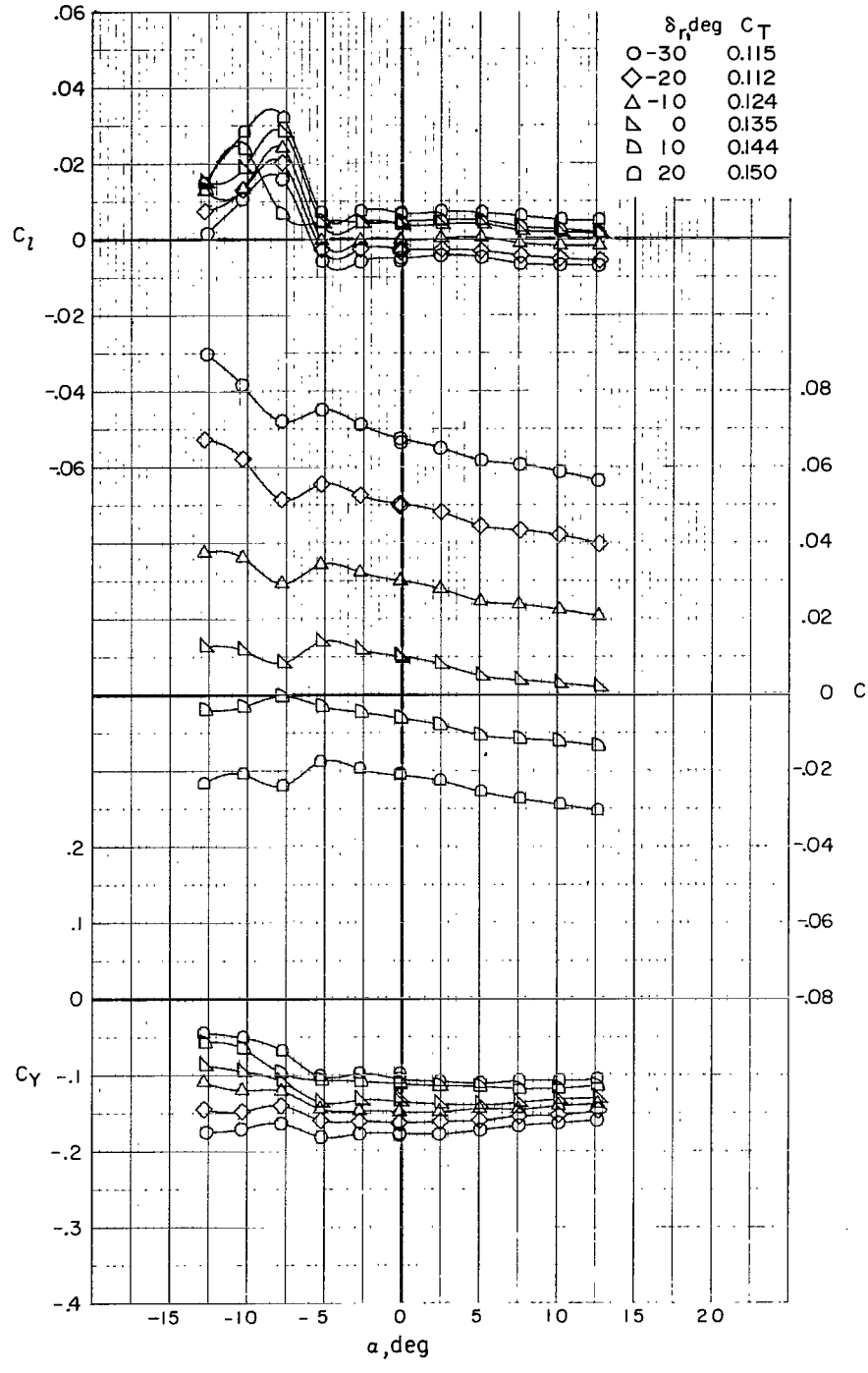

(a) $i_w = -9^o$; $\delta_f = 0^o$; $\beta \approx 5^o$.

Figure 35.- Effect of rudder deflection on lateral-directional characteristics of Phase III baseline configuration. Trim thrust.

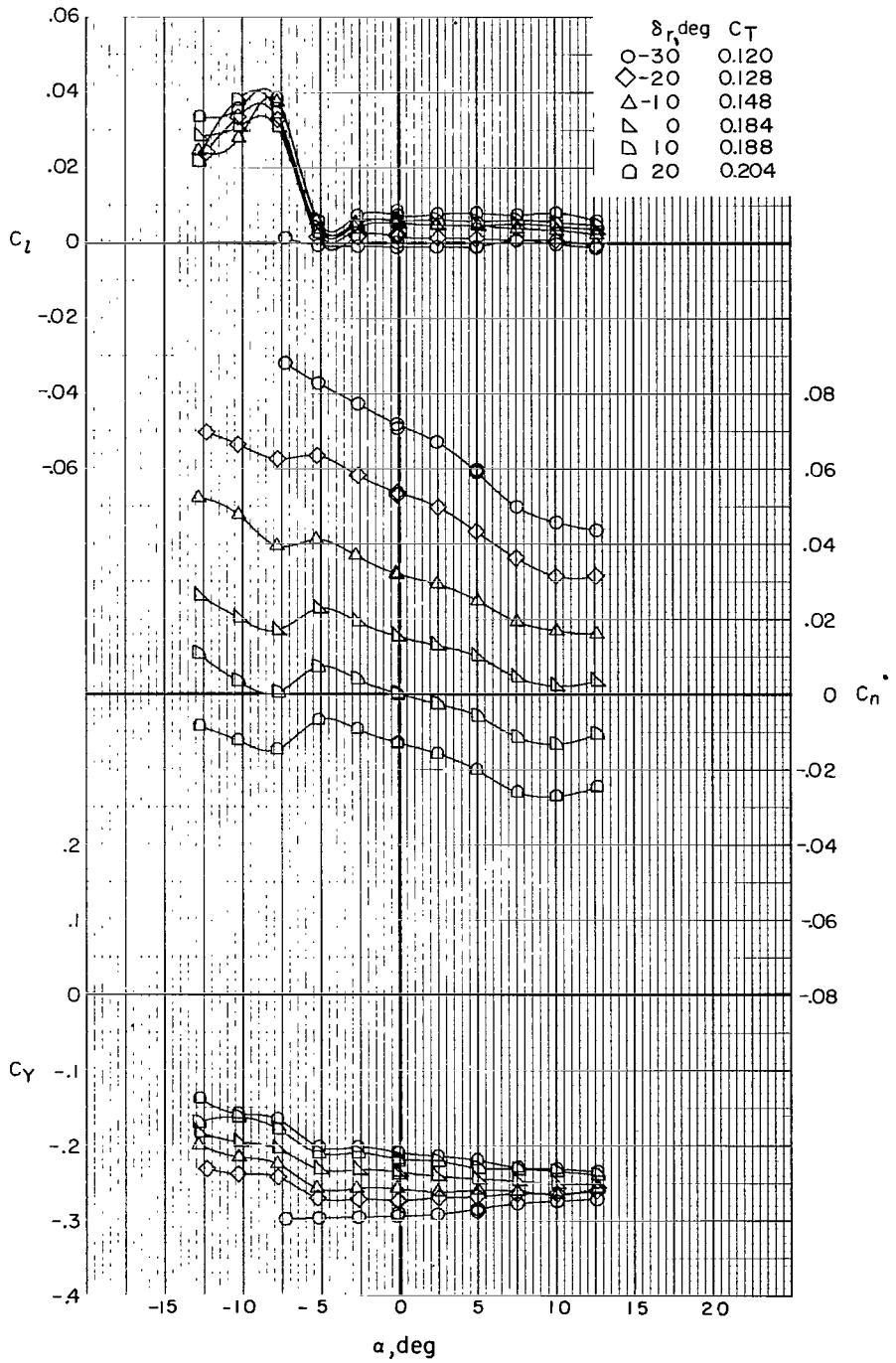

(b) $i_w = -9^o$; $\delta_f = 0^o$; $\beta \approx 10^o$.

Figure 35.- Continued.

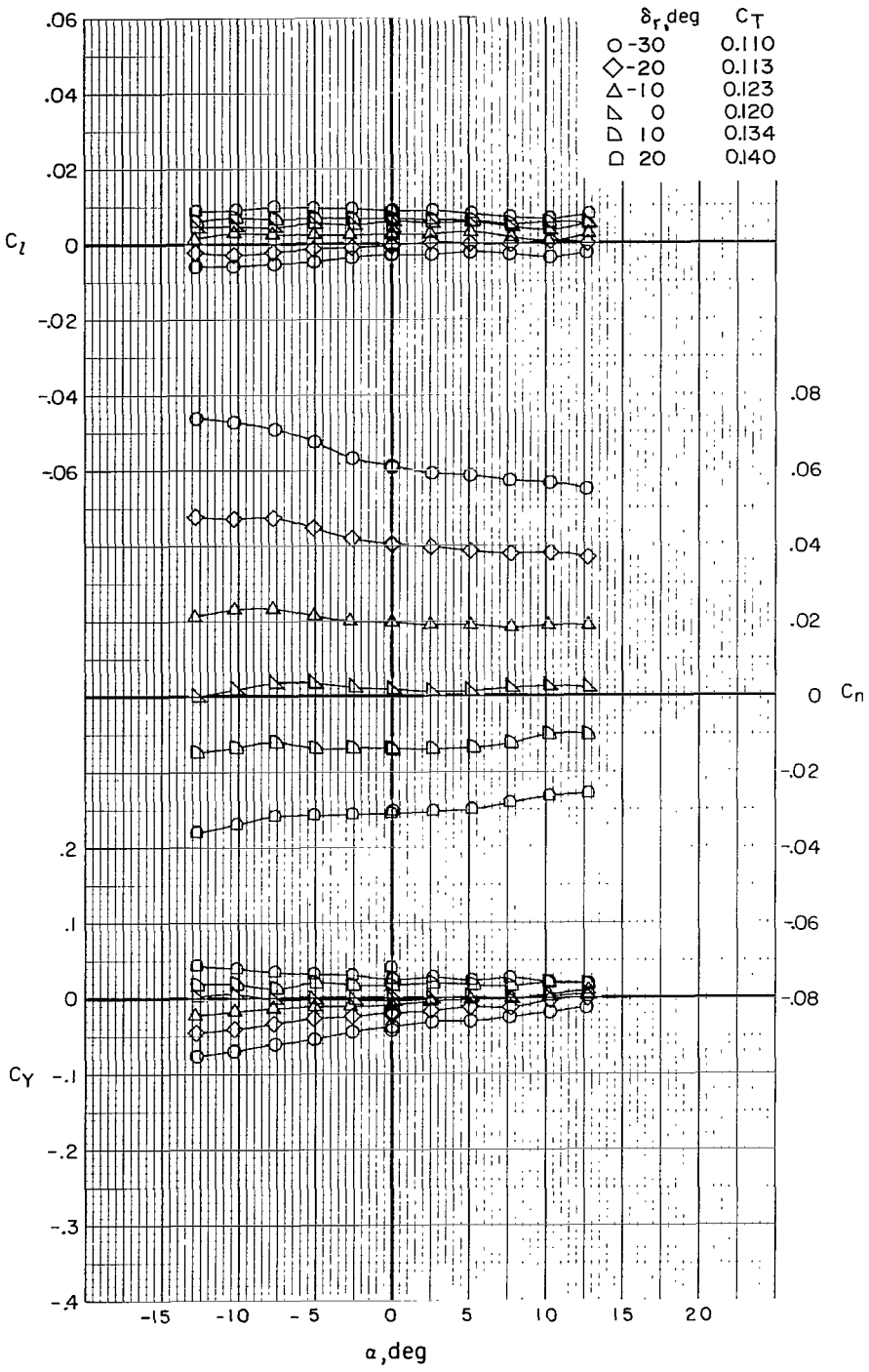

(c) $i_W = 0^o$; $\delta_f = 0^o$; $\beta = 0^o$.

Figure 35.- Continued.

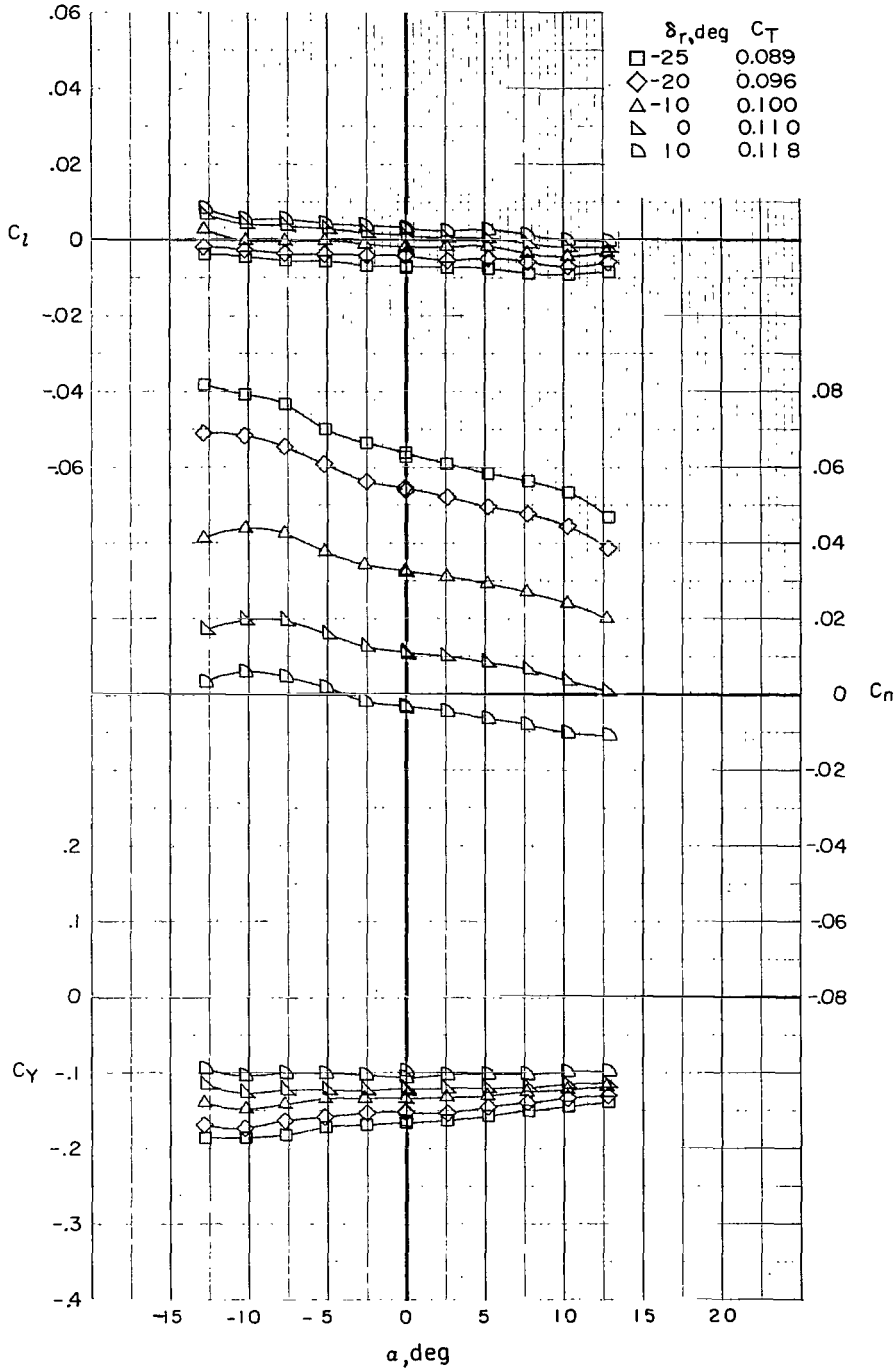

(d) $i_w = 0^o$; $\delta_f = 0^o$; $\beta \approx 5^o$.

Figure 35.- Continued.

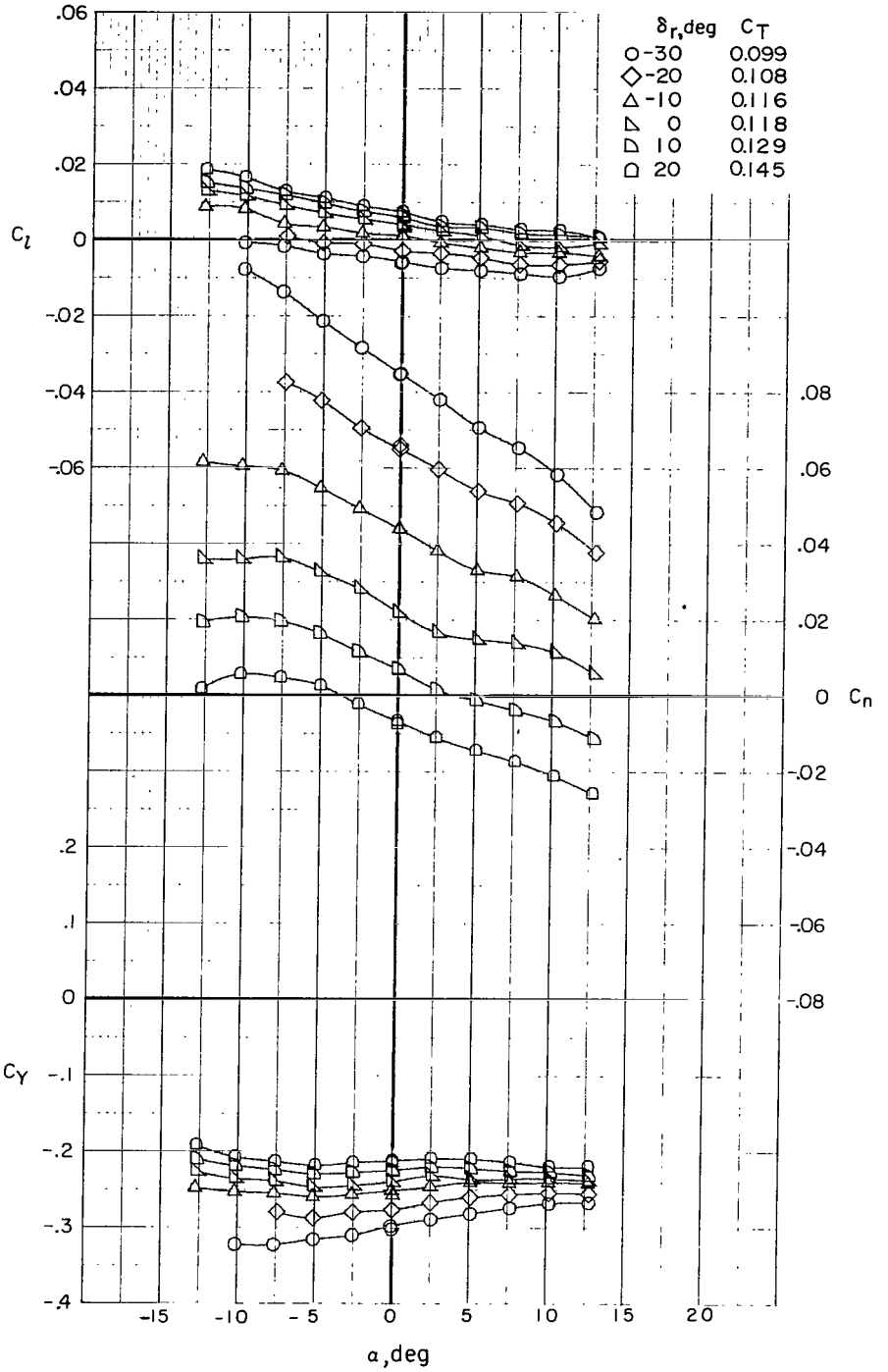

(e) $i_W = 0^O$; $\delta_f = 0^O$; $\beta \approx 10^O$.

Figure 35.- Continued.

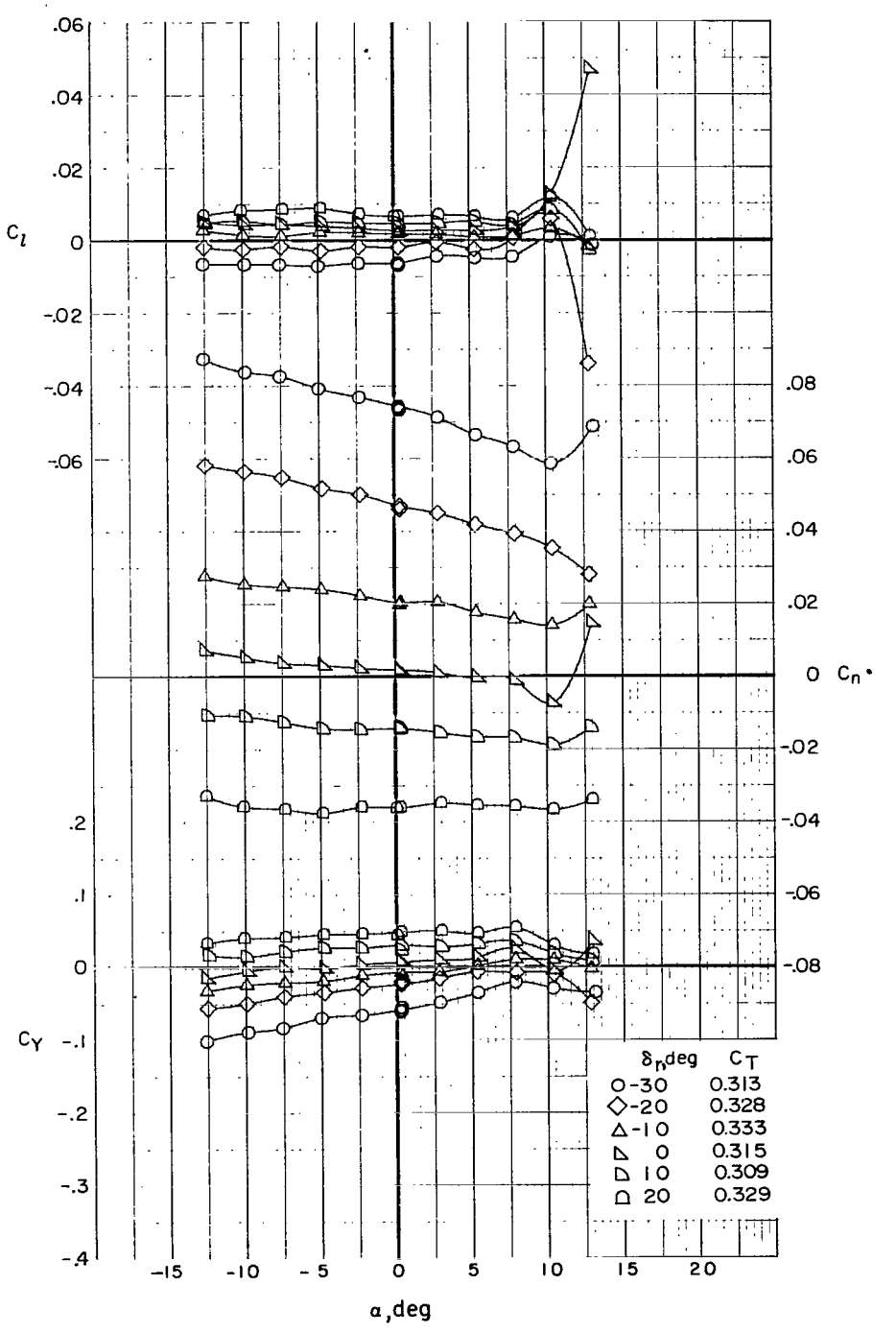

(f) $i_w = 7.5^o$; $\delta_f = 30^o$; $\beta = 0^o$.

Figure 35.- Continued.

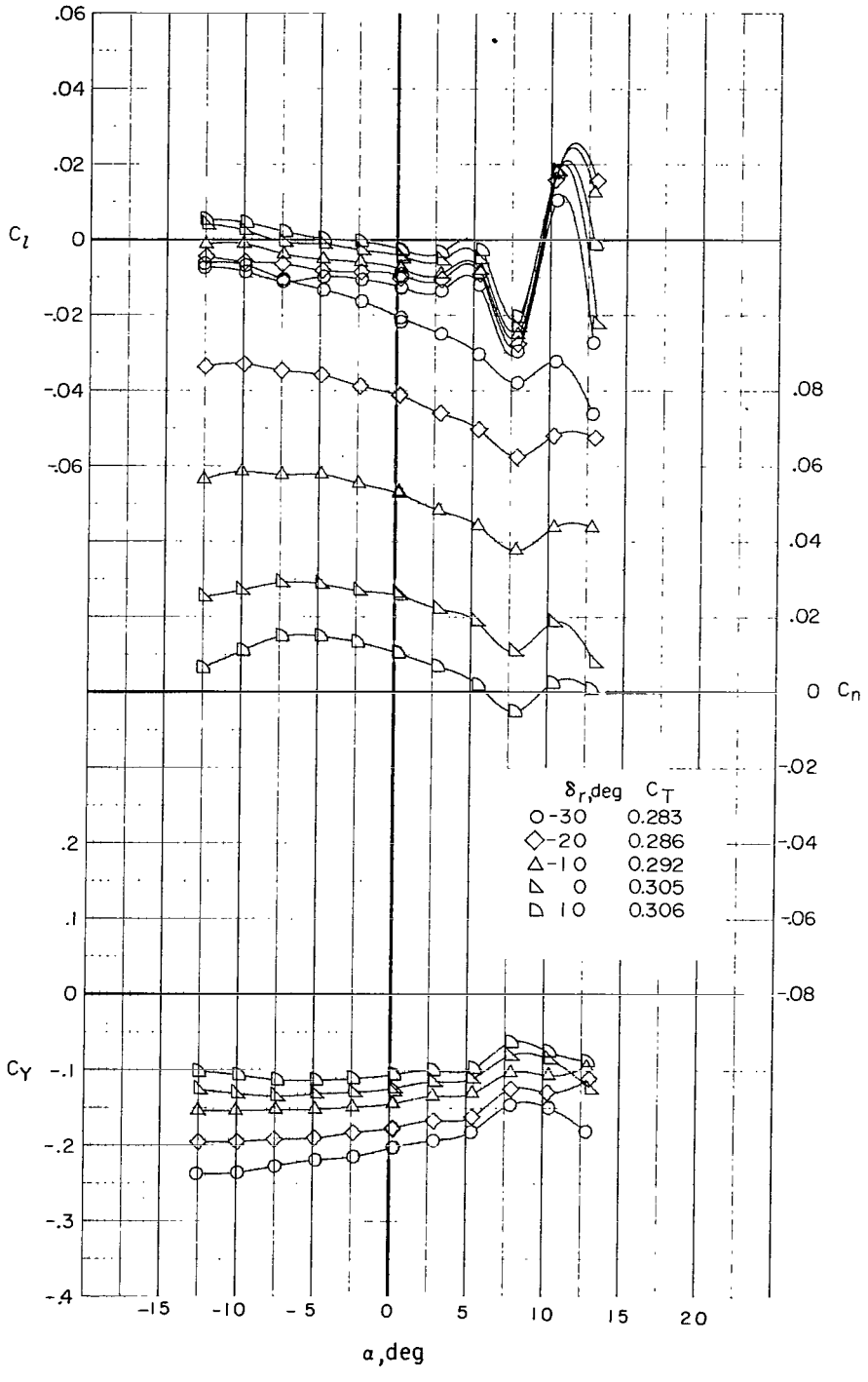

(g) $i_w = 7.5^o$; $\delta_f = 30^o$; $\beta \approx 5^o$.

Figure 35.- Continued.

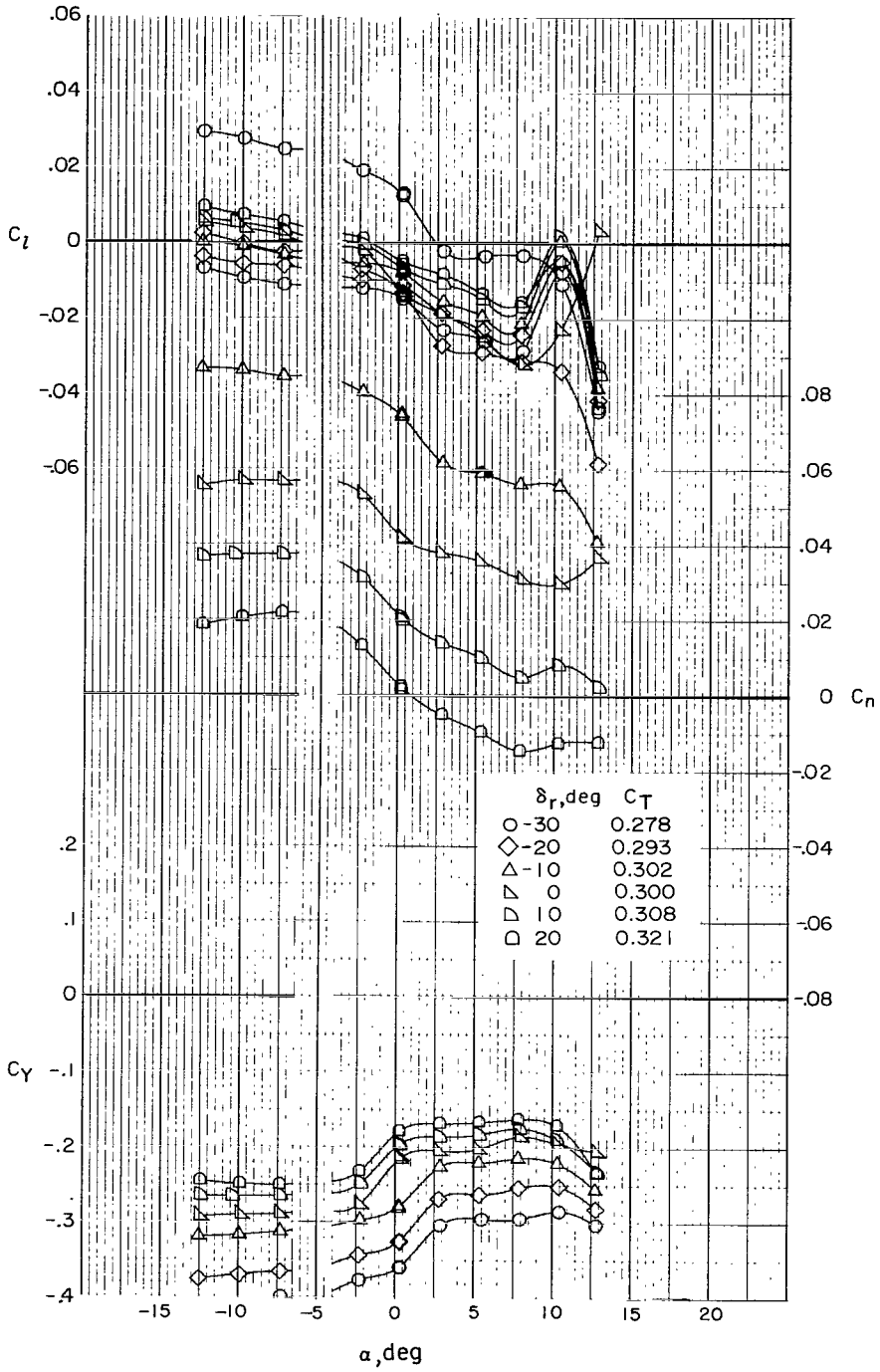

(h) $i_w = 7.5^o$; $\delta_f = 30^o$; $\beta \approx 10^o$.

Figure 35.- Concluded.

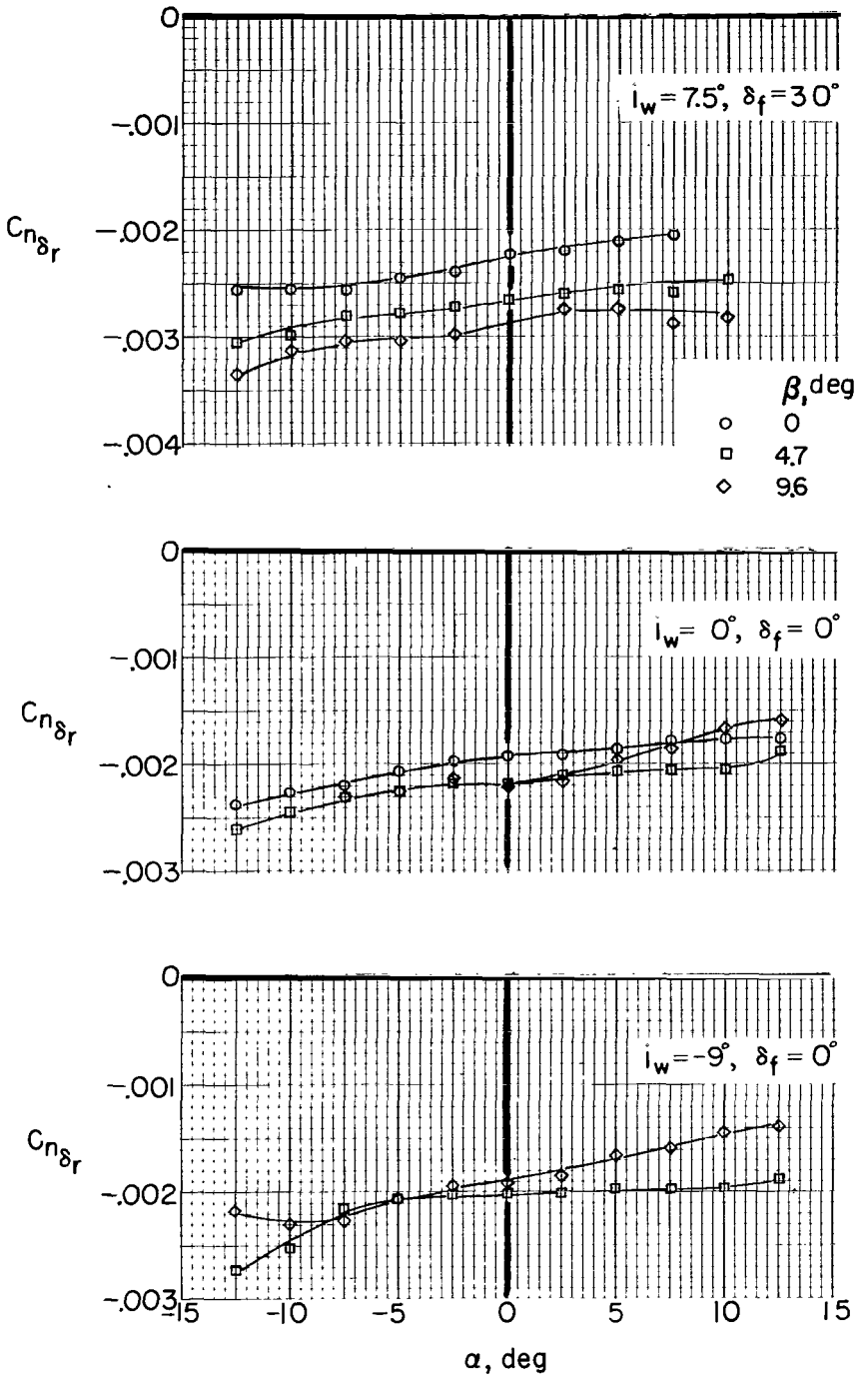

Figure 36.- Rudder effectiveness for Phase III baseline configuration. Trim thrust.

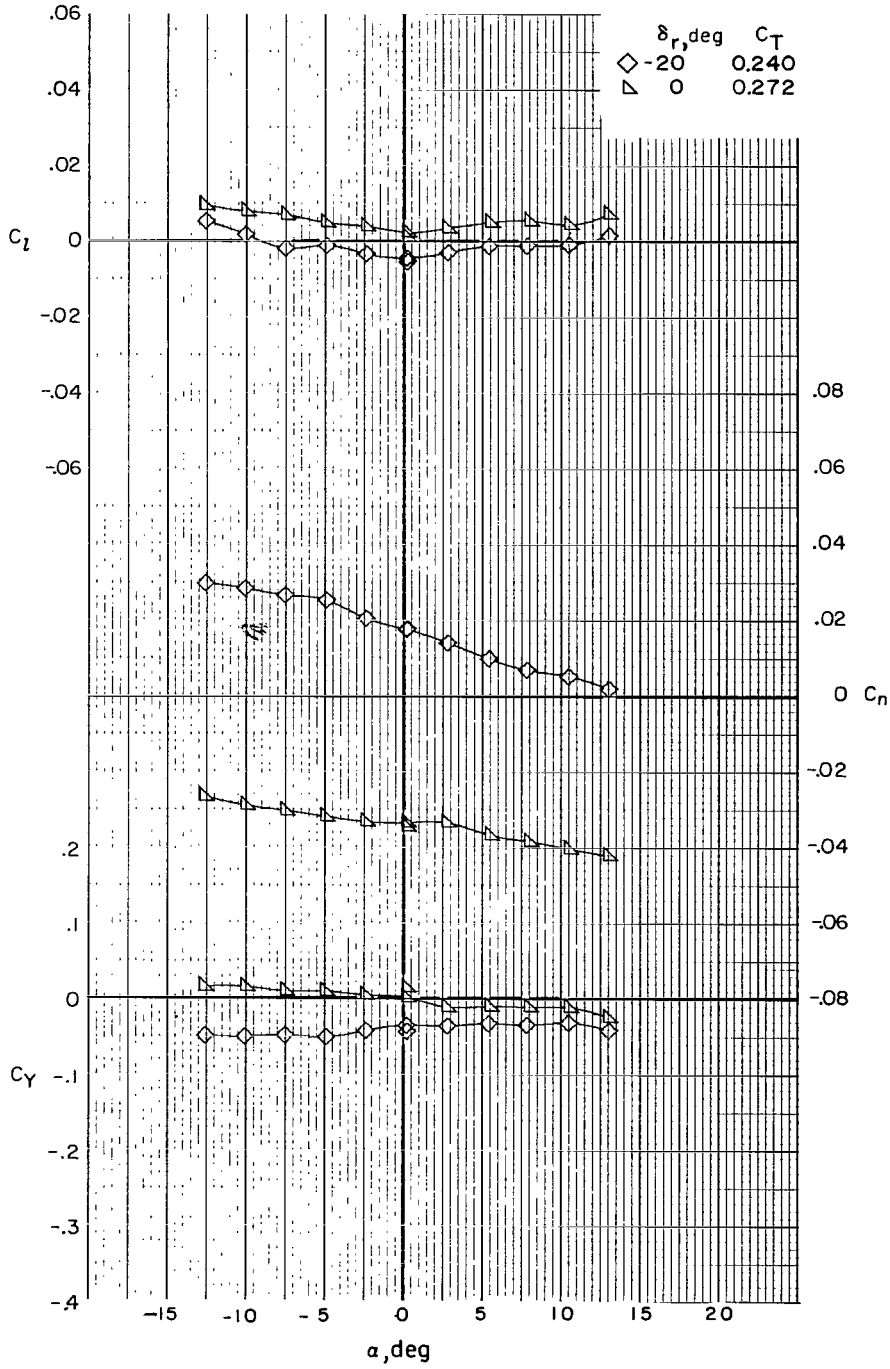

(a) $i_w = 0^o$; $\delta_f = 30^o$; trim thrust; $\beta = 0^o$.

Figure 37.- Effect of rudder deflection on lateral-directional characteristics of Phase III baseline configuration with left engine windmilling.

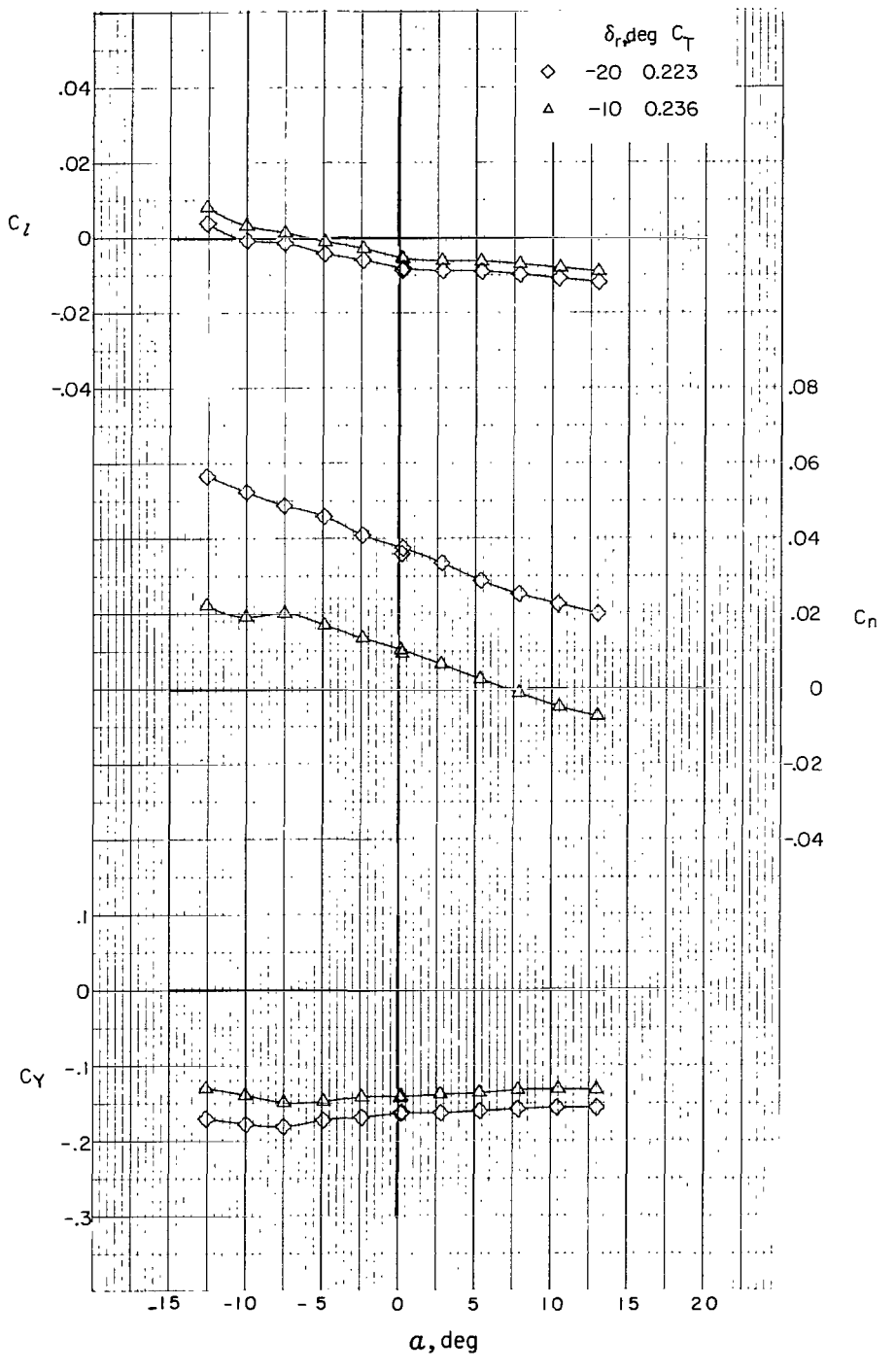

(b) $i_w = 0^o$; $\delta_f = 30^o$; trim thrust; $\beta \approx 5^o$.

Figure 37.- Continued.

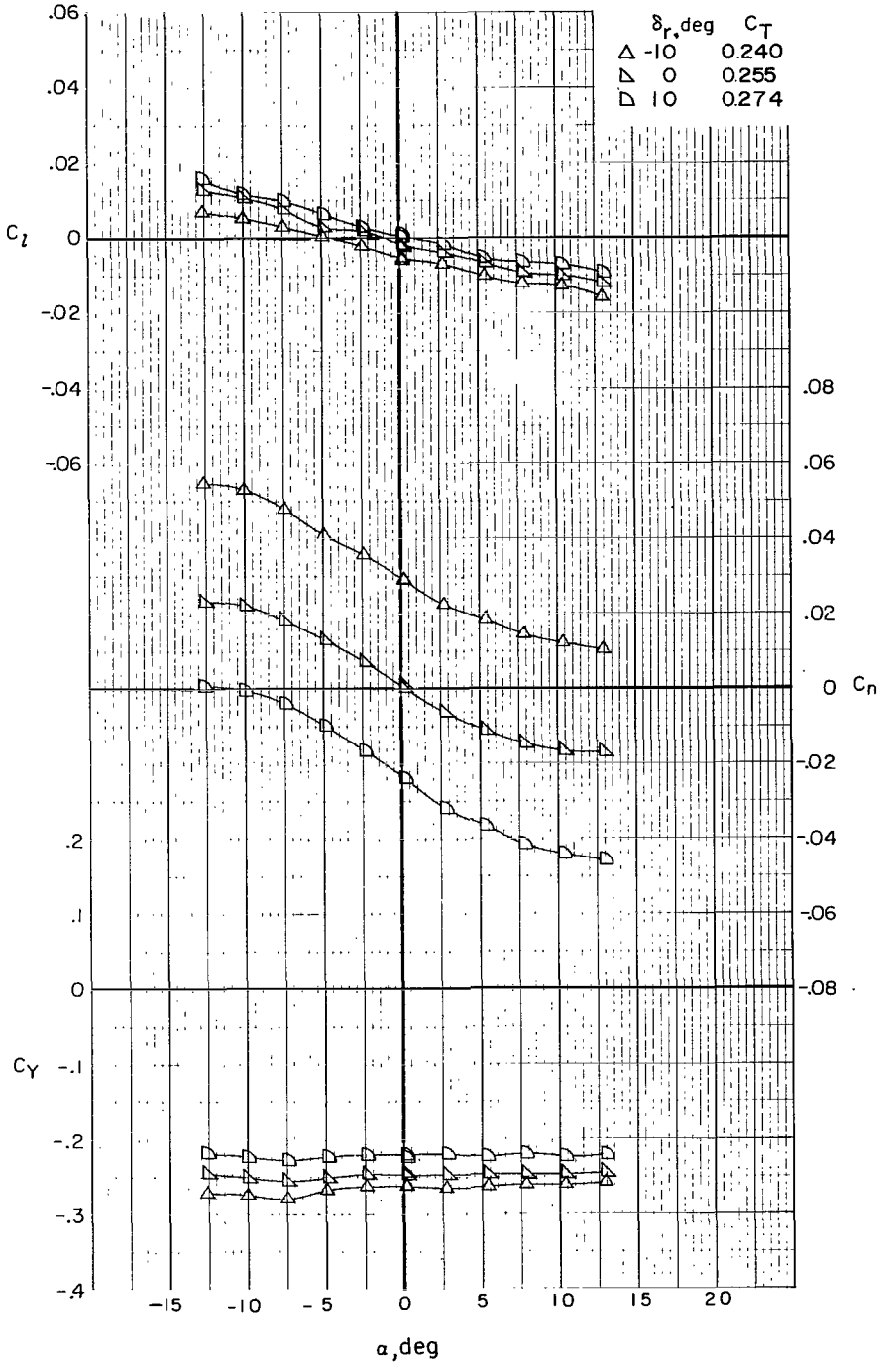

(c) $i_w = 0^o$; $\delta_f = 30^o$; trim thrust; $\beta \approx 10^o$.

Figure 37.- Continued.

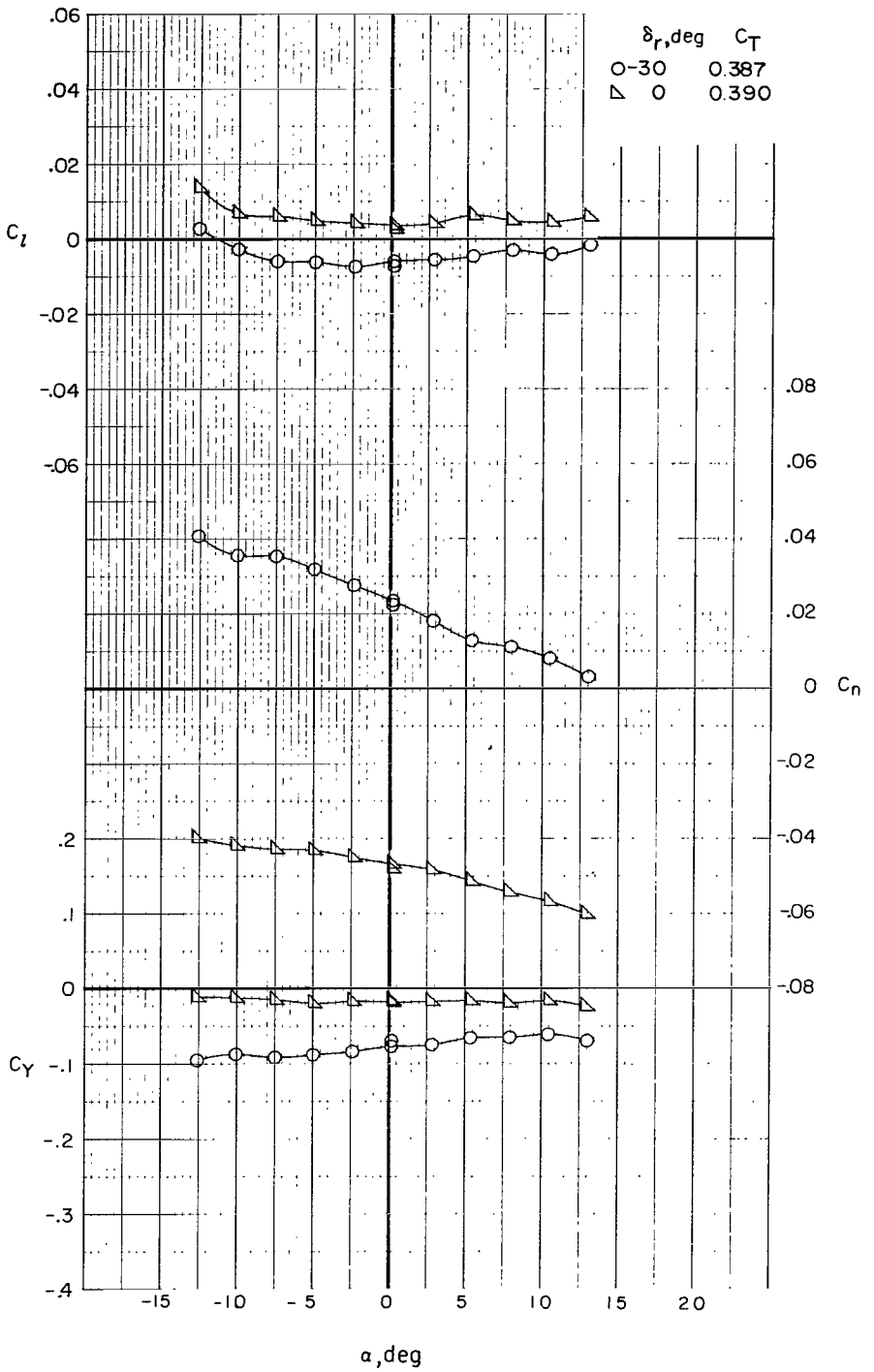

(d) $i_w = 0^o$; $\delta_f = 30^o$; excess thrust; $\beta = 0^o$.

Figure 37.- Continued.

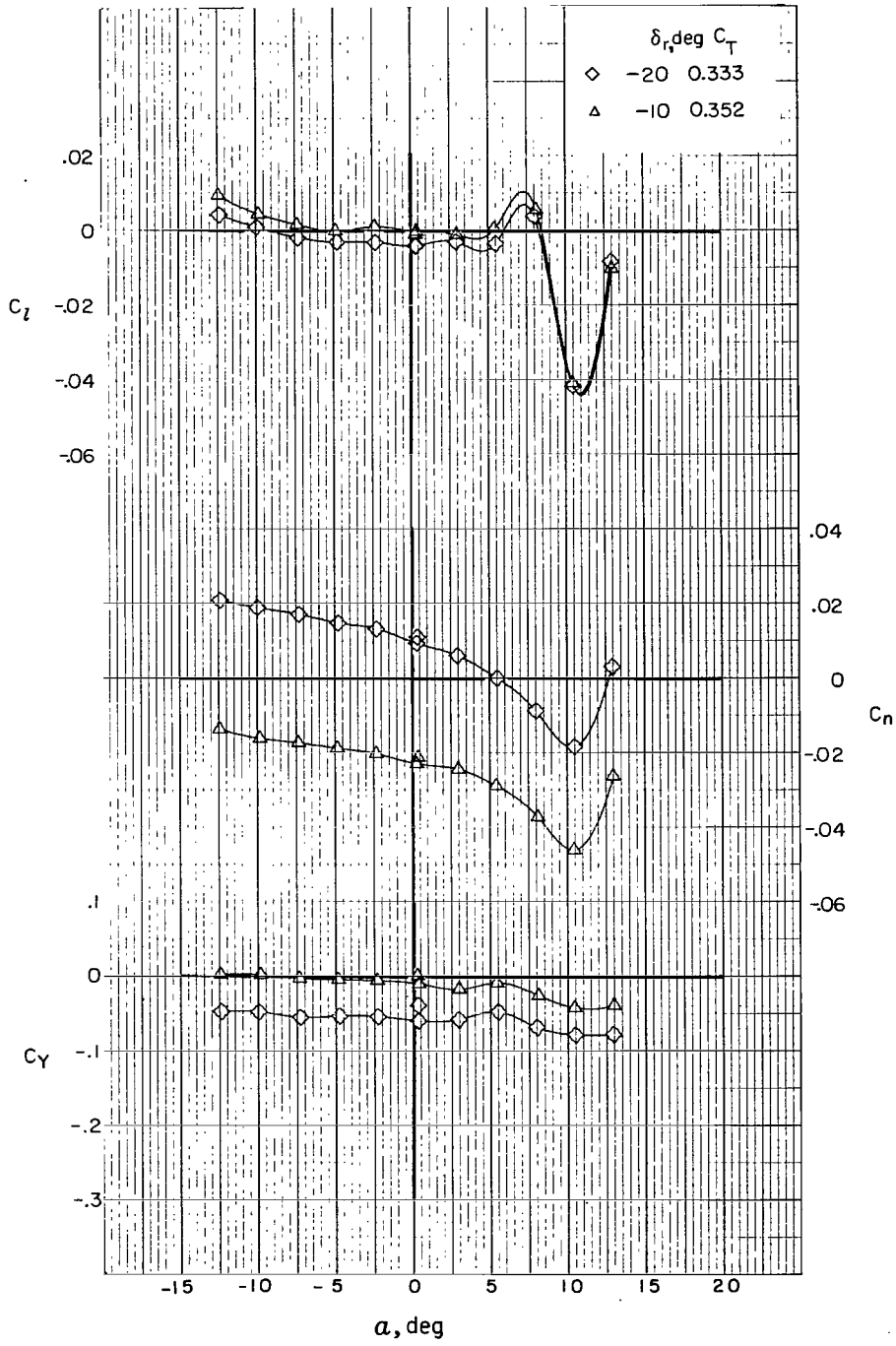

(e) $i_w = 7.5^o$; $\delta_f = 30^o$; trim thrust; $\beta = 0^o$.

Figure 37.- Continued.

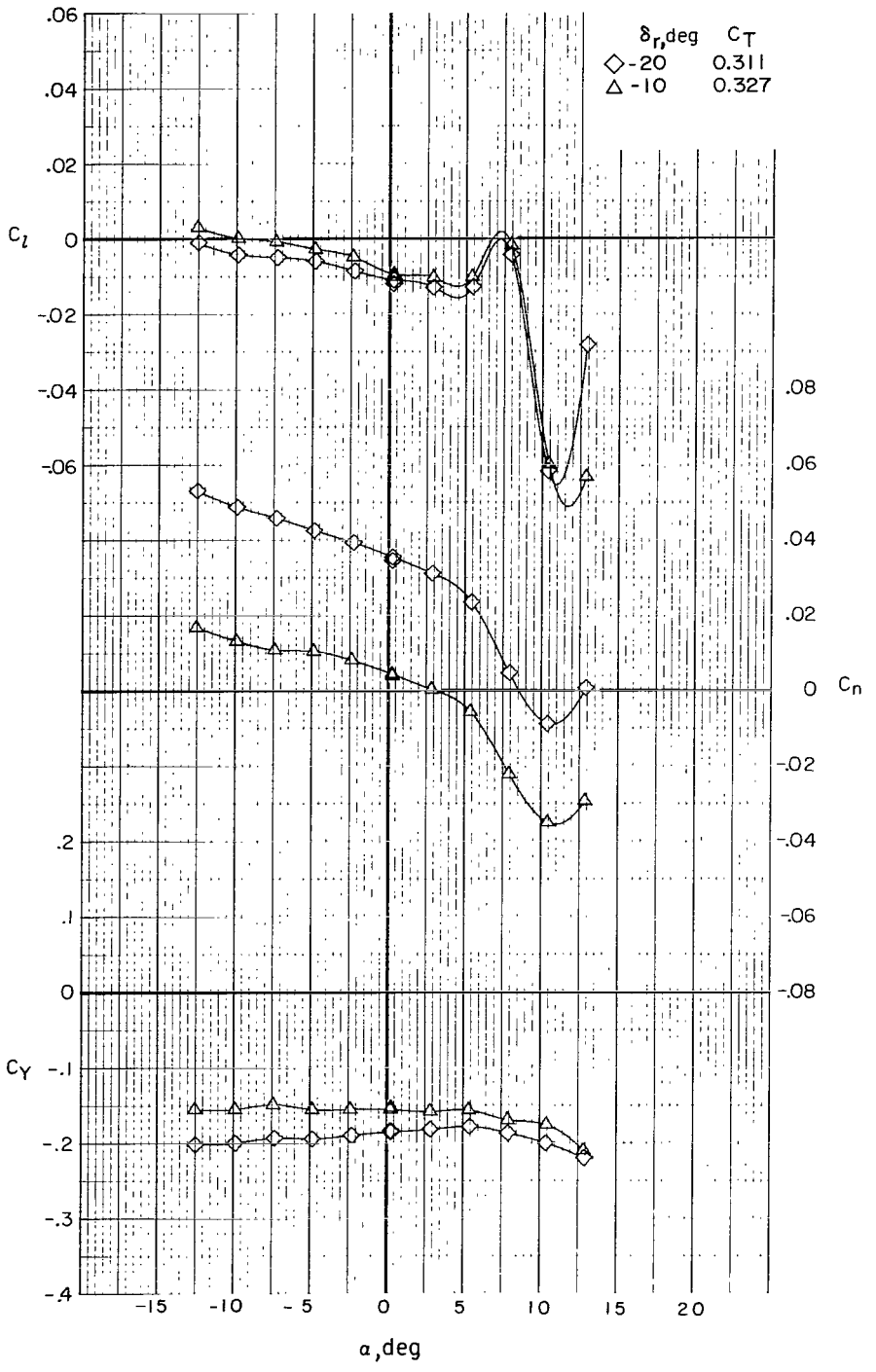

(f) $i_W = 7.5^o$; $\delta_f = 30^o$; trim thrust; $\beta \approx 5^o$.

Figure 37.- Continued.

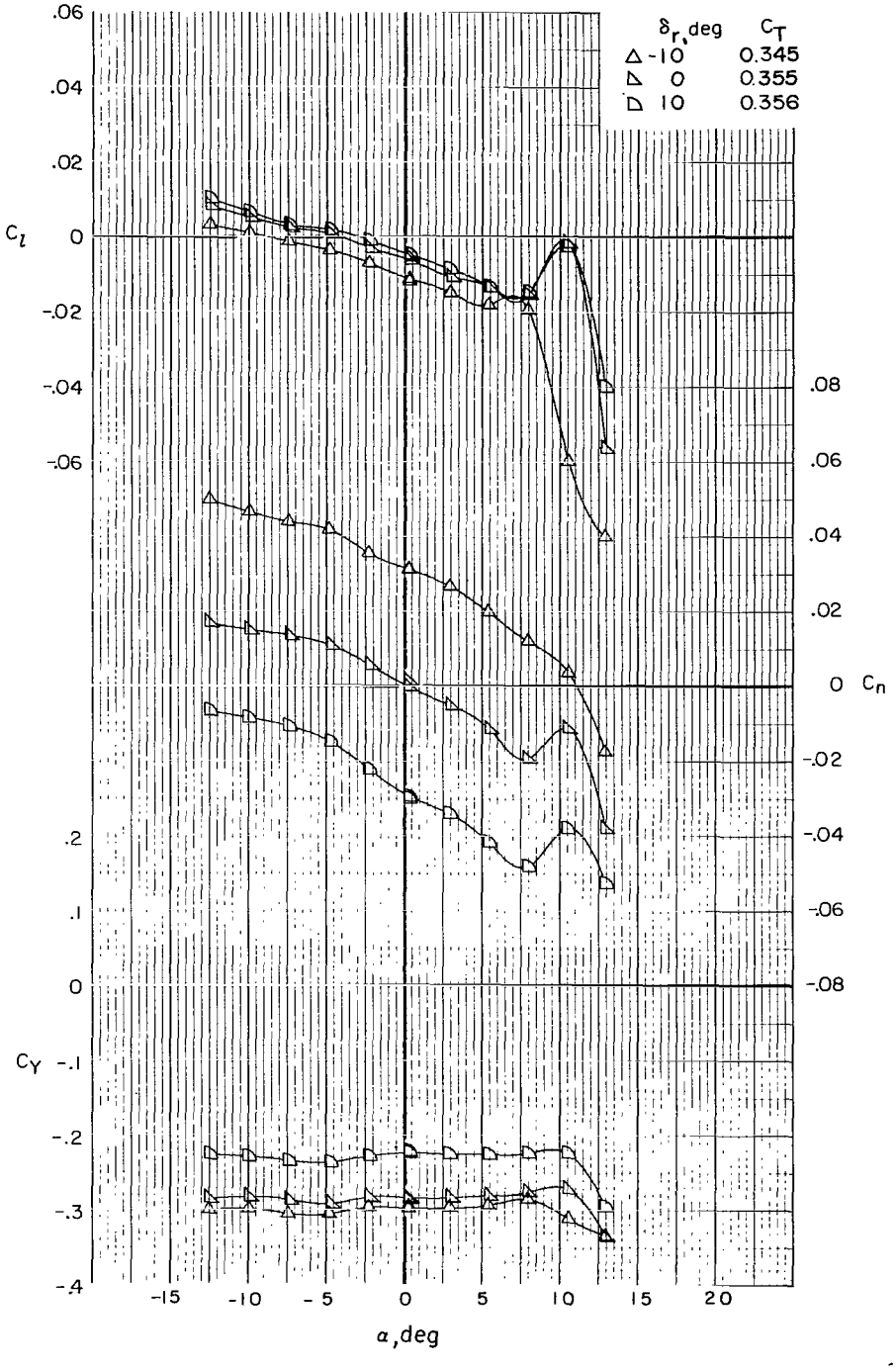

(g) $i_w = 7.5^o$; $\delta_f = 30^o$; trim thrust; $\beta \approx 10^o$.

Figure 37.- Continued.

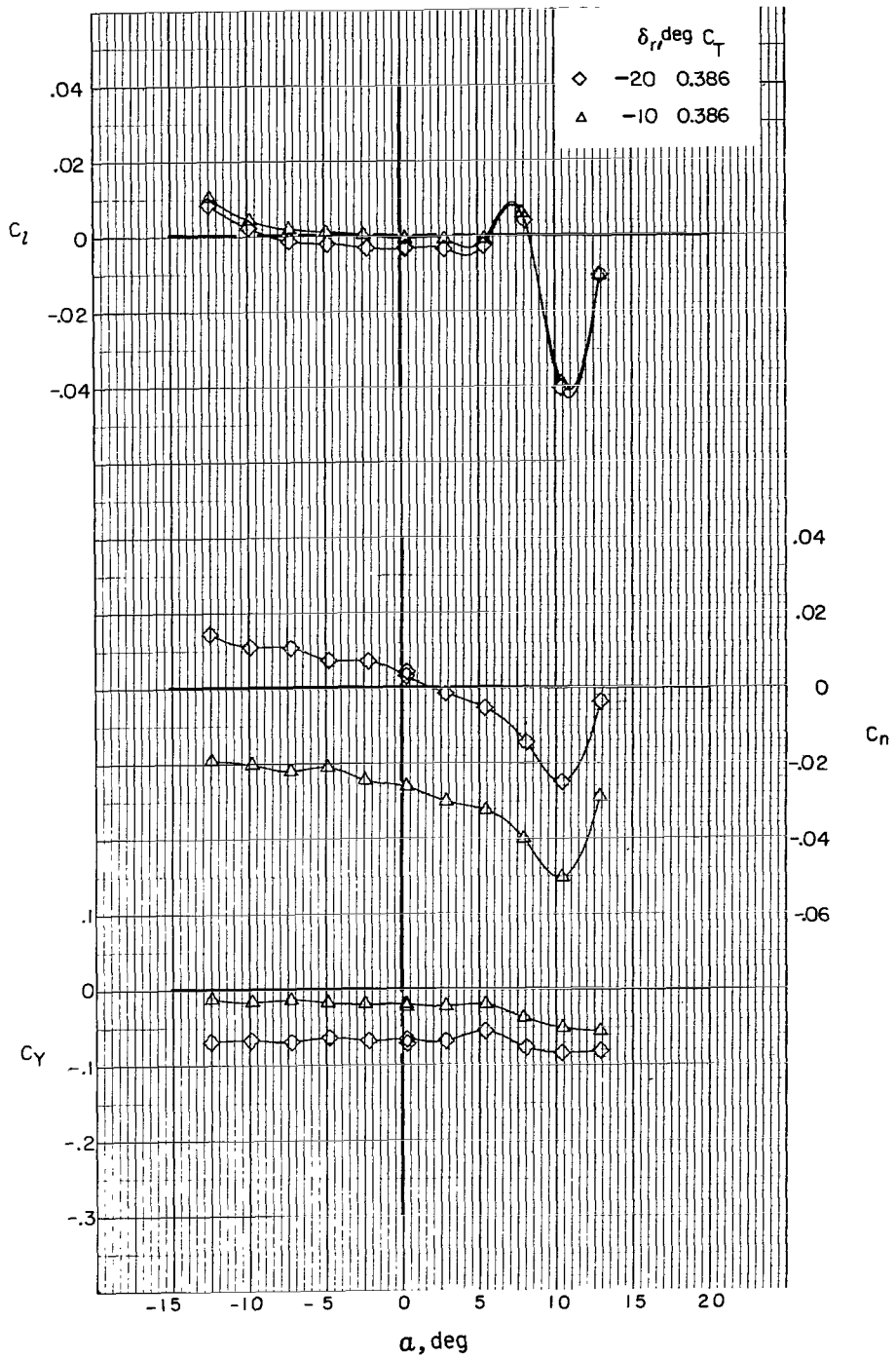

(h) $i_w = 7.5^o$; $\delta_f = 30^o$; excess thrust; $\beta = 0^o$.

Figure 37.- Concluded.

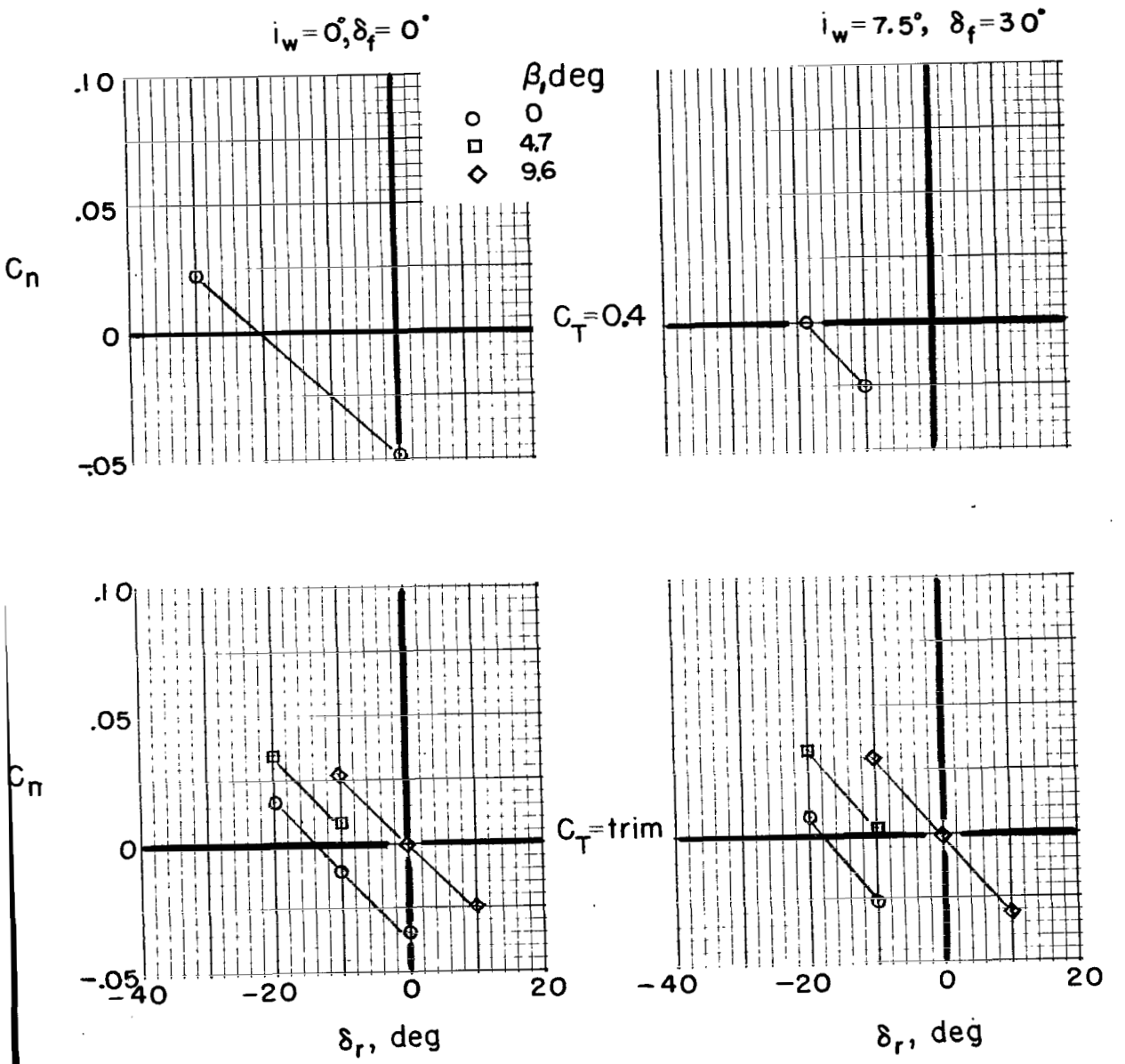

Figure 38.- Variation of C_n with δ_r for Phase III baseline configuration with left engine windmilling.

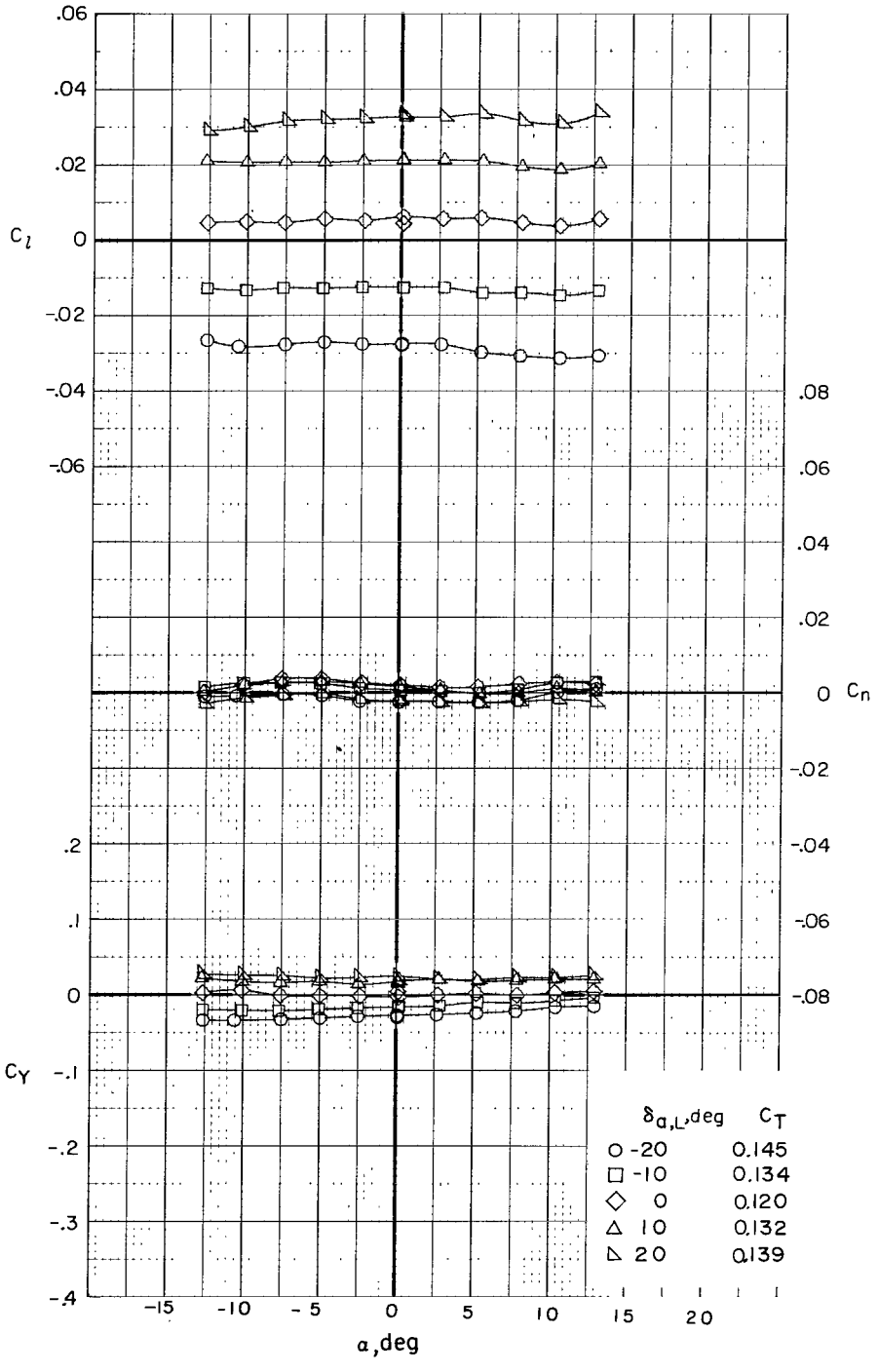

(a) $i_W = 0^o$; $\delta_f = 0^o$; $\beta = 0^o$.

Figure 39.- Effect of left aileron deflection on lateral-directional characteristics of Phase III baseline configuration. Trim thrust.

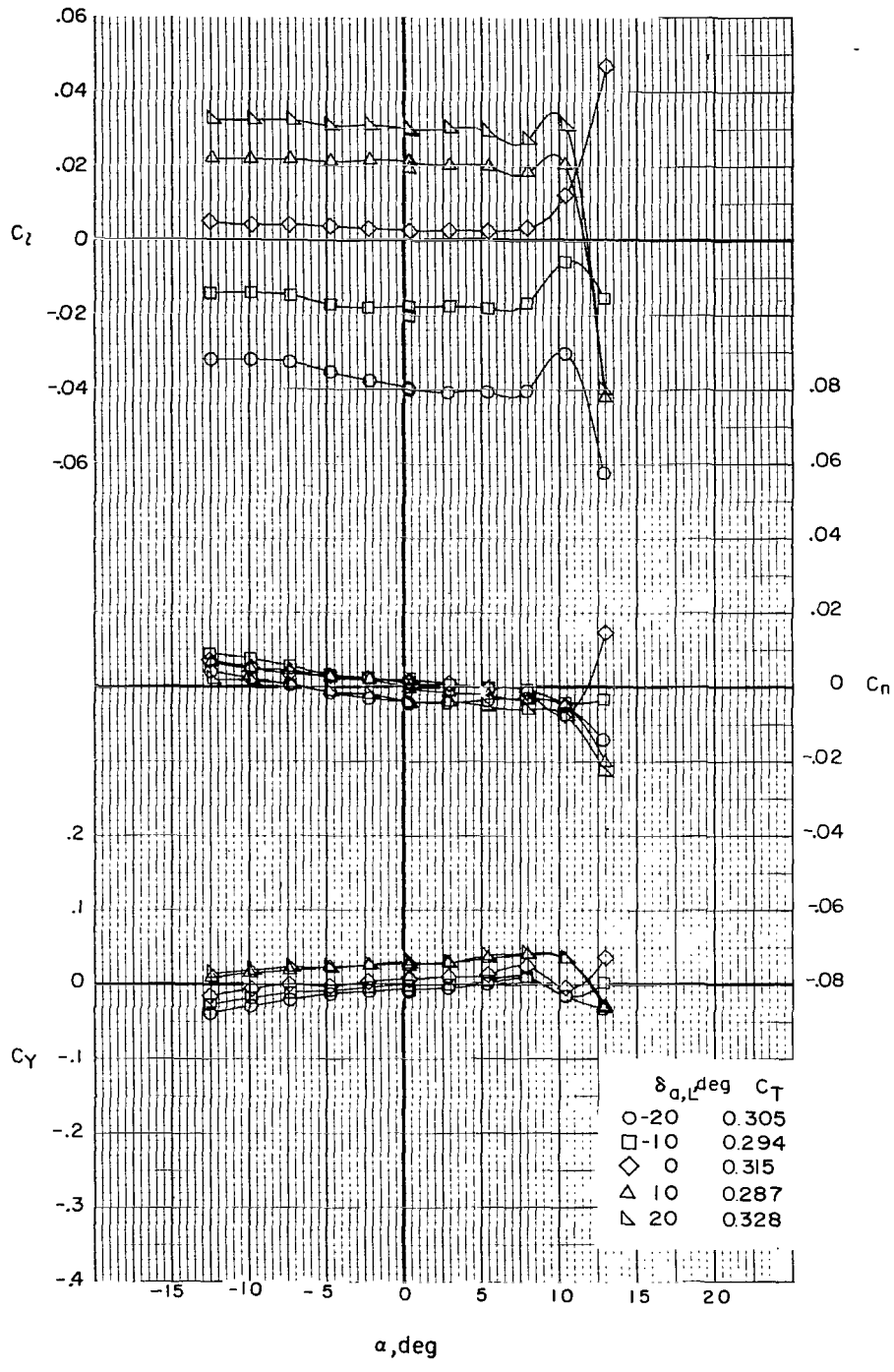

(b) $i_w = 7.5^o$; $\delta_f = 30^o$; $\beta = 0^o$.

Figure 39.- Concluded.

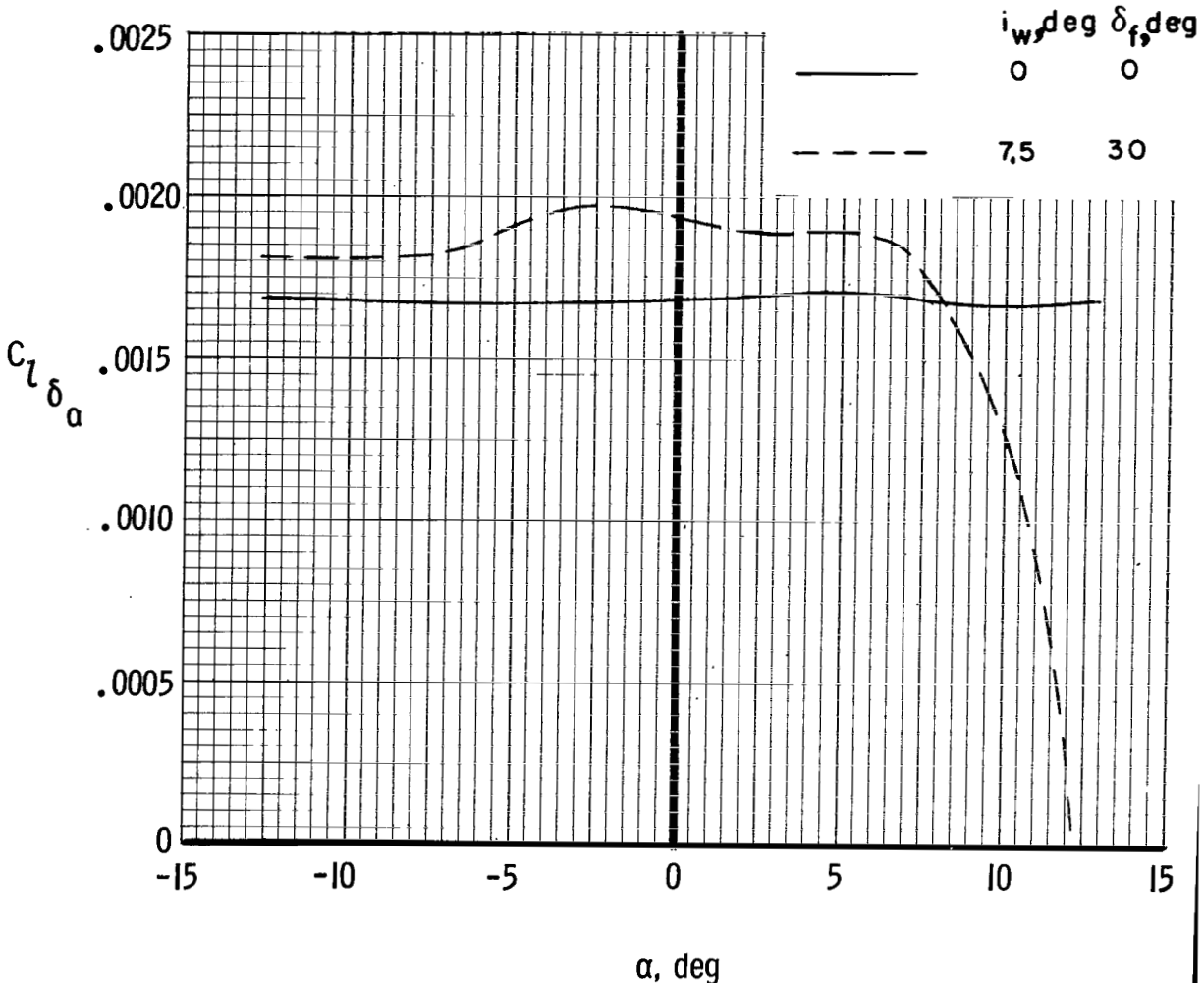

Figure 40.- Variation of left aileron effectiveness with angle of attack for Phase III baseline configuration. $\beta = 0^{o}$; trim thrust.

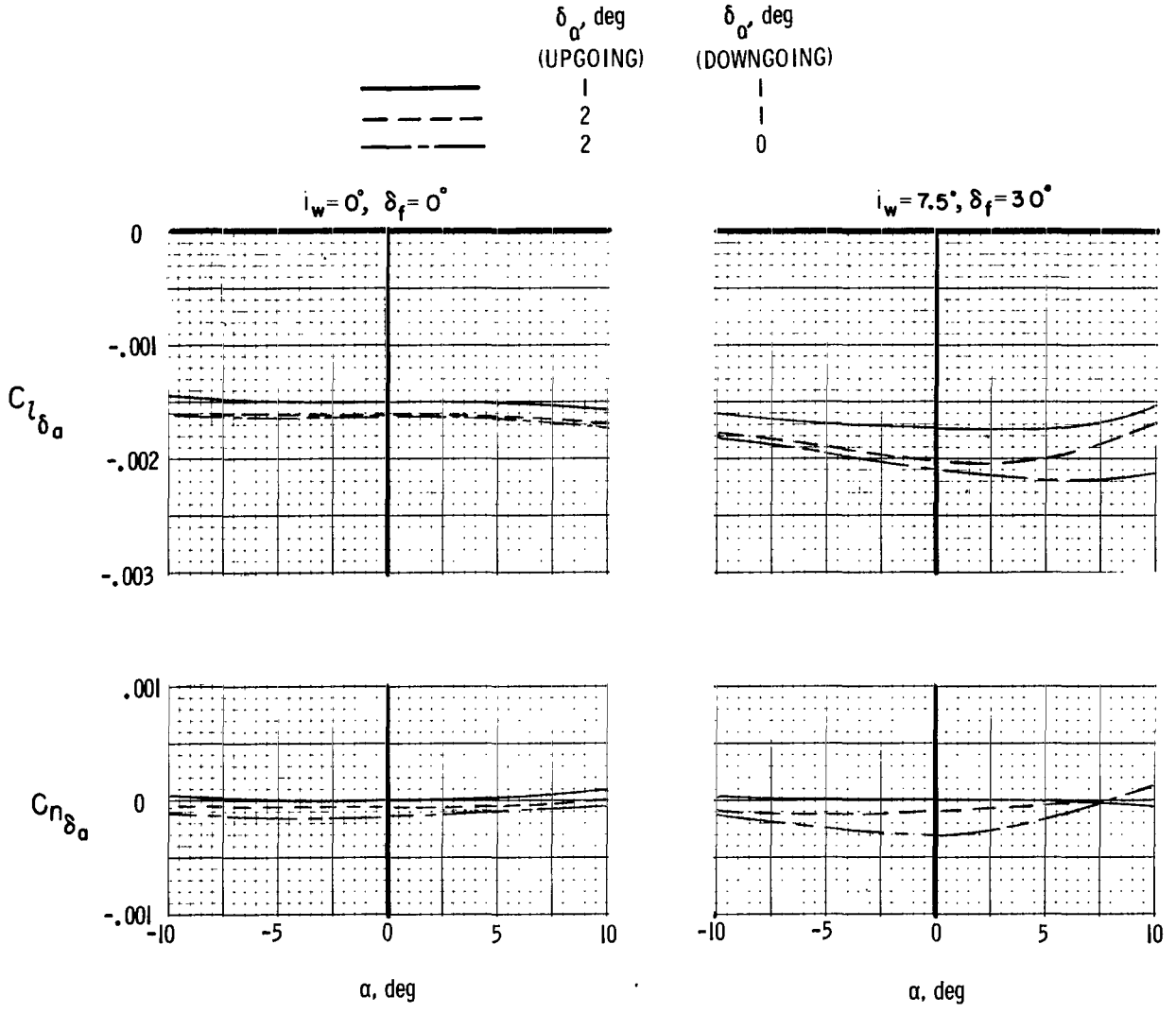

Figure 41.- Effect of differential aileron deflection on lateral control parameters $C_{l_{\delta_a}}$ and $C_{n_{\delta_a}}$ for Phase III baseline configuration.

"The aeronautical and space activities of the United States shall be conducted so as to contribute . . . to the expansion of human knowledge of phenomena in the atmosphere and space. The Administration shall provide for the widest practicable and appropriate dissemination of information concerning its activities and the results thereof."

—NATIONAL AERONAUTICS AND SPACE ACT OF 1958

NASA SCIENTIFIC AND TECHNICAL PUBLICATIONS

TECHNICAL REPORTS: Scientific and technical information considered important, complete, and a lasting contribution to existing knowledge.

TECHNICAL NOTES: Information less broad in scope but nevertheless of importance as a contribution to existing knowledge.

TECHNICAL MEMORANDUMS: Information receiving limited distribution because of preliminary data, security classification, or other reasons. Also includes conference proceedings with either limited or unlimited distribution.

CONTRACTOR REPORTS: Scientific and technical information generated under a NASA contract or grant and considered an important contribution to existing knowledge.

TECHNICAL TRANSLATIONS: Information published in a foreign language considered to merit NASA distribution in English.

SPECIAL PUBLICATIONS: Information derived from or of value to NASA activities. Publications include final reports of major projects, monographs, data compilations, handbooks, sourcebooks, and special bibliographies.

TECHNOLOGY UTILIZATION PUBLICATIONS: Information on technology used by NASA that may be of particular interest in commercial and other non-aerospace applications. Publications include Tech Briefs, Technology Utilization Reports and Technology Surveys.

Details on the availability of these publications may be obtained from:

SCIENTIFIC AND TECHNICAL INFORMATION OFFICE

NATIONAL AERONAUTICS AND SPACE ADMINISTRATION

Washington, D.C. 20546